Universität Zürich[UZH]

Physik-Institut

Annual Report
April 2012 - March 2013

Winterthurerstrasse 190, CH-8057 Zürich/Schweiz

Front picture: the first step in a spin- and angle-resolved photoemission experiment at the COPHEE end station of the Swiss Light Source at PSI (see Sec.: 15.2): Dr. Hugo Dil places samples of topological insulators onto the manipulator of the fast entry lock of the vacuum chamber. The picture on the back cover gives an overall view of the end station with the entry lock now closed, featuring a long transfer rod for bringing the samples to the measurement chamber.

Sekretariat	044 635 5721	secret@physik.uzh.ch
Prof. C. Amsler	022 767 2914	amsler@cern.ch
Prof. L. Baudis	044 635 5777	lbaudis@physik.uzh.ch
Prof. F. Canelli	044 635 5784	canelli@physik.uzh.ch
Prof. V. Chiochia	022 767 6041	vincenzo.chiochia@cern.ch
Prof. H.-W. Fink	044 635 5801	hwfink@physik.uzh.ch
Prof. H. Keller	044 635 5748	keller@physik.uzh.ch
Prof. B. Kilminster	044 635 5802	bjk@physik.uzh.ch
Prof. J. Osterwalder	044 635 5827	osterwal@physik.uzh.ch
Prof. A. Schilling	044 635 5791	schilling@physik.uzh.ch
Prof. U.D. Straumann	044 635 5768	strauman@physik.uzh.ch

The annual reports are available on the internet: http://www.physik.uzh.ch/reports.shtml.

Preface

Scientific research at the Physik-Institut covers a broad spectrum of experimental physics, including the physics of biological systems, of nanometer structures, of fundamental properties of materials and of high temperature superconductors as well as surface physics and accelerator and non-accelerator based elementary particle and astroparticle physics. During the reporting period the institute's 104 employees from 21 countries achieved an impressive number of results, as documented by no less than 71 presentations at international scientific conferences and 249 original publications. Nine PhD theses, six master and nineteen bachelor theses have been completed.

This report summarizes the activities of our ten research groups during the past year. The discovery of what meanwhile was confirmed to be the Higgs boson is no-doubt one of the greatest scientific breakthroughs of recent years, linking a very fundamental theoretical prediction from the early 1960's with an enormous experimental effort culminating in its verification half a century later. Four of our research groups contributed to this result.

The scientific and technical portfolio of our institute contains many more topics, in which our results are highly recognized worldwide, as is documented by the seventeen contributions to this report. I'd like to mention three more highlights of the past year:

- Our institute plays a prominent role in the search for the constituents of the mysterious dark matter in the universe, performed in the low-background underground laboratory at Gran Sasso near Roma. XENON100 published the world's most stringent limits on WIMP [a]-nucleon cross sections, both spin-independent and spin-dependent (Sec. 4).

- New imaging techniques with coherent low energy electrons are explored for applications in, for instance, biological systems. Last year a combination of holography and coherent diffraction with low energy electrons has revealed the arrangement of the 660'000 unit cells of a freestanding graphene sheet with 2Å resolution (Sec. 16).

- A long hunt for the decay mode $B_s \to \mu\mu$ has finally come to success with its first observation by the LHCb collaboration (Sec. 11). This decay is very sensitive to hypothetical new physics contributions and a large region of model space can now be excluded. The rare decay $B \to K^*\mu\mu$ was studied in detail the first time ever. Relevant parts of both analyses were done in our LHCb group.

In summer 2012 two new professors joined our institute, both working in the field of experimental particle physics. Prof. Dr. Florencia Canelli joined us in August 2012. She was a member of the ATLAS collaboration at the LHC where her group was mainly involved in the development of the fast track trigger and physics searches including the Higgs boson. Previously her research was based at the D0 and CDF experiments of

[a] *Weakly Interacting Massive Particles*

the Tevatron collider at Fermilab. She left ATLAS in November 2012 and is presently building up her own team within CMS. The CMS experiment is now preparing an upgrade to the silicon pixel tracking detector which is necessary to maintain tracking efficiency and heavy quark identification capability at the future increased interaction rates. Prof. Dr. Florencia Canelli's group is involved in setting up and testing the full readout chain and associated data acquisition software.

The second new group, lead by Prof. Dr. Ben Kilminster, is currently involved in several projects. As a years-long member and former convener of the CDF Higgs group, Ben Kilminster played an important role in the observed evidence for a Higgs boson decaying into b quarks. His work towards improved b-jet and missing energy determinations, multivariate analysis techniques, and b-tagging was instrumental for reaching this result. He joined CMS in time to contribute to the CMS Higgs discovery which is based on the multiple evidence from different final states. The group contributes to technical developments like new cooling systems and prototype supply tube structures. They also plan to integrate the electronics boards, cables and sensor modules of the pixel detector after its upgrade. Kilminster's group is also involved in a development for using CCD detectors in dark matter searches, in order to reach the lowest possible energy thresholds (DAMIC and CONNIE).

Two members of our institute were elected as assistant professors by the Swiss national science foundation (SNF), receiving significant grants to build up their own research groups. Prof. Dr. Hugo Dil, present member of the surface physics group, will join EPFL, while Prof. Dr. Nicola Serra, member of the LHCb group, will start his own group at our institute (both from July 1st, 2013). Based on their longstanding experience the surface physics group (Sec. 15) could join the European *Future & Emerging Technologies* (FET) flagship program on applications of Graphene. In addition they participate in the University Research Priority Program (UFSP) *Light to Chemical Energy Conversion* together with the chemists of our faculty.

By the end of July 2012 Prof. Claude Amsler, a long term member of the institute, retired. Claude started at our institute in 1982 in Peter Truöl's group and was elected Associate Professor in 1987 and Full Professor in 1999. He successfully lead one of the particle physics groups of our institute primarily residing and working at CERN. The group was active in a wide range of experimental research, such as low energy antiproton annihilation, antihydrogen spectroscopy and one of the LHC collaborations. He also served on the board of the Swiss National Science foundation and was a member of the Particle Data Group, where his expertise on meson spectroscopy was highly appreciated. His introductory *Particle and Nuclear Physics* courses were well received by the students and lead to a textbook, which continues to be used by his successors. Claude co-authored more than 500 papers, among them a highly cited article on glueballs. A more detailed presentation of Claude's scientific career follows further below.

Besides pushing back the frontiers of knowledge in our different research projects, communicating our achievements to the public remains a major task which goes beyond the obvious responsibility for the physics education of students at our university. Members of the institute gave talks for the general public and contributed to public events like *Nacht der Forschung* and *Scientifica*. We guided school children through our labs, organized information days for pupils of the *Gymnasium* and visited high schools. We regularly participate in the *European Masterclass for Particle Physics* and have built a model railway, which demonstrates magnetic aspects of superconductivity. There were 25 such outreach events in 2012, corresponding to about 840 working hours in total.

About 800 students have to be taught physics at any point in time. These include students in the medical faculty and those in our own faculty studying biology, chemistry, geography or mathematics. We follow the traditional European concept to unite research and education, so all our 81 physicists are involved in teaching. This includes the 21 Postdocs and 39 PhD students who may teach lab courses or lead problem solving classes. In addition, typically 15 undergraduate physics students and some outside senior physicists support us in teaching.

Members of the institute are active in numerous scientific organisations like the Swiss national research council, and advisory boards and panels of numerous research institutions including CERN and PSI. They also contribute to the academic administration of the university as a whole and are involved in many national and international search committees for new professors.

An important part of the success of our experimental research and our international visibility is based on the excellent technical infrastructure (mechanical and electronics workshop, information technology) and on the highly qualified and strongly motivated technical experts. This allows us to construct state-of-the-art laboratory equipment, and push experimental methods beyond existing technical limits. Our reliable and efficient administrative staff plays a very important role in creating the excellent working climate which is so beneficial for all of us.

Allen Mitarbeitenden möchte ich an dieser Stelle für ihren uneigennützigen Einsatz, ihre Eigeninitiative und die gute Arbeitsstimmung am Institut herzlich danken.

Zürich, June 2013

Prof. Dr. Ueli Straumann

Claude Amsler and co-workers at 46.2019^0 N, 7.1689^0 E, during a recent trip around Ovronnaz

the Scientific Career of Prof. Dr. Claude Amsler

Claude Amsler was born in Solothurn. He studied experimental physics at the ETH-Zürich and obtained his PhD in 1975 with the first particle physics experiment performed at the Paul Scherrer Institute, a measurement of pion scattering on polarized protons. He then joined Queen Mary College (London) as a Research Associate and was delegated to TRIUMF in Vancouver to work on nucleon-nucleon scattering experiments. In 1978 he moved to Brookhaven National Laboratory as a Research Assistant Professor from the University of New Mexico to work on antiproton experiments.

In 1979 he obtained a CERN Fellowship. After a brief leave at the University of Munich he joined in 1982 the Physik-Institut of the University of Zürich, where he submitted his Habilitation in 1987 on nucleon-antinucleon bound states and resonances. He was elected Associate Professor in 1987, then Full Professor in 1999. He has supervised some 40 PhD & Master theses at the Faculty of Sciences.

Claude Amsler contributed to several projects at CERN such as meson spectroscopy in low energy proton-antiproton annihilation - the ASTERIX and CRYSTAL BARREL experiments (which led to the discovery of four mesons), to the first production of cold antihydrogen with ATHENA, and to the first observation of electromagnetically bound kaon-pion pairs (DIRAC experiment). His group joined CMS at the LHC in 1995. He also contributed to the development of liquid argon detectors for dark matter searches (ArDM and ASPERA-DARWIN projects) and to a measurement of the neutrino magnetic moment at the Bugey nuclear power plant (MUNU-experiment).

Claude Amsler is currently involved in the Compact Muon Solenoid (CMS), that has recently discovered a new heavy boson consistent with the Standard Model Higgs particle. His CMS group has also discovered a new particle containing a beauty quark, the Ξ_b^{*0} baryon. Furthermore, he currently participates to the AEgIS-experiment at CERN to measure the gravitational acceleration of antihydrogen.

He is a member of the Particle Data Group, dealing in particular with mesons. Between 1996 and 2003 he led the Forum of High Energy Physicists in Switzerland and coordinated the foundation of CHIPP (Swiss Institute of Particle Physics). He represented Switzerland in the European nuclear physics board NuPECC between 2003 and 2008 and was a member of the ASPERA Evaluation Committees, and is currently advising the Swiss National Research Council, of which he was a full member until 2008.

Since summer 2012 Claude Amsler is Professor Emeritus at the University of Zürich and associated as senior staff member with the Albert Einstein Center for Fundamental Physics of the University of Bern.

Personnel

Scientific personnel

PD Dr. Christof	Aegerter	Phys. Systems Biology
Dr. Ernest	Aguiló	CMS
Prof. Claude	Amsler	AEgIS, DARWIN, DIRAC, CMS
Dr. Jonathan	Anderson	LHCb
Daniel	Assmann	Phys. Systems Biology
Dr. Martin	Auger	XENON
Peter	Barrow	XENON
Prof. Laura	Baudis	DARWIN, GERDA, XENON
Annika	Behrens	DARWIN, XENON
Giovanni	Benato	GERDA
Dr. Markus	Bendele	Superconductivity/Magnetism
Dr. Angela	Benelli	DIRAC
Carlo	Bernard	Surface Physics
Dr. Roland	Bernet	LHCb
Saskia	Bosma	Superconductivity/Magnetism
Olaf	Bossen	PTMA
Espen	Bowen	LHCb
Albert	Bursche	LHCb
Dr. Carlo	Canali	AEgIS
Prof. Florencia	Canelli	CMS
Dr. Luca	Castiglioni	Surface Physics
Nicola	Chiapolini	LHCb
Prof. Vincenzo	Chiochia	CMS
William	Creus	DARWIN
Dr. Huanyao	Cun	Surface Physics
Dr. Michel	De Cian	LHCb
Dr. Simon Marie	de Visscher	CMS
Dr. Jan-Hugo	Dil	Surface Physics
Christian	Elsasser	LHCb
Dr. Andreas	Engel	PTMA
Dr. Conrad	Escher	Biological Systems
Carlotta	Favaro	CMS
Dr. Alfredo	Ferella	DARWIN, GERDA, XENON
Prof. Hans-Werner	Fink	Biological Systems
Arno	Gadola	CTA
Giulia	Ghielmetti	Phys. Systems Biology
PD Dr. Thomas	Greber	Surface Physics
Roman	Gredig	Mu3e
Michael	Greif	Surface Physics
Henrik	Grundmann	PTMA
Zurab	Guguchia	Superconductivity/Magnetism
Dr. Kiran K.	Guthikonda	GERDA
Patrick	Helfenstein	Biological Systems
Adrian	Hemmi	Surface Physics
Dr. Matthias	Hengsberger	Surface Physics
Dr. Ludovic	Howald	Superconductivity/Magnetism
Dr. Ben	Huber	CTA
Kevin	Inderbitzin	PTMA
Dr. Lars	Jörgensen	AEgIS
Prof. Hugo	Keller	Superconductivity/Magnetism
Gaudenz	Kessler	XENON
Prof. Benjamin	Kilminster	CMS, CDF, DAMIC
Dr. Mitsuhiro	Kimura	AEgIS
Dr. Alexander	Kish	DARWIN, XENON
Gabriel	Landolt	Surface Physics
Flavio	Lanfranconi	Phys. Systems Biology
Dr. Tatiana	Latychevskaia	Biological Systems
Dr. Jean-Nicolas	Longchamp	Biological Systems
Dr. Alexander	Maisuradze	Superconductivity/Magnetism
Dr. Aaron	Manalaysay	CTA, DARWIN
Dr. Teresa	Marrodan-Undagoitia	DARWIN, XENON
Prof. Fumihiko	Matsui	Surface Physics
Daniel	Mayani Paras	XENON
Barbara	Millán Mejías	CMS
Stefan	Muff	Surface Physics
Dr. Katharina	Müller	H1, LHCb
Ulrike	Nienhaus	Phys. Systems Biology
Jennifer	Ngadiuba	CMS
Prof. Jürg	Osterwalder	Surface Physics
Payam	Pakarha	XENON
Francesco	Piastra	XENON
Dr. Christian	Regenfus	AEgIS, DARWIN
Mirena Ivova	Rikova	CMS
Dr. Peter	Robmann	CMS, H1, $\pi \to e\nu$, Mu3e
Silvan	Roth	Surface Physics
Ronny	Rüttimann	Surface Physics
Mirna	Saliba	Biological Systems
Dr. Christophe	Salzmann	LHCb
Prof. Andreas	Schilling	PTMA
Thomas	Schluck	Phys. Systems Biology
Adrian	Schuler	Surface Physics
Dr. Marc	Schumann	DARWIN, XENON
Dr. Nicola	Serra	LHCb
Dr. Bartosz	Slomski	Surface Physics
Dr. Hella	Snoek	CMS
Roland	Stania	Surface Physics
Dr. Olaf	Steinkamp	LHCb
Evelyn	Stilp	Superconductivity/Magnetism
Dr. Barbara	Storaci	LHCb
Dr. James	Storey	AEgIS, CMS
Prof. Ulrich	Straumann	H1, LHCb, CTA, Mu3e
Dr. Silvia	Taroni	CMS
Dr. Mark	Tobin	LHCb
Marco	Tresch	LHCb
Dr. Salvatore	Tupputi	CMS
Dr. Andries	van der Schaaf	$\pi \to e\nu$
Mauro	Verzetti	CMS
Dr. Achim	Vollhardt	Electronics, LHCb, CTA

Fabian	von Rohr	PTMA
Manuel	Walter	DARWIN, GERDA
Dr. Rasmus	Westerström	Surface Physics
Dr. Stephen	Weyeneth	Superconductivity/Magnetism
Flavio	Wicki	Biological Systems

Technical and adminstrative personnel

Alessandro	Basili	CTA
Kurt	Bösiger	Mechanical Workshop
Tiziano	Crudeli	Technical Drawings
Denis	Dürst	Mechanical Workshop
Daniel	Florin	Electronics
Dario	Gabrielli	Mechanical Workshop
Carmelina	Genovese	Secretariat
Ruth	Halter	Secretariat
Alina	Horwege	Biological Systems
Andreas	James	GERDA,XENON
Thomas	Kälin	Surface Physics
Hanspeter	Koch	Support Lectures
Bruno	Lussi	Mechanical Workshop
Reto	Maier	Mechanical Workshop
Lucien	Pauli	Vorlesungsbetrieb
Jacky	Rochet	AEgIS, CMS, DIRAC, DARWIN
Monika	Röllin	Secretariat
Dr. Jean-Pierre	Ruder	CHIPP
Sandra	Saornil Gamarra	LHCb
Marcel	Schaffner	Mechanical Workshop
Silvio	Scherr	Mechanical Workshop
Stefan	Siegrist	PTMA, Superconductivity/Magnetism
Peter	Soland	Electronics
Stefan	Steiner	CAD, LHCb, CTA

Contents

1 Liquid Ar scintillation from neutron induced recoils

C. Amsler, W. Creus, A. Ferella, C. Regenfus, and J. Rochet

Weakly Interacting Massive Particles (WIMPs) are prime candidates for dark matter. The interaction of WIMPs in scintillators (e.g. noble liquids such as liquid argon, LAr) leads to nuclear recoils generating scintillation light. Unfortunately, the light signal from highly ionizing particles is heavily quenched and detection thresholds of a few keV (electron equivalent) are required. The reduced light yield relative to minimum ionizing particles (such as electrons) is described by the scintillation efficiency $\mathcal{L}_{\mathrm{eff}}$ which depends on the recoil energy. Since quenching in LAr is poorly known we are investigating the response to neutrons. For this purpose we have built a neutron scattering facility in our laboratory at CERN (see Fig. 1.1).

Up to $2{\cdot}10^6\mathrm{s}^{-1}$ 2.45 MeV neutrons from the two-body fusion reaction $dd \rightarrow {}^3\mathrm{He} + n$ are emitted isotropically. The reaction chamber is shielded by a 1.6 t polyester cylinder with 2 mm Pb cladding, keeping an acceptable radiation dose from neutrons and X-rays. The structure of the cryogenic cell is shown in the inset of Fig. 1.1. Scintillation light was detected by two Hamamatsu R6091-01 photomultipliers (PMTs) separated by 47 mm defining a cylindrical sensitive volume of 0.2 ℓ. The inner walls of the cell were lined with Tetratex (Teflon) reflector foil. Both this foil and the PMT windows were coated with tetraphenyl-butadiene (TPB) by vacuum evaporation. TPB shifts the 128 nm wavelength of the VUV scintillation light to the range of maximum sensitivity of the bialkali photocathodes around 420 nm.

Neutrons scattering off the LAr are detected by an organic liquid scintillator at varying angle θ which defines the energy of the recoiling argon nucleus. Pulse shape discrimination allows to distinguish between neutrons and photons. In addition, the neutron time of flight helps to reduce background, mainly from inelastic collisions.

1.1 Pulse shape analysis

Liquid argon generates fast and slow light with decay times of $\tau_1 \simeq 6$ ns (from the excimer singlet state) and
$\tau_2 \simeq 1.6$ μs (from the triplet state). Above 10 keV heavily 1
ionizing particles feed mostly the fast component, while electrons contribute mostly to the slow component[1].

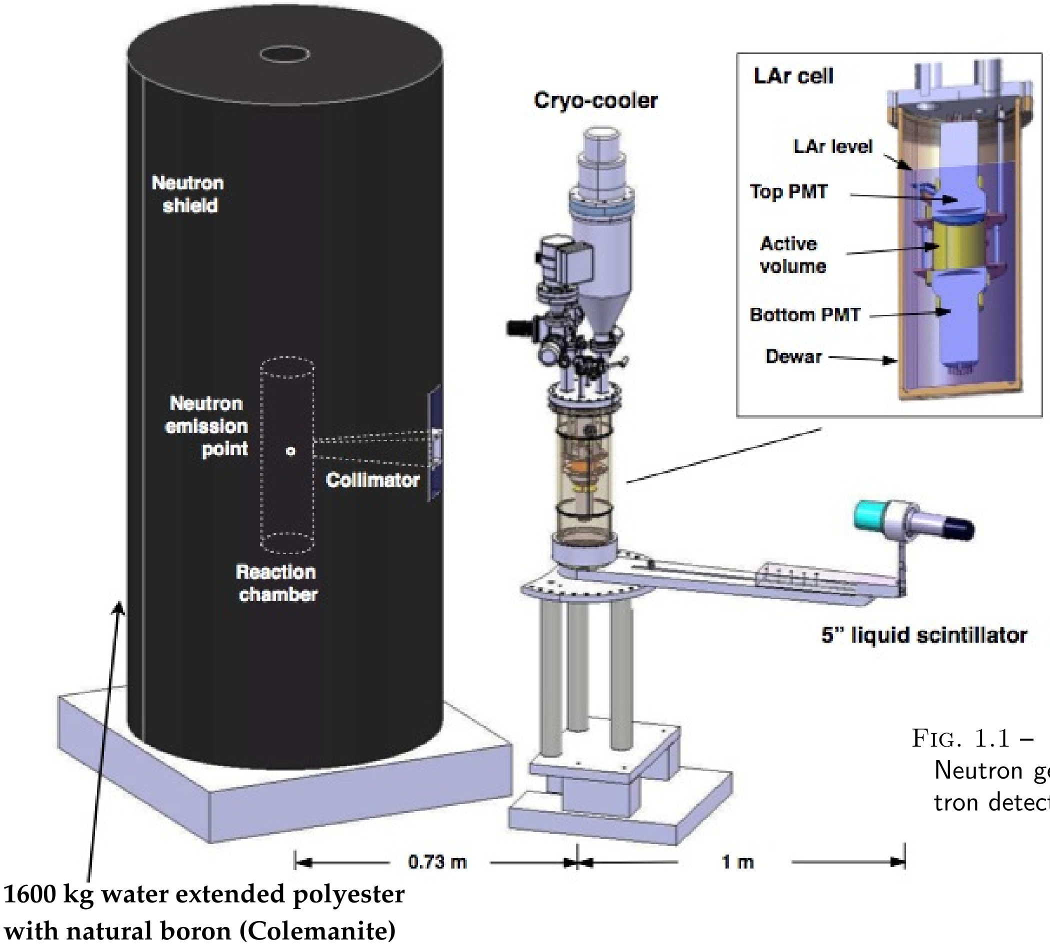

FIG. 1.1 – Neutron generator, LAr target and neutron detector. Inset: LAr target cell.

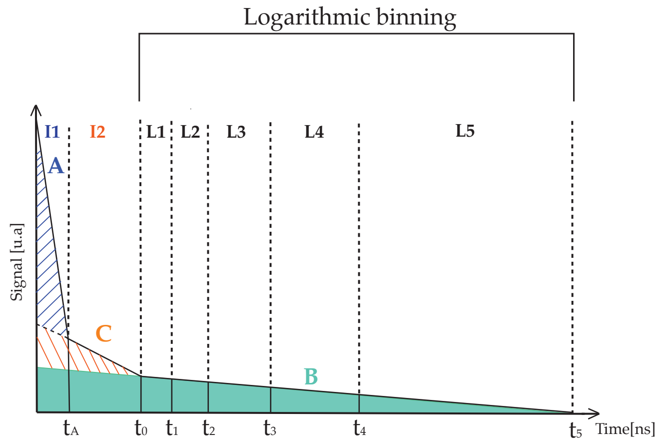

FIG. 1.2 – LAr scintillation signal (logarithmic scale) with the three exponential components A - C, and the time intervals used in the waveform analysis for particle identification (see text).

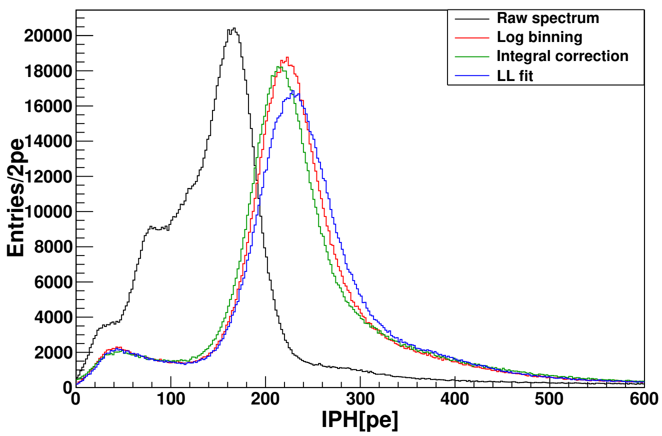

FIG. 1.3 – Distribution of number of photoelectrons (p.e.) observed from a ^{241}Am source (60 keV-γ) combining runs with various LAr purity levels which broadens the energy distribution (black curve). Applying the log binning method (see text) improves the spectrum significantly.

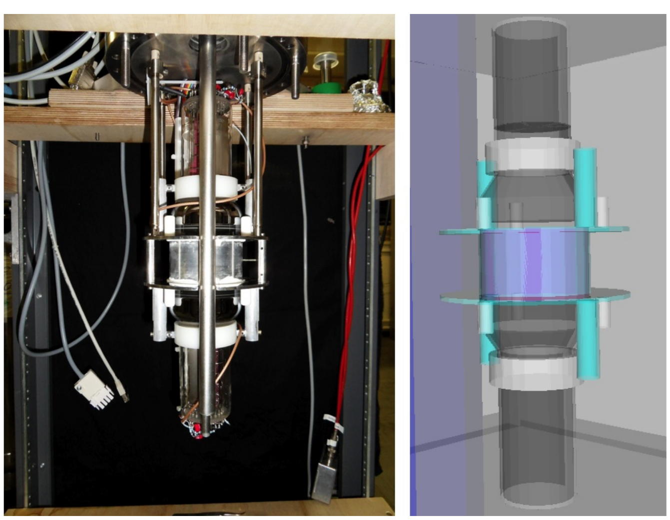

FIG. 1.4 – Picture (left) and GEANT4 model (right) of the LAr cell.

Impurities in LAr (such as N_2, O_2, H_2O and CO+CO_2) can absorb VUV scintillation light or quench argon excimer states. The latter process decreases the measured τ_2 and induces losses in the scintillation light (slow part) [2].

In 2012 we developed a method to reconstruct the undisturbed scintillation components from the measured pulse shape. The light pulse is divided in time intervals (Fig.1.2) corresponding to fast (I1) and slow (L) light emission, as well as to a weak intermediate state (I2) [1]. Impurities only affect the late regions of the light pulse so only the slope of slow component B but not its amplitude at t=0. The latter is found most accurately from the weighted mean of the (equal) entries in logarithmically sized integration intervals L1...L5 (spaced according to the *measured* slope of B). Once B is reconstructed, C is found from the I2 integral after subtraction of the contribution from B and, finally, A is found from the I1 integral after subtraction of the contributions from B and C. The total light yield is given by the sum of all components, where the observed B is replaced by the undisturbed distribution (green component in Fig.1.2) based on the measured amplitude at t=0 and the true decay time of 1.6 μs. Details on this technique can be found in [3] and [1].

Figure 1.3 shows light yield spectra of ^{241}Am 60 keV photons from a mix of LAr data samples with varying purity levels. Different pulse shape analysis schemes are compared. The logarithmic binning method described above gives both the best resolution and the smallest systematic error.

1.2 $\mathcal{L}_{\mathrm{eff}}$

A GEANT4 description of the neutron experiment includes the neutron generator with its shielding and collimator, the various components of the LAr detector (cryostat, vessel, reflector foil, PMTs, support frame, etc.) and the liquid scintillators. In Fig.1.4 the simulated LAr cell is compared with the real piece of equipment.

Neutrons of 2.45 MeV were generated isotropically in 4π and 10^8 events were simulated for each scattering angle. In Fig. 1.5 the recoil energy distribution for a scattering angle of 40° is decomposed in various contributions. As can be seen the majority of the events undergo a single scattering in the LAr cell.

A comparison with the measured spectrum shown in Fig. 1.6 enables a determination of the LAr light yield $\mathcal{L}_{\mathrm{eff}}$ for neutron interactions. A χ^2 minimization was performed which uses the energy resolution as a second free parameter. The best fit, illustrated by the red histogram in Fig. 1.6, is obtained for $\mathcal{L}_{\mathrm{eff}} = 0.289 \pm 0.012$.

Finally, we show in Fig. 1.7 and Table 1.1 our results for the light yield $\mathcal{L}_{\mathrm{eff}}$, as a function of scattering angle.

[1] The nature of this component is uncertain. It could be due, for example, to recombining ionisation charge or to collisional triplet to singlet transitions.

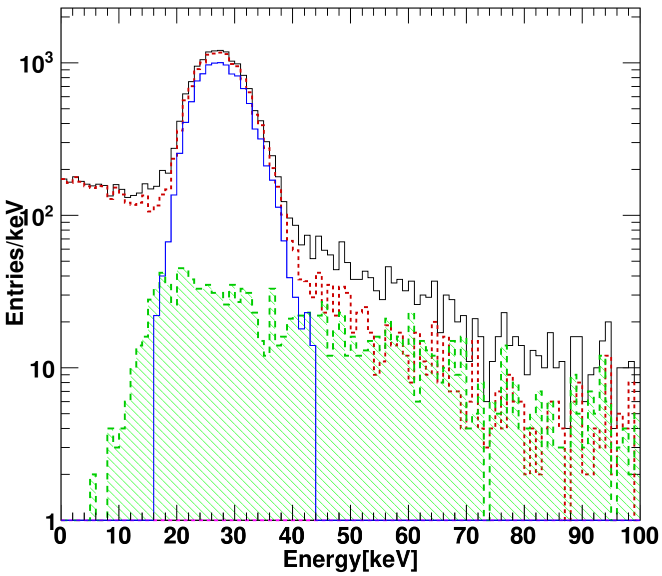

FIG. 1.5 –
Simulated spectrum at $\theta = 40^o$ after a time of flight cut at 41 - 48 ns. 58% of the events are contained in a dominant peak (blue) at the 28.5 keV energy deposit expected for a single elastic scattering at this angle. 9.4% of them scatter more than once in the cell resulting in a high-energy tail (green). In 33% of the cases the neutron scatters elsewhere before and/or after the interaction with argon (dashed red). The contribution from inelastic neutron scattering is negligible.

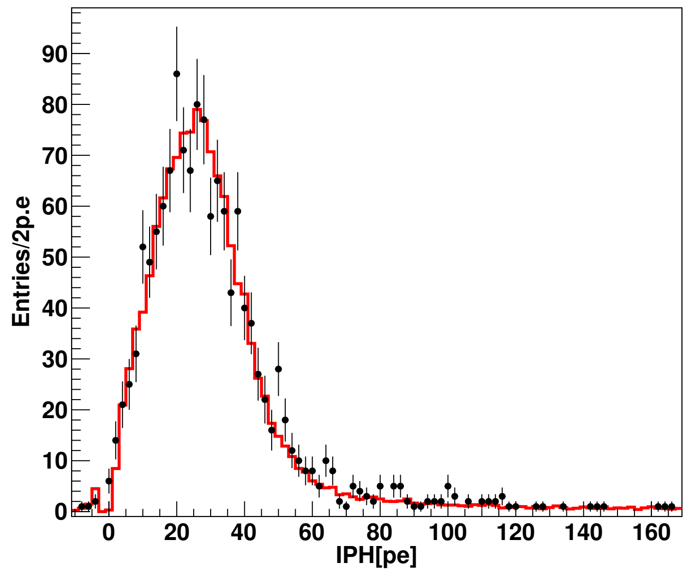

FIG. 1.6 –
Measured pulse height distribution at 40^o and best fit of the simulated recoil spectrum (red histogram).

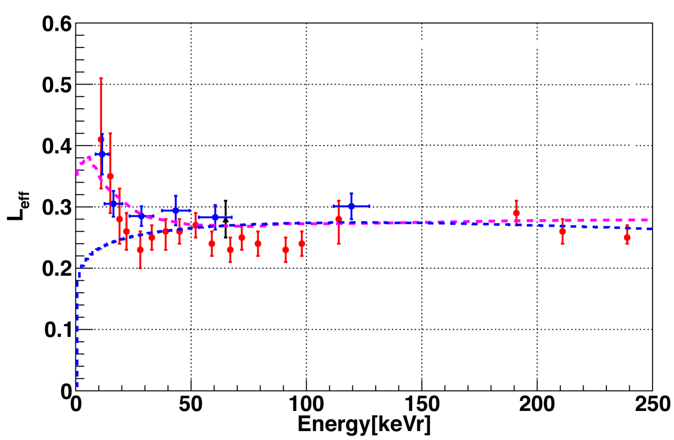

FIG. 1.7 – $\mathcal{L}_{\text{eff}}$ vs. recoil energy. The data points are from this work [3] (blue), from micro-Clean [4] (red) and from WARP [5] (black point at 67 keV). The blue and pink dashed lines are predictions from the Mei [6] and the NEST [7] models, respectively. These values update the preliminary results [1].

TAB. 1.1 –
Results for $\mathcal{L}_{\text{eff}}$ from argon recoils (relative to electrons) vs. scattering angle θ.

θ [°]	Recoil energy [keV]	$\mathcal{L}_{\text{eff}}$
25	11.4	0.386 ± 0.033
30	16.4	0.305 ± 0.021
40	28.5	0.289 ± 0.012
50	43.4	0.294 ± 0.024
60	60.5	0.283 ± 0.020
90	119.5	0.301 ± 0.021

[1] C. Regenfus *et al.*, Journal of Physics: Conference Series **375** (2012) 012019, arXiV:1203.0849.

[2] V. Boccone *et al.*,
J. of Instrumentation **4** (2009) P06001.
C. Amsler et al.,
J. of Instrumentation **5** (2010) P11003.

[3] W. Creus, PhD-thesis, Universität Zürich (submission in June 2013).

[4] D. Gastler *et al.*, Phys. Rev. **C 85** (2012) 065811.

[5] R. Brunetti *et al.*, New Ast. Rev. **49** (2005) 265.

[6] D.–M. Mei *et al.*, Astropart. Phys. **30** (2008)12.

[7] M. Szydagis *et al.*, arXiv: 1106.1613.

2 Test of the equivalence principle with antihydrogen

C. Amsler, C. Canali, L. Jörgensen, M. Kimura, C. Regenfus, J. Rochet, and J. Storey

in collaboration with AEC University of Bern (A. Ariga, T. Ariga, A. Ereditato, J. Kawada, C. Pistillo, and P. Scampoli), INFN Bescia - Firenze - Genova - Milano - Padova - Pavia - Trento, CERN, MPI-K (Heidelberg), Kirchoff Inst. of Phys. (Heidelberg), INR (Moscow), ITEP (Moscow), Univ. Claude Bernard (Lyon), Univ. of Oslo, Univ. of Bergen, Czech Tech. Univ (Prague), ETH-Zurich, Politecnico Milano, Laboratoire Aimé Cotton (Orsay)

(AEgIS Collaboration)

The main goal of the AEgIS experiment (CERN/AD6) is to test the Weak Equivalence Principle (WEP) using antihydrogen ($\bar{H}$). This principle of the universality of free fall has been tested with high precision for matter, but not with antimatter, due to major technical difficulties related to stray electric and magnetic fields. In contrast, the electrically neutral $\bar{H}$ atom is an ideal probe to test the WEP, and the antiproton decelerator (AD) at CERN is a worldwide unique antihydrogen factory. In AEgIS the gravitational deflection of $\bar{H}$ atoms launched horizontally and traversing a moiré deflectometer will be measured with an initial precision of 1% on $|\Delta g|/g$, using a position sensitive annihilation detector. Details on the experiment can be found in ref. [1, 2].

The number of antihydrogen annihilations required to achieve a given precision decreases dramatically with increasing tracking resolution. In the proposal [1] a resolution of some 10 μm was to be achieved with a silicon strip annihilation detector. In 2012 we tested the use of emulsion films to achieve a resolution of the order of 1 μm [3, 4], and completed the construction of the annihilation detector (FACT) used to characterize the antihydrogen cloud prior to its acceleration into an $\bar{H}$ beam. Most of the AEgIS apparatus (apart from the gravity section) was commissioned in 2012, including the antiproton capture trap and the positron line. A photograph of the apparatus is shown in Fig. 2.1.

[1] G. Drobychev *et al.*, http://doc.cern.ch/archive/electronic/cern/preprints/spsc/public/spsc-2007-017.pdf.

[2] A. Kellerbauer *et al.*, Nucl. Instr. and Meth. **B 266** (2008) 351.

[3] C. Amsler *et al.*, J. of Instrumentation **8** (2013) P02015.

[4] M. Kimura *et al.*, 13th Vienna Conference on Instrumentation, (2013).

2.1 Nuclear emulsions

Nuclear emulsions [1] are photographic films with extremely high spatial resolution. A track produced by

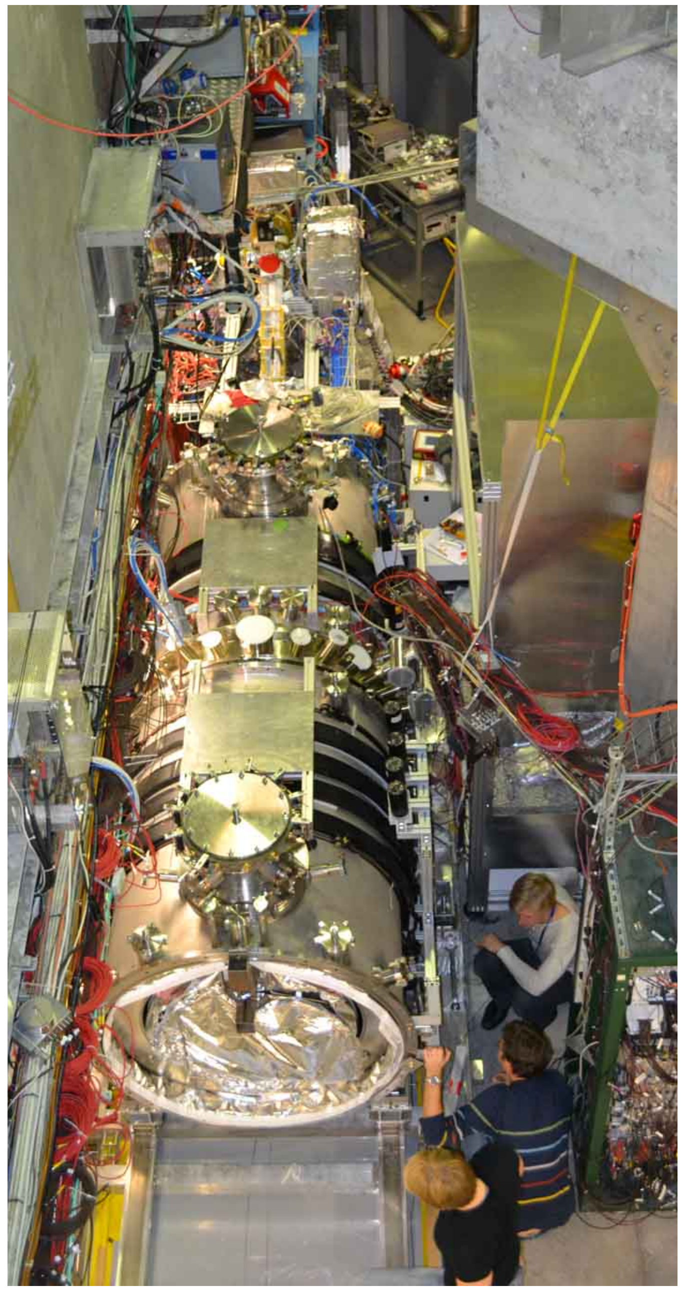

FIG. 2.1 – The AEgIS apparatus in the AD-hall at CERN in December 2012.

Fig. 2.2 – Schematics of the AEgIS detectors. The vertex detector is based on nuclear emulsions. The time-of-flight detector (TOF) measures the velocities of the $\bar{H}$ atoms.

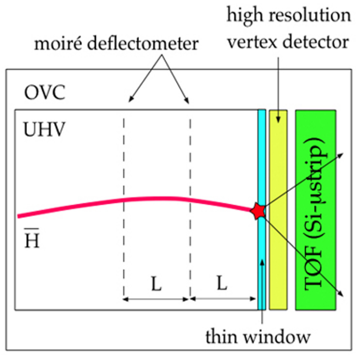

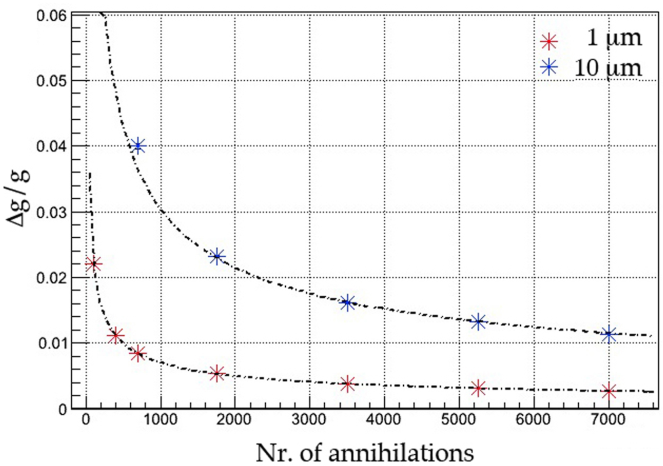

Fig. 2.3 – $\Delta g/g$ vs. number of particles for vertex resolutions of 1 μm and 10 μm.

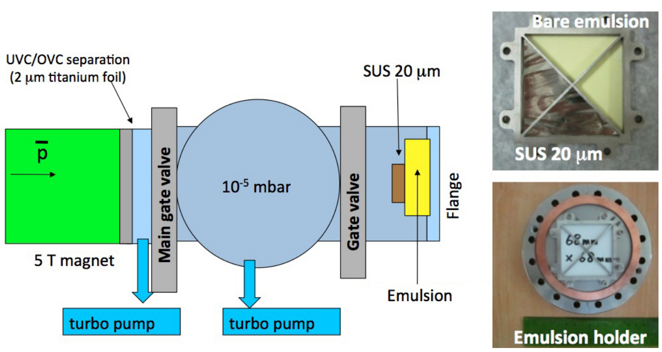

Fig. 2.4 –
Test setup with a picture of the vacuum flange holding the emulsion stack attached by a crossed bar frame.

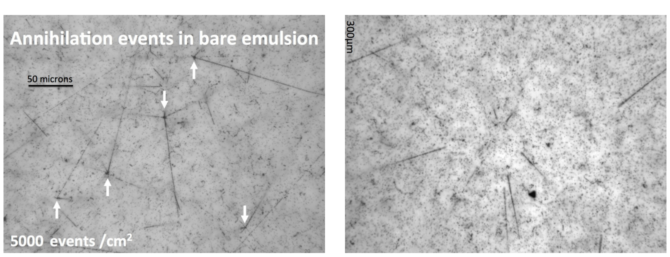

Fig. 2.5 – Typical antiproton annihilation vertices in the bare emulsion (left) and tracks observed behind a thin silver foil in which the antiprotons annihilate (right).

a charged particle is detected as a sequence of silver grains, where about 36 Ag grains per 100 μm are created by a minimum ionizing particle. The intrinsic spatial resolution is around 50 nm. For AEgIS we developed nuclear emulsions which can be used in ordinary vacuum (OVC, 10^{-5} – 10^{-7} mbar). Figure 2.2 shows the setup envisaged for the g-measurement. The expected performance is shown in Fig. 2.3.

A sketch of the setup used for test exposures with stopping antiprotons in 2012 is shown in Fig. 2.4. The emulsion detector consisted of 5 sandwiches made of emulsion films (OPERA type). A thin foil will be needed in the g-measurement as a window to separate the $\bar{H}$ beam line at UHV pressure from the OVC section containing the emulsion detector. Thus for the tests half of the emulsion surface was covered by a 20 μm (SUS) stainless steel foil.

In December 2012 we also carried out measurements with a series of thin foils of varying compositions (Al, Si, Ti, Cu, Ag, Au, Pb) to determine the relative contributions from protons, nuclear fragments and pions as a function of atomic number. Figure 2.5 shows annihilation vertices on the bare emulsion surfaces and tracks behind a 5 μm thick silver foil. Tracks emerging from the annihilation vertex are clearly observed. Tracks from nuclear fragments, protons, and pions were reconstructed and the distance of closest approach between pairs of tracks was calculated. With *e.g.* a 20 μm steel window a vertex resolution of ~ 1 μm can be achieved.

Products from annihilating antiprotons (or $\bar{H}$ atoms) are emitted isotropically, in contrast to the τ-decay products measured in OPERA. The scanning efficiency must be improved for tracks traversing at large angles. We are also investigating the emulsions with higher sensitivity which were developed at Nagoya University and coated onto glass substrates in Bern. Glass is well suited for highest position resolutions thanks to its superior mechanical stability compared to plastic.

A proof of principle of the deflectometer to be used AEgIS was also performed in 2012 with emulsion films irradiated with antiprotons passing through a small moiré deflectometer shown in Fig. 2.6. The device contained several pairs of gratings with different spacings,

Fig. 2.6 – The miniature moiré deflectometer.

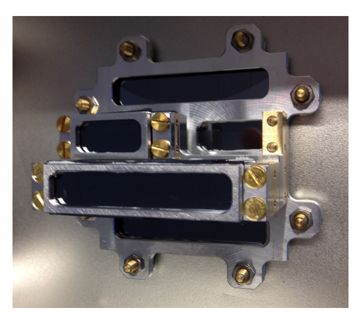

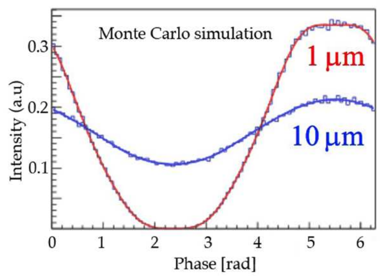

Fig. 2.7 – Simulated distributions of reconstructed vertices with position resolutions of 1 and 10 μm.

as well as gratings in direct contact with the films. Figure 2.7 shows as an example the simulated interference pattern at the emulsion layer, generated by a pair of gratings (12 μm slit, 40 μm pitch, separated by $L = 25$ mm). The antiproton data is being analyzed and preliminary results are quite encouraging.

[1] G. de Lellis, A. Ereditato, K. Niwa, *Nuclear Emulsions*, C. W. Fabjan and H. Schopper eds., Springer Materials, Landolt-Börnstein Database (http://www.springermaterials.com), Springer-Verlag, Heidelberg, (2011).

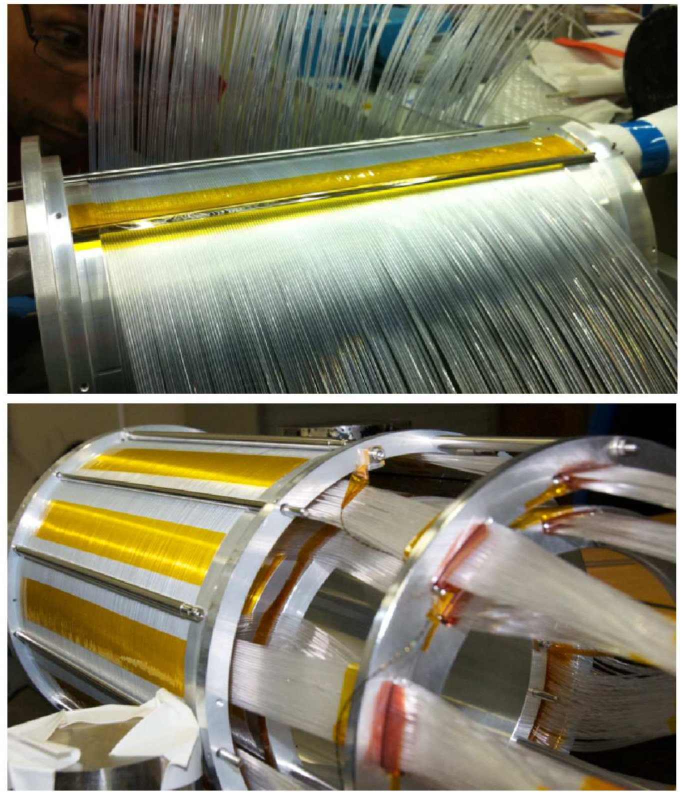

Fig. 2.9 – Scintillating fibers before (top) and after (bottom) being mounted on the support structure. Groups of 25 fibers emerging from the support structure are guided by a ring with rectangular slots.

2.2 Fast Annihilation Cryogenic Tracking detector

6 The FACT detector [1] will determine the position of the annihilation vertex along the beam axis, which will enable measurements of antihydrogen production, temperature and beam creation. Charged pions from annihilations are traced back to determine the r, z - coordinates of the annihilation vertex. Simulations predict a vertex resolution of $\sigma = 2.1$ mm which satisfies our requirements. The detector (Fig. 2.8) must identify each of the $\sim$1000 annihilations in the 1 ms interval of pulsed $\bar{H}$ production, operate at 4 K inside a 1 T field, and produce less than 10 W of heat.

The detector consists of two concentric cylindrical layers of scintillating fibers at radial distances of 70 mm and 98 mm from the beam axis. Each layer consists of 400 scintillating fibers (1 mm diameter Kuraray SCSF-78M) separated by 0.6 mm, located in U-shaped grooves, with alternate fibers displaced radially by 0.8 mm. Figure 2.9 shows the fibers before and after being mounted on the support structure.

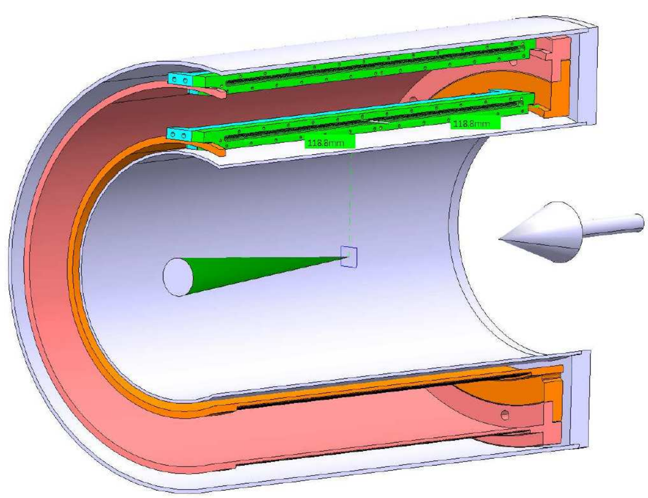

Fig. 2.8 – Support structure of the FACT detector. The beam axis is indicated by the arrow and the green cone illustrates the $\bar{H}$ beam enveloppe.

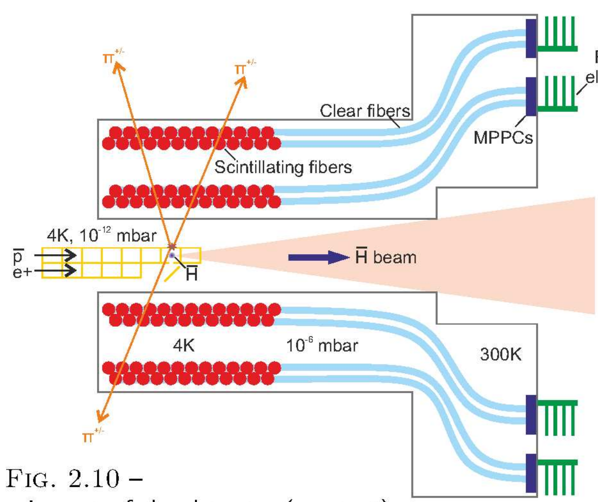

Fig. 2.10 – Layout of the detector (see text).

FIG. 2.11 – Clear fibers connected to the MPPCs.

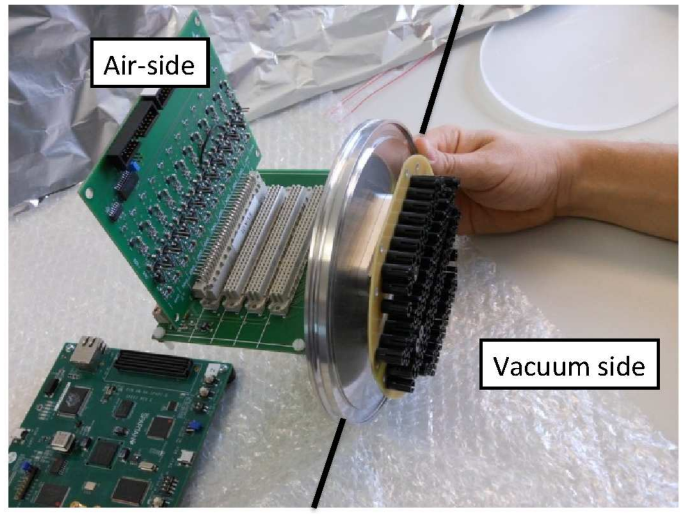

FIG. 2.12 – Air and vacuum side electronics for the FACT detector. On the bottom a Xilinx Spartan-6 FPGA development board.

The scintillating light is transported from the cryogenic region to the room temperature readout electronics by means of 2 m long clear fibers (Fig. 2.10). Particular attention was given to the routing of the clear fibers to ensure that the bending radius always exceeds 50 mm to avoid light losses. A plastic connector developed by the T2K collaboration is used to couple the clear fibers to Hamamatsu Multi-Pixel Photon Counters (MPPC) consisting of 100 Geiger mode Avalanche Photo Diodes (APDs). To minimise the heat load to the cryogenic region only the MPPCs are placed inside the vacuum vessel. A photograph of an assembled vacuum feedthrough is shown in Fig. 2.11.

Figure 2.12 shows a photograph of the readout electronics, designed to continuously detect the light from the scintillating fibers for the duration of the 100 ms period during which $\bar{H}$ is produced. The signals from 96 MPPCs on the vacuum side are routed via the backplane PCB to one of four analogue boards. The signals are amplified and connected to fast discriminators which are read directly by a Field Programmable Gate Array (FPGA). The readout is supervised by a Xilinx Spartan-6 FPGA development board. The complete readout system consists of 9 vacuum feedthroughs, 18 backplane PCBs, 67 analogue boards and 16 Spartan-6 development boards.

Cosmic ray tests of the plastic scintillating fibers at 4 K have been performed to study the light yield, the decay time and the lifetime of the fibers at cryogenic temperatures. The apparatus to perform this measurement consisted of 3 layers of 1 mm diameter scintillating fibers arranged in loops at the bottom of a liquid helium cryostat. The event rate decreased $\approx 10\%$ from room to liquid helium temperature. Examination of the fibers under a microscope after many cycles to 4 K revealed no sign of mechanical damage.

The FACT detector was installed in the AEgIS apparatus in 2012 and is currently undergoing commissioning with cosmic-rays. FACT will be used to study $\bar{H}$ formation, when the low energy antiproton physics programme resumes at CERN in 2014.

[1] J. Storey *et al.*, 13th Vienna Conference on Instrumentation, Vienna (2013).

3 GERDA: Neutrinoless Double Beta Decay in ^{76}Ge

L. Baudis, G. Benato, K. Guthikonda, and M. Walter

in collaboration with INFN Laboratori Nazionali del Gran Sasso LNGS, Institute of Physics, Jagellonian University Cracow, Institut für Kern- und Teilchenphysik Technische Universität Dresden, Joint Institute for Nuclear Research Dubna, Institute for Reference Materials and Measurements Geel, Max Planck Institut für Kernphysik Heidelberg, Universitá di Milano Bicocca e INFN Milano, Institute for Nuclear Research of the Russian Academy of Sciences, Institute for Theoretical and Experimental Physics Moscow, Russian Research Center Kurchatov Institute, Max-Planck-Institut für Physik München, Dipartimento di Fisica dell Universitá di Padova e INFN, and Physikalisches Institut Eberhard Karls Universität Tübingen

(GERDA Collaboration)

When neutrinos propagate over macroscopic distances they can change their observed flavor eigenstate (so lepton flavor is not conserved). Neutrino oscillations demonstrate that neutrinos have mass but to explain these observations, it is necessary to understand a number of other properties of neutrinos and their interactions. The following issues are to be addressed:

- the absolute mass scale of the neutrinos,
- the full neutrino mixing matrix (including CP-violating phases), and
- are neutrinos Dirac or Majorana particles?

The Majorana nature of neutrinos can be studied in experiments searching for neutrinoless double beta decay ($0\nu\beta\beta$), which would involve a nucleus emitting two electrons that share the full Q-value of the decay. If the neutrino is a Majorana particle, this process is allowed in all isotopes that undergo the standard double beta decay ($2\nu\beta\beta$).

GERDA is an experiment searching for the $0\nu\beta\beta$ decay in ^{76}Ge ($Q = 2039.01 \pm 0.05$ keV). The source material is enriched in ^{76}Ge, which simultaneously acts as detector with an energy resolution of 0.1-0.2 % FWHM at 2 MeV. A novel shielding concept features bare germanium diodes operated in a 65 m^3 cryostat filled with liquid argon and surrounded by a 3 m thick water Cerenkov shield which moderates and captures external and muon-induced neutrons. The argon is used for cooling of the diodes and as a passive shield against the residual environmental background.

The experiment proceeds in two phases. Phase I uses eleven HPGe detectors, eight enriched in ^{76}Ge and three detectors made of ^{nat}Ge, with total masses of 17.7 kg and 7.6 kg, respectively. The goal at this stage is to improve the current limits and scrutinize the results of the Heidelberg-Moscow experiment [2]. Phase II, to start in the summer of 2013, will use additional enriched broad-energy germanium (BEGe) detectors, aiming for a total exposure of 100 kg·yr. With a background goal of 10^{-3} counts/(keV·kg·yr), the half-life sensitivity is $T_{1/2} = 2 \times 10^{26}$ yrs. The corresponding range of effective neutrino masses, taking into account the uncertainty in the matrix element and neglecting new lepton number violating interactions, is $0.09-0.15$ eV.

The operation of GERDA Phase I started in November 2011. Soon after, two enriched detectors showed an increase in the leakage current, and have been excluded from the analysis, resulting in a reduced total mass of the enriched detectors of 14.63 kg. Energy calibration for each detector is made with a ^{228}Th source assuming second-order polynomials. The average energy resolution at $Q_{\beta\beta} = 2039$ keV is 4.5 keV at FWHM.

The $2\nu\beta\beta$ decay in ^{76}Ge was measured with unprecedented signal-to-background ratio using an initial exposure of 5.04 kg·yr (126 live days acquired in the period November 2011 - March 2012), resulting in

$$T^{2\nu}_{1/2} = 1.84^{+0.14}_{-0.10} \times 10^{21}\ \text{yr [3]}.$$

A much larger dataset with an exposure of 18.4 kg·yr reached in March 2013 is currently under analysis, and a precise background model is under development. The background level in the energy region of interest ($Q_{\beta\beta}\pm$100 keV) is 1.7×10^{-2} counts/(keV·kg·yr), one order of magnitude lower than in the Heidelberg-Moscow and IGEX experiments. The energy window $Q_{\beta\beta}\pm$20 keV is masked, with the unblinding scheduled for June 2013.

3.1 Data analysis in Zurich

We have implemented an automated calibration routine in the general GERDA analysis framework (GELATIO) and are responsible for the analysis of the weekly calibration runs and monitoring the stability of the energy calibration and resolution of the Ge diodes. For each detector we extract the position of the various peaks and the corresponding calibration curves.

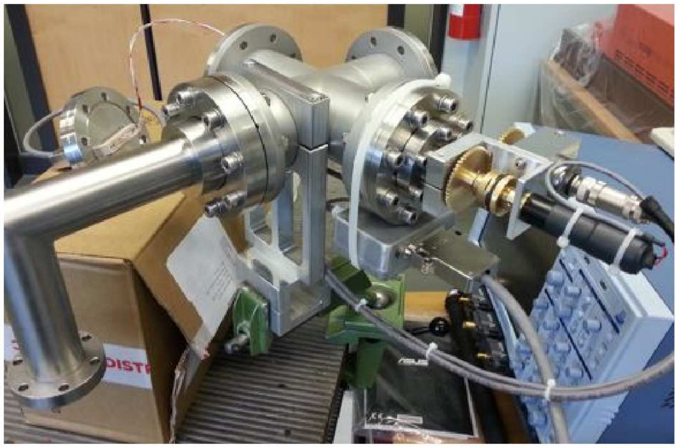

FIG. 3.1 – Source Insertion System.

FIG. 3.2 – Control Box.

We are also involved in the selection of the final datasets for the $0\nu\beta\beta$ physics analysis, focusing on quality cuts applied to raw data signals, and in the development of the statistical analysis. We are developing cuts removing saturated and pile-up events and events with nonstandard rise-times and determine the associated efficiency factors.

3.2 Phase II calibration system

As a leader of the calibration working group, we are responsible for the calibration system hardware. The weekly calibration is performed using three motor-controlled source insertion systems (SISs, designed and built at UZH), which lower encapsulated ^{228}Th sources on tantalum holders into the cryostat on steel bands.

In Phase II, 30 new BEGe detectors will be deployed at LNGS in a new, single-arm lock system which can house seven detector strings. One string will consist of four pairs of BEGe detectors mounted back-to-back in a single holder system made from low-background copper and silicon plates. In order to evaluate the required number of SISs and of calibration positions for each detector string, we perform Monte Carlo simulations with GEANT4, where we study how to reach sufficient statistics for energy and pulse shape calibrations within a reasonable amount of time.

Since the height of the new Phase II lock will be considerably increased (the distance from the top of the lock to the center of the cryostat will be 8.5 m), the existing steel belts holding the calibration sources will be replaced. We have constructed a new SIS at UZH (Fig. 3.1), along with the control unit for three systems offering redundancy in case of failure (Fig. 3.2). The system is currently under test and fine tuning for best agreement between the position determinations with the two encoders is in progress.

3.3 Tests of enriched BEGe detectors

From 37.5 kg of available enriched ^{76}Ge, thirty working BEGe detectors were produced, with a total mass 20.1 kg. We have participated in the characterization of all detectors at the Hades underground facility in Belgium. A dedicated study of germanium detectors depleted in ^{76}Ge content, to which our group contributed [4], was crucial in verifying all the production steps. We also contributed to the optimization of the acceptance protocol which considers parameters such as depletion and operational voltage, energy resolution, and leakage current. Measurements were performed to study the charge collection features of each diode and to determine the detector active volume and mass, as well as the dead-layer thickness and the uniformity over the crystal surface.

We are involved in the analysis of the ^{228}Th calibration data regarding pulse shape discrimination and estimation of the dead-layer of the diodes. The dead-layer is found by comparing measured energy spectra from ^{133}Ba and ^{241}Am sources with simulated spectra with varying dead-layer thickness. The dead-layer thickness at the n^+ contact ranges from 0.7 mm to 1.2mm, and the active volume fractions are between 86% and 92%.

3.4 Liquid argon instrumentation

In Phase II of the GERDA experiment, the background level in the region of interest (ROI) is to be reduced by one order of magnitude compared to Phase I. Some background events in the ROI occur in coincidence with a signal in the liquid argon (LAr) surrounding the Ge detectors. The LAr scintillation signal (λ = 128 nm) produced in such events will be detected and used in an active veto system which is presently being designed.

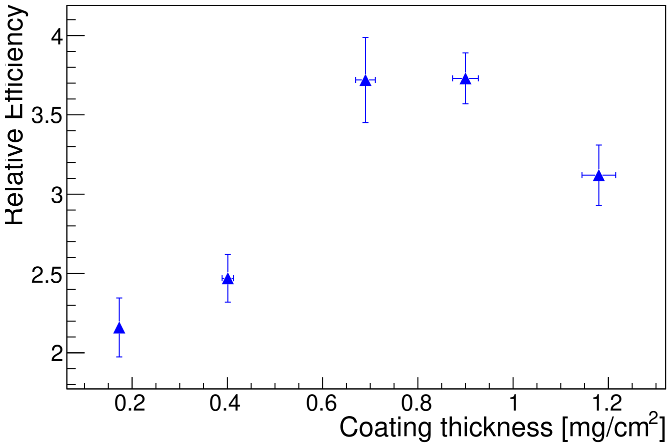

FIG. 3.3 – Wavelength shifting efficiency of Tetratex coated with TPB relative to uncoated VM2000 as a function of the coating thickness.

FIG. 3.4 – Coated foil in our LAr setup, illuminated with a UV lamp.

The LAr instrumentation system will consist of both low-radioactivity Hamamatsu R11065 PMTs and of SiPMs coupled to an optical fiber curtain for the light readout. Since the quartz windows of the PMTs and the optical fibers absorb light at 128 nm reflector foils with wavelength-shifting (WLS) coatings will surround the instrumented LAr volume.

The WLS coatings should meet the following requirements: high conversion efficiency, long-term stabiliy in LAr, and high radio-purity. We have studied several WLS solutions consisting of a polymer coated with the WLS in our LAr detector at UZH, equipped with an R11065-10 Hamamatsu PMT. The WLS is usually tetraphenyl butadiene (TPB), but can also be a plastic scintillator, as well as BCF-10 fiber dissolved in toluene. The studies have been performed on a specular highly reflective multilayer polymer foil VM2000, and on Tetratex, a diffuse highly reflective PTFE fabric. The fabric nature of Tetratex allows coatings with pure TPB which would otherwise not be stable. The best results were obtained (Fig. 3.3) for a combination of 0.8 mg/cm^2 of pure TPB wet-coated onto Tetratex, showing efficiency which is about 3 times higher than for VM2000 alone. This coating-reflector foil combination also showed high mechanical stability during thermal cycling between room and LAr temperatures. Final tests on the optimal thickness and the long-term behavior study in LAr are ongoing (see Fig. 3.4).

[1] E. Majorana, Il Nuovo Cimento B 14, 171-184 (1937).

[2] H.V. Klapdor-Kleingrothaus *et al.*, Eur. Phys. J. A12 (2001) 147-154.

[3] M. Agostini *et al.*, J. Phys. G40, 035110 (2013).

[4] L.B. Budjas, M. Agostini *et al.*, *Isotopically modified Ge detectors for GERDA: from production to operation*, arXiv:1303.6768 (2013).

4 Cold Dark Matter Search with XENON

M. Auger, P. Barrow, L. Baudis, A. Behrens, G. Kessler, A. Kish, T. Marrodan Undagoitia (until September 2012), D. Mayani, P. Pakarha, F. Piastra, and M. Schumann (until December 2012)

in collaboration with Columbia University, UCLA, INFN, University of Münster, Coimbra University, Subatech, The Weizmann Institute of Science, University of Mainz, SJTU, MPIK Heidelberg, Rice University, University of Bologna, Nikhef, Purdue University, University of Bern

(XENON Collaboration)

XENON100 is a 161 kg double-phase Xe time-projection chamber (TPC) operated at LNGS. It employs two arrays of low-radioactivity, VUV-sensitive photomultipliers (PMTs) to detect the prompt (S1) and proportional (S2) scintillation light signals induced by particles interacting in the target volume, containing 62 kg of ultra-pure liquid xenon (LXe). The remaining 99 kg of LXe act as an active veto shield against background events. The instrument is described in Ref. [1], and the analysis procedure is detailed in Ref. [2].

Using 13 months of data taken during 2011 and 2012, with a final exposure of 224.6 live days $\times$ 34 kg, XENON100 has reached its initial aim to probe spin-independent WIMP-nucleon cross sections down to $2 \times 10^{-45}\,\mathrm{cm}^2$ at a 55 GeV/c^2 WIMP mass [3]. New limits on spin-dependent WIMP-nucleon couplings were derived [4], yielding the world's best sensitivity on WIMP-neutron couplings. After a further distillation run the ^{nat}Kr level was reduced below $\simeq$20 ppt in the latest XENON100 run. A new dark matter search run is to start in spring 2013. Concurrently, several additional analyses are ongoing: a search for solar and dark matter axions, for SuperWIMPs, a search for low-mass WIMPs, and a study of inelastic WIMP-nucleus collisions.

The next phase in the XENON dark matter search program, the XENON1T experiment, has been approved and founded, and will be constructed in Hall B at LNGS. It will use a total of 3 t of LXe operated in a 9.6 m diameter water Cerenkov shield. The cryostat will be a double-walled super-insulated pressure vessel, made of stainless steel. The inner vessel will house the liquid xenon, the TPC and two arrays of 3-inch Hamamatsu R11410 PMTs. The TPC will be made of interlocking PTFE panels, and the drift field homogeneity will be achieved with equidistant OFHC field shaping rings connected with high-ohmic HV resistors. The photosensors will be arranged in two (top and bottom) arrays, containing 127 and 121 sensors.

4.1 Background studies

The nuclear recoil (NR) background from radiogenic and cosmogenic neutrons has been predicted for the XENON100 experiment based on Monte Carlo studies, using a detailed model of the detector and its shield. The simulation accounts for the energy resolution, veto efficiency, and the efficiency loss introduced by the S2/S1 electronic recoil discrimination cut to define a benchmark WIMP search region [6]. The total NR background predicted for the 224.6 days measurement leading to the WIMP search result of 2012 [3] is $(0.17^{+0.12}_{-0.07})$ events, to be compared to the total electronic recoil (ER) background estimate of (0.8 ± 0.2) events. It can be concluded that neutron background does not limit the sensitivity of the XENON100 detector for WIMP detection.

In order to select materials for the construction of the XENON1T detector and determine their intrinsic radioactivity, the samples are being screened with gamma- and mass-spectrometry methods. The measured activities are used as input information for our GEANT4 simulations [7] aiming at predictions of the electronic and nuclear recoils backgrounds from the detector and shield materials, which are used for the optimization of the TPC design and the detailed background characterization.

Preliminary simulations with a simplified detector model predict a background from the PMTs of 0.2 events/years for NRs, and 0.04 events/year for ERs. The total background from the cryostat is predicted to be 0.23 events/year, where NR and ER events give approximately equal contributions. These studies will be extended using a detailed detector model based on the materials selected in the screening studies.

4.2 XENON1T TPC, cables and connectors

Our group is partially responsible for the design and construction of the XENON1T TPC, together with Bern, Columbia and UCLA. An up-to-date CAD drawing of the TPC is shown in Fig. 4.1. We will design and construct the field cage and the field shaping rings. The design proce-

FIG. 4.1 – A schematic of the XENON1T TPC.

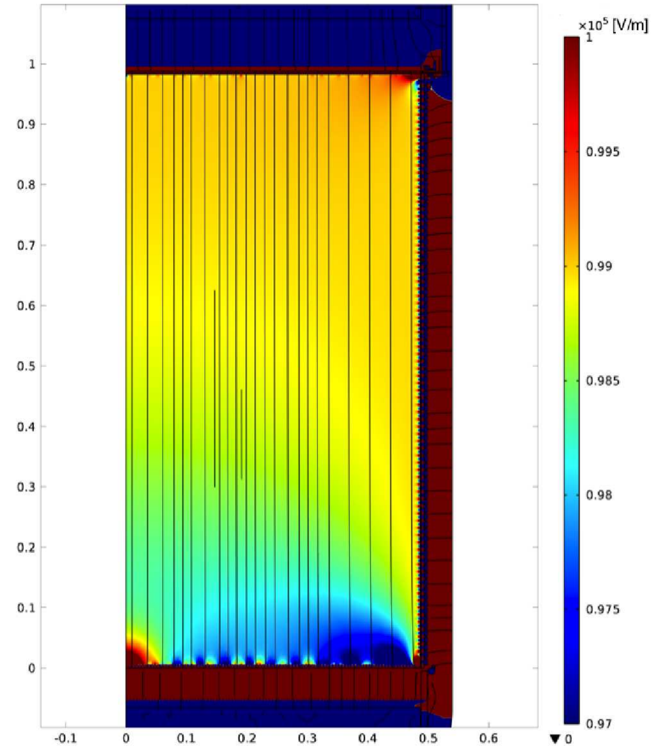

FIG. 4.2 – Electric field simulation of XENON1T after the optimisation, displaying a half cross-section. Electrical field lines are shown for clarity.

FIG. 4.3 – The 1:16 scale mockup using stainless steel field shaping rings during a cryogenic test in LN.

dure involves accurate electric field simulations, based on finite element method software, to determine the uniformity and variations of the electrical field within the detector (see an example in Fig. 4.2). A full-scale model of a section of the full field cage has been produced and successfully subjected to rigorous cryogenic and structural integrity tests in or laboratory; one example is shown in Fig. 4.3.

We are also responsible for the signal transfer from the PMTs to the DAQ. Due to strict background requirements of the experiment, and since the cabling will be located near the active volume of the TPC, ultra-low radioactivity cables and connectors have to be used. We have designed and built a custom-made connector pro prototype that is made of PTFE and copper, shown in Fig. 4.4). The connectors were tested for both the PMT signal transmission and for the high-voltage for the PMTs. Figure 4.5 shows the transmission of a single photoelectron spectrum from one of the PMTs that will be used in XENON1T for three different

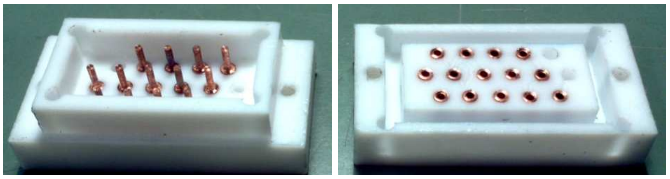

FIG. 4.4 –
The current version of the low-radioactivity connector.

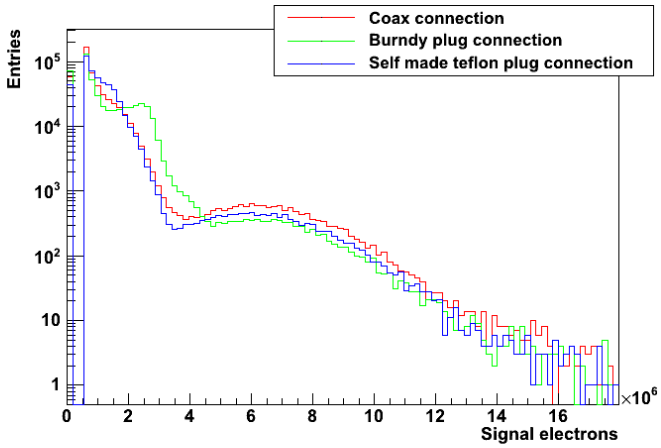

FIG. 4.5 – Single photoelectron spectra of a R11410 PMT taken with the three different connectors mentioned in the legend.

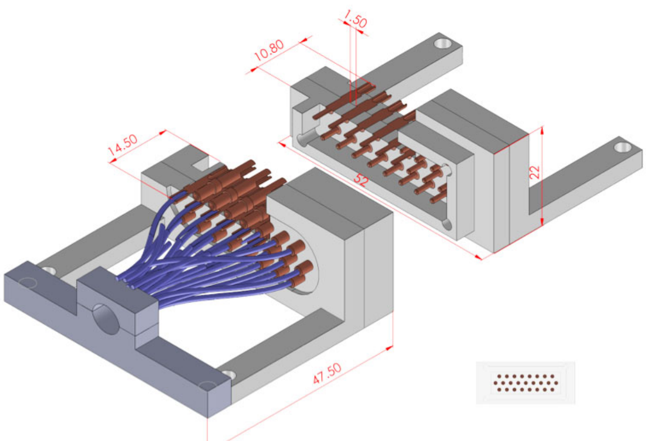

FIG. 4.6 – A CAD drawing of the next generation connector with 25 pins and increased mechanical robustness.

kinds of connections. The prototype connector has superior transmission properties compared to the connector type used in the XENON100 experiment (Burndy).

Based on these preliminary results, an optimization study is ongoing with the goal of reducing the mass, increasing the signal transmission, and improving the mechanical robustness. A schematic of a next-generation connector model is shown in Fig. 4.6.

The Hamamatsu R11410 3-inch PMT has been selected as the light sensor for XENON1T. It was developed to be used at cryogenic temperatures, has a very low intrinsic radioactivity and a quantum efficiency at 178 nm (Xe scintillation wavelength) around 30%. We have carried out several tests aimed at the performance study in environments similar to those in a dark matter detector, examining in particular the long-term behavior and stability in LXe.

Two R11410-MOD and R11410-10 PMTs were characterized at room temperature and in LXe, showing a typical gain of 5×10^6, a peak-to-valley ratio >3 and an afterpulse rate $<10\%$. Long-term stability tests and thermal cycling have demonstrated that these PMTs can be operated stably for several months at cryogenic temperatures with a gain variation of $\pm2\%$. In addition, the PMTs can withstand rapid temperature changes while cooling down and returning back to ambient conditions for several times in periods of a couple of weeks [8].

4.3 Material screening

The Gator facility [9], operated by our group at LNGS, has been extensively used in the XENON100 screening campaign [10], and is currently employed to screen XENON1T components: material samples for the construction of the inner and outer cryostat vessels (copper, titanium and stainless steel), PTFE as support structure and reflector, signal and high-voltage cables, individual parts of R11410 photosensor, etc. We are starting to screen all 300 R11410 PMTs that were purchased for XENON1T. For this purpose, we have designed and fabricated a low-radioactivity PTFE holder, which will house 15 PMTs at a time.

[1] E. Aprile *et al.*, Astropart. Phys. 35 (2012) 573-590.

[2] E. Aprile *et al.*, *Analysis of the XENON100 Dark Matter Search Data*, (2012) arXiv:1207.3458.

[3] E. Aprile *et al.*, Phys. Rev. Lett. 109, (2012) 181301.

[4] E. Aprile *et al.*, *Limits in Spin-dependent WIMP-nucleon Cross Sections from 225 Live Days of XENON100 Data*, (2013) arXiv:1301.6620.

[5] E. Aprile *et al.* (XENON100 Collaboration), Phys. Rev. Lett. 107, (2011) 131302.

[6] E. Aprile *et al.* (XENON100 Collaboration), in preparation.

[7] GEANT4 Collaboration, NIM A506, (2003) 250.

[8] L. Baudis, A. Behrens, A. Ferella, A. Kish, T.M. Undagoitia, JINST 8 (2013) P04026.

[9] L. Baudis, A. Ferella, A. Askin, J. Angle, E. Aprile *et al.*, JINST 6, (2011) P08010.

[10] E. Aprile *et al.*, Astropart. Phys. 35, (2011) 43-49.

5 DARWIN: Dark matter WIMP search with noble liquids

L. Baudis, A. Behrens, G. Benato, A. Kish, A. Manalaysay, T. Marrodan Undagoitia (until September 2012), M. Schumann (until december 2012), and M. Walter

in collaboration with ETHZ, University of Bern, INFN, University of Münster, TU Dresden, Subatech, Weizmann Institute of Science, University of Mainz, MPIK Heidelberg, Rice University, University of Bologna, Nikhef, Karlsruhe University, Columbia University, UCLA, Princeton University, University of Naples, Imperial College London, Arizona State University

(DARWIN Consortium)

The rates of WIMP interactions with target nuclei are below one event per kilogram and year, and momentum transfers are around 10-100 MeV [1, 2]. Thus, searches for these hypothetical particles require large target masses and low energy thresholds and detectors are situated deep underground where background can be low. Sensitivities of $\sim 10^{-45}$ cm^2 have been achieved for spin-independent WIMP-nucleon scattering cross sections in xenon [3, 4] and argon [5]. The near-future ton-scale experiments [6, 7] will probe the region down to $\sim 5 \times 10^{-47}$ cm^2. Nevertheless, in order to eventually measure WIMP properties such as mass, scattering cross section and possibly spin [8], significantly larger detectors are required.

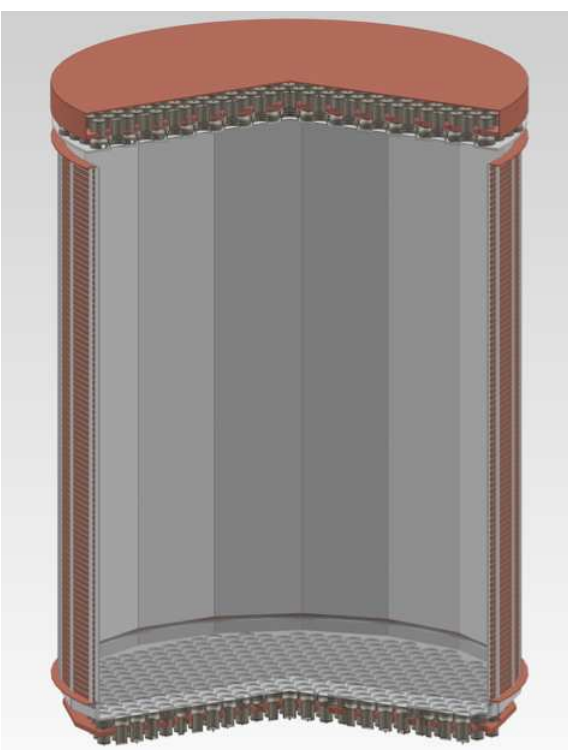

Fig. 5.1 – A CAD model of the 20 t LXe DARWIN TPC.

Dark matter WIMP search with noble liquids (DARWIN) is an R&D and design study for a multi-ton dark matter detector [9]. Its primary design goal is to probe the spin-independent scattering cross section down to 10^{-48} cm^2 and, in case WIMPs are discovered, to perform a high-statistics measurement of the WIMP-induced nuclear recoil spectrum, which would allow to constrain the WIMP mass and scattering cross section [8]. Besides WIMP search other physics goals are the search for neutrinoless double beta decay in ^{136}Xe, and the real-time detection of pp-neutrinos from the sun.

DARWIN will be based on a large, unsegmented target mass capable of reducing the fiducial volume by utilizing the time projection chamber (TPC) technique. The TPC will detect the prompt scintillation light from primary particle interactions in the active detector volume, and the delayed proportional scintillation signal, produced by ionization electrons drifting towards the gas phase. A simplified CAD model of the DARWIN TPC is shown in Fig. 5.1. The background originating from cosmic muons will be suppressed to negligible levels by a large water Cherenkov shield, surrounding the noble liquid cryostats (see Fig. 5.2).

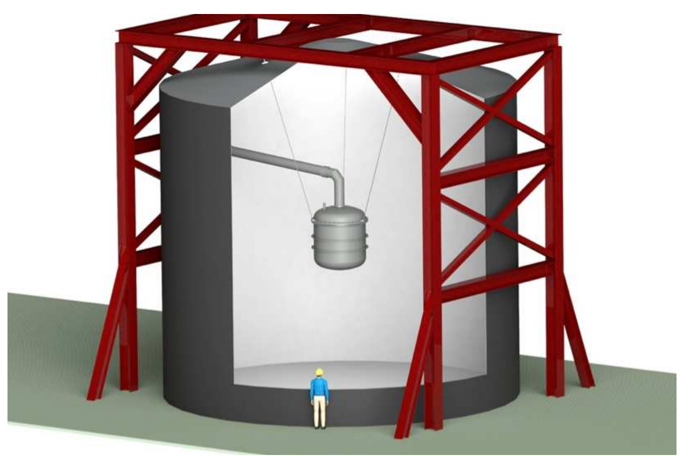

Fig. 5.2 – Schematic view of the DARWIN experiment.

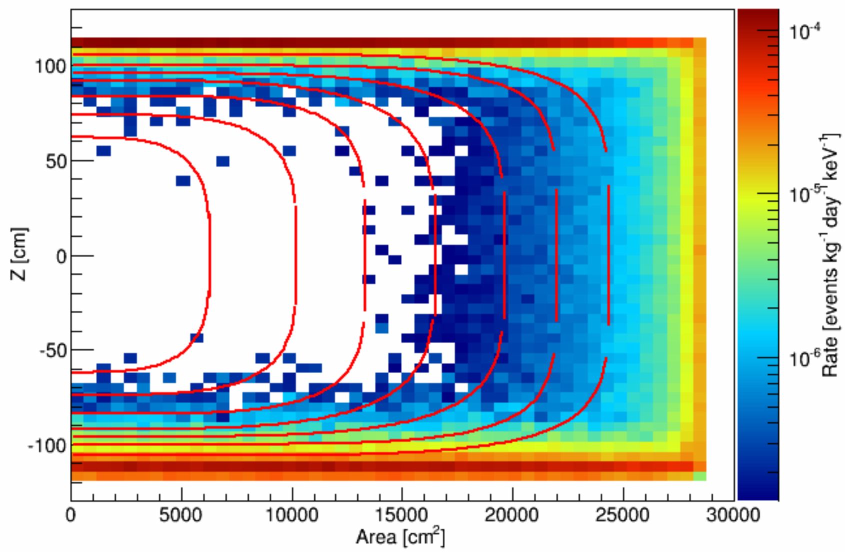

FIG. 5.3 – Spatial distribution of background events in the 2404.6−2553.4 keV 2β-energy region of interest for the ^{136}Xe $0\nu\beta\beta$ decay search. The red contours indicate fiducial volumes of 14, 12, 10, 8, 6, 4 and 2 t.

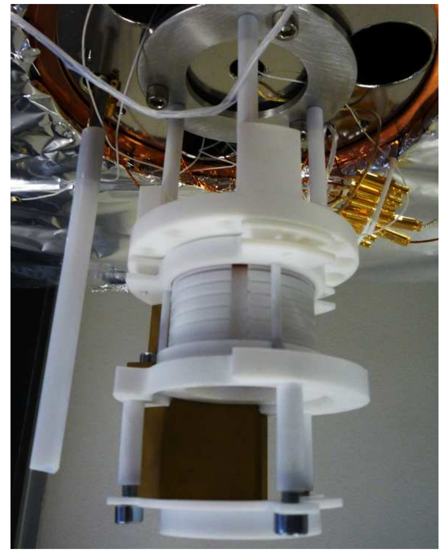

FIG. 5.4 – The new *Xürich II* detector will be used to measure light and charge yields in LXe for low-energy nuclear recoils.

Our group is a leading member of the DARWIN Consortium, involved in TPC design, Monte Carlo simulations of the electronic and nuclear recoil backgrounds, new light read-out schemes and tests of light sensors in noble liquids, material screening, and measurements of charge and light yield of low-energy nuclear recoils.

We have performed GEANT4 simulations of the potential electromagnetic and neutron backgrounds associated with the natural radioactivity (^{238}U, ^{232}Th, ^{60}Co, ^{40}K) in the construction materials. The background as a function of fiducial detector volume was studied for the low-energy region (<100 keV), relevant for the dark matter and solar neutrino detection, and for the high-energy region (around 2.5 MeV), relevant for the neutrinoless double beta decay search in ^{136}Xe. As an example, we show in Fig. 5.3 the background rates in the energy region 2404.6−2553.4 keV which corresponds to a $\pm 3\sigma$ window around $Q_{\beta\beta}$ = (2457.83±0.37) keV for the assumed detector resolution σ = 1%. As illustrated the background falls rapidly when moving away from the detector boundaries.

For the study of the light yield from electronic and nuclear recoils at low energies, we have designed and built a small dual-phase LXe TPC (*Xürich II*, see Fig. 5.4) which will be exposed to the 2.45 MeV neutron beam provided by the UZH *D-D* fusion neutron generator. Its predecessor, *Xürich I*, was used to measure the light yield of low-energy electronic recoils in LXe, down to 1.5 keV [10]. Those results are relevant for the analysis of the electronic recoil spectrum of XENON100 regarding the observed annual modulation signal by the DAMA/LIBRA experiment in the region around 2-5 keV [11], as well as to non-WIMP dark-matter candidates that might interact with electrons.

The detector design is based on extensive electric field simulations aimed at optimizing the field uniformity within this small volume [12]. Fig. 5.5 shows the simulated field distribution. The vertical box located at

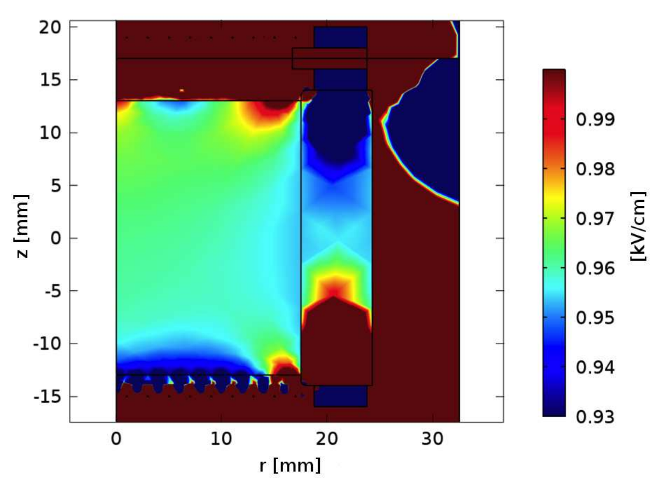

FIG. 5.5 – The simulated electric field map for *Xürich II*. The active region of the detector extends to r = 17.5 mm. Note the color scale expanded to the upper 7% only.

$r \simeq 20$ mm indicates the polytetrafluoroethylene (PTFE) ring that marks the boundary of the active region. This particular simulation investigates the use of a special type of PTFE that has the resistance that results in a uniformly varying electric potential at the surface. As a result, the variation in field strength is below 4% which is essential for collecting all emitted charges.

The *Xürich II* detector is currently being assembled and tested in our laboratory. After initial characterization and calibration runs with electron (^{83m}Kr), gamma (^{57}Co) and neutron (^{241}AmBe, ^{88}YBe) sources, it will be operated in coincidence with two liquid scintillator neutron detectors in the neutron generator beam.

[1] G. Jungmann, M. Kamionkowski, K. Griest, Phys. Rep. 267, 195 (1996).

[2] J.D. Lewin and P.F. Smith, Astropart. Phys. 6, 87 (1996).

[3] E. Aprile *et al.* (XENON Collaboration), Phys. Rev. Lett. 109, 181301 (2012).

[4] V.N. Lebedenko *et al.* (ZEPLIN-III Collaboration), Phys. Rev. D 80, 052010 (2009); V.N. Lebedenko *et al.*, Phys. Rev. Lett. 103, 151302 (2009); D.Yu. Akimov *et al.*, Phys. Lett. B 709, 14-20 (2012).

[5] R. Brunetti *et al.* (WARP Collaboration), Astropart. Phys. 28, 495 (2008).

[6] A. Wright, *The DarkSide Program at LNGS*, arXiv:1109.2979.

[7] E. Aprile (for the XENON1T Collaboration), *The XENON1T Dark Matter Search Experiment*, arXiv:1206.6288, Proceedings of DM2012 at UCLA.

[8] M. Pato, L. Baudis, G. Bertone, R.R. de Austri, L.E. Strigari and R. Trotta, Phys. Rev. D. 83, 083505 (2011).

[9] L. Baudis (DARWIN Consortium), J. Phys. Conf. Ser. 375. 012028 (2012).

[10] L. Baudis *et al.*, *Response of Liquid Xenon to Compton Electrons Down to 1.5 keV*, arXiv:1303.6891 (2013).

[11] R. Bernabei *et al.* (DAMA Collaboration, LIBRA Collaboration), Eur. Phys. J. C67, 39.

[12] H. Dumjovic, *Simulation and optimization of the electric field in a liquid xenon time projection chamber*, bachelor thesis, University of Zurich, (2012).

6 Search for the rare decay $\mu^+ \to e^+e^-e^+$

R. Gredig, P. Robmann, and U. Straumann

in collaboration with University of Geneva, PSI Villigen, ETH Zürich, and University of Heidelberg

(Mu3e Collaboration)

In the standard model lepton flavour is conserved at tree level. The observation of neutrino oscillations by experiments such as SuperKamiokande [1], SNO [2], and KamLAND [3] is, however, a direct proof of lepton flavour violation (LFV). Charged LFV (CLFV) would lead to $\mu \to e$ and $\tau \to \mu$ transitions without neutrinos in the final state. In the standard model CLFV can only be induced by neutrino mixing (see Fig. 6.1 for the decay of interest here) but such processes are highly suppressed by the tiny neutrino masses. The resulting branching ratios are below 10^{-50}, way beyond the experimental sensitivity. The observation of CLFV would therefore directly signal physics beyond the standard model. Two examples are shown in Fig. 6.1 as well.

Muon number violation has already been investigated in different channels (see Tab. 6.1). When these processes would be observed their relative strengths would guide the attempts to identify the underlying mechanism.

A new $\mu^+ \to e^+e^-e^+$ search has been proposed at the Paul Scherrer Institute aiming at a hitherto un-reached sensitivity down to $B < 10^{-16}$ [8], four orders of magnitude more sensitive than reached by its 25 years old predecessor SINDRUM.

TAB. 6.1 –
Experimental upper limits on the branching ratios B of LFV muon decays

Decay channel	Experiment	B upper limit	Ref.
$\mu \to e\gamma$	MEGA	1.2×10^{-11}	[4]
	MEG	2.4×10^{-12}	[5]
$\mu \to eee$	SINDRUM	1.0×10^{-12}	[6]
$\mu^-\mathrm{Au} \to e^-\mathrm{Au}$	SINDRUM II	7×10^{-13}	[7]

[1] Y. Fukuda *et al.* (Super-Kamiokande Collaboration), Phys. Rev. Lett. 81 (1998) 1562.
[2] Q.R. Ahmad *et al.* (SNO Collaboration), Phys. Rev. Lett. 87 (2001) 071301.
[3] K. Eguchi *et al.* (KamLAND Collaboration), Phys. Rev. Lett. 90 (2003) 021802.
[4] M. L. Brooks *et al.* (MEGA Collaboration), Phys. Rev. Lett. 83 (1999) 1521.
[5] J. Adam *et al.* (MEG Collaboration), Phys. Rev. Lett. 107 (2011) 171801.
[6] U. Bellgardt *et al.* (SINDRUM Collaboration), Nucl. Phys. B299 (1988) 1.
[7] W. Bertl *et al.* (SINDRUM II Collaboration), Eur. Phys. J. C47 (2006) 337.
[8] A. Blondel *et al.* (Mu3e Collaboration), *Research Proposal for an Experiment to Search for the Decay $\mu \to eee$*, Research proposal submitted to the PSI Committee for Particle Physics at the Ring Cyclotron (2013), ArXiv 1301.6113.

6.1 Experimental Requirements

The $\mu^+ \to e^+e^-e^+$ decay signal shows three decay particles with a momentum vanishing sum

$$|\vec{p}_{\mathrm{tot}}| = |\sum_i p_i| = 0\ \mathrm{MeV}/c$$

with the total energy equal to the muon mass. The most severe backgrounds are the internal conversion process $\mu^+ \to e^+e^-e^+\nu_e\overline{\nu_\mu}$ and accidental $e^+e^+e^-$ combi-

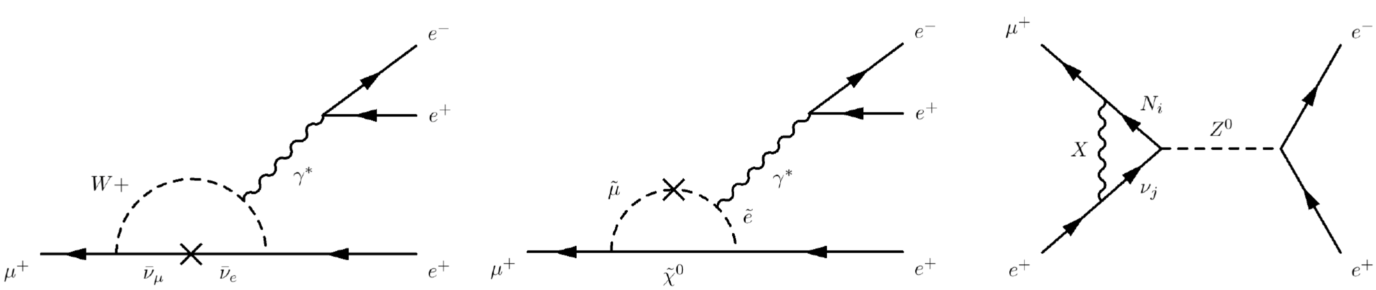

FIG. 6.1 – Possible $\mu^+ \to e^+e^-e^+$ mechanisms. From the left: neutrino mixing allowed within the standard model, a supersymmetric contribution, and a penguin diagram in the little Higgs model.

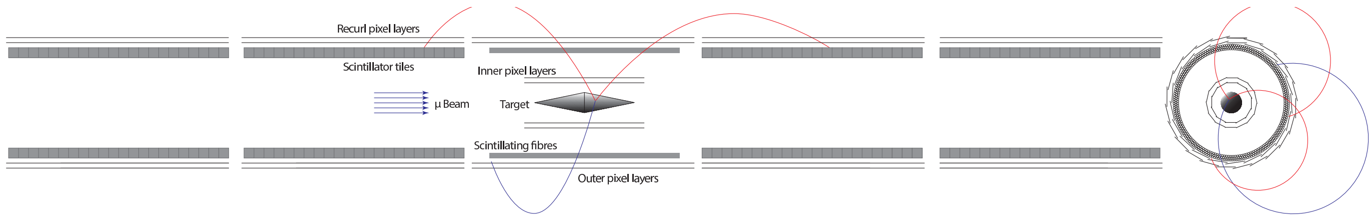

FIG. 6.2 – zr and xy views of the proposed detector.

nations. The suppression of this random background requires high time and vertex resolutions (below $\simeq$100 ps and $\simeq$100 μm, respectively). To reach the proposed high sensitivity within a few years the muon stopping rate must be at least $2\times10^9\mathrm{s}^{-1}$.

6.2 Proposed Detector

The proposed setup is shown in Fig. 6.2. A cylindrical detector is situated inside a 1 Tesla solenoidal magnetic field of 1 m diameter and 2.5 m length. In the centre there is a hollow aluminium double cone target with a length of 10 cm and 2 cm diameter. The muons enter along the symmetry axis. In this configuration the muons are distributed over a large area which is another measure to suppress accidental coincidences by a vertex constraint.

The detector is divided in five sub-stations along the beam-axis with a length of 36 cm each. All stations have an outer tracker built with three layers of 250 μm scintillating plastic fibres with an inner radius of 6.0 cm and two layers of silicon pixels at 7.6 cm and 8.9 cm. The central sub-detector has an additional 12 cm long inner tracker with silicon pixels at radii 1.9 cm and 2.9 cm (Fig. 6.3). This design concept is highly modular allowing a staged approach:

- Phase Ia
  This stage only uses the Si layers of the central sub-station capable of handling the muon rate of $2\times10^7\mathrm{s}^{-1}$ provided by the πE5 beam line at the PSI.
- Phase Ib
  The detector will have the first pair of re-curl stations with the corresponding scintillating tile detectors and the fibre detectors in the centre module. The improved timing resolution will allow to run at the highest πE5 rate of about $1\times10^8\mathrm{s}^{-1}$.
- Phase II
  In this final phase all five sub-stations will be available and a new beam line (HiMB) will provide the $2\times10^9\mathrm{s}^{-1}$ muon rate required for the ultimate sensitivity

6.3 Scintillating Fibres

The Mu3e group at UZH develops the scintillating fibre tracker in close collaboration with the University of Geneva and the ETH Zürich. The light of the fibres will be read out with silicon photomultipliers (SiPM). The advantages of such light detectors are the small size and that they can be operated in a high magnetic field.

In a first step a simulation tool-kit using GEANT4 has been developed to study the optical response of the fibres. The simulation has two sequential modes of operation which minimises the required computer time:

- For a detailed analysis of a specific fibre geometry it is used standalone. The generation, propagation and absorption of the photons in the fibre are simulated and the fibre response as a function of the crossing position and energy deposit is parametrized.

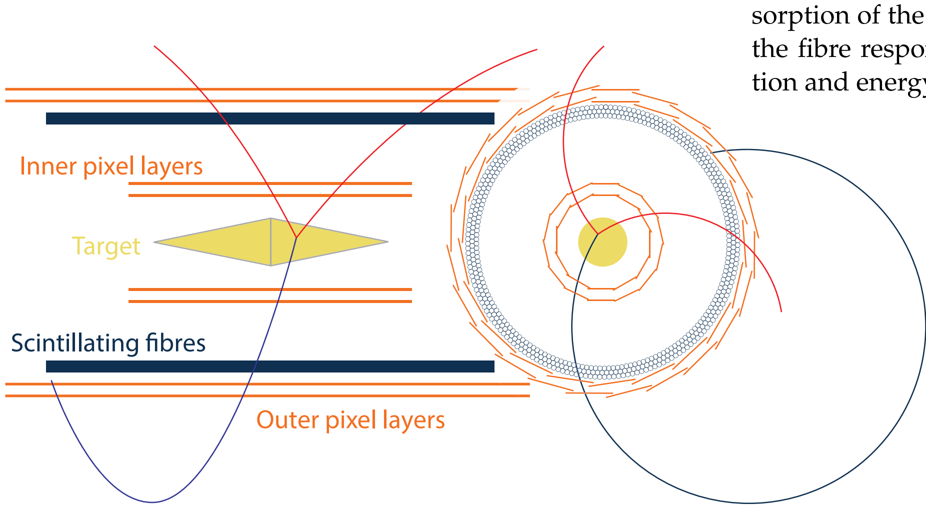

FIG. 6.3 – Expanded view of Fig. 6.2 with the scintillating fibres highlighted in blue. The fibres are not to scale.

- The simulation covering the whole detector no longer tracks the scintillation light but uses the parametrized fibre response instead.

The simulation of the light propagation allows to compare different fibre geometries, coatings and staggering schemes. Not only the spatial distribution of the photons (see Fig. 6.5) but also their time distribution has been studied. For a single fibre typically 12 photons reach one end of the fibre (see Fig. 6.6) where they will be detected with an efficiency of typically 50% with a SiPM array. The signal shape has been studied including the response of the light sensor [1] and the results indicate a time resolution of $\sim$400 ps.

[1] P. Eckert *et al.*, JINST 7 (2012) P08011.

6.4 Test Setup

A test setup is currently under development at the institute to verify the simulation results. The setup includes a support for the scintillating fibres, several photomultiplier tubes to measure the generated light and a radioactive source. It will also allow to analyse different fibre staggering geometries (Fig. 6.4) and to study the corresponding light yield and the optical crosstalk.

Currently the photomultiplier tubes (PMT) are being calibrated with a pulsed laser to obtain the single-photoelectron response. The PMTs are exposed to a strongly attenuated laser resulting in zero photons most of the time. The signal gating is triggered by the laser. Fig. 6.7 shows the resulting charge distribution for a Burle S83062E PMT. A narrow spike at zero originates in events with zero photoelectrons (p.e.). Broad bumps originate from events with 1, 2 or 3 p.e. where the widths result from the gains in the first dynodes as reproduced by a model of the PMT response [1].

After positioning three fibres in a row the photon yield of the central fibre will be determined by using the signals from the two other fibres as a trigger. Finally, the test setup will be completed with SiPM sensors, amplification and digitisation electronics as used later on.

[1] E. H. Bellamy *et al.*, NIM 339 (1994) 468.

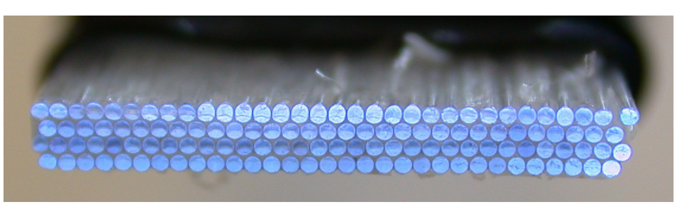

FIG. 6.4 – Ribbon of glued scintillating fibres (produced by the Geneva group).

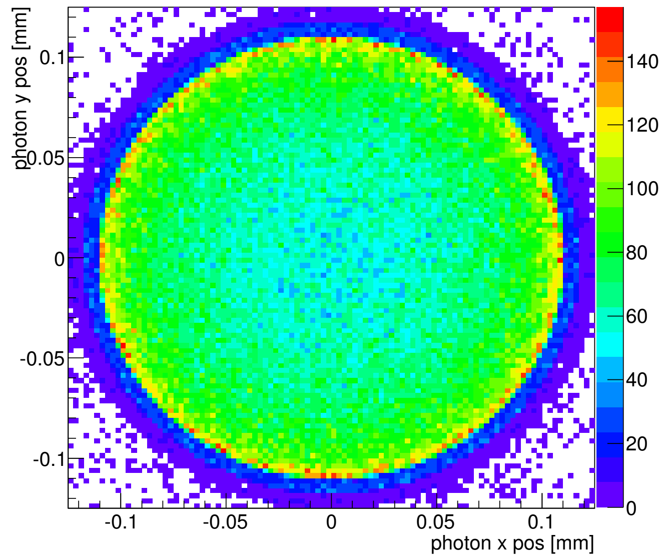

FIG. 6.5 – xy distribution of the photon at the fibre end. 30 thousand events were generated in which a 15 MeV positron is emitted towards the fibre centre.

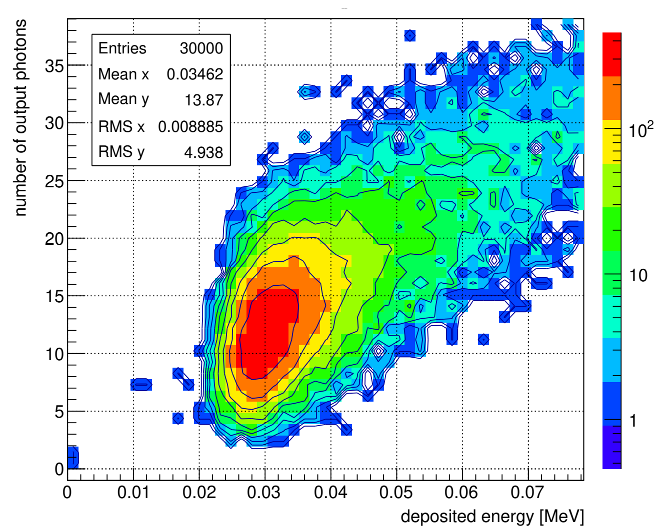

FIG. 6.6 – Photon yield at one fibre end versus energy deposit for a 15 MeV positron crossing the fibre centre.

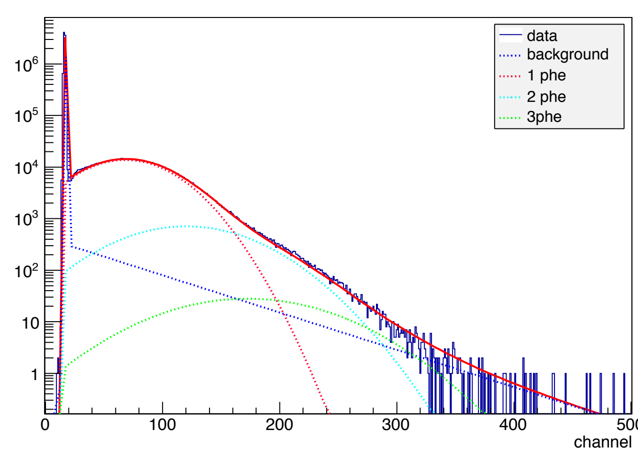

FIG. 6.7 – Charge response (arbitrary units) of a Burle S83062E PMT to 1×10^7 laser triggers. The measured data are well reproduced by a model [1].

7 Very High Energy Gamma Ray Astronomy with CTA

D. Florin, A. Gadola, B. Huber (until December 2012), A. Manalaysay, S. Steiner, U. Straumann, and A. Vollhardt

in collaboration with ETH Zürich, Jagiellonian University Cracow, MPI für Kernphysik Heidelberg, Universität Tübingen and 109 more institutes from 23 countries

(CTA)

The Cherenkov Telescope Array (CTA) is a planned next generation array of Imaging Atmospheric Cherenkov Telescopes (IACTs), and the successor to current IACT arrays including MAGIC [1], H.E.S.S [2], and VERITAS [3]. The goal is to build a larger and improved version of these current IACT arrays.

Various exotic (i.e. non-thermal) astrophysical sources such as quasars, supernovae and their remnants, gamma-ray bursts, and dark matter annihilations emit gamma rays in the energy range of tens of GeV to tens of TeV. When these gamma rays enter the earth's atmosphere they produce an e^+e^- pair that initiates an electromagnetic shower comprising many highly-energetic charged particles. Many of these particles travel at speeds exceeding the speed of light in the atmosphere, and as a result produce Cherenkov photons that travel in a narrow cone to the ground. The IACTs may detect time and direction of individual Cherenkov photons and allow to reconstruct the electromagnetic shower by combining the signals from many telescopes. This information is used to determine the direction and energy of the initial gamma ray.

CTA is currently in a phase of heavy research and development. New technologies may be exploited that have arisen in the years since the current arrays were designed. Our own efforts include modular and distributed clock generation techniques, primary mirror alignment, optical components of a novel Geiger-mode Avalanche Photodiode IACT camera, and development of the first fully digital IACT camera.

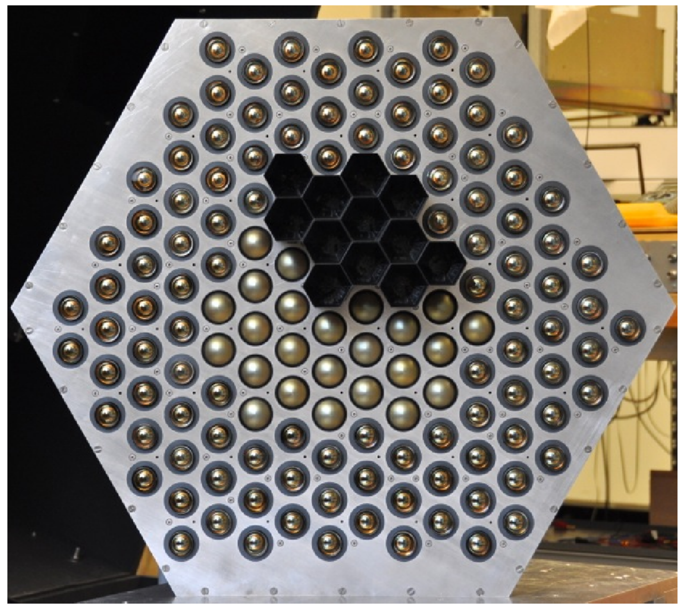

FIG. 7.1 – 144-pixel prototype for FlashCam. Note the two different types of PMT (see text). The hexagonal black structures are mechanical prototypes of the light concentrator.

7.1 FlashCam

FlashCam is a possible camera design for CTA that focuses on a fully digital data and trigger pathway: data is digitized continuously without the need of an analog trigger used to decide whether to digitize the stored analog data. Traditional techniques typically feature an effective sampling rate around 2 GS/s. Costs and power consumption of continuous digitization at 2 GS/s are, however, prohibitive for an array of hundreds of cameras with thousands of readout channels each. Interestingly, our collaborators at the Max Plank Institute for Nuclear Physics (MPI-K) in Heidelberg have shown that adequate instrumental and timing resolution can be achieved at a reduced sampling rate of 250 MS/s. This scheme looks feasible and is currently being prototyped.

The validation of the FlashCam concept, from the collection of photons at the detection plane up to the final data storage, is undertaken in several steps. The very front of the chain, the Photon Detection Plane (PDP), contains photomultiplier tubes (PMTs), their high-voltage supplies, preamplifiers, and slow control electronics. These electronic components are housed on two printed circuit boards to which the PMTs are soldered. The initial twelve-pixel FlashCam prototype, described in the previous Jahresbericht, was constructed to test this aspect of the FlashCam concept. It used Hamamatsu PMTs developed specifically for CTA. Meanwhile, we have built the 144-pixel prototype shown in Figs. 7.1 and 7.2.

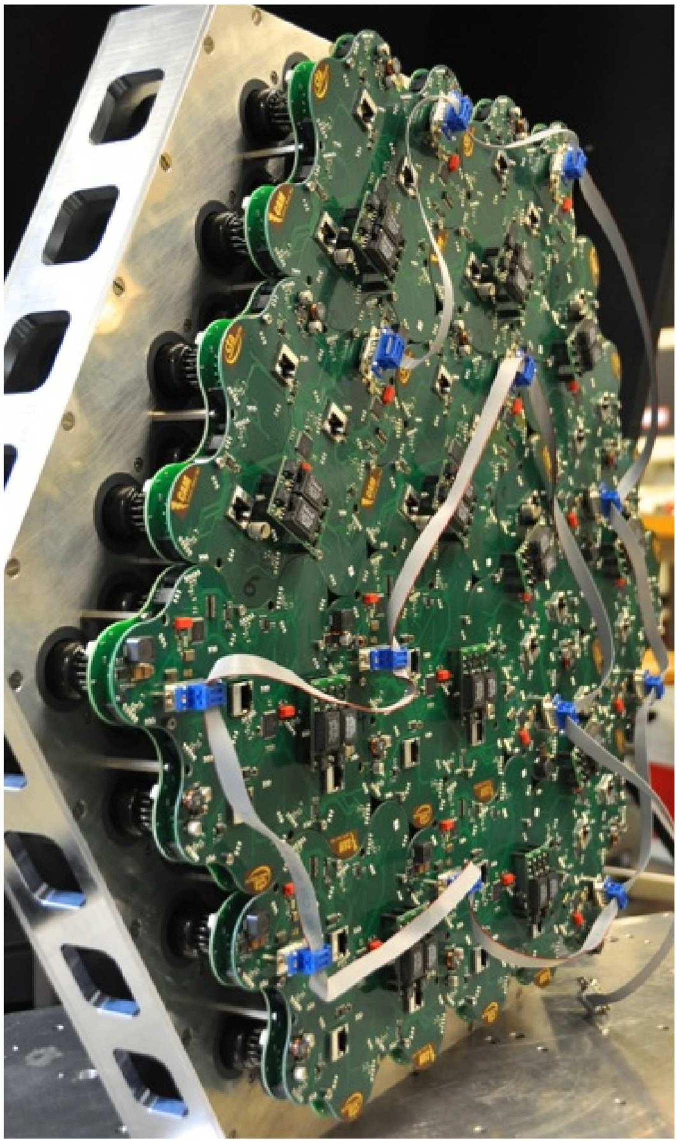

FIG. 7.2 – Rear view of the 144-pixel prototype showing the control boards.

The next step in validating the FlashCam concept is a full system test, including analog signal transmission, signal digitization on custom-made ADC boards, digital signal processing and transmission over custom backplanes, and real-time digital triggering. Due to the considerable cost of the PMTs, this 144-pixel prototype has been constructed with two types of PMTs. The inner 36 PMTs are the same Hamamatsu CTA PMTs, while for the remaining 108 positions Photonis PMTs (spare H.E.S.S. equipment) are used. The PDP electronics of this 144-pixel prototype has been tested and verified. The fully digital chain is due to arrive mid 2013 which will mark a milestone of FlashCam.

[1] J. A. Coarasa *et al.* (MAGIC Collaboration), J. Phys. Soc. Jap. Suppl. 77B (2008) 49.

[2] B. Opitz *et al.* (HESS Collaboration), AIP Conf. Proc. 1223 (2010) 140.

[3] D. Hanna *et al.* (VERITAS Collaboration), J. Phys. Conf. Ser. 203 (2010) 012118.

8 The $\pi^+ \to e^+\nu_e$ / $\pi^+ \to \mu^+\nu_\mu$ branching ratio

P. Robmann, A. van der Schaaf and P. Truöl

in collaboration with University of Virginia, Charlottesville, USA; Institute for Nuclear Studies, Swierk, Poland; JINR, Dubna, Russia; PSI, Villigen, Switzerland and Rudjer Bošković Intitute, Zagreb, Croatia

(PEN Collaboration)

Mesons with positive electric charge (π^+, K^+, D^+, etc.) are described as bound states of an up-type quark and a down-type antiquark. They decay through the electroweak interaction with a (virtual) W propagator which may result in final states with a charged and a neutral lepton (plus γ or e^+e^- pair). As shown in Tab. 8.1 these modes dominate for pions and kaons [2]. The decay rate can be factorized (ignoring numerical constants) in:

- the decay constant F_P accounting for the overlap between the two quark wave functions,
- g^2/m_W^2 for the W propagator, with g the weak coupling constant,
- $V_{CKM}^{q\bar{q}}$ squared describing the reduced strength for the W-quark vertex through quark mixing,
- a correction factor when lepton universality is allowed to be violated so g for the W-lepton vertex depends on generation number (lepton flavor)
- a kinematic factor $m_P(1 - m_l^2/m_P^2)^2$ for the Q-value,
- a helicity factor proportional to m_l^2 originating in the $V-A$ structure of the weak interaction.

The first three factors mostly cancel when normalizing to the total decay rate. An almost perfect cancellation occurs in the ratio $R^P_{e/\mu}$ of the rates for $P \to e^+\nu_e$ and $P \to \mu^+\nu_\mu$:

$$R^P_{e/\mu} \equiv \frac{\Gamma(P \to e^+\nu_e)}{\Gamma(P \to \mu^+\nu_\mu)} \simeq (\frac{m_e}{m_\mu})^2 \times (1 - \frac{m_\mu}{m_P})^2 \times (\frac{g_e}{g_\mu})^2 \,, \tag{8.1}$$

TAB. 8.1 –
SM predictions for the $P \to \bar{l}\nu_l$ branching fractions.

initial state			final state		
P	$q\bar{q'}$	$V_{CKM}^{q\bar{q}}$	$e^+\nu$	$\mu^+\nu$	$\tau^+\nu$
π^+	$u\bar{d}$	0.974	1.22×10^{-4}	99.99%	-
K^+	$u\bar{s}$	0.226	1.55×10^{-5}	63.5%	-
D^+	$c\bar{d}$	0.22	7.5×10^{-9}	3.2×10^{-4}	7.2×10^{-4}
D_s^+	$c\bar{s}$	0.98	7.5×10^{-8}	3.2×10^{-3}	2.9×10^{-2}
B^+	$u\bar{b}$	0.003	1.0×10^{-11}	5×10^{-7}	1.0×10^{-4}

[2] In π^+ decay the only alternative decay mode is $\pi^+ \to \pi^0 e^+\nu$ with a branching ratio $O(10^{-8})$.

TAB. 8.2 – SM predictions and measured values for $R^P_{e/\mu}$ ($P = \pi, K$) defined in Eq. 8.1.

	$\Gamma_{\pi^+\to e^+\nu}/\Gamma_{\pi^+\to\mu^+\nu}$	$\Gamma_{K^+\to e^+\nu}/\Gamma_{K^+\to\mu^+\nu}$
theory	$1.2353(1)\times10^{-4}$[1]	$2.477(1)\times10^{-5}$[1]
experiment	$1.2312(37)\times10^{-4}$[2]	$2.488(12)\times10^{-5}$[3]

where g_i denotes the coupling strength of the $Wl_i\nu_i$ vertex. One readily identifies the factors associated with the helicity suppression, the Q-value, and the universality violation. Table 8.2 compares the theoretical values including all bells and whistles, which are a few percent below the simple estimate, with the published experimental values for π and K.

[1] V. Cirigliano and I. Rosell, JHEP **10** (2007) 5.
V. Cirigliano and I. Rosell,
Phys. Rev. Lett. **99** (2007) 231801.

[2] G. Czapek *et al.*, Phys. Rev. Lett. **70** (1993) 17; D. I. Britton *et al.*, Phys. Rev. Lett. **68** (1992) 3000.

[3] C. Lazzeroni *et al.* (NA62 Collaboration), Phys. Lett. B719 (2013) 326-336

8.1 $\pi^+ \to e^+\nu_e$ measurements

The measured value of the $\pi^+ \to e^+\nu$ / $\pi^+ \to \mu^+\nu$ branching ratio, even if 20 years old by now, still gives the best constraint on deviations from the SM assumption of a flavour independent coupling of W bosons to leptons. Two new experiments [1] are underway which aim at improvements in accuracy by almost one order of magnitude.

For pions at rest the decay $\pi^+ \to e^+\nu$ is characterized by an electron with $E = \frac{1}{2}m_\pi c^2 = 69.8$ MeV emitted with an exponential time distribution with $\tau_{\pi^+} = 26.0$ ns. Since the 4.2 MeV muon from $\pi^+ \to \mu^+\nu$ at rest travels just $\sim$0.1 g/cm^2 and stays in the π^+ stopping target this decay is only observed through the subsequent decay $\mu^+ \to e^+\nu\bar{\nu}$. The decay chain is characterized by an electron with $E < \frac{1}{2}m_\mu c^2 < 52.8$ MeV emitted with a time distribution first rising with τ_{π^+} and then falling with $\tau_\mu = 2.20$ μs. Ideally, the two decay modes can be perfectly distinguished by the positron energy alone but corrections apply since pions and muons may decay in flight tens of ps before they would have stopped. Radiative corrections and imperfections in the experimental setup result in a low-energy tail in the $\pi^+ \to e^+(\gamma)\nu$ positron energy distribution leaking into the region populated by $\pi^+ \to \mu^+\nu$. The uncertainty in this tail fraction is in fact the major source of systematic error in determinations of $R^{\pi}_{e/\mu}$.

[1] PEN Collaboration, PSI experiment R-05-01 (2005), D. Pocanic and A. van der Schaaf, spokespersons; PIENU Collaboration, TRIUMF proposal 1072 (2006), D. Bryman and T. Numao, spokespersons.

8.2 the PEN experiment

PEN[3] took data at the πE1 beam line at PSI during 2008 – 2010. The beam momentum was typically 75 MeV/c with a spread of $\pm 1\%$. The main trigger for data readout required a decay positron within a (-30,+220) ns window around the time of an incoming pion. Events with positron energies below $\sim$48 MeV were pre-scaled by 1:64. Whereas $\sim$95% of $\pi \to e\nu$ events in the 3π sr geometric acceptance were recorded the much more abundant $\pi \to \mu\nu$, $\mu \to e\nu\bar{\nu}$ decay chain was suppressed by two orders of magnitude. Still, the recorded number of events in the $\pi \to \mu$ branch is much larger than for $\pi \to e$ and the statistical error in $R^{\pi}_{e/\mu}$ is practically equal to the statistical error in the number of reconstructed $\pi \to e\nu$ events (see Tab. 8.3) so a few 10^{-4}. This is more than ten times smaller than reached before in both π and K decay.

A PEN event contains at least a beam pion and a decay positron. The pions crossed various beam counters before stopping in the target scintillation detector. All scintillators were read with 2 GHz waveform digitizers and after 2008 the beam particle trajectories were measured with a TPC (Fig. 8.1). Based on the measured *individual* pion velocity and energy deposits (corrected for light quenching) the pion energy when entering the target is known to a few percent for each event. This knowledge is crucial when testing the target waveform for the occurrence of a decay muon. The decay positrons were tracked in MWPCs and crossed a plastic hodoscope before reaching the pure CsI spherical calorimeter. The active target may be called the heart of the detection system since all particles leave their traces there. At the other hand, the signatures of the two decay branches differ so much that there is little hope to understand a target waveform analysis at the precision required for $R^{\pi}_{e/\mu}$. Still, the target waveforms of well separated π-μ-e sequences (*gold plated* $\pi \to \mu$ events) allow a very accurate calibration of the offset of the decay time calculated from the time signals of the dedicated beam and decay particle detectors.

TAB. 8.3 –
PEN vital statistics during the three years of operation.

	2008	2009	2010	total	
calendar days	111	98	68	277	
pion stops	7.5	13.1	16.4	37.0	$\times 10^{10}$
$\pi \to e\nu$ events	4.4	7.8	10.1	22.3	$\times 10^{6}$

Detector calibrations are almost done now for all years and reconstruction algorithms have been pushed close to perfection. State of the art event simulation all the way down to the data format of the measured events is basically ready for the 2008 data set, and is under development for later years when many readout systems were upgraded.

The data analysis is challenging indeed when the systematic error has to be pushed below the statistical error. An un-binned maximum likelihood program was written, capable of fitting the contributions of 4-5 event types characterized by 3-4 dimensional PDFs in samples of 10^8 events. This achievement is far from trivial.

Crucial in a precision measurement such as PEN is a blind analysis in which adjustments affecting the physics result are only allowed as long as that result is unknown: the result is final by the time it is obtained first. This explains why no preliminary results can be presented.

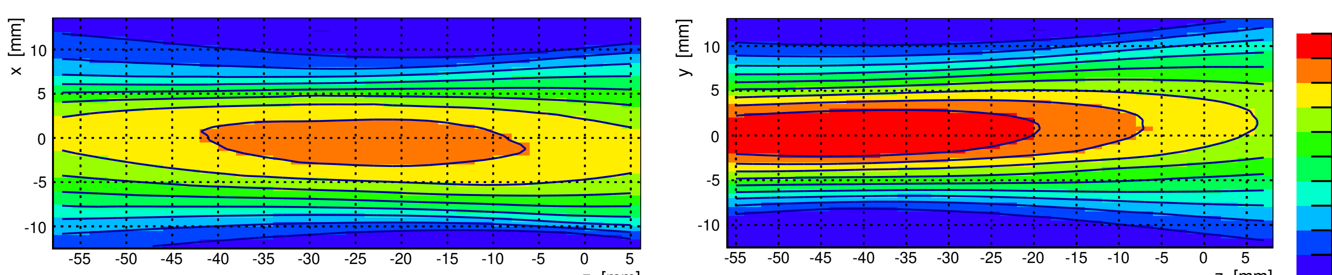

FIG. 8.1 –
xz and yz beam profiles (z is beam axis) during 2010, measured with the mini TPC. The target with 15 mm radius starts at z = -5 mm. Beam tracking not only helps to suppress random background through a constraint on the π-e vertex but also helps to define the 5-dimensional beam phase space used in the simulations.

[3]see previous annual reports for more details

9 Study of πK atoms

C. Amsler, A. Benelli, and J. Rochet

(DIRAC Collaboration)

The main initial goal of the DIRAC experiment was to produce $\pi^+\pi^-$ atoms (pionium) and to measure the $\pi\pi$ scattering lengths a_0 and a_2 (isospins 0 and 2) [1]. The difference in the scattering lengths was measured,

$$|a_0 - a_2| = 0.2533 \pm 0.0109\ m_\pi^{-1}$$

based on the observation of 21'227 $\pi^+\pi^-$ atoms. This value corresponds to a mean life of 3.15 ± 0.28 fs. Details can be found in ref. [2].

We joined the DIRAC collaboration in 2007 with the goal to search for πK atoms and to measure the πK scattering lengths $a_{1/2}$ and $a_{3/2}$ (isospins 1/2 and 3/2).

An artist's view of the DIRAC spectrometer and a photograph of the experiment in the CERN-PS-South Hall is shown in figures 9.1 and 9.2, respectively. The 24 GeV/c proton beam passes through a thin target (such as 100 μm Ni). The secondary particles traverse a scintillation fiber detector (SFD). The secondary hadrons produced in target are analyzed in a double-arm magnetic spectrometer measuring the momentum vectors of two oppositely charged hadrons. The spectrometer is slightly tilted upwards with respect to the proton beam. Electrons and positrons are vetoed by N_2-Čerenkov detectors (N) and muons by their signals in scintillation counters (Mu) behind steel absorbers. The preshower detector (PSh) provides an additional electron/hadron separation to the N_2-Čerenkov. Details can be found in previous annual reports and in ref. [3].

In 2007 we modified the DIRAC setup to study πK atoms while at the same time collecting more data for $\pi\pi$ atoms. In both arms the N_2-Čerenkov counters were cut to leave space for heavy gas (C_4 F_{10}) Cerenkov detectors (HG). They identify pions with an efficiency of more than 99% while not responding to kaons nor to (anti)protons. On the left side we installed an aerogel Čerenkov detector (Ae) to identify kaons and reject protons. The detector consists of two modules with refractive index 1.015 and one module with refractive index 1.008 to cover the high momentum range of kaons between 5.5 and 8 GeV/c. Our group has developed and built the 37ℓ aerogel Čerenkov counter [4] and the gas system for the C_4F_{10} counters [5].

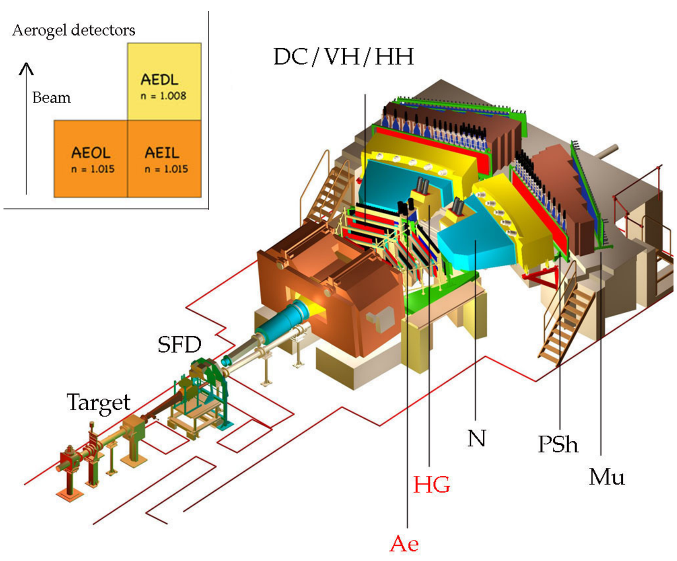

FIG. 9.1 – DIRAC spectrometer:
SFD: scintillating fibre detector, DC: drift chambers, VH (HH): vertical (horizontal) scintillating hodoscopes, PSh: preshower, Mu: muon counters, Ae: aerogel, and HG: heavy gas and N: N_2-Čerenkov counters.
The inset shows the arrangement of the aerogel modules.

FIG. 9.2 – The DIRAC apparatus.

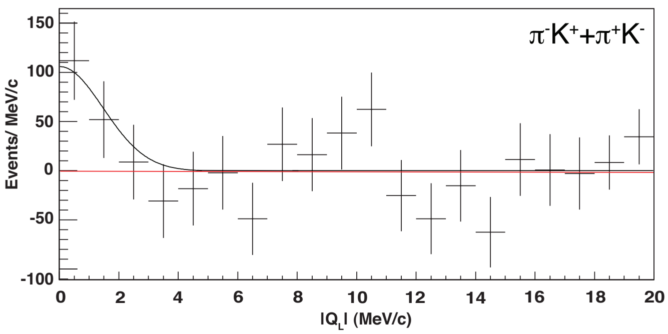

FIG. 9.3 – Distribution of the πK relative momentum in the c.m.s system after background subtraction. A Gaussian fit (solid line) illustrates the signal distribution.

Using only the downstream part of DIRAC for tracking we published the first evidence for πK atoms [6, 7]. A signal of 173 $\pm$ 54 (3.2σ) πK-pairs was observed at very low relative momenta (typically $|Q_L| < 3$ MeV/c in the c.m.s system), see Fig. 9.3. The evidence was strengthened by the simultaneous observation of interacting unbound Coulomb-pairs from which the fraction of expected bound pairs can be calculated. The latter is in excellent agreement with the number of observed atoms. This result corresponds to a lower limit on the mean life of πK-atoms of 0.8 fs in the 1s-state (confidence level of 90%), which translates to [6, 7]:

$$|a_{1/2} - a_{3/2}| < 0.58\ m_\pi^{-1}.$$

More data was collected in 2008 – 2011 from which the total number of reconstructed πK atoms will be around 600. Assuming the central value as in 2007 the significance will increase to 5.3σ corresponding to an uncertainty of about 25% on $|a_{1/2} - a_{3/2}|$.

In 2012 DIRAC also studied the energy splitting ΔE between the pionium $2p$- and $2s$-states by mean of the following method: pionium atoms produced in the target interact with an applied electric field and some of them leave the target in the $2p$-state. The decay into $\pi^0\pi^0$ is forbidden from p-states and hence the main decay process is the $2p - 1s$ radiative transition with subsequent annihilation from $1s$ into $\pi^0\pi^0$. Thus the mean life of the atom in the $2p$-state is determined by radiative transition, $\tau(2p) \simeq 12$ ps, which is much slower than annihilation from the $1s$-states. We refer to these $2p$-states as *long-lived* 2π atoms. One then measures ΔE by observing the field dependence of the number of long-lived 2π atoms breaking up into $\pi^+\pi^-$ pairs in a second foil downstream of the production target. This measures the combination $2a_0 + a_2$. Combined with the measurements from the $1s$-state, the $\pi\pi$ scattering lengths a_0 and a_2 can be determined separately.

Data taking for the DIRAC experiment was completed at the end of 2012 and the apparatus was subsequently dismantled.

[1] B. Adeva *et al.* (DIRAC Collaboration), Phys. Lett. **B 704** (2011) 24.

[2] A. Benelli, EPJ Web of Conferences **37** (2012) 01011, doi: 10.1051/epjconf/20123701011.

[3] B. Adeva *et al.* (DIRAC Collaboration), Nucl. Instrum. Methods in Phys. Res. **A 515** (2003) 467.

[4] Y. Allkofer *et al.*, Nucl. Instr. Meth. in Phys. Res. **A 582** (2007) 497; Y. Allkofer *et al.*, Nucl. Instr. Meth. in Phys. Res. **A 595** (2008) 84; C. Amsler, Proc. of Science PoS EPS-HEP (2009) 078.

[5] S. Horikawa *et al.*, Nucl. Instr. Meth. in Phys. Res. **A 595** (2008) 212.

[6] B. Adeva *et al.* (DIRAC Collaboration), Phys. Lett. **B 674** (2009) 11.

[7] Y. Allkofer, PhD Thesis, University of Zurich (2008).

10 Particle Physics at DESY/HERA (H1)

K. Müller, P. Robmann, U. Straumann, and P. Truöl

in collaboration with C. Grab (Institut für Teilchenphysik der ETH, Zürich), S. Egli, M. Hildebrandt and R. Horisberger (Paul–Scherrer–Institut, Villigen), and 39 institutes outside Switzerland

(H1 - Collaboration)

As mentioned already in last years annual report the improved extraction of the parton-density functions (PDFs) remained a central topic of the recent publications based on the data collected until 2007 by the H1-collaboration at the HERA electron-proton storage ring. Statistical and systematic errors of both neutral and charged current cross sections as a function of Q^2 and Bjorken-x [4] have been reduced either by combining all available H1 data or by combining data from the H1 and ZEUS experiments.

The completion of the analysis of inclusive neutral (NC) and charged (CC) current cross sections with the HERA I and HERA II H1 data samples at $\sqrt{s} = 319$ GeV is documented in a long article [1] which is briefly reviewed below. The combination of the charm production data from the two experiments and their impact on the extraction of PDFs examplifies the second approach [2].

10.1 Neutral and charged current cross sections

For the measurement of the inclusive deep-inelastic scattering (DIS) cross sections [1] for $e^{\pm}$ interactions data from 333.7 pb^{-1} of integrated luminosity were available. The e^-p data correspond to an almost tenfold increase in luminosity over the HERA I data set. Moreover, the operation of the HERA collider with left and right handed longitudinally polarised electron and positron beams allowed measurements in the NC and CC channels with four distinct initial states. The cross sections cover the region $Q^2 \geq 100$ GeV^2 and Bjorken-$x \geq 10^{-3}$, and were obtained differentially in Q^2 and double-differentially in x and Q^2. In the NC channel a systematic uncertainty of 1.5% was attained in the kinematic region $Q^2 < 1000$ GeV^2 and $y > 0.1$ [5], compared to a statistical accuracy of 1 - 3 %. An important input leading to this higher precision stemmed from the new determination of the integrated luminosity using elastic QED Compton scattering $e^+p \rightarrow e^+p\gamma$ events [3]. The high inelasticity region of $0.63 \leq y \leq 0.90$ for $60 \leq Q^2 \leq 800$ GeV^2 was covered in the NC analy-

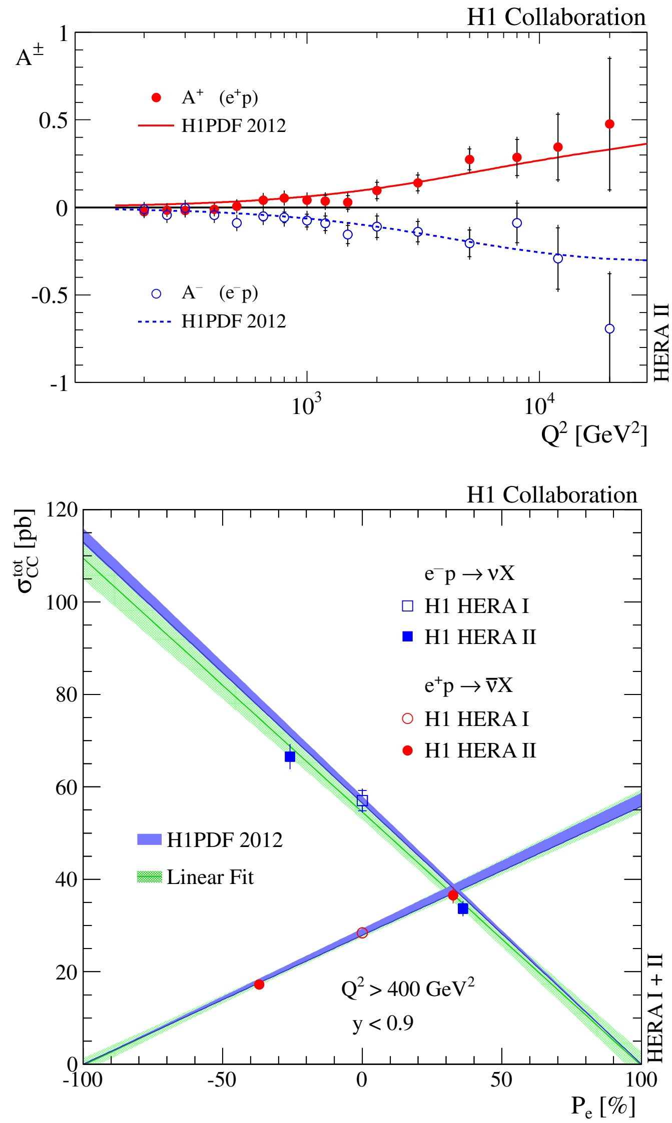

FIG. 10.1 – Top: Q^2 dependence of the polarisation asymmetries A^+ and A^- for e^+p and e^-p, respectively. Bottom: dependence of the $e^{\pm}p$ total CC cross sections on the lepton beam polarisation. In both plots the measurements are compared to the Standard Model expectation based on the H1PDF 2012 parametrisation. The green band (bottom) corresponds to the $\pm 1\sigma$ error of a linear fit. Inner and outer error bars represent the statistical and total errors, respectively.

[4] Q^2: square of the four-momentum exchanged in the hard $e^{\pm}$ scattering process,
x: longitudinal component of the incoming proton's momentum carried by the interacting parton (quark or gluon).
[5] inelasticity $y \equiv Q^2/x \cdot s$ with s: total centre-of-mass energy

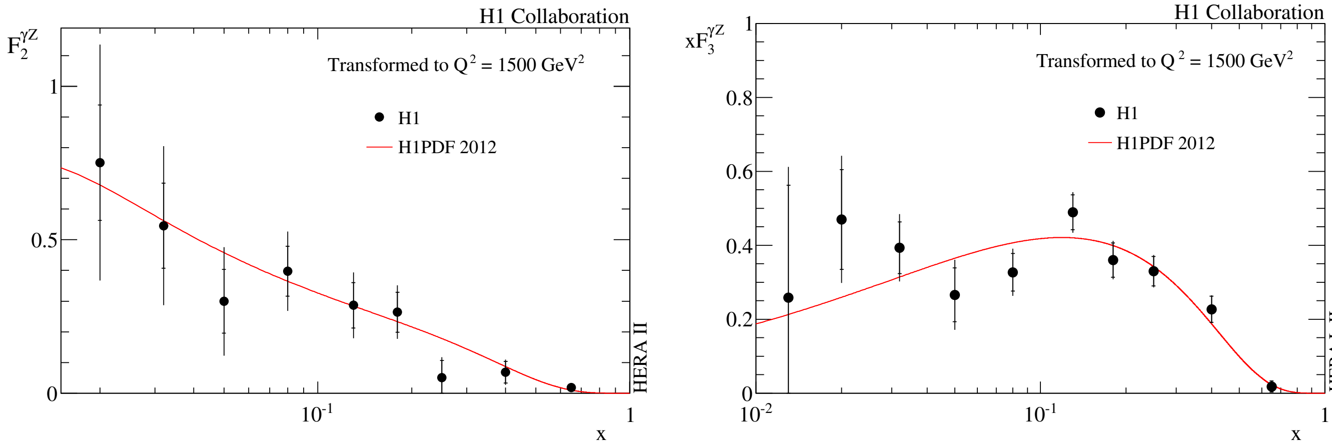

FIG. 10.2 –
Measured structure functions $F_2^{\gamma Z}$ and $xF_3^{\gamma Z}$ transformed to $Q^2 = 1500$ GeV^2 compared to the H1PDF 2012 predictions.

sis for unpolarised $e^{\pm}p$ scattering. This region of phase space is sensitive to the F_L structure function. The article includes the results of a next-to-leading order (NLO) QCD analysis for $Q^2 \geq 3.5$ GeV^2 including all previously published H1 NC and CC cross section measurements (H1PDF2012). The measurements are well described by the QCD fit over the full phase space (χ^2 per degree of freedom 1570/1461). The new results at high Q^2 provide better constraints on the PDFs. In particular the CC e^+p data enabled an improved flavour separation at high x. The NC lepton polarisation asymmetry $A^{\pm}$, sensitive to parity violation, was determined both for e^+p and e^-p scattering and found to increase with Q^2 in agreement with the expectation of the Standard Model (see Fig. 10.1).

The structure function $F_2^{\gamma Z}$ (which is associated with the photon-Z interference, see below for definition) was measured for the first time using the polarisation dependence of the $e^{\pm}p$ NC cross section. At high Q^2 the structure function $xF_3^{\gamma Z}$ is determined using unpolarised NC cross sections obtained from the complete HERA I and HERA II data sets. The $xF_3^{\gamma Z}$ results cover the range $0.013 \leq x \leq 0.65$. Integrated over x the measurement validates a sum rule for charged lepton scattering. Figure 10.2 shows the averaged results for both these structure functions at $Q^2 = 1500$ GeV^2.

The structure functions F_2 and F_3 appear in the general expression for the neutral current cross section:

$$\frac{d^2\sigma^{\pm}_{\rm NC}}{dx\,dQ^2} = \frac{2\alpha\pi^2}{xQ^4}\left(Y_+\tilde{F}_2^{\pm} \mp Y_- x\tilde{F}_3^{\pm} - y^2\tilde{F}_L^{\pm}\right)\left(1+\Delta^{\rm weak}_{\rm NC}\right)$$

where $Y_{\pm}$ are kinematical functions and y is the lepton energy loss. The generalized structure functions, $\tilde{F}_{2,3}$ may be written as linear combinations of the proton structure functions F_2, $F_{2,3}^{\gamma Z}$ and $F_{2,3}^{Z}$ which contain information on the parton dynamics as well as on the electroweak couplings of the quarks to the neutral vector bosons. F_2 is associated to pure photon exchange terms, $F_{2,3}^{\gamma Z}$ to photon-Z interference and $F_{2,3}^{Z}$ to pure Z-exchange. $\tilde{F}_L$ may be decomposed similarly, but is important only at high y and negligible at large x and Q^2.

The sensitivity to the quark (antiquark) $q(\bar{q})$ distribution functions arises as

$$\begin{aligned}\left[F_2, F_2^{\gamma Z}, F_2^{Z}\right] &= x\sum_i \left[e_i^2, 2e_i v_i, v_i^2 + a_i^2\right](q_i + \bar{q}_i)\\ \left[xF_3^{\gamma Z}, xF_3^{Z}\right] &= 2x\sum_i \left[e_i a_i, v_i a_i\right](q_i - \bar{q}_i)\end{aligned}$$

The linear combinations for $\tilde{F}_2$ and $x\tilde{F}_3$ for a lepton beam with polarisation P_e are given as

$$\begin{aligned}\tilde{F}_2^{\pm} &= F_2 - (v_e \pm P_e a_e)\kappa\lambda(Q^2)F_2^{\gamma Z} + \\ &\quad (a_e^2 + v_e^2 \pm P_e 2v_e a_e)[\kappa\lambda(Q^2)]^2 F_2^{Z}\\ x\tilde{F}_3^{\pm} &= -(a_e \pm P_e v_e)\kappa\lambda(Q^2)xF_3^{\gamma Z} + \\ &\quad (2a_e v_e \pm P_e[v_e^2 + a_e^2])[\kappa\lambda(Q^2)]^2 xF_3^{Z}\end{aligned}$$

with $\kappa^{-1} = 4(M_W/M_Z)^2[1-(M_W/M_Z)^2]$, $\lambda(Q^2) = Q^2/(Q^2+M_Z^2)$, and $a(v)$ designating the axialvector (vector) couplings of the quarks and leptons.

Similar expressions hold for the charged current cross section yielding a flavor decomposition:

$$\frac{d^2\sigma^{-}_{\rm CC}}{dx\,dQ^2} = (1 \pm P_e)\frac{G_F^2}{4\pi x}\left[\frac{M_W^2}{M_W^2+Q^2}\right]^2\left(Y_+W_2^{\pm} \mp Y_- xW_3^{\pm} - y^2 W_L^{\pm}\right)\cdot\left(1+\Delta^{\rm weak}_{\rm CC}\right)$$

with:

$$W_2^- = x(U + \overline{D}) \qquad W_2^+ = x(\overline{U} + D)$$
$$xW_3^- = x(U - \overline{D}) \qquad xW_3^- = x(-\overline{U} + D)$$
$$U = u + c \qquad \overline{U} = \overline{u} + \overline{c}$$
$$D = d + s \qquad \overline{D} = \overline{d} + \overline{s}.$$

The polarisation dependence of the CC total cross section for $Q^2 > 400$ GeV^2 and $y < 0.9$ was measured and compared to the unpolarised HERA I measurements. As evident from Fig. 10.1 the data exhibit a linear scaling of the cross sections with P_e which is positive for e^+p and negative for e^-p scattering. The data are consistent with the absence of right handed weak currents.

10.2 Open charm production

Measurements of open charm production in deep-inelastic ep scattering by the H1 and ZEUS experiments using different charm tagging methods were combined, accounting for the systematic correlations [2]. The measurements were extrapolated to the full phase space using a NLO QCD calculation to obtain the reduced charm quark-pair cross sections in the region of photon virtualities $2.5 \leq Q^2 \leq 2000$ GeV^2. The combined data are compared to QCD predictions in the fixed-flavour-number-scheme (FFNS) and in the general-mass variable-flavour-number-scheme (GM-VFNS) [2].

In FFNS the charm quark is treated as massive and not as a parton in the proton. The number of active flavours is fixed to three, and charm quarks are assumed to be produced only in the hard scattering process via boson-gluon-fusion in leading order. In GM-VFNS charm production is treated as in FFNS in the low Q^2 region where the mass effects are largest, and the charm quark mass is set to zero at high Q^2.

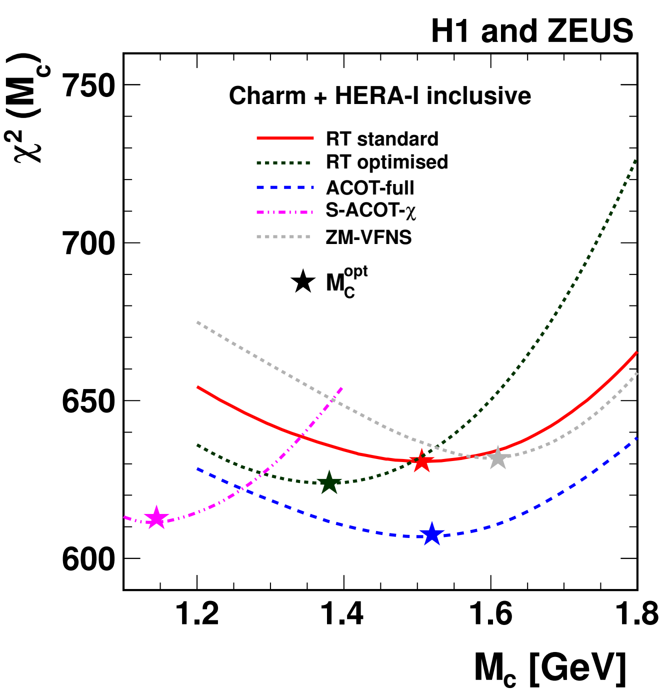

FIG. 10.3 – $\chi^2(M_c)$ for the PDF fit to the combined HERA inclusive DIS and charm measurements. Different heavy flavour schemes used in the fit are presented. The best-fit values $M_c^{\rm opt}$ for each scheme are indicated by the stars.

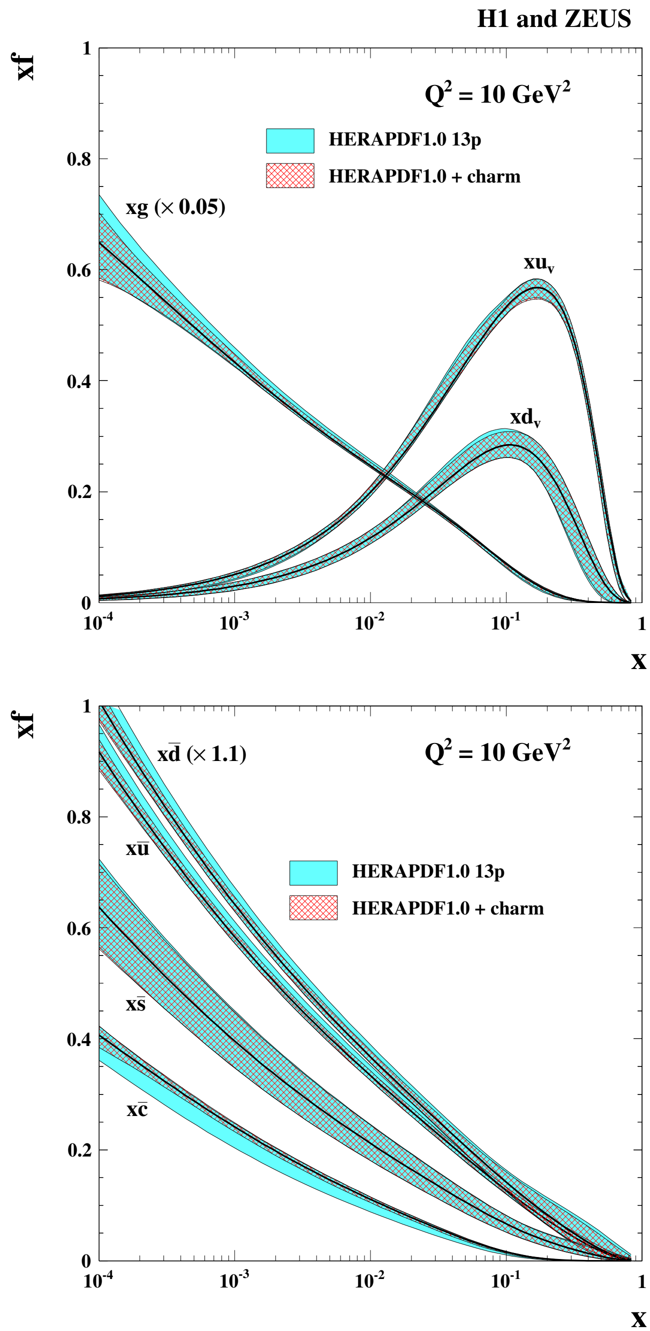

FIG. 10.4 – Parton density functions $x \cdot f(x, Q^2)$ with $f = g, u_v, d_v, \overline{u}, \overline{d}, \overline{s}, \overline{c}$ for (top) valence quarks and gluon and for (bottom) sea anti-quarks obtained from the combined QCD analysis of the inclusive DIS data and $\sigma_{\overline{c}c}$ as a function of x at $Q^2 = 10$ GeV^2. The results of the QCD analysis of the inclusive DIS data only are also shown. For better visibility the gluon distribution function is scaled by 0.05 and the $x\overline{d}$ distribution function by 1.1.

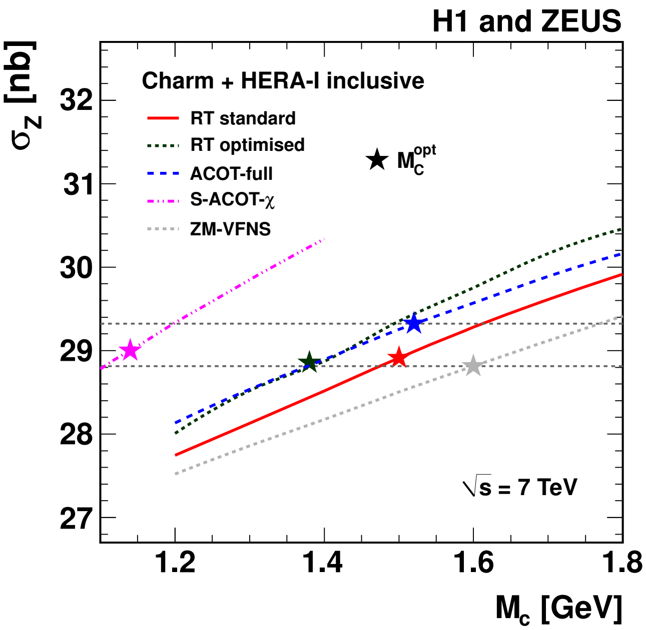

FIG. 10.5 – NLO predictions for the Z production cross sections at the LHC for $\sqrt{s} = 7$ TeV as a function of M_c used in the corresponding PDF fit. Predictions for different implementations of the VFNS are indicated. The predictions obtained with PDFs evaluated with the M_c^{opt} values for each scheme are indicated by the stars. The horizontal dashed lines show the resulting spread of the predictions when choosing $M_c = M_c^{\mathrm{opt}}$.

The best description of the data in the whole kinematic range is provided by the most recent NNLO FFNS prediction [4]. Some of the NLO GM-VFNS general-mass predictions significantly underestimate the charm production cross section at low Q^2, which is improved at NNLO. Using the combined charm cross sections together with the combined HERA inclusive DIS data, a NLO QCD analysis was performed based on different VFNS implementations. All schemes are found to describe the data well when treating the charm mass as a free parameter even when the resulting M_c^{opt} may differ considerably (see Fig. 10.3). The use of M_c^{opt} and its uncertainty in the QCD analysis significantly reduces the parton density uncertainties, mainly for the sea quark contributions from charm, down and up quarks (see Fig. 10.4). The QCD analysis was also performed in the FFNS at NLO using the MS running mass definition [4]. The running charm quark mass is determined as $m_c = 1.26 \pm 0.05\,(\mathrm{exp.}) \pm 0.03\,(\mathrm{model}) \pm 0.02\,(\mathrm{param}) \pm 0.02\,(\alpha_s)$ GeV. This value agrees well with the world average based on lattice calculations and on measurements of time-like processes. The PDFs obtained from the corresponding QCD analyses using different M_c are used to predict $W^{\pm}$ and Z production cross-sections at the LHC (see Fig. 10.5). A sizeable spread in the predictions is observed, when the charm mass parameter M_c is varied between 1.2 and 1.8 GeV, or when different schemes are considered at fixed value of M_c. The spread is significantly reduced when the optimal value of M_c is used for each scheme.

10.3 Other subjects

Other subjects which have been addressed in the articles published last year include:

- photoproduction of charm and beauty [5–8];
- diffractive cross sections measured with the forward proton spetrometer [9] and their combination with similar ZEUS-data [10];
- inclusive diffractive contribution to [11] and charged particle spectra from DIS [12].

[1] H1-Collaboration, F.D. Aaron *et al.*, JHEP **09** (2012), 061.
[2] H1- and ZEUS-Collaboration, H. Abramowicz *et al.*, Eur. Phys. J. C **73** (2013), 2311.
[3] H1-Collaboration, F.D. Aaron *et al.*, Eur. Phys. J. C **72** (2012), 2163.
[4] S. Alekhin and S. Moch, Phys. Lett. B **699**, (2011) 345.
[5] H1-Collaboration, F.D. Aaron *et al.*, Eur. Phys. J. C **72** (2012), 1995.
[6] H1-Collaboration, F.D. Aaron *et al.*, Eur. Phys. J. C **72** (2012), 2047.
[7] H1-Collaboration, F.D. Aaron *et al.*, Eur. Phys. J. C **72** (2012), 2148.
[8] H1-Collaboration, C. Alexa *et al.*, *Elastic and Proton Dissociative J/Ψ-Meson Photoproduction at HERA*, submitted to Eur. Phys. J. C (2013), DESY 13 – 058, arXiv:1304.5162 [hep-ex].
[9] H1-Collaboration, F.D. Aaron *et al.*, Eur. Phys. J. C **72** (2012), 1970.
[10] H1- and ZEUS-Collaboration, F.D. Aaron *et al.*, Eur. Phys. J. C **72** (2012), 2175.
[11] H1-Collaboration, F.D. Aaron *et al.*, Eur. Phys. J. C **72** (2012), 2074.
[12] H1-Collaboration, C. Alexa *et al.*, Eur. Phys. J. C **73** (2013), 2406.

11 Particle Physics with LHCb

J. Anderson, R. Bernet, E. Bowen (since October 2012), A. Bursche, N. Chiapolini, M. De Cian, Ch. Elsasser, K. Müller, C. Salzmann (until June 2012), S. Saornil, N. Serra, St. Steiner, O. Steinkamp, B. Storaci (since November 2012), U. Straumann, M. Tobin (until January 2013), M. Tresch, and A. Vollhardt

The full LHCb collaboration consists of 63 institutes from Brazil, China, France, Germany, Ireland, Italy, Pakistan, Poland, Romania, Russia, Spain, Switzerland, The Netherlands, Turkey, Ukraine, the United Kingdom and the United States of America.

(LHCb - Collaboration)

The main goal of the LHCb experiment [1] at CERN's Large Hadron Collider (LHC) is the search for possible contributions from "New Physics" (NP) beyond the Standard Model (SM) by performing precision measurements of *CP* violating observables and rare decays of hadrons containing a b quark or a c quark. Of special interest are processes that involve loop diagrams with internal quark lines, such as box or penguin diagrams. Heavy new particles, which are predicted by most NP models, can appear in the internal lines of these loop diagrams and modify the observables with respect to SM predictions. Precision measurements of these observables therefore can reveal the presence of NP. The Zurich group has made important contributions to several key analyses of rare B decays.

The unique acceptance coverage of the detector and the ability to trigger on particles with moderately high transverse momentum, p_{T}, gives LHCb very interesting possibilities in particle production studies. The Zurich group has a leading role in measurements of W, Z and low mass Drell-Yan production. These constitute a test of QCD at LHC energies and will provide valuable input to the knowledge of the parton density functions (PDF) of the proton in a previously unexplored kinematic region.

Several members of the Zurich group have taken up leadership roles in the collaboration: U. Straumann completed his term as chair of the LHCb Collaboration Board; O. Steinkamp served as chair of the Speakers' Bureau; K. Müller acts as co-convener of the "QCD, Electroweak & Exotica" physics working group, while J. Anderson and N. Serra are co-conveners of the sub-working groups "Electroweak bosons" and "Rare electroweak penguin decays", respectively.

11.1 The LHCb experiment

The LHCb detector[1] is a single-arm forward spectrometer with pseudo-rapidity coverage in the range 2 to 5. The detector has excellent vertex and momentum resolution to separate primary and secondary vertices and provides good invariant mass resolution. It is able to trigger on particles with p_{T} down to a few GeV. Two Ring Imaging Cherenkov detectors (RICH) allow discrimination between pions and kaons over a wide momentum range. The detector and its performance have been described in previous annual reports [2].

The experiment has performed outstandingly well during the first three years of LHC operation. Many competitive and world-best measurements have been obtained from the analysis of the 2011 data set, corresponding to an integrated luminosity of 1.0 fb^{-1} of pp collisions collected at a centre of mass energy of 7 TeV. An additional 2 fb^{-1} of good quality data at a centre of mass energy of 8 TeV have been collected in 2012 and are being analysed. The total integrated luminosity in the forthcoming period (2015-2017), following the first long shutdown (LS1) of the LHC, is expected to be about 5 fb^{-1}. A comprehensive upgrade of the LHCb apparatus is then foreseen for the second long shutdown (LS2) of the LHC accelerator in 2018/2019. The main goals of the LHCb upgrade are to operate the experiment at higher instantaneous luminosities and to improve further the trigger efficiency for heavy quark decays to purely hadronic final states.

[1] A. A. Alves Jr. *et al.* [LHCb collaboration], JINST 3 S08005 (2008).

[2] Physik-Institut, University of Zürich, Annual Reports 1996/7 ff.; available at *http://www.physik.unizh.ch/reports.html*.

11.1.1 LHCb detector performance and operation

The LHCb experiment continued to demonstrate excellent running performance in 2012. Data taking efficiency exceeded 95%. The centre-of-mass energy of 8 TeV in 2012, lead to a 15 % higher $b\bar{b}$ production cross section compared to 2011. The output rate of the LHCb high-level trigger (HLT) could be increased from 3.5 kHz in 2011 to

5 kHz in 2012 by an upgrade of the HLT farm (which was partially funded by a special contribution from the SNF) and the introduction of a deferred trigger scheme. About 10 % of the events were temporarily stored on local disks and then processed during the gaps in between two proton fills in the LHC. The increased HLT output rate permitted to further reduce p_T thresholds, benefiting in particular charm and production particle studies.

LHCb also participated in the LHC proton–ion runs at the end of the data taking period in February 2013. About 2 nb^{-1} of proton-lead collisions were recorded with very loose trigger settings. The study of these data will help to gain better understanding of nucleus-nucleon collisions.

The LHC accelerator is now undergoing a two-year shutdown for maintenance and consolidation work, which will allow to operate at a centre-of-mass energy of $\sqrt{s} = 13$ TeV from 2015 onwards.

11.1.2 The Tracker Turicensis

N. Chiapolini, Ch. Elsasser, C. Salzmann, S. Saornil, M. Tobin

The Zurich group continued to be responsible for the operation and maintenance of the Tracker Turicensis (TT), a large planar silicon-strip tracking detector located in front of the LHCb dipole magnet. The TT had been designed and constructed in Zurich. A description of this detector can be found in previous annual reports [1]. At the end of the 2012 data taking period, 99.7 % of the 143 360 readout channels of the TT were fully operational. This is still the highest reliability figure of any silicon tracking detector at the LHC.

Ageing effects in the detector were studied using two complementary methods. One method makes use of the well understood relation between the detector leakage current and the fluence the detector is exposed to. The second method uses charge collection efficiency (CCE) scans which are used to estimate the full depletion voltage V_{fd} of the sensors. The full depletion voltage V_{fd} is related to the received fluence through the so-called Hamburg model [2]. Such CCE scans have been regularly performed every few months. As shown in Fig. 11.1, the results of the analysis are in good agreement with expectations from the Hamburg model.

[1] Physik-Institut, University of Zürich, Annual Reports 1996/7 ff.; available at *http://www.physik.unizh.ch/reports.html.*

[2] M. Moll, *Radiation Damage in Silicon Particle Detectors*, DESY-THESIS-1999-040.

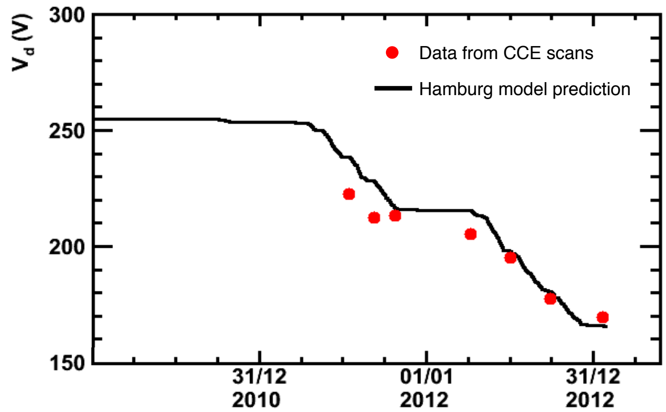

FIG. 11.1 – The full depletion voltage V_{fd} in the inner most region of TT measured from Charge Collection Efficiency scans compared with the evolution expected from the Hamburg model [2].

11.2 The LHCb upgrade

Assuming that LHCb will collect about 5 fb^{-1} during the LHC run following LS1, and taking into account the factor of two higher heavy quark production cross sections at 13 TeV, the size of the collected event samples will have increased by more than a factor of ten by the time of LS2 compared to the 2011 data set used for the currently published results.

The LHCb collaboration is then preparing a comprehensive upgrade of the detector and its readout for LS2. The physics case and details of the upgrade plans are described in the Letter of Intend [1] and the Framework Technical Design Report [2] for the upgrade. The Framework TDR was submitted to the LHCC in May 2012 and endorsed by the committee in September. In its November 2012 session, the CERN Research Board approved the upgrade of LHCb to be part of the long-term exploitation of the LHC. Sub-system Technical Design Reports are scheduled for the end of 2013.

The upgrade plan contains two main components: to prepare the detector for operation at a five times increased instantaneous luminosity compared to 2011 and to read out the full detector at the LHC bunch crossing rate of 40 MHz. By overcoming the limitations of the current hardware based trigger level, the 40 MHz readout will gain a factor of two in trigger efficiencies for b hadron decays to fully hadronic final states. Together with the increased heavy quark production cross section, the expected gains in event yields per year, compared to 2011, are a factor 10 in channels involving muons in the final state and a factor 20 in channels to fully hadronic final states. In total, the upgraded experiment is expected to collect an integrated luminosity of 50 fb^{-1} over 10 years of operation. The upgrade will significantly increase the physics reach in very rare decays, provide unique opportunities for NP searches in B_s^0 decays and be competitive in B^0 decays, and will deliver unprecedented charm yields.

[1] R. Aaij *et al.* [LHCb collaboration], *Letter of Intent for the LHCb Upgrade* CERN-LHCC-2011-001, LHCC-I-018.

[2] I. Bediaga *et al.* [LHCb collaboration], *Framework TDR for the LHCb Upgrade: Technical Design Report*, CERN-LHCC-2012-007, LHCb-TDR-12.

11.2.1 Upgrade studies

E. Bowen, O. Steinkamp and B. Storaci

The present TT detector will need to be replaced as part of the LHCb upgrade foreseen for LS2 since its front-end electronics is not compatible with the foreseen 40 MHz readout. The main purpose of the upgraded TT (UT) will be to improve the speed of the track reconstruction at trigger level by providing an early momentum estimate for track candidates. The Zurich group is responsible for the optimisation of the relevant reconstruction algorithms. These studies will also provide important input for the optimisation of the layout of the UT.

No significant changes to the LHCb detector are foreseen for LS1. The HLT strategy will, however, be revised and optimised to prepare for the higher particle densities and detector occupancies expected at 13 TeV collision energy. As part of the upgrade studies performed by the Zurich group, we also investigate the possibility of reducing the processing time of the HLT by using information from the existing TT to provide an early momentum estimate for track candidates. The momentum estimate could be used to reject track candidates that are expected to miss the tracking stations after the magnet and to optimise search windows in these tracking stations for the remaining candidates.

11.3 Physics Results

The LHCb collaboration has submitted more than 100 papers for publication and almost 80 preliminary results to conferences. Some highlights are the first evidence for the very rare decay $B_s^0 \to \mu^+\mu^-$ [1] and the first measurement of the zero crossing point of the forward-backward asymmetry in the rare decay $B^0 \to K^{0\star}\mu^+\mu^-$ [2], two measurements in which the Zurich group made significant contributions as described below; the world's most precise measurement of the *CP* violating phase ϕ_s in the decays $B_s^0 \to J/\psi K^+K^-$ and $B_s^0 \to J/\psi\pi^+\pi^-$ and the first observation of a non-zero lifetime difference $\Delta\Gamma_s$ between the two mass eigenstates in the $B_s^0\overline{B}_s^0$ system; the determination of the sign of this lifetime difference; the first observation of the doubly Cabibbo suppressed decay $B^- \to DK^-$ with $D \to K^+\pi^-$ and a competitive measurement of the CKM angle γ from a combination of $B^\pm \to DK^\pm$ decay modes; and the observation of $D^0 - \overline{D}^0$ oscillations with a statistical significance of $10\,\sigma$. In addition, a wealth of results has been obtained in the field of heavy quark production and spectroscopy, including a first determination of the quantum numbers of the $X(3872)$ state. The full list of papers and conference contributions can be found at the LHCb web site [3], implications of the first measurements on classes of extensions to the SM are discussed in [4].

[1] R. Aaij *et al.* [LHCb collaboration], Phys. Rev. Lett. 110,' 021801 (2013).

[2] R. Aaij *et al.* [LHCb collaboration], *Differential branching ratio and angular analysis of the decay $B^0 \to K^*\mu^+\mu^-$*, arXiv:1304.6325 [hep-ex].

[3] `http://lhcbproject.web.cern.ch lhcbproject/CDS/cgi-bin/index.php`

[4] R. Aaij *et al.* [LHCb Collaboration], *Implications of LHCb measurements and future prospects*, arXiv:1208.3355 [hep-ex].

11.3.1 The decays $B_s^0 \to \mu^+\mu^-$ and $B^0 \to \mu^+\mu^-$

Ch. Elsasser, N. Serra and O. Steinkamp

The decays $B_s^0 \to \mu^+\mu^-$ and $B^0 \to \mu^+\mu^-$ are predicted to be very rare in the Standard Model of particle physics. Possible contributions from NP could be of the same order of magnitude as the contributions from the SM. The determination of the branching fractions of these decays strongly constrains the allowed parameter space for various NP models and is one of the key measurements for LHCb.

A combined analysis of 1.0 fb^{-1} collected in 2011 at a centre-of-mass energy of $\sqrt{s} = 7$ TeV and 1.1 fb^{-1} collected in 2012 at $\sqrt{s} = 8$ TeV, has yielded the first evidence for the decay $B_s^0 \to \mu^+\mu^-$. The observed excess of $B_s^0 \to \mu^+\mu^-$ candidates with respect to the background expectation (see Fig. 11.2) has a statistical significance of 3.5 standard deviations, and corresponds to a probability of $5.3 \cdot 10^{-4}$ for a background fluctuation [1]. The measured branching fraction is

$$\mathcal{B}(B_s^0 \to \mu^+\mu^-) = (3.2^{+1.4}_{-1.2}(\text{stat})^{+0.5}_{-0.3}(\text{syst})) \times 10^{-9},$$

in very good agreement with the the SM prediction of $(3.23 \pm 0.27) \times 10^{-9}$ [2].

The sensitivity for B^0 decays is four times larger than for B_s^0 due to the different hadronization fractions ($f_s/f_d = 0.256 \pm 0.020$). For $B^0 \to \mu^+\mu^-$, the observed number of candidates is consistent with the background expectation, and yields the world's best

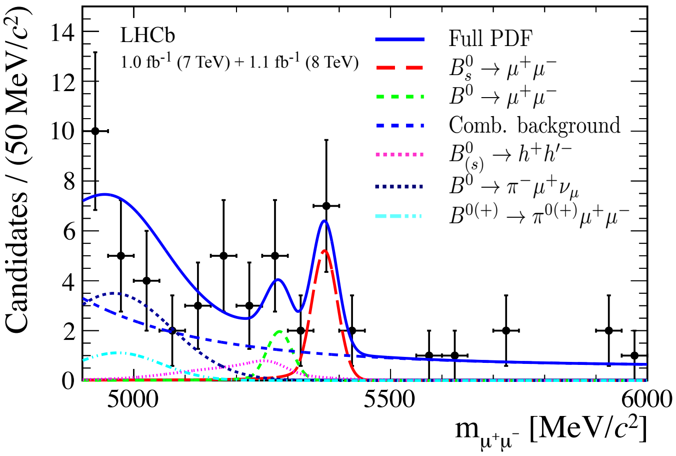

FIG. 11.2 – Invariant mass distribution of $B^0 \to \mu^+\mu^-$ and $B_s^0 \to \mu^+\mu^-$ event candidates. The result of a fit including the various sources of background is shown as well. Most background involves at least one hadron mis-identified as a muon. The $B^0 \to \mu^+\mu^-$ branching fraction obtained from the fit is statistically insignificant.

upper limit on the branching fraction of

$$\mathcal{B}(B^0 \to \mu^+\mu^-) < 9.4 \times 10^{-10}$$

at 95 % confidence level [1]. The predicted SM branching fraction is $(1.07 \pm 0.10) \times 10^{-10}$ [2].

The Zurich group has made significant contributions to this measurement. The main responsibilities of our group are the calibration of the invariant di-muon mass and the multivariate classifier used to distinguish signal from background. The distributions of both variables were determined from the measured exclusive $B^0_{(s)} \to h^+h^-$ decays, where $h^\pm$ is a kaon or a pion. Information from the RICH detectors is used to separate kaons and pions. The particle identification efficiencies were evaluated using the control channels $B^\pm \to J/\psi(1S)K^\pm$ and $B_s^0 \to J/\psi(1S)\phi$. An alternative method to estimate the invariant mass resolution for $B_s^0 \to \mu^+\mu^-$ and $B^0 \to \mu^+\mu^-$ is the interpolation between the observed resolutions for the di-muon resonances J/ψ, $\psi(2S)$, $\Upsilon(1S)$, $\Upsilon(2S)$ and $\Upsilon(3S)$. The result from this method is in perfect agreement with that from the analysis using $B^0_{(s)} \to h^+h^-$.

[1] R. Aaij *et al.* [LHCb collaboration], Phys. Rev. Lett. 110,‘ 021801 (2013).

[2] A. J. Buras, J. Girrbach, D. Guadagnoli, and G. Isidori, Eur. Phys. J. C72 (2012) 2172.

11.3.2 Other very rare B-decays

Ch. Elsasser, N. Serra and O. Steinkamp

The LHCb experiment also offers unprecedented sensitivity to other very rare B-decays such as $B^0_{(s)} \to \tau^+\tau^-$ and to Lepton Flavour Violating (LFV) decays such as $B^0_{(s)} \to e^\pm\mu^\mp$ and $B^0_{(s)} \to \mu^\pm\tau^\mp$. LFV decays are practically forbidden in the SM but can be accommodated in several NP scenarios. In the Pati-Salam model [1], for example, lepto-quark exchange mediates these decays already at tree level.

Our group makes important contributions to studies of the reconstruction and selection of τ leptons in LHCb. As a first step, more frequent decays involving τ leptons, such as $B_c^\pm \to J/\psi(1S)\tau^\pm\nu_\tau$ and $Z \to \tau^+\tau^-$ are investigated. We collaborate with other analysis groups that study semi-leptonic B decays involving τ leptons.

[1] J. Pati and A. Salam, Phys. Rev. **D10** (1974), 275.

11.3.3 $B^0 \to K^\star\mu^+\mu^-$

M. De Cian, N. Serra and M. Tresch

The rare decay $B^0 \to K^{0\star}\mu^+\mu^-$ is a flavour-changing neutral current process that proceeds via box and loop diagrams. This decay has been widely studied in literature from the theoretical point of view, since its angular distributions and differential branching fraction are sensitive to a large number of NP scenarios (see Ref. [1] and references therein). Particularly interesting is the forward-backward asymmetry $A_{\rm FB}$, described by the opening angle between the μ^- and the B^0 in the $\mu^+\mu^-$ rest frame. The A_{FB} as a function of the di-muon invariant mass squared, q^2, changes sign at a well defined value in the SM and is sensitive to NP contributions. The so-called *transverse asymmetry* A_T^2, built using the angle between the $K^{0\star}$ and the di-muon decay planes in the B^0 rest frame, is sensitive to extensions of the SM with right-handed currents. A measurement of A_{FB} and $A_T^{(2)}$ was performed based on the dataset of 1.0 fb^{-1} collected in 2011 [2]. The results are shown in Fig. 11.3. In addition to these observables, world's best determinations have been performed for longitudinal polarisation, F_L, of the $K^{0\star}$, the differential branching ratio and the CP asymmetry A_9. All results show good agreement with SM predictions.

Our group played a key role in designing a strategy for this analysis. One of the challenges was to account for detector acceptance effects in a model independent way. This was achieved using a Monte Carlo (MC) based procedure after the simulation was properly tuned using a set of control channels. Our group contributed to the tuning of the MC and the

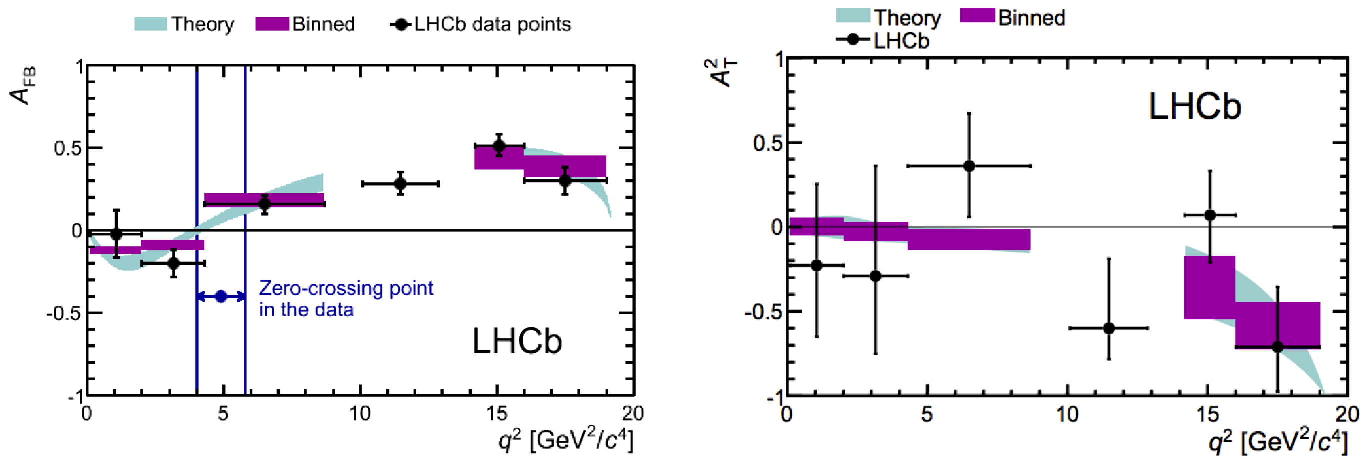

FIG. 11.3 – Left: A_{FB} as a function of the di-muon invariant mass squared q^2. The 68% CL region for the zero-crossing point is indicated. Right: The observable $A_T^{(2)}$ as a function of q^2. The turquoise band is the SM prediction. The violet bands indicate the rate weighted SM predictions in the same bins as chosen for the measurement [3].

extraction of the acceptance corrections. The procedure was validated using the decay $B^0 \to J/\psi K^{0*}$, with $J/\psi \to \mu^+\mu^-$. This decay has the same final state as $B^0 \to K^{0*}\mu^+\mu^-$ but is more abundant by a factor of 50. Our group has also contributed to the development of the maximum likelihood fit used to the extract the results for the angular observables and the differential branching ratio. Finally, we have been responsible for the first measurement of the zero-crossing point of A_{FB}. The result was extracted using a novel "unbinned counting" technique which avoids biases introduced by assumptions on the shape of A_{FB} as a function of q^2. The result is in agreement with SM predictions but its statistical uncertainty is still large and significant contributions from NP cannot be excluded so far. Significant improvements are expected from the analysis of the 2012 data set which is currently ongoing.

Other angular observables of interest in $B^0 \to K^{0*}\mu^+\mu^-$, which had not been measured so far, are known as P_4' and P_5' in literature. These are particularly sensitive to possible NP contributions since they result from the interference of different transversity amplitudes [4]. We proposed a new method that allowed early measurements of P_4' and P_5' using the 2011 dataset. This work has been documented in the Ph.D. thesis of M. De Cian [5] and is currently under review in the collaboration.

[1] J. Matias *et al.*, *Complete Anatomy of $\bar{B}_d \to \bar{K}^{*0}(\to K\pi)l^+l^-$ and its angular distribution*, JHEP 04 (2012) 104.

[2] R. Aaij *et al.* [LHCb collaboration], *Differential branching ratio and angular analysis of the decay $B^0 \to K^*\mu^+\mu^-$*, arXiv:1304.6325 [hep-ex].

[3] C. Bobeth *et al.*, *More Benefits of Semileptonic Rare B Decays at Low Recoil: CP Violation*, arXiv:1105.0376 [hep-ex].

[4] S. Descotes-Genon *et al.*, *Optimizing the basis of $B^0 \to K^*\mu^+\mu^-$ observables in the full kinematic range*, arXiv:1303.5794 [hep-ph].

[5] M. De Cian, *Track Reconstruction Efficiency and Analysis of $B^0 \to K^*\mu^+\mu^-$ at the LHCb Experiment*, Ph.D. thesis.

11.3.4 Electroweak boson and low mass Drell-Yan production

J. Anderson, A. Bursche, N. Chiapolini, and K. Müller

W and Z boson production cross sections and their ratios have been measured by LHCb in the $W \to \mu\nu$ and $Z \to \mu\mu$ decay channels [1] using 36 pb^{-1} of data collected in 2010. Z boson production has also been measured in final states with two electrons [2] or two taus [3] using the much larger dataset collected in 2011 with 1 fb^{-1}. These measurements provide valuable input to the knowledge of the parton density functions (PDF) of the proton

A preliminary measurement of Z boson production in the di-muon channel based on the 2011 dataset has just been released [4]. All the efficiencies are calculated from data using a tag and probe method. Our group played a leading role in this measurement which will be published this summer. Figure 11.4 shows the differential Z cross section as a function of p_{T} of the Z boson. The next-to-next-to-leading order (NNLO) prediction from FEWZ [5] fails to describe the shape of the distribution. Resbos [6], which interfaces a NLO calculation to PYTHIA [7], and Powheg [8], which resums the leading contribution to next-to-next-to-leading logarithms and matches the result to a NLO QCD calculation, describe the data reasonably well.

A method was developed in our group to compare the LHCb results to the published results of ATLAS and CMS [9]. As the fiducial volumes of the measurements are slightly different, extrapolation factors are needed. These factors are calculated at NLO. Figure 11.5 shows the differential W boson cross section as a function of the pseudorapidity of the muon together with the results from ATLAS [10]. The plot illustrates the complementarity of the two experiments.

The analysis of Z boson production is being extended to events containing jets in the final state (A. Bursche in close collaboration with the Cambridge group). Measurements of Z boson production together with a jet are sensitive to the gluon content in the proton. The dominant uncertainty originates in the jet energy scale. The relative cross section as a function of the rapidity y of the Z boson is shown in Fig. 11.6. These results have been presented at a conference [11] and a publication is being prepared.

In order to further exploit the unique phase space region of LHCb a measurement is performed of Z bosons with associated production of charmed mesons and baryons using the final states $D^0 \rightarrow K^-\pi^+$, $D^+ \rightarrow K^-\pi^+\pi^+$, $D^+ \rightarrow K^-K^+\pi^+$ and $\Lambda_c^+ \rightarrow p^+K^-\pi^+$. These processes may give insight into the correlations of the partons in double parton scattering events. This measurement is performed by A. Bursche and a master student (E. Crivelli).

The analysis of low mass Drell-Yan production in the di-muon channel is performed by the Zurich group (J. Anderson, N. Chiapolini, K. Müller). This measurement is sensitive to Bjorken-x values as low as 8×10^{-6} where x is the momentum fraction carried by the struck quark. A preliminary result has come out in spring 2012 [12]. The analysis has been updated since to include the full 2011 dataset. A precise measurement at low masses is challenging as the backgrounds are very high; the $\approx$30% uncertainty on the purity at low masses was the dominant systematic uncertainty in [12]. A new variable for the fit of the purity, based on the total p_T in the cone around the muon, was studied. It does not depend on the mass and can therefore be extracted from the Z sample which is almost background free. Also the background templates are extracted from data. A toy study confirmed the reliability of the new method down to di-muon masses of 10 GeV/c^2. It is planned to publish the 2011 results within the next months. An analysis of the 2012 dataset will allow to extend the kinematic reach to even lower x due to the higher centre of mass energy.

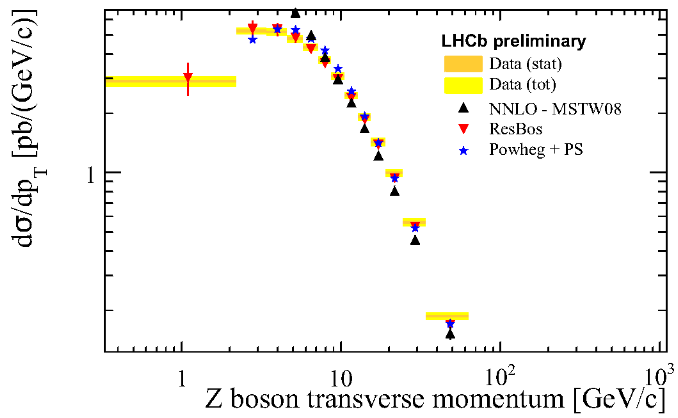

FIG. 11.4 – Differential Z production cross-section as a function of p_T of the Z boson as observed in the $Z \rightarrow \mu\mu$ channel. Statistical and total uncertainties are indicated. Superimposed are the predictions from FEWZ [5] (NNLO), Resbos [6] and Powheg [8].

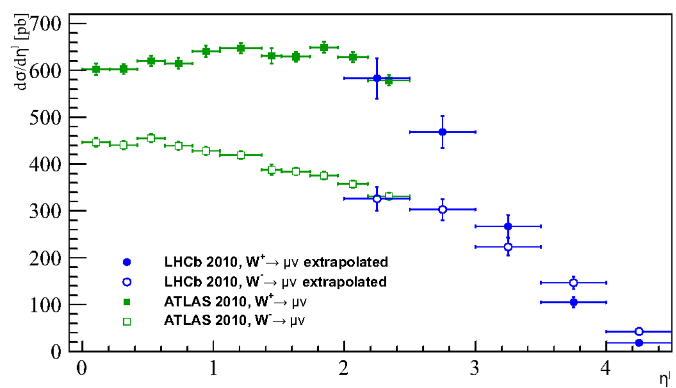

FIG. 11.5 – Differential cross-section for W boson production observed in the $W \rightarrow \mu\nu$ channel as a function of the pseudorapidity of the muon. LHCb results, corrected for the different definition of the fiducial volumes, are shown together with results from ATLAS.

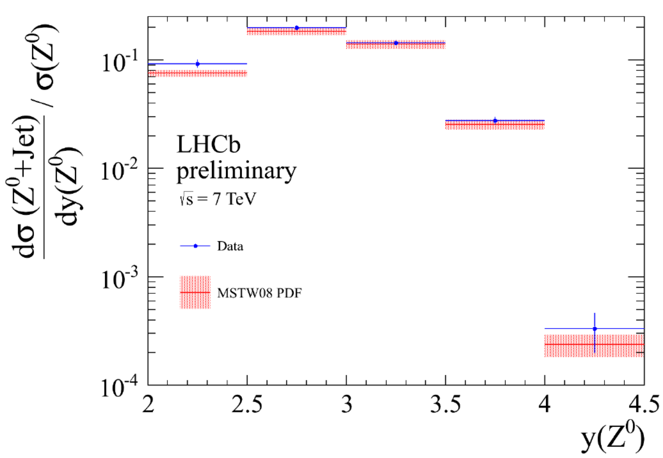

FIG. 11.6 – Rapidity distribution of Z production with associated jets normalised to the inclusive Z production cross section.

[1] R. Aaij *et al.* [LHCb Collaboration], JHEP **1206** (2012) 058.

[2] R. Aaij *et al.* [LHCb Collaboration], JHEP **1302** (2013) 106.

[3] R. Aaij *et al.* [LHCb Collaboration], JHEP **1301** (2013) 111.

[4] LHCb collaboration, *Measurement of the cross-section for $Z \to \mu\mu$ production with 1 fb^{-1} of pp collisions at $\sqrt{s}$=7 TeV*, LHCb-CONF-2013-005.

[5] Y. Li and F. Petriello, Phys. Rev. D **86** (2012) 094034.

[6] G. A. Ladinsky and C. P. Yuan, Phys. Rev. D **50** (1994) 4239.

[7] T. Sjostrand, S. Mrenna and P. Z. Skands, JHEP **0605** (2006) 026.

[8] P. Nason, JHEP **0411** (2004) 040.

[9] LHCb collaboration, *Graphical comparison of the LHCb measurements of W and Z boson production with ATLAS and CMS*, LHCb-CONF-2013-007.

[10] ATLAS collaboration, Phys. Rev. D **85** (2012) 072004.

[11] LHCb collaboration, *Measurement of jet production in $Z/\gamma^* \to \mu\mu$ events at LHCb in $\sqrt{s} = 7$ TeV pp collisions*, LHCb-CONF-2012-016.

[12] LHCb collaboration, *Inclusive Drell-Yan production in the forward region at $\sqrt{s} = 7$ TeV*, LHCb-CONF-2012-013.

11.4 Summary and Outlook

The LHCb experiment has performed very well throughout the 2012 LHC run. More than 2 fb^{-1} of data have been recorded, with a data taking efficiency exceeding 95%. The results obtained from data collected so far have allowed the LHCb experiment to take a leading role in the field of b and c-physics; to considerably reduce the parameter space for many models beyond the SM and to show world best and world first measurements of B-hadron branching ratios.

12 Particle physics with the CMS experiment at CERN

E. Aguiló, C. Amsler, V. Chiochia, S. de Visscher, C. Favaro, M. Ivova Rikova, B. Millán Mejías, P. Robmann, H. Snoek, S. Taroni, S. Tupputi, and M. Verzetti

in collaboration with the:

(CMS - Collaboration)

The Compact Muon Solenoid (CMS) experiment at the Large Hadron Collider (LHC) participates in one of the most challenging scientific endeavours, the search for the Higgs boson and other elementary particles. In 2012 the CMS experiment has significantly increased the size of the collected datasets, reaching a delivered integrated luminosity of 23.3 fb^{-1} at the center-of-mass energy $\sqrt{s}$ = 8 TeV, as shown in Fig. 12.1. The samples delivered in 2011 and 2010 at $\sqrt{s} = 7$ TeV correspond to an integrated luminosity of 6.1 fb^{-1} and 44.2 pb^{-1}, respectively. The LHC concluded the first three-year running period on February 14, 2013 and entered a two-year shutdown period (Long Shutdown 1, LS1). Proton beams colliding at the center-of-mass energy of 13 TeV are expected in early 2015.

2012 was a very productive year for CMS, with over hundred articles published in refereed journals. The year constitutes a real milestone for particle physics with the discovery of a Higgs-like boson in July by ATLAS and CMS. In this period, several members of our group played important coordination roles within the collaboration. One of us (V. C.) co-chaired the B-physics analysis group, that has so far released eighteen journal articles on quarkonium, b hadron decays and b-quark production measurements. H. S. convened the pixel calibration and reconstruction group and S. d.V. coordinated the simulation efforts in the standard model (SM) physics group.

In this report we describe the recent contributions of our group to the CMS experiment in the field of Higgs boson searches, measurements of SM processes and heavy flavour physics. In early 2012 we observed a new *usb*-baryon (the first new particle observed by CMS before the Higgs discovery) decaying into $\Xi_b^- \pi^+$, followed by $\Xi_b^- \to J/\psi\ \Xi^-$, with $J/\psi \to \mu^+\mu^-$ and $\Xi^- \to \Lambda\pi^-$, $\Lambda \to \pi^- p$. We observed 29 candidates (with a background of 6.6 $\pm$ 2.6) and obtained a mass of 5944.9 $\pm$ 2.8 MeV. This state is 154 MeV heavier than the spin 1/2 Ξ_b^-. According to theoretical models this would be the Ξ_b^{*0} with spin $\frac{3}{2}$. Details can be found in a recent CMS publication [1] and in our previous (2011) annual report. Furthermore, we discuss the performance studies done on the pixel detector, the innermost component of the CMS experiment. This detector was developed and commissioned by our group in col-

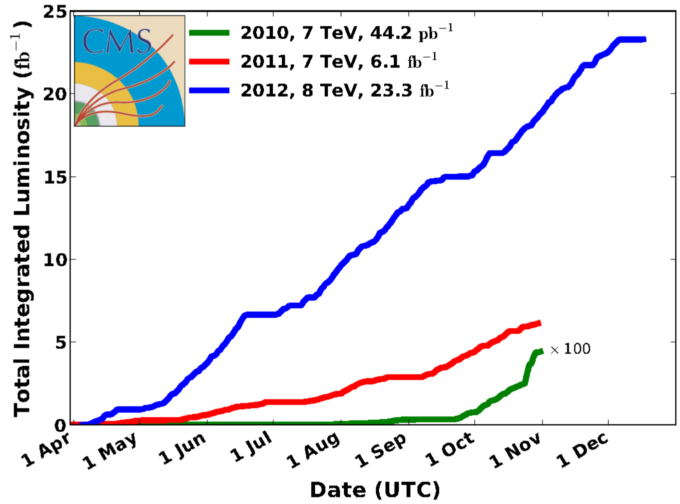

FIG. 12.1 – Cumulative luminosity delivered to CMS for p-p collisions during the three years of operation.

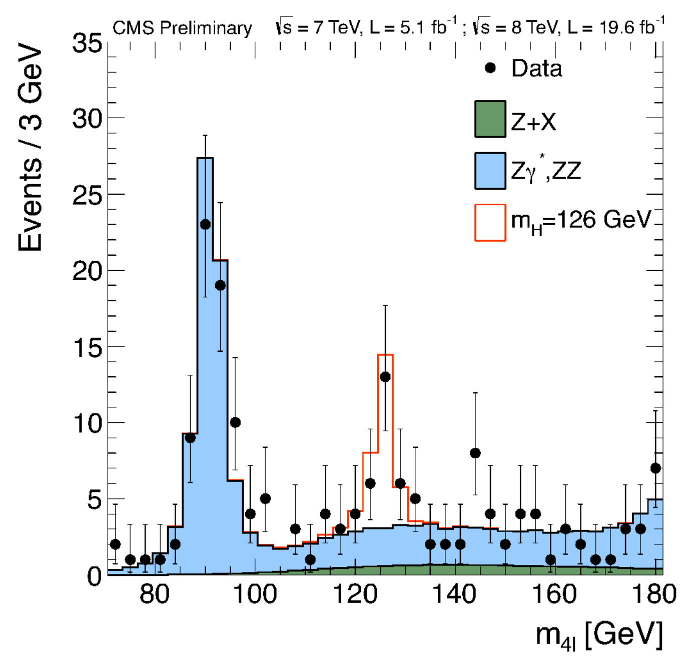

FIG. 12.2 – Distribution of the four-lepton reconstructed mass for the sum of the $4e$, 4μ, and $2e+2\mu$ channels. Measured data are compared with predictions for background and the signal for a Higgs boson at 126 GeV.

laboration with PSI and ETH Zurich. It allows the precise reconstruction of charged particle tracks as well as the identification the primary collision vertex and secondary vertices from long-lived particles. This device is crucial for our research using b-quarks and tau-leptons.

[1] CMS Collaboration, Phys. Rev. Lett. **108** (2012) 252002.

12.1 Higgs boson searches in tau pairs

On July 4, 2012 the CMS and ATLAS collaborations announced the observation of a Higgs-like resonance with a mass of about 126 GeV [1, 2]. The resonance was observed with significance larger than three standard deviations in decays to pairs of vector bosons, such as W^+W^-, ZZ, and $\gamma\gamma$. The analysis of all the data collected until the end of 2012 further consolidated the evidence for a new particle. Figure 12.2 shows the invariant mass distribution of ZZ candidates with decaying into four leptons from the combined analysis of the complete 2011 and 2012 datasets [3]. A clear excess is observed slightly above 120 GeV with a local significance of about 7 standard deviations. The mass determined from a combination of the three leptonic channels ($4e$, 4μ, $2e+2\mu$) is $125.8 \pm 0.4(\text{stat.}) \pm 0.2(\text{syst.})$ GeV. The signal strength modifiers associated with the vector bosons and fermions in production were found to be consistent with the SM expectations. The spin-parity of the boson was also studied and the pure scalar hypothesis ($J^P = 0^+$) was found to be consistent with the observation when compared to six other spin-parity hypotheses [3, 4].

In the fermionic decay channels, such as $\tau^+\tau^-$ and $b\bar{b}$, the observed excess with respect to background expectation is below three standard deviations. Of particular interest is the decay mode into two tau leptons, which is expected to have the second largest branching ratio for a mass of 126 GeV, with relatively small background. Among the possible production modes and final states our group focused on the associate production of a Higgs boson and a Z or W boson [5]. While this production mode has a lower cross section than the direct production, it has a smaller background and may allow a better measurement of the Higgs coupling constant with the tau leptons in the future.

Three- and four-lepton events were used to search for Higgs bosons produced in association with vector bosons, with the leptonic decay of the W boson (WH) or Z boson (ZH), respectively. The search for WH production was performed in three-lepton final states. Two final states with two light leptons and a hadronic tau decay, $e\mu\tau_h$ and $\mu\mu\tau_h$, and two final states with one lepton and two hadronic tau decays, $e\tau_h\tau_h$ and $\mu\tau_h\tau_h$, were considered. The resulting invariant mass distribution of the event candidates with two light leptons and a hadronic tau decay is shown in Fig. 12.3. The search for ZH production was performed in four-lepton events

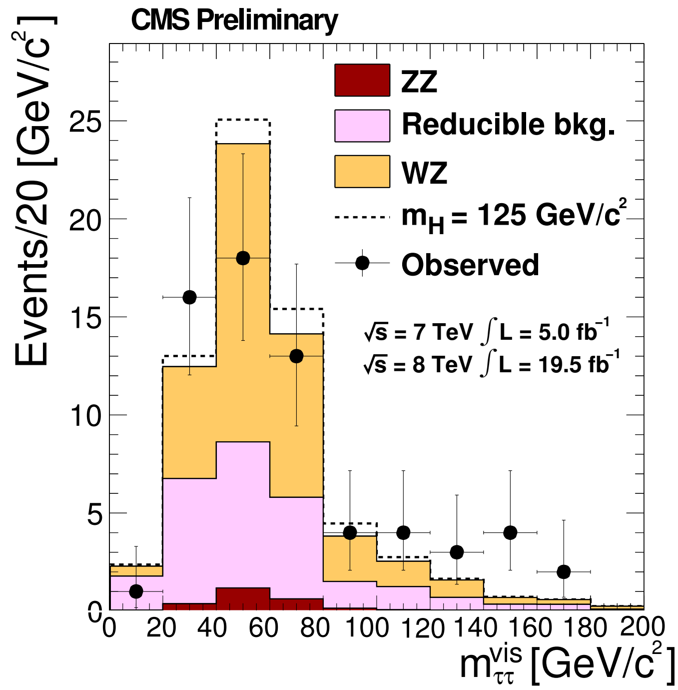

FIG. 12.3 – Observed and expected Higgs boson candidate mass spectra in the channels with two leptons and a hadronic tau decay. The expected contribution from the associated production of a SM Higgs boson with mass of 125 GeV is shown by the dashed line.

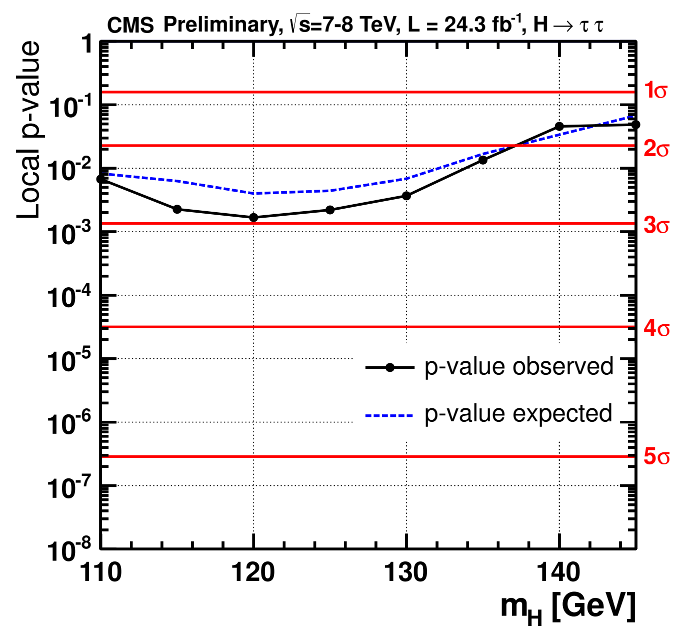

FIG. 12.4 – Observed and expected p-value $1 - CL_b$, and the corresponding significance in number of standard deviations for the combination of Higgs boson searches in tau pairs.

with a pair of electrons or muons consistent with the decay of a Z boson, and a Higgs boson candidate with one of the following final states: $e\mu$, $e\tau_h$, $\mu\tau_h$, or $\tau_h\tau_h$. In all channels the data were found to be compatible with both the background-only prediction and the presence of a SM Higgs boson.

The results of this analysis were combined with the inclusive Higgs boson search in tau decays. In this analysis the tau-lepton pair invariant-mass spectrum was studied in five different final states corresponding to the decay modes of the two tau leptons. After the combination an excess of events was observed over a broad mass range, with a maximum local significance of 2.9 standard deviations at a mass of 120 GeV, as shown in Fig. 12.4. This excess is compatible with the presence of a SM Higgs boson of mass 125.8 GeV, for which the local significance is 2.85 σ. This is an indication that the new boson discovered on July 4, 2012 couples to τ leptons, with a strength compatible to the one predicted by the SM.

Our group also had a strong involvement in the validation and data quality monitoring (DQM) of tau lepton identification in CMS. The DQM system provides basic information on the collected data once the events are reconstructed. This information is used to establish whether a given period of data taking is suitable for further analysis or not, and to check the functionality of the event reconstruction algorithms. In 2012 our group has implemented the necessary DQM software for the tau identification and further improved it following the feedback collected during data taking operations.

[1] S. Chatrchyan *et al.* [CMS Collaboration], Phys. Lett. B **716** (2012) 30.

[2] G. Aad *et al.* [ATLAS Collaboration], Phys. Lett. B **716** (2012) 1.

[3] S. Chatrchyan *et al.* [CMS Collaboration], CMS-PAS-HIG-13-002.

[4] S. Chatrchyan *et al.* [CMS Collaboration], Phys. Rev. Lett. **110** (2013) 081803.

[5] S. Chatrchyan *et al.* [CMS Collaboration], CMS-PAS-HIG-12-053.

12.2 Angular correlations of b hadrons in association with a Z boson

The production of b-quark pairs in association with Z bosons is the main SM background to the Higgs boson searches in b-quark decays and other searches for new physics. Monte Carlo (MC) simulations of this process have been performed assuming massive or massless b quarks, usually referred as four- and five-flavor calculation schemes, respectively. The validation of the different calculation techniques is of great importance for the correct background estimates in future searches.

Our group performed the measurement of the total cross section and angular correlations of b hadrons produced in this process, using a data sample corresponding to an integrated luminosity of 5 fb^{-1} at the center-of-mass energy of 7 TeV [1, 2]. Four variables were considered to describe the angular correlations of the final-state particles:

- the three-dimensional and transverse angular separation between the b hadrons (ΔR_{BB} and $\Delta\phi_{BB}$), sensitive to the $pp \rightarrow Z + b\bar{b}$ production mechanism,

- the three-dimensional angle between the Z boson momentum and the closest B hadron ($\min\Delta R_{ZB}$), and

- the asymmetry between the Z boson momentum and the b-hadron system, which are affected by the additional parton radiation.

The cross sections are evaluated in several regions of the Z boson transverse momentum, p_T. The total cross section as a function of the Z p_T was also measured.

Events containing a Z boson decay were selected by requiring the presence of two isolated leptons — muons or electrons — with opposite charge, high p_T, and invariant mass in the Z boson mass range. B hadrons were identified through the displaced vertices from their decays, using the inclusive vertex finder (IVF) technique. The IVF algorithm is independent from jet reconstruction, hence it does not suffer from the geometrical limitations due to the jet cone size and can access collinear b hadron production. Only events with two reconstructed B hadron candidates with $p_T > 8$ GeV and pseudorapidity $|\eta| < 2.0$ were retained. Additional requirements were imposed on the decay vertex invariant mass and decay length to reduce the contamination from charm quark decays.

The differential cross section as a function of ΔR_{BB} and the total cross section for different requirements on the Z boson p_T are shown in Fig. 12.5 and Fig. 12.6, respectively. The measurements are compared to the tree-level predictions by MADGRAPH MC, in the four- and five-flavour calculation schemes. The four-flavour predictions provide the best description of the measured data.

In parallel with the data analysis we have also worked on improving the simulation of this process with MADGRAPH 5. In particular, we have optimised the four-flavour jet matching technique, which is relevant for processes with one or more massive quarks emitted from the initial or final state radiation, such as $Z + b\bar{b}$, $W + b\bar{b}$, $t(W)/b$, and $H + b\bar{b}$. The new MAD GRAPH release is expected to be an important improvement for future searches.

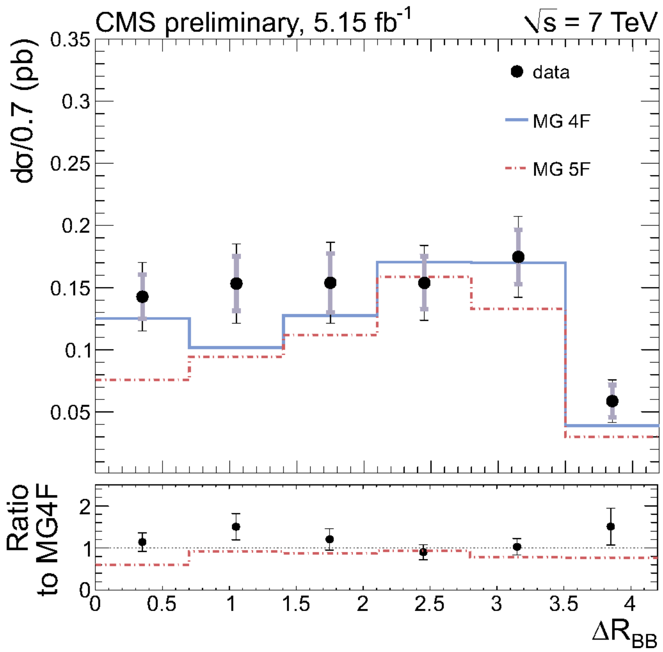

FIG. 12.5 – Differential cross section for pp $\rightarrow$ Zb$\bar{b}$ as a function of the three-dimensional angle between the b hadrons, ΔR_{BB}. Measured data are compared with MADGRAPH MC predictions for the four- and five-flavor schemes.

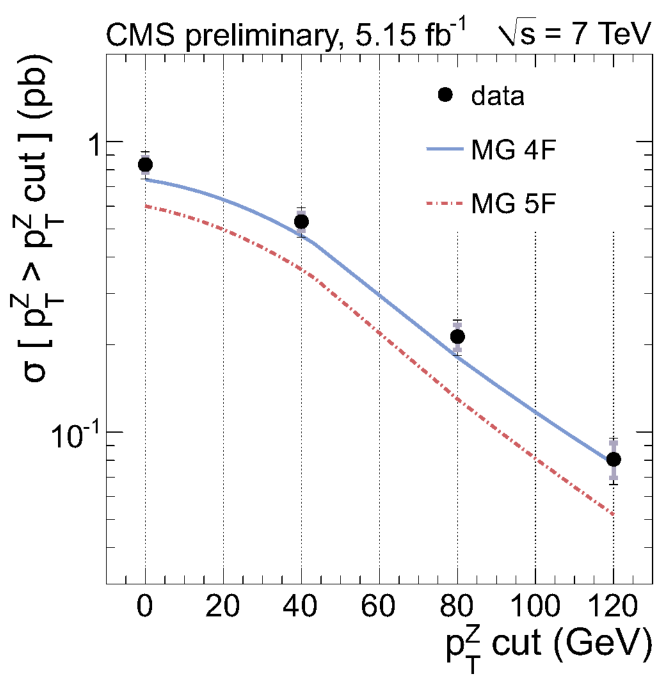

FIG. 12.6 – Total pp $\rightarrow$ Zb$\bar{b}$ production cross section as a function of the minimum Z boson p_T.

[1] S. Chatrchyan *et al.* [CMS Collaboration], CMS-PAS-EWK-11-015.

[2] C. Favaro, PhD-thesis, Universität Zürich (in preparation)

12.3 Polarization of the Λ_b baryon

Polarization studies in b baryon decays provide important information on heavy quark decay dynamics [1]. We performed a measurement of the Λ_b polarization in pp collisions at 7 TeV using the decay sequence $\Lambda_b \rightarrow J/\psi(\rightarrow \mu^+\mu^-)\Lambda(\rightarrow p\pi^-)$ [2]. From a sample of 5 fb^{-1} of integrated luminosity we obtained $\sim$1800 reconstructed Λ_b and $\overline{\Lambda}_b$ candidates (the $\overline{\Lambda}_b$ decaying into the charge conjugated particles). The $(J/\psi)\Lambda$ invariant mass distribution shows a pronounced peak on top of a $\sim$ 10% continuous background.

The analysis exploits the angular correlations between the daughter particles. The physics parameters (such as polarization and analyzing power) are extracted by a multi-dimensional likelihood fit to the angular distributions. Three angular distributions are employed: $\cos\theta_\Lambda$, $\cos\theta_p$ and $\cos\theta_\mu$, where θ_Λ, θ_p and θ_μ are the polar angles of the Λ, the proton and the μ^+ in the rest frames of Λ_b, Λ and J/ψ, respectively, as shown in Fig. 12.7. The distortions of the angular distributions caused by the geometrical acceptance of the detector and the event selection are determined by Monte Carlo simulation. The contribution from background is determined with data events in the sidebands of the Λ_b mass peak. For a better separation of signal and background the mass distribution is also included in the fit. Note that the polarizations of the Λ_b and $\overline{\Lambda}_b$ are not necessarily equal since their production mechanisms are not identical. Each step of the analysis is therefore performed independently for Λ_b and $\overline{\Lambda}_b$.

Figure 12.8 shows the measured angular and mass distributions together with the fits for Λ_b candidates. Similar fits are also performed for the antiparticles. The fit is performed on events within the mass peaks. Our preliminary results show that both Λ_b and $\overline{\Lambda}_b$ are produced with polarizations smaller than 10%. We find for the polarizations of the Λ_b and $\overline{\Lambda}_b$, $P_{\Lambda_b} = 0.03 \pm 0.09 \pm 0.02$ and $P_{\bar{\Lambda}_b} = 0.02 \pm 0.08 \pm 0.05$, respectively, where

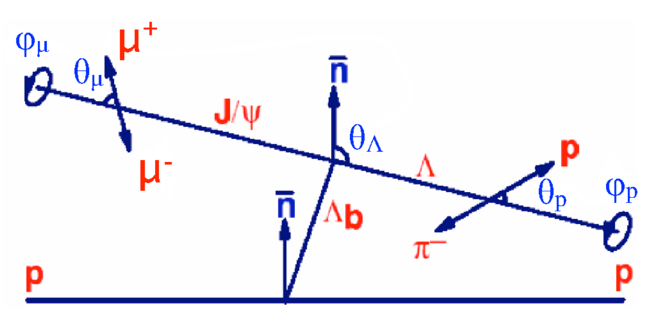

FIG. 12.7 – Definitions of the reference frames and angles used in the Λ_b polarization analysis.

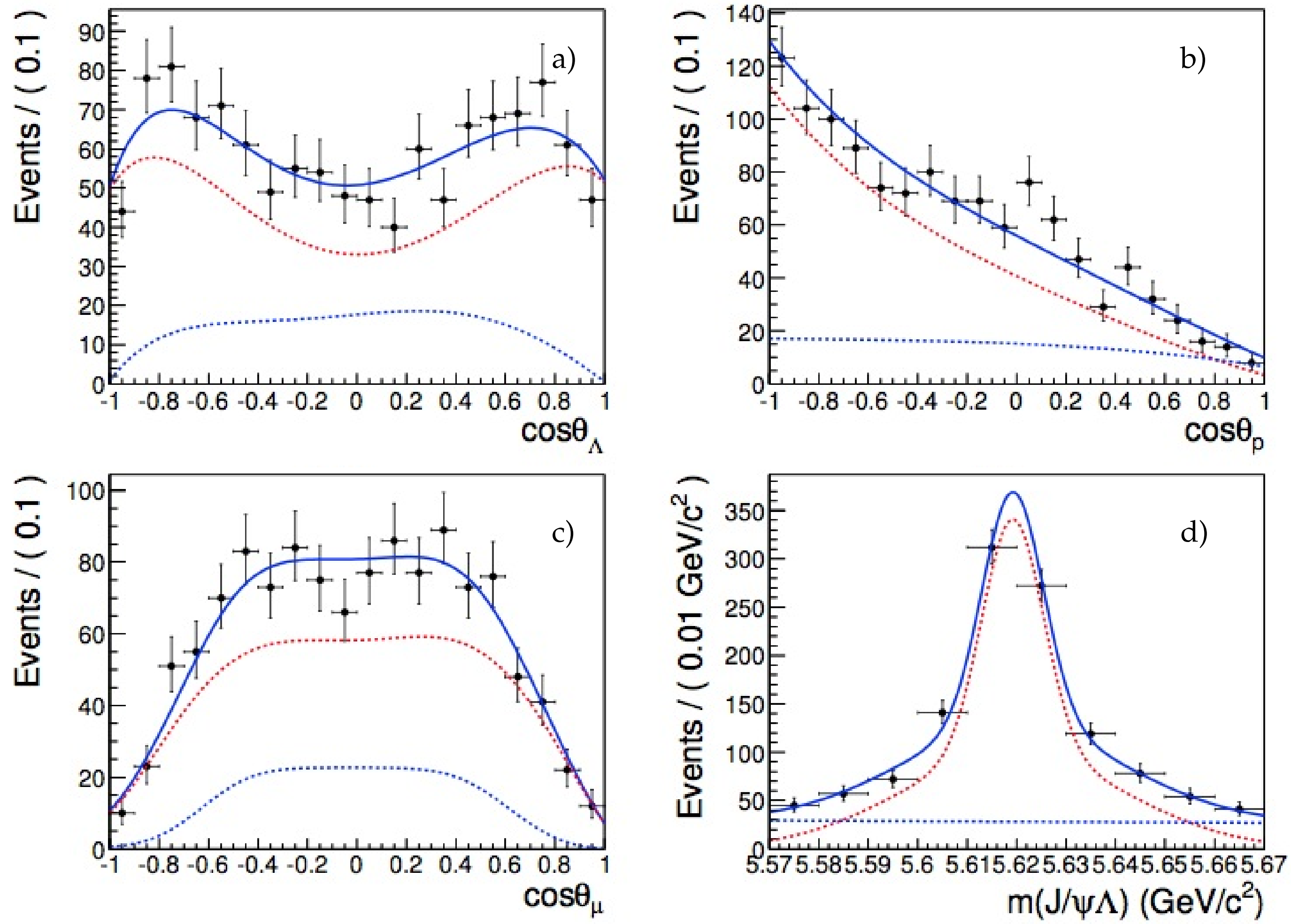

FIG. 12.8 –
a) Angular distribution of the Λ in the Λ_b rest frame; b) angular distribution of the proton in the Λ rest frame;
c) angular distribution of the muon in the J/ψ rest frame; d) mass distribution in the Λ_b region.
The black dots represent the measured data. The lines show the results from a multi-dimensional likelihood fit: total fit (solid blue), signal folded with efficiency (dashed red) and background contribution (dashed blue).

the first uncertainty is statistical and the second systematic. These results are compatible with expectations from perturbative QCD which predict polarization not exceeding 10% in high energy pp collisions [3]. Our results agree with a recent measurement from LHCb which, however, does not distinguish between Λ_b and $\overline{\Lambda}_b$ [4].

[1] M. Krämer and H. Simma, Nucl. Phys. **B 50** (1996) 125

[2] M. Ivova Rikova, PhD-thesis, Universität Zürich (Submission in June 2013)

[3] G. Hiller *et al.*, Phys. Lett. **B 649** (2007) 15

[4] LHCb Collaboration, arXiv:1302.5578 (2013)

12.4 Lifetime of the B_s meson

Our analysis focuses on the study of the B_s meson decaying into $(J/\psi)\phi$, where J/ψ decays into two muons of opposite charges, and $\phi(1020)$ into two kaons of opposite charges ($B_s \to J/\psi\ [\to \mu^+\mu^-]\ \phi[\to K^+K^-]$) [1]. We are measuring the width difference $\Delta\Gamma_s = \Gamma_L - \Gamma_H$ of the two CP-eigenstates of the B_s-meson, B_L (CP $= +1$) and B_H (CP $= -1$). $\Delta\Gamma_s$ is positive [2] and the CP-violating phase ϕ_s is set to zero. This phase has been measured [3], $\phi_s = 0.07 \pm 0.09$, and is indeed predicted to be small in the SM, $\phi_s = -0.036 \pm 0.002$.

Since the B_s meson is pseudoscalar and the J/ψ and $\phi(1020)$ are vectors, the orbital angular momentum of the two decay products is $L = 0$, 1, or 2. For L even we have thus CP $= +1$ (B_L), for L odd CP $= -1$ (B_H). Hence the angular correlations between the decay products are different for the two states [4, 5].

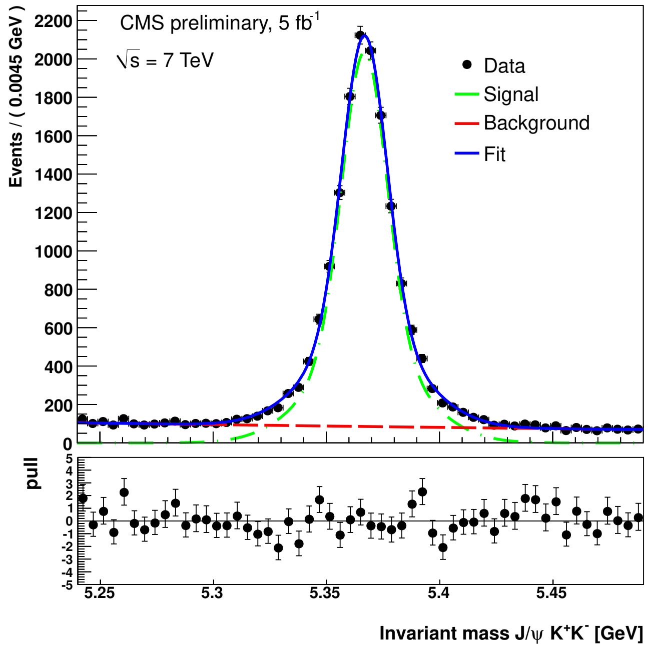

FIG. 12.9 – Invariant mass distribution of the B_s candidates (see legend).

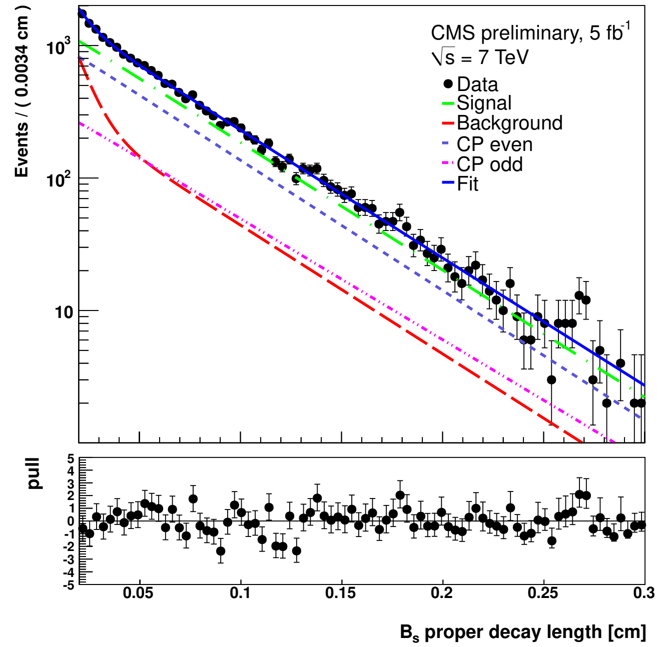

FIG. 12.10 – Projection of the proper decay length from the 5D maximum likelihood fit (see legend).

The following cuts are applied to select the $B_s \to (J/\psi)\phi$ candidates:

- Two muons emerge from a secondary vertex as expected from a J/ψ decay.
- Their invariant mass is equal to the J/ψ mass within ±150 MeV/c^2.
- Their transverse momentum is larger than 7 GeV/c.
- The transverse momentum of the kaon pair is larger than 0.7 GeV/c.
- Their invariant mass is equal to the $\phi(1020)$ mass within ±5 MeV/c^2.

The selected events show a pronounced peak of 19 200 B_s events in the B_s invariant mass distribution, as shown in Fig 12.9.

The likelihood analysis is based on probability density functions (PDF) for signal and background. The signal PDF is from a theoretical model that includes the fit parameters [4, 5]. The background PDF is parameterized with an empirical model. A one-dimensional mass fit is performed first on the B_s candidates between 5.24 and 5.49 GeV. The sidebands are then fitted with the empirical model. In the final step the full likelihood fit is performed.

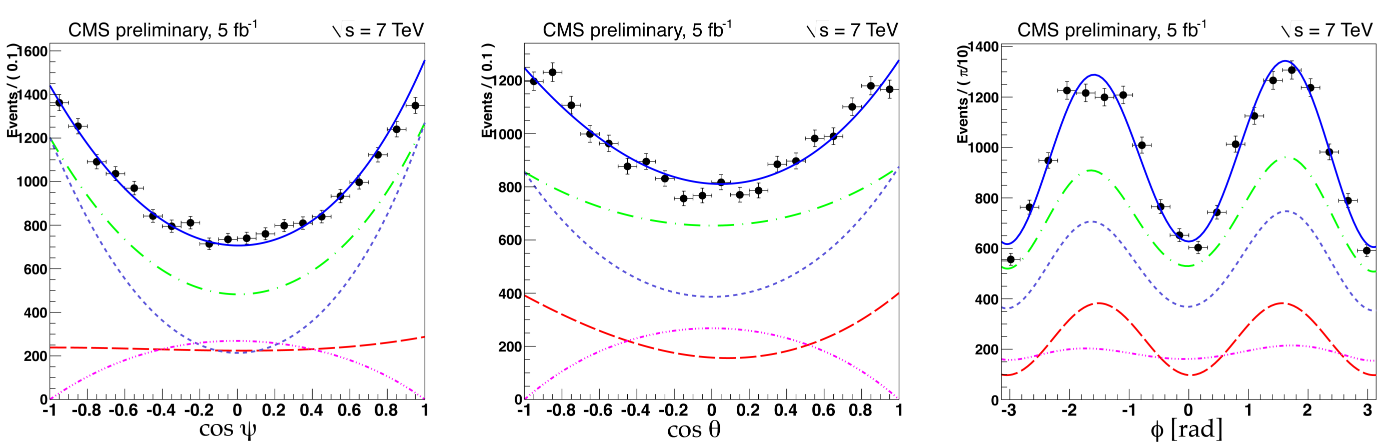

FIG. 12.11 – Angular distributions of $\cos\psi$, $\cos\theta$ and ϕ (see text). The solid blue lines are the fit, the green lines the signal component, the red lines the background component, and the black points are the data. The magenta dashed line are the CP odd component, the purple dashed line the CP even component.

TAB. 12.1 –
Measurements of Γ_s and $\Delta\Gamma_s$ from $B_s \to (J/\psi)\phi$ at the LHC. The SM prediction is $\Delta\Gamma_s = 0.147(60) \times \Gamma_s = 0.097(39)$ ps^{-1}.

Experiment	Γ_s [ps^{-1}]	$\Delta\Gamma_s$ [ps^{-1}]
CMS [6]	0.655(10)	0.048(24)
ATLAS [7]	0.677(8)	0.053(23)
LHCb [3]	0.663(8)	0.100(17)

Figure 12.9 and 12.10 show the fits on the invariant mass and the lifetime distributions, respectively. Figure 12.11 shows the angular distributions. The angles θ and ϕ denote the flight direction (polar and azimuthal angles) of the μ^+ in the J/ψ rest frame. The angle ψ is the polar angle of the K^+ in the rest frame of the $\phi(1020)$ with respect to the negative B_s flight direction [1]. From the 19 200 candidates we find $14\,310 \pm 138$ B_s events, leading to a mean mass of $5\,366.8 \pm 0.1$ MeV [6]. We also obtain $\Delta\Gamma_s = 0.048 \pm 0.024$ (stat.) $\pm\, 0.003$ (syst.) ps^{-1}, and $\tau_{B_s} = 1.528 \pm 0.020$ (stat.) $\pm\, 0.010$ (syst.) ps. Our measurements are compared with the ATLAS and LHCb results in Table 12.1, where the systematic and statistical uncertainties are added in quadrature. The LHC results are in good agreement with predictions from the SM.

[1] B. Millán Mejías, PhD-thesis, Universität Zürich (Submission in June 2013)

[2] LHCb Collaboration, Phys. Rev. Lett. **108** (2012) 241801

[3] LHCb Collaboration, arXiv:1304.2600 (2013)

[4] A.S. Dighe, I. Dunietz and R. Fleischer, Eur. Phys. J. **C 6** (1999) 647

[5] I. Dunietz, R. Fleischer and U. Nierste, Phys. Rev. **D63** (2001) 114015

[6] S. Chatrchyan *et al.* [CMS Collaboration], CMS PAS BPH-11-006.

[7] ATLAS Collaboration, arXiv: 1208.0572 (2013)

12.5 Studies of pixel detector performance and improvements to the hit reconstruction

The CMS pixel detector is the innermost tracking device of the CMS experiment, providing charged particle trajectories and production vertices. It includes three cylindrical layers in the barrel region and four end cap disks, two at each side of the barrel. The three layers are located at 4.4, 7.3, and 10.2 cm from the beam axis. Due to the short distance to the interaction region the detector operates in a very harsh environment characterised by a high radiation dose. The current pixel detector must operate until the second LHC long shutdown, foreseen in 2017. A detailed study of its current performance and the comparison with the detector simulations are required for the optimal continuation of the physics program.

The pixel detector plays a key role in the reconstruction of charged particles in CMS. A particle passing through the silicon sensors deposes charge and activates "clusters" of consecutive pixels above the readout threshold. The cluster shape and the deposited charge is used by the reconstruction algorithms to determine the track incident point and its uncertainties. Since the hit detection efficiency was found to be dependent on the instantaneous luminosity, our group has studied the dependence of the cluster size and charge. The instantaneous luminosity was about 7×10^{33} cm^{-2}s^{-1} at the beginning of a data taking run and decreased of a factor 3 before beams were dumped and new beams were injected in the accelerator. To simulate the varying conditions, we divided the analysed run into 20 subsamples corresponding to different instantaneous luminosities and for each subsample we have simulated a dedicated MC sample using the corresponding distribution of simultaneous collisions extracted from measured data. While no significant dependence of the cluster size was observed on the instantaneous luminosity, the collected charge shows interesting features.

The average cluster charge increases with the distance from the interaction point as expected from the decreasing irradiation dose. The difference in collected charge between layers can be as large as 11%. Furthermore, we observed a dependence of the cluster charge on the instantaneous luminosity. The most probable value (MPV) of the cluster charge distribution was measured as function of the instantaneous luminosity fitting the data with a Landau convoluted with a Gaussian, as shown in Fig. 12.12. The effect is most prominent in the innermost layer, where the MPV was found to decrease by about 6% within a data taking run. The effect is currently attributed to the operating temperature of the pixel readout electronics, which is expected to be higher at larger particle occupancies. Further studies of the charge collection are currently in progress.

When two charged particles traverse the sensitive material in close proximity, the clusters overlap and merge into one larger cluster. In the innermost layer of the pixel detector this effect occurs if the opening angle between the two particle trajectories is below 5 mrad. For a typical three-prong τ decay this corresponds to a transverse momentum of about 150 GeV. The merging of clusters deteriorates the measurement of the particle trajectories through the tracking volume and the reconstruction of the τ lepton and of the b-quark jets.

We have shown that merged clusters can be identified by calculating the charge deposited in the cluster corrected for the incident angle of the trajectory. The incident angle is determined assuming a straight line from

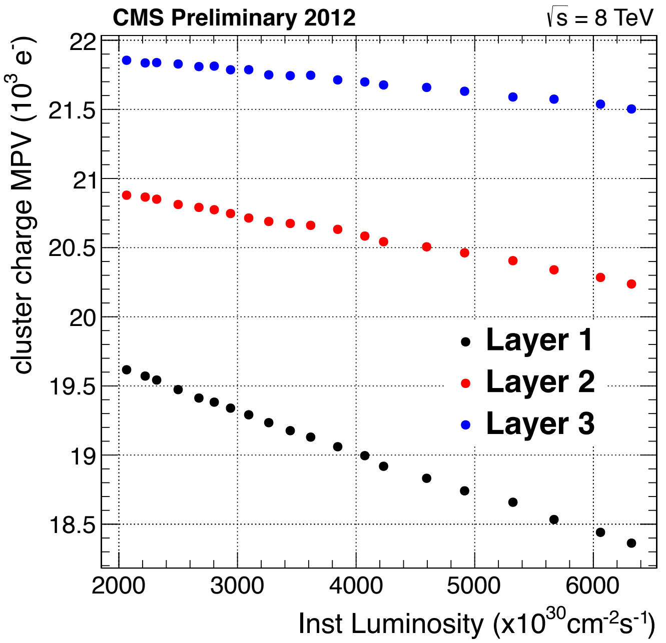

FIG. 12.12 –
Most probable value of the pixel cluster charge as function of the instantaneous luminosity. The datasets correspond to the three layers of the barrel pixel detector.

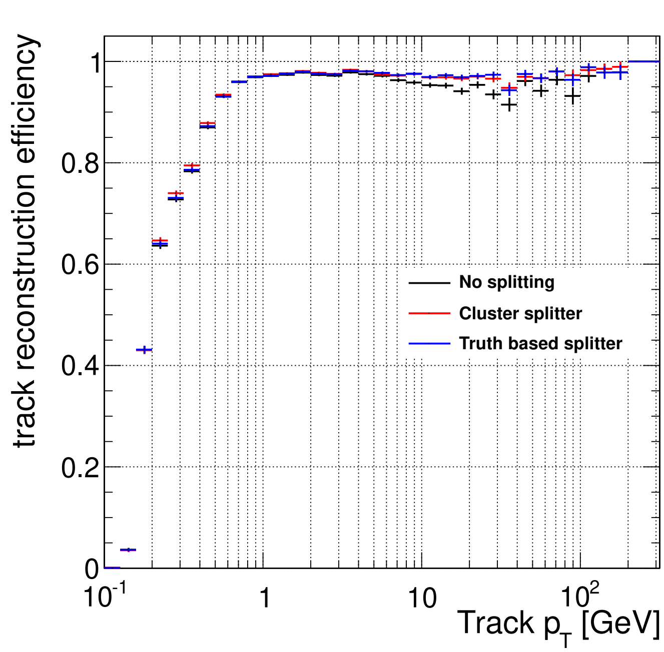

FIG. 12.13 –
Track reconstruction efficiency for boosted top events with and without the pixel hit splitting technique.

the vertex in the event with the highest summed transverse momentum. This hypothesis works well for the high momentum tracks that are usually associated to the origin of merged clusters. Two template clusters are fit to the identified merged cluster and replace the merged cluster for the subsequent tracking algorithms.

We have recently tested the algorithm both on simulated collision events and on data. Figure 12.13 shows the track reconstruction efficiency in a sample of boosted top quark pairs. The default tracking algorithm (black) is compared to the ideal scenario without cluster merging (red) and to the cluster splitting algorithm (blue). Clear improvement is observed for the high transverse-momentum tracks. For tracks with $p_T > 10$ GeV the efficiency enhancement can be up to 5%. We are currently finalising the implementation of the new algorithm in the CMS reconstruction software and we plan to utilise it in several physics analyses.

13 Superconductivity and Magnetism

M. Bendele (till May 2012), S. Bosma, Z. Guguchia, L. Howald, H. Keller, A. Maisuradze, S. Siegrist, E. Stilp, and S. Weyeneth

Visiting scientists: M. V. Eremin, B. I. Kochelaev, R. Puzniak, and A. Shengelaya
Emeritus members: M. Mali, K. A. Müller, J. Roos, and T. Schneider

in collaboration with:
Bayerische Akademie der Wissenschaften Garching, (A. Erb), Brookhaven National Laboratory (I. Bozovic, A. Gozar), Commissariat à l'énergie atomique Grenoble (G. Lapertot, P. Dalmas de Réotier, A. Yaouanc), EPFL Lausanne (H. Berger, D. Pavuna), ETH Zürich (J. Karpinski, N. D. Zhigadlo), Leibniz-Institut für Festkörper- und Werkstoffforschung Dresden (R. Hühne, P. Pahlke), Kazan State University (M. V. Eremin, B. I. Kochelaev), Max Planck Institute Stuttgart (A. Bussmann-Holder, J. Köhler, G. Logvenov), Paul Scherrer Institute (K. Conder, R. Khasanov, E. Morenzoni, A. Suter), Polish Academy of Sciences (R. Puzniak), Tbilisi State University (A. Shengelaya), University of British Columbia, Canada (R.F. Kiefl, W. Hardy)

We report recent results of active research projects in the field of unconventional superconductors, magnetism and magneto-electric materials. Different experimental techniques were combined for our studies, including muon-spin rotation (μSR), torque magnetometry, electron paramagnetic resonance (EPR), and standard characterization probes (specific heat, superconducting quantum interference device (SQUID) magnetometry and resistivity). Several experiments were performed under hydrostatic pressure (0-8 GPa).

In the first section the coupling between spins and phonons in $EuTiO_3$ was observed to occur at temperatures far above the onset of the magnetic order. In Cu_2OSeO_3 the magneto-electric properties were studied using an electric field modulated ferromagnetic resonance technique recently internally developed. μSR experiments revealed a strong variation of the number of superconducting pairs under pressure in the heavy fermions superconductor $CeCoIn_5$. The magnetic phase diagram of thin films of the high-temperature cuprate superconductor (HTC) $La_{2-x}Sr_xCuO_4$ was established by means the low energy μSR technique. Finally, an unusual *lock-in* effect was found in the HTC $YBa_2Cu_3O_{7-\delta}$ by torque magnetometry.

13.1 Magnetic field enhanced structural instability in $EuTiO_3$

Multi-functional systems with properties that can be tuned by different external sources have attracted attention for many years. The focus in this research field is mainly on multiferroics where a magnetic field modifies the dielectric properties, and an electric field may influence the magnetic characteristics.

In the search for novel multiferroic materials, the work of Katsufuji and Takagi [1] on the perovskite $EuTiO_3$ (ETO) has recently invoked hopes of having a new compound with the desired properties. It was demonstrated that the dielectric constant of ETO shows a dramatic decrease upon the onset of the anti-ferromagnetic (AFM) phase transition at T_N = 5.5 K. This unexpected behaviour clearly demonstrates that a strong spin-lattice coupling is present in the system. In addition to the observed low-T AFM phase, very recent experimental and theoretical studies have revealed the presence of a structural phase transition in ETO at T_s = 282 K [2–4]. This structural phase transition has been suggested to be caused by the oxygen octahedral tilting instability as in $SrTiO_3$ (STO) [5]. However, in STO the transition is observed at much lower temperature T_s = 105 K.

Recently, we have investigated magnetic field effects on the structural instability of ETO at T_S = 282 K [6]. The motivation for these experiments stems from our previous observation of the existence of a damped muon spin rotation (μSR) decay rate λ_{para} at temperatures far above T_N, which follows closely the temperature dependence of the transverse acoustic zone boundary mode [4]. This finding suggests that a strong paramagnon-phonon coupling exists far above T_N. We identify the structural phase transition temperature by specific heat measurements and perform these measurements under an applied magnetic field [6].

At high temperatures the anomaly stemming from the structural phase transition is visible as a distinct peak (Fig. 13.1). T_S increases non-linearly with magnetic field [6]. The substantial increase of T_S with magnetic field indicates a strong spin-phonon coupling at temperatures far above the actual magnetic order. This interaction between the applied magnetic field and the crystallographic structure may provide a new path towards the realisation of multi-functionality in complex perovskite lattices by tuning dielectric, piezoelectric, and magnetoelectric couplings.

[1] T. Katsufuji and H. Takagi, Phys. Rev. B **64**, 054415 (2001).

[2] A. Bussmann-Holder *et al.*, Phys. Rev. B **83**, 212102 (2011).

[3] Z. Guguchia *et al.*, Phys. Rev. B **85**, 134113 (2012).

[4] A. Bussmann-Holder *et al.*, New J. Phys. **14**, 093013 (2012).

[5] K. A. Müller *et al.*, Phys. Rev. B **19**, 3593 (1979).

[6] Z. Guguchia *et al.*, J. Phys.: Condens. Matter **24**, 492201 (2012).

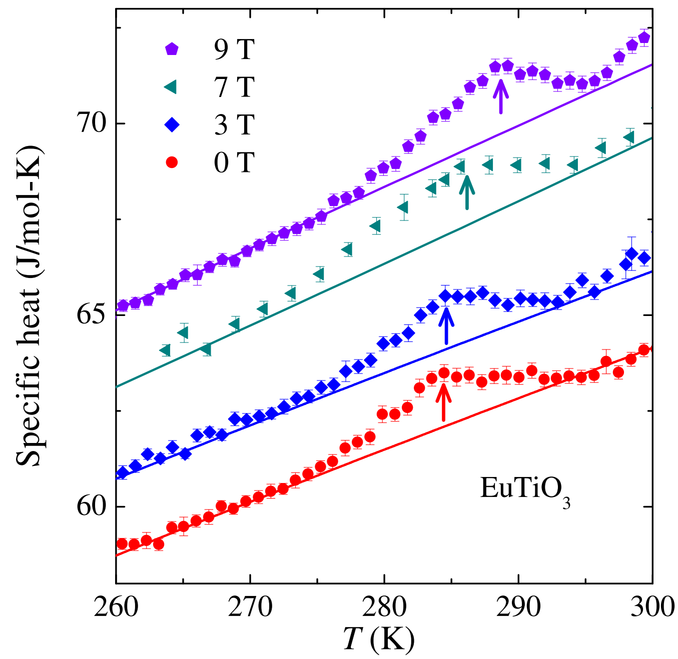

FIG. 13.1 – The specific heat of $EuTiO_3$ as a function of temperature within a limited temperature regime around the structural phase transition temperature T_S for fields of 0, 3, 7, and 9 T. For clarity the data are shifted by $2 Jmol^{-1}K^{-1}$ relative to each other with increasing magnetic field [6].

13.2 Magneto-electric effect on spin-wave resonances in Cu_2OSeO_3

Magneto-electric (ME) materials, exhibiting coupled and microscopically coexisting magnetic and electric polarizations, have attracted considerable interest in recent years [1, 2]. This coupling allows one to influence the magnetic state of a ME material via an external electric field, thus opening a broad range of possible technical applications of such materials.

In collaboration with the EPFL we investigated magnetic and magneto-electric properties of Cu_2OSeO_3 by means of the novel electric field modulated (EFM) ferromagnetic resonance (FMR) technique [3]. In standard FMR or spin-wave resonance (SWR) experiments a resonant absorption of microwave radiation by a Zeeman-split spin system is observed. In order to increase the sensitivity of FMR a lock-in detection method is used. A reference frequency of the lock-in detector is used for a weak quasi-static modulation of the Zeeman splitting, *e.g.* by magnetic field modulation (MFM) of the applied field. This leads to a weak modulation of the absorbed microwave power signal which is supplied to the input of a lock-in amplifier. As a result the lock-in detected signal is proportional to the amplitude of MFM and vanishes when there is no modulation of the Zeeman splitting. The situation is different for ME materials where the Zeeman splitting can also be modulated by an applied electric field. Due to ME coupling EFM leads to microscopic MFM proportional to the ME coupling strength. This modulation is present only in magneto-electrics and allows one to detect selectively FMR and SWR of ME materials. Thus, FMR with EFM

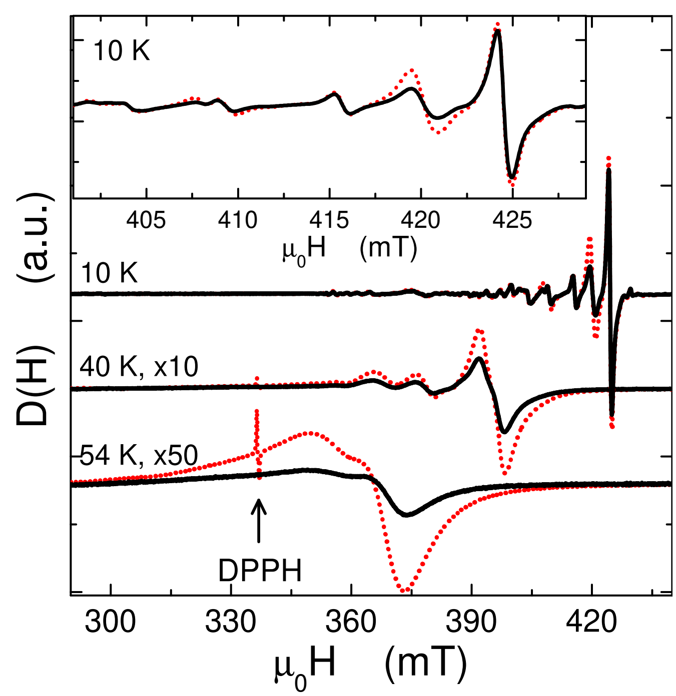

FIG. 13.2 – Temperature dependence of SWR signals of single-crystal Cu_2OSeO_3 detected using the MFM technique (dotted line) and the EFM technique (solid line). The sharp peak visible at 340 mT and 54 K is the signal of the marker sample DPPH which is present only in the case of MFM. The inset shows the expanded spectra at 10 K around 415 mT.

can serve as a sensitive microscopic tool for investigation of ME phenomena.

We applied this technique for investigating the ferrimagnetically ordered Cu^{2+} spin system in Cu_2OSeO_3 [3]. In Fig. 13.2 we show the results of FMR experiments using MFM and EFM techniques. While ME Cu_2OSeO_3 induces a SWR signal for both MFM and EFM, the paramagnetic resonance signal of $C_{18}H_{12}N_5O_6$ (DPPH) is present only for MFM. We observed for the first time series of SWR signals induced via ME coupling. An external electric field $\mathbf{E}$ induces a magnetic field component $\mu_0 H^i = \gamma E$ along the applied magnetic field $\mathbf{H}$ with $\gamma = 0.7(1)\ \mu\mathrm{T/(V/mm)}$ at 10 K consistent with our previous μSR studies [4]. Temperature and angular dependencies of $\alpha = \gamma / C$ ($C = 1.76\ \mu\mathrm{T{\cdot}mm{\cdot}V^{-1}}$ a calibration constant) are shown in Fig. 13.3. $\gamma(T)$ nearly follows that of the spin susceptibility J^{M} and rapidly decreases above the Curie temperature $T_c = 57$ K [3]. The ratio $\langle\alpha\rangle / J^{\mathrm{M}}$ varies slowly with temperature and shows no anomaly at T_c, suggesting that ME effect is not related to the long range magnetic order.

[1] N. A. Spaldin and M. Fiebig,
Science **309**, 391 (2005).

[2] M. Fiebig,
J. Phys D: Appl. Phys. **38**, R123 (2005).

[3] A. Maisuradze *et al.*,
Phys. Rev. Lett. **108**, 247211 (2012).

[4] A. Maisuradze *et al.*,
Phys. Rev. B **84**, 064433 (2011).

13.3 Strong reduction of the magnetic penetration depth in $CeCoIn_5$ under pressure

In the tetragonal heavy fermion system $CeCoIn_5$ the unconventional superconducting state was probed by means of transverse field muon spin rotation (TF μSR) [1]. In a μSR experiment the muons act as highly sensitive local probe of the magnetic field. TF μSR experiments were performed above and below the superconducting transition temperature (T_c) in single crystals of $CeCoIn_5$ under pressure. An example of the obtained magnetic field profiles is shown in inset of Fig. 13.4. Above T_c (black squares) the mean magnetic field corresponds to the applied value and the magnetic field distribution is due to the nuclear moments. Below T_c (red circles) the mean value of the magnetic field is reduced due to diamagnetism and the field distribution is asymmetric. The asymmetry arises from an additional contribution to the field distribution generated by the vortex lattice (pink area represents half of the vortex lattice contribution) which is uniquely determined by the value of the magnetic penetration depth (λ).

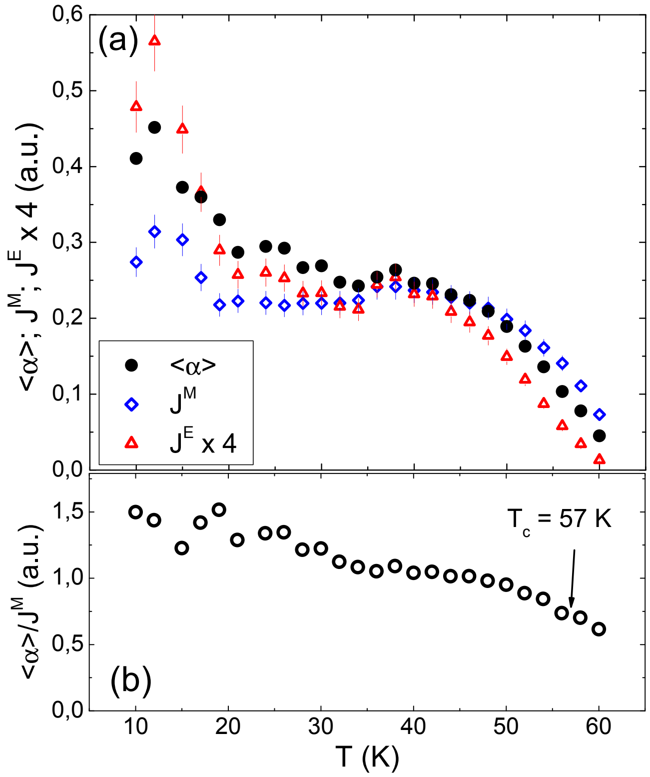

FIG. 13.3 – (a) Temperature dependence of the average ME effect parameter $\langle\alpha\rangle$ and the signal intensities J^E and J^M of Cu_2OSeO_3 detected by EFM and MFM, respectively. (b) Temperature dependence of the ratio $\langle\alpha\rangle / J^M$ showing no anomaly at $T_c = 57$ K.

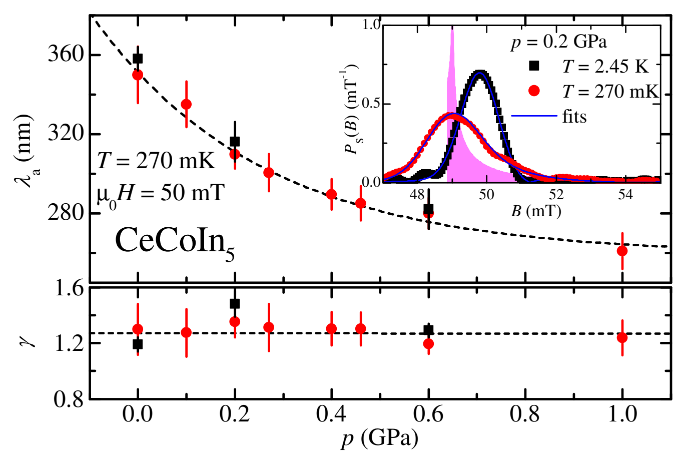

FIG. 13.4 – Pressure dependence of the in-plane magnetic penetration depth (λ_a) and the penetration depth anisotropy ($\gamma = \lambda_c / \lambda_a$). In the inset a typical field distribution probed by μSR is shown.

Using the field distribution probed by μSR, the pressure dependence ($0 - 1$ GPa) of the basal-plane magnetic penetration depth (λ_a), the penetration depth anisotropy

($\gamma = \lambda_c/\lambda_a$), and the temperature dependence of $1/\lambda_i^2$ ($i = a, c$) was studied. A strong decrease of λ_a with pressure was observed, while γ is pressure independent (Fig. 13.4). Furthermore, no significant variations in $\lambda_i^2(0)/\lambda_i^2(T)$ with pressure were obtained. A linear relationship between $1/\lambda_a^2(270\text{mK})$ and T_c was also found. Within the London model the large decrease of λ_a with pressure indicates an increase of the number of superconducting quasi-particles by a factor of about 2. This increase is probably related with the presence of a quantum critical point in this pressure range.

[1] L. Howald *et al.*,
Phys. Rev. Lett. **110**, 017005 (2013).

13.4 Thin film phase diagram of $La_{2-x}Sr_xCuO_4$

Thin-film studies open the door to new physics, since the properties of thin-film materials can be tailored which is difficult or even impossible for bulk samples. The magnetic phase diagram of $La_{2-x}Sr_xCuO_4$ (LSCO) thin films was intensively studied. The samples used are MBE grown and have a thickness of 53 nm. They cover a doping range of $x = 0.00 - 0.06$. XRD and resistivity measurements confirm that the c axis of LSCO thin films depends linearly on the doping level x, as in the bulk case. The resistance is higher at low x compared to bulk samples and decreases with increasing x over two decades.

To study the magnetic phase diagram more in detail, low energy muon spin rotation (LE-μSR) measurements were performed. Muon energies in the range $1 - 30$ keV allow to investigate thin film samples, because muons stop on a nano-meter scale in condensed matter. From weak transverse magnetic field (wTF) μSR measurements magnetic transition temperatures as well as magnetic volume fractions were determined. From measurements without an applied magnetic field the internal magnetic field B_{loc} present at the muon stopping site was identified.

The phase diagram of LSCO consists of several regimes as shown in Fig. 13.5: the high temperature paramagnetic (PM) phase, the anti-ferromagnetic (AF) dome, the low temperature spin freezing (SF) region, and the *cluster spin glass* (CSG) phase. The PM phase is present for all doping levels at higher temperatures. In the AF phase ($x < 0.02$) static moments are present which lead to oscillations in the μSR time spectra. The Néel temperatures T_{N} of the thin film samples determined from wTF-μSR measurements are reduced compared to those of bulk material (Fig. 13.5). At low temperatures a freezing of the additional charge carriers is expected from bulk measurements for $x > 0.00$ (SF phase). The temperature dependence of B_{loc} shows instead no increase of the slope dB_{loc}/dT at low temperatures T. This implies that no spin freezing is observed down to 5 K. Surprisingly, for $x = 0.00$ two local magnetic fields of $B_{\text{loc},1}(0\text{ K}) = 40.9(4)$ mT and $B_{\text{loc},2}(0\text{ K}) = 11.2(1)$ mT were detected at the muon stopping site in zero field measurements in the AF phase. In bulk only one local magnetic field of $B_{\text{loc}}(0\text{ K}) = 43$ mT is reported [4]. This difference could arise from changes in the spin arrangement of copper electronic magnetic moments. In the so called *cluster spin glas* phase ($x \geq 0.02$) dynamical spin and charge stripes are present in cuprate systems due to micro-segregation of mobile holes. AF hole-poor areas are separated by non-magnetic hole-rich domain walls. At low temperatures the dynamics of the stripes slow down and oscillations are observed in the LE-μSR zero field asymmetry time spectra. The determined glass transition temperatures T_g are all well above the bulk values. Strain induced changes of the higher order magnetic coupling constants as well as oxygen off-stoichiometry are unlikely to explain the observed differences to bulk. It is concluded that strain induced disorder is probable the main reason of the observed differences to bulk. The magnetic phase diagram was determined for LSCO thin films, is a base for future studies of multi-layer and super-lattices.

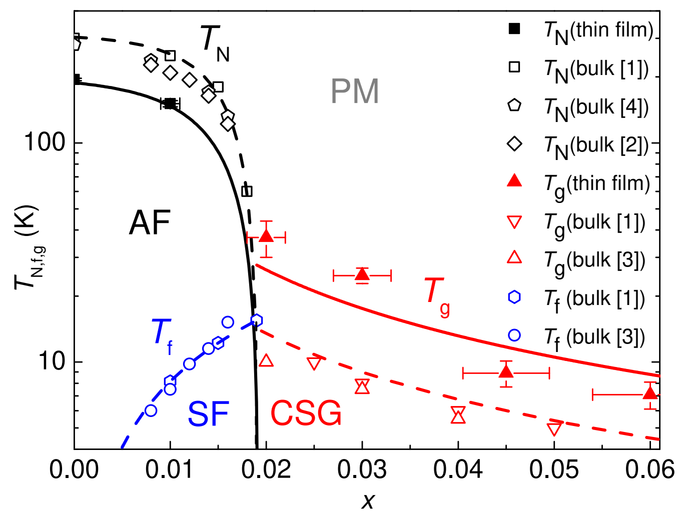

FIG. 13.5 – Magnetic phase diagram of LSCO for thin film samples (solid lines) and bulk material (dashed lines). Néel temperatures T_{N}, freezing temperatures T_{f} and glass transition temperatures T_g are shown in dependence of the Sr content x [1–4]. The black lines are guides to the eye, the blue and red lines follow the relations $T_{\text{f}} \propto x$ and $T_g \propto 1/x$.

[1] Ch. Niedermayer *et al.*,
Phys. Rev. Lett. **80**, 3843 (1998).

[2] J. H. Cho *et al.*,
Phys. Rev. Lett. **70**, 222 (1993).

[3] F. C. Chou *et al.*,
Phys. Rev. Lett. **71**, 2323-2326 (1993).

[4] F. Borsa *et al.*,
Phys. Rev. B **52**, 7334 (1995).

13.5 Vortex lock-in transition in $YBa_2Cu_3O_{7-\delta}$

In low anisotropy superconductors, a three-dimensional (3D) to two-dimensional (2D) crossover can take place when the superconducting coherence length along the *c*-axis becomes smaller than the distance between the planes supporting superconductivity. For $YBa_2Cu_3O_{7-\delta}$, this happens at $T_{cr} \simeq 76$ K.

When the applied magnetic field direction is nearly parallel to the *ab*-plane, a lock-in transition of the vortices may take place [1]. In this case, the vortex is confined between the superconducting layers, even if the field is not aligned with these layers. This minimizes superconducting condensation energy at the cost of magnetic energy coming from the misalignment of vortices and field, since the cores do not cross the layers anymore. The lock-in was observed mainly in high anisotropy materials, but also in $YBa_2Cu_3O_{7-\delta}$ and other layered superconductors. $YBa_2Cu_3O_{7-\delta}$ is of particular interest for lock-in studies, since its low anisotropy allows one to observe the onset of lock-in far below T_c, where critical fluctuations make the analysis difficult. The theoretical models for lock-in which are relevant for $YBa_2Cu_3O_{7-\delta}$ are presented in [2] and [3].

We performed angular torque measurement on clean detwinned $YBa_2Cu_3O_{7-\delta}$ single crystals [4]. A simple geometric calculation of the torque in the locked-in regime yields a linear torque dependence on the angle θ between the applied field H and the crystallographic *c*-axis. The measured shape of the torque as a function of θ is the same as predicted in [2], although this model was originally developed for quasi-2D superconductors. Figure 13.6 shows the torque in the lock-in region. The lock-in angle θ_{lock} is the point at which the torque ceases to follow the linear dependence observed around the *ab*-plane, corresponding to the locked-in state. θ_{lock} is smaller at low temperatures, as expected for a pinning-like effect. Surprisingly, it also is smaller at high fields. The lock-in should happen when the perpendicular component of the field $H^{||c}$ goes below $H_{c1}^{||c}$. Field penetration across the layers is then impossible, thus locking the vortices between the planes. In this model, $\pi/2 - \theta_{lock}$ is inversely proportional to H, as observed in high-anisotropy cuprates.

Torque data present an angular irreversibility between the clockwise (CW) and counter-clockwise (CCW) branches, which is usually due to pinning and can be reduced by the shaking technique [5]. The difference between the 3D London prediction and the CW-CCW averaged torque, which is interpreted as lock-in, is too large to be an artifact of irreversibility. The shaking efficiency limit is reached when a small peak appears at the limit of the lock-in domain; in our case this happens at low temperature and high fields. This peak usually masks the lock-in effect in lower quality crystals.

The lock-in angle θ_{lock} can also be defined as the angle where the torque slope diverges from the *ab*-plane value. With this definition, θ_{lock} still increases at low temperatures and at high fields. This could be due to the fact that θ_{lock} becomes more difficult to identify at higher temperatures and lower fields due to the increased curvature of the graph. However, the simple model of θ_{lock} is not observed in $La_{2-x}Sr_xCuO_4$ [6]. It is thus possible that the 1/H model holds only for high-anisotropy superconductors.

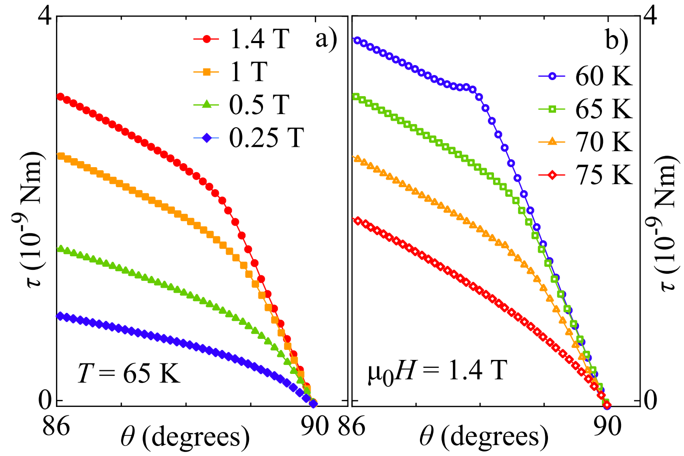

FIG. 13.6 – a) Torque of detwinned single crystal $YBa_2Cu_3O_{7-\delta}$ as a function of angle θ for various fields at 65 K. b) $\tau(\theta)$ for various temperatures at 1.4 T.

[1] D. Feinberg and C. Villard,
Phys. Rev. Lett. **65**, 919 (1990).

[2] D. Feinberg and A. M. Ettouhami,
Int. J. Mod. Phys. B **7**, 2085 (1993).

[3] L. N. Bulaevskii, Phys. Rev. B **44**, 910 (1991).

[4] S. Bosma *et al.* , Phys. Rev. B **86**, 174502 (2012).

[5] M. Willemin *et al.* , Phys. Rev. B **58**, R5940 (1998).

[6] V. Vulcanescu *et al.* , Phys. Rev. B **50**, 4139 (1994).

14 Phase Transitions, Materials and Applications

F. von Rohr, H. Grundmann, O. Bossen, K. Inderbitzin, S. Siegrist, A. Engel, and A. Schilling

in collaboration with Tohoku University (N. Toyota), Karlsruhe Institut für Technologie (K. Il'in), Deutsches Zentrum für Luft- und Raumfahrt (H.-W. Hübers, A. Semenov), FIRST Lab ETH Zürich, PSI Villigen (M. Medarde, K. Conder), McMaster University (H. Dabkowska), IFW Dresden (V. Kataev, A. Alfonsov), University of São Paulo (A. Paduan-Filho), Institute of Nuclear Physics, Tashkent (A. Rakhimov), ETH Zürich (R. Nesper), and Princeton University (R. J. Cava)

(PTMA)

14.1 Superconducting nanowire single-photon detectors for optical and X-ray photons

In the previous annual report we described the successful development and testing of an X-ray superconducting nanowire single-photon detector (X-SNSPD) from a 100 nm thick Nb film [1]. We observed ultrafast, dark count-free keV-photon detection and a significant dependence of the pulse amplitude distribution on the photon energy. However, this Nb X-SNSPD latched (i.e. was not operational) for bias currents larger than 5.5% of the critical current I_c, due to the low resistance of the normal domains forming in a Nb nanowire at photon detection.

In order to reduce this susceptibility to latching, TaN was used as a detector material, as it has an about two orders of magnitude larger resistivity and a larger keV X-ray absorptance and magnetic penetration depth (and thus leads to a larger detector kinetic inductance) than Nb. Two X-SNSPDs from a 100 nm thick TaN film were fabricated with different nanowire widths w (Fig. 14.1), TaN-A with $w \simeq$ 310 nm and TaN-B with $w \simeq$ 1.85 μm, and their properties were compared with those of the Nb X-SNSPD [2]. The TaN detectors indeed latch for significantly higher bias currents, at 52% I_c (TaN-A) and 32% I_c (TaN-B).

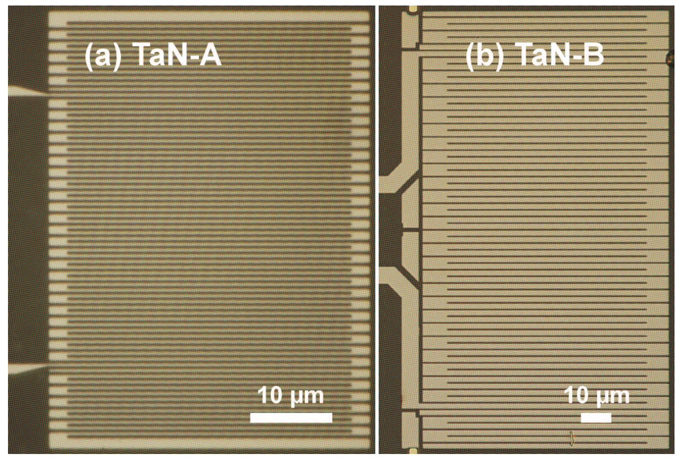

FIG. 14.1 – Optical images of the examined X-SNSPDs from 100 nm thick TaN [2]:
(a) TaN-A with $w \simeq$310 nm and
(b) TaN-B with $w \simeq$1.85 μm wide nanowires.

The increased resistivity of TaN also reduces the problem of differentiating small-amplitude photon detection pulses from electronic noise, and a device detection efficiency (DDE) of 1.4% for 5.9 keV photons was determined for TaN-A, which is significantly larger than the lower limit of 0.03% found for the Nb X-SNSPD.

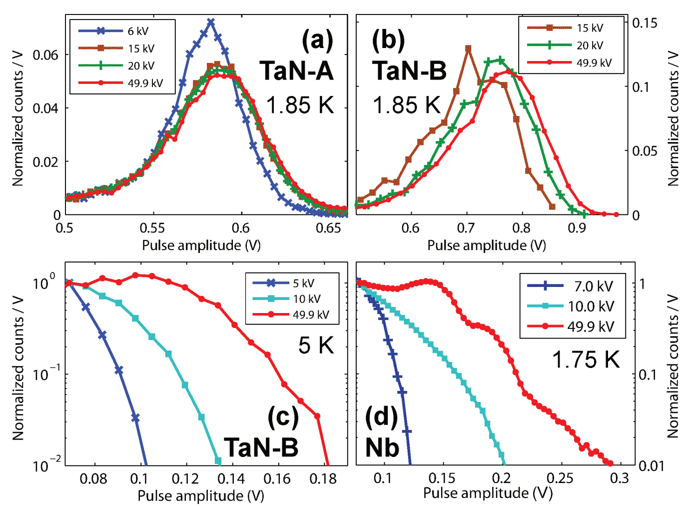

FIG. 14.2 – Pulse-amplitude histograms for different X-ray tube acceleration voltages [2]
(a) TaN-A (at $I_b = 54\ \mu$A)
(b) TaN-B (at $I_b = 243\ \mu$A)
(c) TaN-B (at $I_b = 121\ \mu$A) at elevated temperature
(d) the Nb X-SNSPD (at I_b=0.61 mA)
The distributions in (a) and (b) are normalized to the total number of events, those in (c) and (d) to the counts at 69 and 79 mV, respectively.

The wide nanowires of detector TaN-B allow for a certain energy-resolving capability (as also demonstrated for the Nb X-SNSPD) in contrast to the narrower nanowires of TaN-A (Fig. 14.2). This observation proves, that small normal-domain resistances are responsible for energy-dependent photon-detection pulse amplitudes. However, the wider nanowires of TaN-B also limit the DDE at low temperatures, which can be explained within a standard hot-spot model [3]. Increasing the operation temperature increases the DDE but also reduces the pulse amplitude due to a decreasing critical current.

We have also achieved important progress on conventional optical SNSPD in the reporting period. There has been growing evidence in recent years that magnetic vortices are the dominating source of fluctuation-based dark-count events in optical SNSPD [4, 5]. Therefore it is obvious to expect a certain dependence of the dark-count rate on an applied magnetic field [6]. This dependence is expected to be symmetric with respect to the direction of the magnetic field perpendicular to the detector plane and the bias-current direction. However, our measurements revealed a surprising asymmetry with respect to the sign change of the magnetic field [7], which we successfully explained by a current-crowding effect in inequivalent corners of the meander shape [8].

In another series of experiments we have for the first time systematically studied the temperature-dependent performance of SNSPD [9]. Our data confirmed what has long been observed: SNSPD not only have a reduced dark-count rate when operated at temperatures below 4 K, but also an increased cut-off wavelength. We could qualitatively explain this surprising behavior by taking into account a temperature-dependent diffusion coefficient for quasi-particles that enters the standard detection model [10].

14.2 Thermodynamic signature of vortex-lattice melting

In type-II superconductors, an external magnetic field penetrates a superconductor in form of magnetic flux lines which arrange themselves in a regular lattice, each one carrying one magnetic flux quantum $\Phi_0 = 2.07 \times 10^{-15}$ Vs. This lattice has been shown to show a first-order melting transition in high-temperature cuprate superconductors $YBa_2Cu_3O_7$ [11] and $Bi_2Sr_2CaCu_2O_8$ [12]. A temperature-driven phase transition of the vortex lattice should, in principle, also occur in sufficiently clean low-temperature superconductors. For Nb, attempts have been made to measure the melting entropy directly, and the absence of a related signal in very pure samples has led to reflections about the complete absence of vortex-lattice melting in this compound [13].

Based on available literature to describe the vortex-state and using the Lindemann criterion, we have determined the melting lines and the related melting entropies, to be able to judge on the compatibility of experimental data with the theoretical predictions, using a few known material parameters.

The Lindemann criterion is based on the idea that melting occurs as soon as the thermal mean-square displacements $\langle u_{th}^2 \rangle^{1/2}$ of the of atoms (or in our case vortices) in a lattice reaches a certain fraction of the lattice constant $a = \sqrt{\Phi_0/B}$, i.e., $\langle u_{th}^2 \rangle^{1/2} \simeq c_L a$ with the Lindemann number $c_L < 1$. Corresponding quantitative calculations for the vortex-lattice melting lines lead to an implicit equation [14]

$$\frac{t_m}{\sqrt{1-t_m^2}} = \frac{2\pi c_L^2}{Gi^{1/2} b^{1/2} f(b)}, \tag{14.2}$$

with $t_m = T_m/T_{c0}$ the reduced melting temperature T_m for $B = B_m$ with respect to the critical temperature T_{c0} in zero magnetic field, $b = B/B_{c2}(T)$ the reduced magnetic induction B with respect to the temperature dependent upper-critical field $B_{c2}(T)$, and Gi the Ginzburg number of the superconductor. Within a collective pinning theory [14], the function $f(b)$ is

$$f(b) = \frac{2\beta_A \sqrt{1+(1+c(b))^2}-1}{(1-b)c(b)(1+c(b))}, \tag{14.3}$$

valid for all values of b throughout the mixed state, with $c(b) = \sqrt{\beta_A(1-b)}/2$ and $\beta_A = 1.16$ the Abrikosov number (other theoretical approaches produce similar results for $f(b)$). In Fig. 14.3 we show the corresponding melting lines according to Eq. (14.2), evaluated for a number of different type-II superconductors.

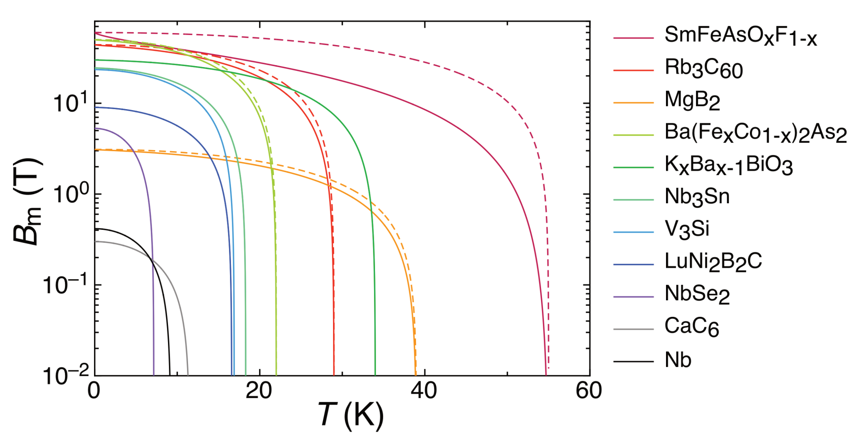

FIG. 14.3 – Expected melting lines $B_m(T)$ for various type-II superconductors, calculated from Eqs. (14.2) and (14.3) with $c_L = 0.20$. The $B_{c2}(T)$-lines (dotted lines) have been plotted only for $SmFeAsO_xF_{1-x}$, Rb_3C_{60}, MgB_2, and $Ba(Fe_xCo_{1-x})_2As_2$ for which they appear distinct from $B_m(T)$ in this representation.

To obtain the melting entropies, we made use of Richard's rule for crystal lattices, in which the configurational melting entropy per particle is assumed to be a constant multiple (or fraction) of k_B. With the volume V_0 occupied by one particle we then have

$$\Delta s_0 V_0 = \eta k_B, \tag{14.4}$$

where Δs_0 is the configurational melting entropy per volume and η is an unknown constant on the order of 1. Using a result by Kierfeld and Vinokur [15], the volume V_0 is

$$V_0 = \frac{\varepsilon a^3}{\sqrt{1-b}}. \tag{14.5}$$

It turned out that the entropy obtained from applying Richard's rule alone considerably underestimates the measured entropy changes Δs upon vortex-lattice melting both in $YBa_2Cu_3O_7$ and in $Bi_2Sr_2CaCu_2O_8$ [16]. Taking the marked temperature dependence of thermodynamic quantities into account, Dodgson *et al.* arrive at an enhancement of Δs_0 of the form [16]

$$\Delta s = \frac{\left[1 - \tilde{b} + (2\tilde{b} - t^2)t^2\right]}{(1 - t^2 - \tilde{b})(1 - t^2)} \Delta s_0, \tag{14.6}$$

with $\tilde{b} = B/B_{c2}(0)$. We have calculated $\Delta s/\eta$ for the compounds analyzed in Fig. 14.3 using Eqs. (14.4) and (14.6) (see Fig. 14.4).

The resulting discontinuities in the magnetization can be derived from the Clausius-Clapeyron equation,

$$\Delta s = -\Delta M \frac{\mathrm{d}B_m}{\mathrm{d}T}, \tag{14.7}$$

with $\Delta M > 0$, i.e., M increases when crossing $B_m(T)$ from the solid to the "liquid" phase. The results of this calculation are displayed in Fig. 14.5.

These magnetization discontinuities ($4\pi\Delta M \simeq 8$ mG to 0.11 G, in cgs-units) are small, but they should still be within the sensitivity specifications of commercial SQUID magnetometers [17]. Moreover, the Δs of the calculated magnitude should, in principle, also be measurable in high-quality single crystals provided that thermodynamic equilibrium is achieved.

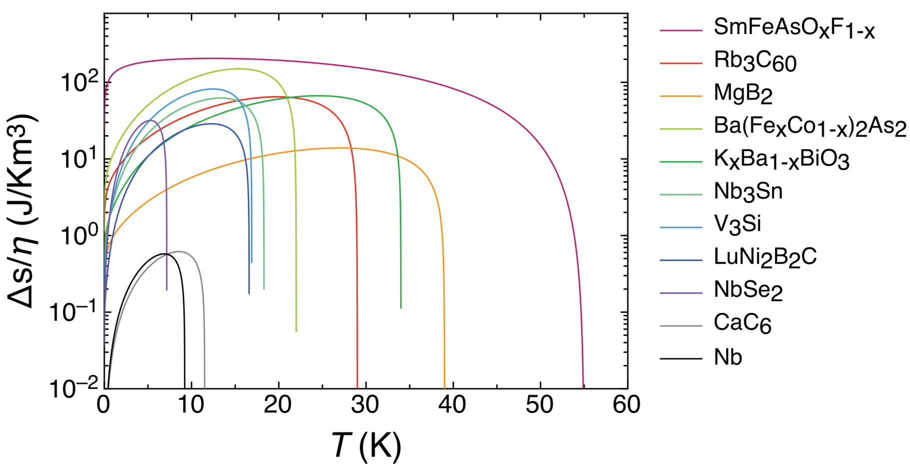

FIG. 14.4 – Vortex-lattice melting entropies $\Delta s/\eta$ for various type-II superconductors at the $B_m(T)$ shown in Fig. 14.3, as a function of T.

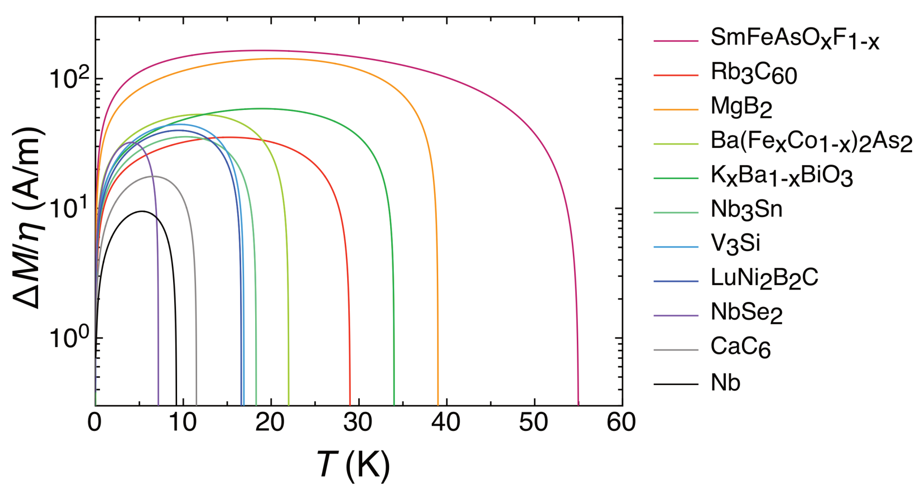

FIG. 14.5 – Discontinuities $\Delta M/\eta$ in magnetization at the $B_m(T)$ of the materials under discussion.

14.3 Material considerations for BEC in magnetic insulators

In the previous annual report, we have suggested to probe the existence of macroscopic phase coherence in so called triplon Bose-Einstein condensates (BEC) that are supposed to form in certain magnetic insulators, with a novel experimental scheme [18]. The proposal is based on using two coupled materials with slightly different chemical potentials for the respective triplon quasiparticles, representing an analogue to a Josephson device for superconductors. The a.c. Josephson effect should then manifest itself in a distinct change of the respective energy spectra. As the construction of such a device relies on the control of the material properties and the quality of the junctions, we decided to investigate two different prototype materials. The mother compounds of the solid solution $Ba_{3-x}Sr_xCr_2O_8$ (i.e. $x = 0$ and $x = 3$) have the same crystal structure but with different lattice parameters and different critical fields ($H_c = 12.5\,T$ and $30\,T$) [19, 20], potentially allowing for the fine-tuning of the magnetic interaction parameters through the stoichiometry. On the other hand, the preparation of Br-doped dichloro-tetrakis-thiourea-nickel (DTN) [22] with different Br contents could allow in a natural way to prepare coupled single crystals with different H_c's, thereby ensuring a high quality of the Josephson junction itself.

14.3.1 $Ba_{3-x}Sr_xCr_2O_8$ as a prototype material

We have synthesized several members of the solid solution $Ba_{3-x}Sr_xCr_2O_8$ and performed a detailed investigation of the structural and magnetic properties, in particular of the magnetic intradimer interaction constant J_d which is important for the strength of the critical field H_c [21]. Single crystals with $x = 0, 0.1$ and 3 (prepared by Hanna Dabkowska at McMaster University in Hamilton, Canada), as well as polycrystalline material with $0 \leq x \leq 3$ have been analyzed using a commercial SQUID magnetometer (*Quantum Design Inc.*). The resulting magnetization as a function of the temperature in the range of $2\,K \leq T \leq 300\,K$ was fitted using the Bleaney-Bowers formula for interacting dimers,

$$M_d(T) = \frac{n_d g^2 \mu_B B_{ext}}{J_e + k_B T \left(3 + e^{\frac{J_d}{k_B T}}\right)}, \qquad (14.8)$$

with an additional Brillouin term for the seemingly increasing paramagnetic background for $0.5 \leq x \leq 2$,

$$M_p(T) = n_P g \mu_B \left(\coth\left(\frac{g\mu_B B_{ext}}{k_B T}\right) - \frac{1}{2}\coth\left(\frac{g\mu_B B_{ext}}{2k_B T}\right)\right).$$

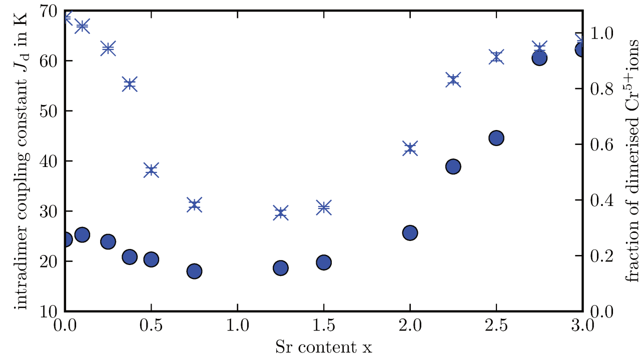

FIG. 14.6 – Estimated intradimer interaction constant J_d in $Ba_{3-x}Sr_xCr_2O_8$ (filled circles) and the fraction of dimerized Cr^{5+}-ions (crosses, prefactor n_d from Eq. 14.8), as a function of the strontium content x.

The thus obtained intradimer interaction constant J_d is shown in Fig. 14.6, together with the estimated fraction n_d of dimerized Cr^{5+} ions. The interaction constant has a broad minimum for intermediate values of x, possibly leading to a decrease of the critical field.

As the drop of the fraction of dimerized Cr^{5+} ions and, conversely, the increase of the paramagnetic background might indicate the presence of impurity phases, and to obtain further structural information about the solid solution, we performed powder-diffraction experiments using $Cu_{K\alpha}$ X-ray radiation on polycrystalline samples and crushed parts of single crystals mentioned above. The diffraction data were analyzed using a Rietveld method. We found the space group to remain the same as for the mother compounds ($R\bar{3}m$). As expected, the lattice constants vary smoothly as functions of x, whereas the atomic positions remain essentially unchanged. Surprisingly, the obtained spectra show no sign of impurity phases. We therefore conclude that the paramagnetic background is intrinsic to $Ba_{3-x}Sr_xCr_2O_8$ and may hint to the formation of unpaired Cr^{5+} ions by the presence of disorder, introduced by the partial substitution of Ba by Sr.

14.3.2 ESR-Experiments on DTN

To search for possible changes in the energy spectra of coupled magnetic insulators with different critical fields, ESR measurements were performed on samples of DTN ($NiCl_2{-}4SC(NH_2)_2$). A sample of pure DTN as well as a specimen of doped DTN with 13% of the Cl atoms replaced by Br, and a third, coupled sample, consisting of a core of pure DTN and a shell of DTN, doped with Br (samples prepared by Armando Paduan-Filho, University of São Paulo) were analyzed using ESR frequencies in the range of $290\,GHz - 450\,GHz$ in magnetic fields up to $\mu_0 H = 16\,T$. At the writing of this report, only measurements for the uncoupled specimens have been conducted in the temperature region of interest ($T \leq 1.2\,K$) (in collaboration with Vladislav Kataev and Alexey Alfonsov, IFW Dresden). We expect results for the coupled device by the end of this year.

14.3.3 Modeling disorder in the quantum magnet $Tl_{1-x}K_xCuCl_3$

Within a scientific visit of Prof. A. Rakhimov (Institute of Nuclear Physics, Tashkent, Uzbekistan) we have attempted to model the effect of crystalline disorder on the density of the triplon condensate in the quantum magnet $Tl_{1-x}K_xCuCl_3$, where the dopant K acts as a source of disorder. A standard formalism for atomic bosonic gases by Huang and Meng [23] turned out not to be satisfactory to fully explain the experimental data. The reason is that the parameters of the Hamiltonian of atomic gases are naturally fixed (*i.e.*, independent of weak disorder), while certain parameters in the Hamiltonian of spin gapped quantum magnets may change with doping, *e.g.*, due to a related variation of the magnetic-coupling energies with varying bond lengths as a function of x. Taking into account these modifications we finally found a good agreement between theory and experiment. Bond random effects in mixed magnetic spin systems manifest themselves in dual way: by modification of internal parameters and by localization on random scatterers. Each of these effects could be studied separately in an appropriate theory, but they should be taken into account simultaneously for an adequate description of, *e.g.*, measured magnetization data. The interplay between these effects leads to a nontrivial behavior of the sound-like speed c: when the external magnetic field H is fixed but x is experimentally varied, c increases for small x, reaches a maximum value and then decreases due to localization effects. While the speed of this mode was measured in dilute BEC of sodium atoms a long time ago, it has never been an intense focus of research in dimerized quantum magnets. It could be systematically studied, for example, by measuring the dispersion relation with inelastic neutron scattering techniques [24].

14.4 Novel Materials for Thermoelectrics and Topological Insulators

Recent studies have shown that $GeBi_4Te_7$ exhibits free-standing topological surface states [25]. Moreover, this material has been under consideration as a potentially good thermoelectric because of its large thermopower and the expected low lattice thermal conductivity due to the large, complex unit cell (see e.g. [26], [27]). For the systematic investigation of the physical properties

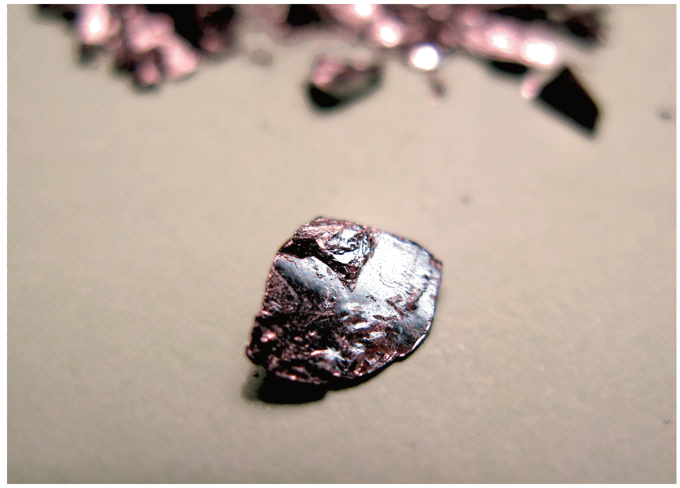

FIG. 14.7 – Photograph of as-grown single crystals of $GeBi_4Te_7$. Sizes are typically 10 mm.

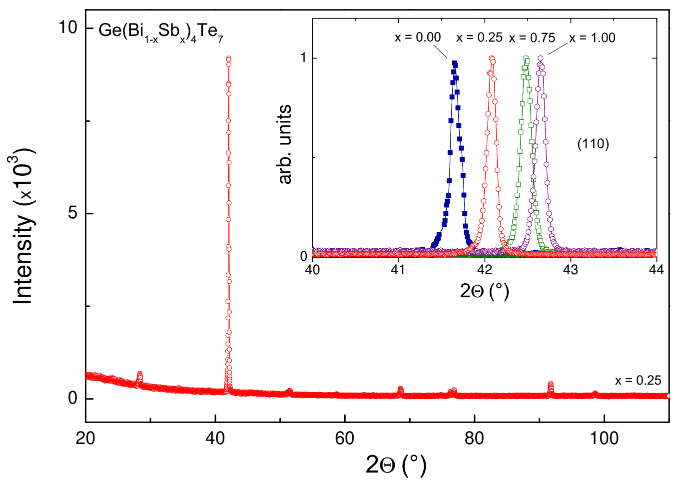

FIG. 14.8 – The X-ray diffraction pattern of $x = 0.25$ showing the reflections from the basal plane of the cleaved single crystal. In the inset we show the change of the (110) reflection for $x = 0$, 0.25, 0.75 and 1.

of this material, we have grown large single crystals of $GeBi_4Te_7$ and the $Ge(Bi_{1-x}Sb_x)_4Te_7$ solid solution by the modified Bridgman method. We have used the isovalent and isostructural substitution of Bi by Sb as a way to manipulate the Fermi-level of these compounds. The as-grown crystals of $GeBi_4Te_7$ are shown in Fig. 14.7. Powder X-ray diffraction patterns of all samples of the solid solution were indexed using the hexagonal space group $P\bar{3}m1$ and were found free of any impurity reflections. The XRD pattern for $x = 0.25$ and the change of the (110) reflection as a function of doping for $x = 0$, 0.25, 0.75 and 1 are shown in Fig. 14.8. Replacing Bi by Sb leads to a decrease of the unit-cell volume due to the smaller ionic radius of Sb. Within this series, the lattice parameters vary from approximately $a = 4.29$ Å, $c = 23.89$ Å for the pure Bi end member, to $a = 4.24$ Å, $c = 23.80$ Å for the pure Sb end member.

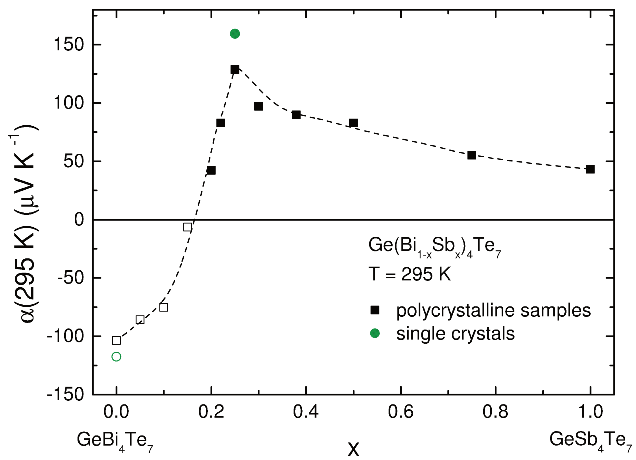

FIG. 14.9 – Composition dependence of the room temperature thermopowers of $Ge(Bi_{1-x}Sb_x)_4Te_7$ for x ranging from 0 to 1, for 12 differently doped polycrystalline samples, and two single crystals (x = 0 and 0.25). The dashed line is a guide to the eye for the room temperature thermopowers of the polycrystalline samples.

Our temperature dependent measurements of the thermopower $\alpha(T)$ in the range from 10 K to 300 K reveal a systematic crossover from n-type to p-type in $Ge(Bi_{1-x}Sb_x)_4Te_7$. The thermopower in this solid solution ranges from -117 μVK^{-1} to +160 μVK^{-1}. The crossover from n-type to p-type is continuous with increasing Sb content and occurs around $x \simeq 0.15$. The room temperature thermopowers α_{295K} of $Ge(Bi_{1-x}Sb_x)_4Te_7$ for the whole range from x = 0 to x = 1, measured for 12 differently doped polycrystalline samples and two single crystals, are shown in Fig. 14.9. The highest positive thermopowers are observed in the vicinity of the transition from n-type to p-type.

All samples show semimetallic behavior that is typical for heavily doped semiconductors, with electrical conductivities $\sigma(T)$ in the range from 150 to 2200 Scm^{-1}. We find that the crossover from n-type to p-type is not accompanied by a semiconducting or insulating resistivity regime. As a general trend, we observe that the electrical conductivity increases with increasing Sb content. The temperature dependent thermal conductivities $\kappa(T)$ range from 0.2 WK^{-1}m^{-1} for x = 0 to 0.8 WK^{-1}m^{-1} for x = 1, and increase as a function of Sb content. The highest resulting thermoelectric efficiencies among the tested n-type and p-type samples are $Z_nT = 0.11$ and $Z_pT = 0.20$, respectively. For an optimal n-p couple in this alloy system, the composite figure of merit is $Z_{np}T = 0.17$ at room temperature.

Our findings suggest a road to obtain better thermoelectric materials in this system [28]. Furthermore, the results indicate future pathways to optimization of the compound as both a thermoelectric and a topological insulator. In future work we will concentrate on the properties of the surface states in the vicinity of the n-p crossover, in collaboration with the group of Prof. Osterwalder at our institute.

[1] K. Inderbitzin, A. Engel, A. Schilling, K. Il'in and M. Siegel, Appl. Phys. Lett., **101** (2012), 162601.

[2] K. Inderbitzin, A. Engel and A. Schilling, IEEE Trans. Appl. Supercond., **23** (2013), 2200505.

[3] A. Gabutti, R. G. Wagner, K. E. Gray, R. T. Kampwirth and R. H. Ono, Nucl. Instrum. Methods A, **278** (1989), 425.

[4] H. Bartolf, A. Engel, A. Schilling, K. Il'in, M. Siegel, H.-W. Hübers and A. Semenov, Phys. Rev. B, **81** (2010), 024502.

[5] L. N. Bulaevskii, M. J. Graf, C. D. Batista and V. G. Kogan, Phys. Rev. B, **83** (2011), 144526.

[6] L. N. Bulaevskii, M. J. Graf and V. G. Kogan, Phys. Rev. B, **85** (2012), 014505.

[7] A. Engel, A. Schilling, K. Il'in and M. Siegel, Phys. Rev. B, **86** (2012), 140506(R).

[8] J. R. Clem, Y. Mawatari, G. R. Berdiyorov and F. M. Peeters, Phys. Rev. B, **85** (2012), 144511.

[9] A. Engel, K. Inderbitzin, A. Schilling, R. Lusche, A. Semenov, H.-W. Hübers, D. Henrich, M. Hofherr, K. Il'in and M. Siegel, IEEE Trans. Appl. Supercon., **23** (2013), 2300505.

[10] A. Semenov, A. Engel, H.-W. Hübers, K. Il'in and M. Siegel, Eur. Phys. J. B, **47** (2005), 495.

[11] A. Schilling, M. Willemin, C. Rossel, H. Keller, R. A. Fisher, N. E. Phillips, U. Welp, W. K. Kwok, R. J. Olsson and G. W. Crabtree, Phys. Rev. B **61** (2000), 3592.

[12] E. Zeldov, D. Majer, M. Konczykowski, V. B. Geshkenbein, V. M. Vinokur and H. Shtrikman, Nature **375** (1995), 373.

[13] C. J. Bowell, R. J. Lycett, M. Laver, C. D. Dewhurst, R. Cubitt and E. M. Forgan, Phys. Rev. B **82** (2010), 144508.

[14] G. P. Mikitik and E. H. Brandt, Phys. Rev. B **64** (2001), 184514.

[15] J. Kierfeld, Phys. Rev. B **69** (2004), 024501.

[16] M. J. W. Dodgson, V. B. Geshkenbein, H. Nordborg and G. Blatter, Phys. Rev. B **57** (1998), 14498.

[17] O. Bossen and A. Schilling, Physica C **483** (2012), 201.

[18] A. Schilling, H. Grundmann and R. Dell'Amore, Journal of Physics: Conference Series **400** (2012), 032081;
A. Schilling and H. Grundmann, Annals of Physics **327** (2012), 2301.

[19] A. A. Aczel, H. A. Dabkowska, P. R. Provencher and

G. M. Luke. Journal of Crystal Growth, **310** (2008), 870;
M. Kofu, H. Ueda, H. Nojiri, Y. Oshima, T. Zenmoto, K. C. Rule, S. Gerischer, B. Lake, C. D. Batista, Y. Ueda and S.-H. Lee, Phys. Rev. Lett., **102** (2009), 177204.

[20] E. Cuno and H. Müller-Buschbaum, Z. anorg. allg. Chemie, **572** (1989), 95; A. A. Aczel, Y. Kohama, C. Marcenat, F. Weickert, M. Jaime, O. E. Ayala-Valenzuela, R. D. McDonald, S. D. Selesnic, H. A. Dabkowska and G. M. Luke, Phys. Rev Lett., **103** (2009), 207203.

[21] H. Grundmann, A. Schilling, C. A. Marjerrison, H. A. Dabkowska and B. D. Gaulin, under review in Material Research Bulletin.

[22] V. Zapf, D. Zocco, B. R. Hansen, M. Jaime, N. Harrison, C. D. Batista, M. Kenzelmann, C. Niedermayer, A. Lacerda and A. Paduan-Filho, Phys. Rev. Lett., **96** (2006), 077204.

[23] K. Huang and H. F. Meng, Phys. Rev. Lett., **69** (1992), 644.

[24] A. Rakhimov, S. Mardonov, E. Ya. Sherman and A. Schilling, New J. Phys., **14** (2012), 113010.

[25] S.-Y. Xu, *et al.*, ArXiv e-prints 1101.3985, (2011).

[26] L. Shelimova, P. Konstantinov, M. Kretova, E. Avilov and V. Zemskov, Inorganic Materials, **40** (2004), 461.

[27] V. Kuznetsov, L. Kuznetsova, D. Rowe, J. Appl. Phys., **85** (1999), 3207.

[28] F. von Rohr, A. Schilling and R. J. Cava, J. Phy.: Cond. Matt., **25** (2013), 075804.

15 Surface Physics

T. Greber, M. Hengsberger, J. H. Dil, F. Matsui, P. Krüger, R. Westerström, L. Castiglioni, H. Cun, B. Slomski, S. Roth, A. Hemmi, G. Landolt, M. Greif, R. Stania, C. Bernard, L. H. de Lima, S. Muff, A. Schuler, F. Dahinden, R. Rüttimann, T. Kälin, J. Osterwalder

The group investigates surface and interface phenomena at the atomic level. For this purpose the surface physics laboratory is well equipped for the preparation and characterization of clean single-crystalline surfaces, metal and molecular monolayer films, as well as covalently bonded single layers, using a wide variety of experimental techniques. In addition to a well equiped laboratory at UZH-Irchel, we currently operate a custom-built end station for spin- and angle-resolved photoemission spectroscopy (SARPES) at the nearby Swiss Light Source (SLS), and we take an active role in the construction and commissioning of the new SLS beamline PEARL (PhotoEmission and Atomic Resolution Laboratory). Moreover, within the NCCR 'Molecular Ultrafast Science and Technology' (MUST), our group has built and commissioned a compact and mobile angle-resolved photoemission instrument, which is currently taking data at the attosecond laser facility in the laboratory of U. Keller at ETHZ[1].

The research carried out during the report period can be grouped into four topics:

- Monolayer films of hexagonal boron nitride (*h*-BN) and graphene on metal surfaces

  Over the last several years the group has built up a considerable expertise in the growth and characterization of sp^2-bonded monolayers on transition metal surfaces. On the one hand, our interest is fueled by the chemical functionality of the adlayers: on Rh(111) and Ru(0001) surfaces, the large lattice misfit induces strongly corrugated sp^2 layers that exhibit also a corrugation in the electrostatic potential landscape that can be exploited for templating molecular adsorbates [2–5]. As a new feature, we could show in this last year that this templating functionality applies also to species intercalated between the sp^2 layer and the metal substrate, induced by gentle ion implantation (see Section 15.1).

  A second line of research is directed towards the synthesis of epitaxial layers of graphene and *h*-BN with a view on future electronic devices based on graphene. Due to its insulating properties and similar crystal structure and lattice constant, *h*-BN appears to be the ideal 'gate oxide'. We have succeeded in growing single-layer graphene on top of single-layer *h*-BN on Cu(111). The two layers are well aligned, but each one maintains its own lattice constant. This leads to the observation of a well defined moiré pattern in scanning tunneling microscopy images, and to the effective decoupling from the substrate of the electrons in the graphene layer (paper submitted).

  Within a Sinergia project of the Swiss National Science Foundation we have built up a growth chamber for handling wafer-size samples, where *h*-BN or graphene films can be grown on four-inch Si(111) wafers covered with monocrystalline Rh(111) films. The chamber is placed in a dedicated clean-room, which enables us to process these samples in a dust-free environment. We are currently working on peel-off methods for producing free-standing mono- or multilayer films of graphene or h-BN on the centimeter scale.

- Molecular adsorbates and molecular monolayers

  One focus here is on endofullerenes that can be viewed as spin shuttles. Samples of $DySc_2@C_{80}$ molecules, obtained from L. Dunsch of the IWF Dresden, show long spin relaxation times at a temperature of 2K [6]. These studies have been extended to other rare earth-nitride cluster endofullerenes, using SQUID and x-ray magnetic circular dichroism measurements.

  An important aspect in designing functionalities in molecular layers is the structure-function relationship. This pertains to magnetic, catalytic and photochemical properties of such layers. Within the NCCR MUST, we are therefore developing the method of ultra-violet photoelectron diffraction for measuring the structure of adsorbed molecules. A study of a monolayer of Sn-phthalocyanine on Ag(111) demonstrates the structural sensitivity of the method (see Section 15.3). In combination with pump-probe experiments using high-harmonic laser pulses, we hope to be able to follow the structural dynamics of adsorbed molecules upon photo-excitation.

- Spin-orbit effects at surfaces

  Our spin-resolved photoemission chamber

(COPHEE) at the SLS has continued to be in high demand as a general user instrument due to its unique performance. The investigations of the Rashba effect in ultrathin Pb films on Si(111) were completed (PhD thesis of B. Slomski), addressing also combined effects of spin-orbit coupling and hybridization between different quantum well states, and their consequences for the spin texture in momentum space. The studies of materials with non-centrosymmetric structure that show a pronounced spin splitting also in bulk electronic states (see Section 15.2) were extended to include also BiTeCl. In collaboration with the group of A. Schilling, the ARPES experiments of the topological insulators of composition $GeBi_{4-x}Sb_xTe_7$ were completed.

- Ultrafast processes at surfaces
  With the MUST photoemission spectrometer attached to the attoline in the group of U. Keller, first traces of sub-femtosecond dynamics have been recorded. In particular, RABBITT (Reconstruction of Attosecond Beating By Interference of Two-photon Transitions) traces could be taken for the first time from a solid surface, and concurrently also from a gas target. In this method, photoelectron spectra are recorded while the surface of an Ag(111) or Au(111) sample is hit by a femtosecond infrared laser pulse and an XUV attosecond pulse train with variable time delay. From such data we hope to gain insight into the dynamical processes involved in electron emission from surfaces. Within two student's projects, two time-resolved optical spectroscopy experiments have been built up in our home laser laboratory: surface second harmonic generation (bachelor thesis, F. Dahinden) and absorption spectroscopy (master thesis, A. Schuler).

[1] See http://www.ulp.ethz.ch/research/Attoline.
[2] S. Berner *et al.*, Angew. Chem. Int. Ed. 46, 5115 (2007).
[3] J. H. Dil *et al.*, Science 319, 1824 (2008).
[4] T. Brugger *et al.*, Phys. Rev. B 79, 045407 (2009).
[5] A. J. Pollard *et al.*, Angew. Chem. Int. Ed. 49, 1794 (2010).
[6] R. Westerström *et al.*, J. Am. Chem. Soc. 134, 9840 (2012).

In the following, three highlights of last year's research are presented in more detail.

15.1 Capturing single argon atoms in boron nitride nanotents

In collaboration with Marcella Iannuzzi, Jürg Hutter, Physikalisch Chemisches Institut, Universität Zürich.

At room temperature, it is very difficult to immobilize single atoms, in particular the least reactive noble gases. Ion implantation into a crystal lattice possesses this capability, but the randomness of the involved processes does not permit much control over their distribution within the solid. However, with the assistance of single layers of hexagonal boron nitride (*h*-BN) or graphene, site-selective immobilizing of atoms at surfaces becomes feasible. The *h*-BN nanomesh [1] is a corrugated single layer with a 3.2 nm honeycomb superstructure formed on a Rh(111) surface [2]. Due to the lattice misfit between *h*-BN and Rh, and the preference of nitrogen to bond on top of Rh, the superstructure features two different bonding areas, the 'pores', where the *h*-BN forms chemical bonds with the substrate, and the 'wires' where the *h*-BN has a pure van der Waals bonding to the substrate. Fig.15.1 shows that after Ar implantation, the nanomesh can trap individual argon atoms at room temperature at distinct subsurface sites to form "nanotents".

For Ar implantation, a kinetic energy window (about 20-60 eV) has been identified where the argon ions can penetrate the *h*-BN layer but not enter the Rh lattice. Scanning tunneling microscopy and photoemission data show the presence of argon atoms at two distinct sites (wire crossing sites WXA and WXB in Fig. 15.2B) within the nanomesh unit cell. Fig. 15.2A shows Ar

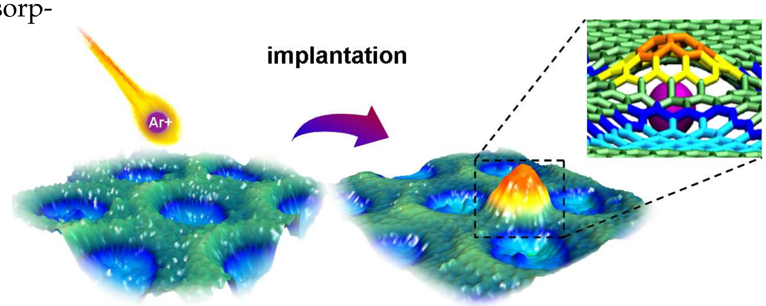

FIG. 15.1 – Nanotent formation by Ar ion implantation (the orange peak) beneath a corrugated monolayer of hexagonal boron nitride. 3D rendered scanning tunneling microscopy images demonstrate one Ar atom implanted beneath the *h*-BN monolayer at a wire crossing site. The purple sphere represents the Ar atom. The *h*-BN wire- and pore- regions are indicated with green and blue color, respectively. The image in the upper right corner is the simulated 3D view of an Ar nanotent.

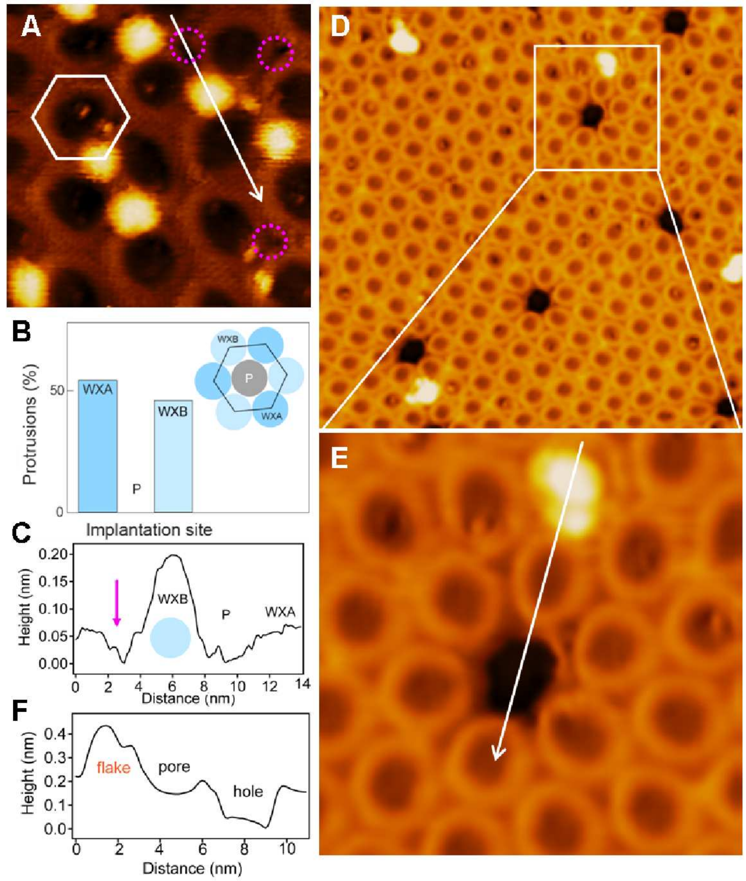

Fig. 15.2 –
Ar implantation and "can-opener" effect.
(A) Atomic-resolution STM image demonstrating Ar implantation beneath the *h*-BN wires (11.4×11.4 nm^2, U = -1.10 V, I = 0.10 nA). The bright protrusions are caused by implanted Ar, and the pink circles indicate vacancy defects generated by the Ar penetration. The hexagon represents the honeycomb supercell, also shown in the inset of (B).
(B) Statistics illustrates the selectivity of the process: Ar stops at two distinct sites beneath nanomesh wire crossings (WXA and WXB), but not in the pores (P).
(C) Cross section along the line in (A) with salient features indicated.
(D) STM image (46×46 nm^2) shows 2 nm holes at pore sites after annealing to 900 K.
(E) High-resolution image (14×14 nm^2, U = -1.10 V, I = 0.50 nA) showing a hole and a flake.
(F) Cross-sectional profile along the line in (E), showing the height difference between the flake and the hole.

atoms implanted beneath the *h*-BN wires as bright protrusions with a large footprint. The two configurations are confirmed by density functional theory calculations - they are metastable. Remarkably, these "nanotents" are predicted to capture up to six Ar atoms, and to be stable in air.

Annealing of implanted structures to 900 K induces the formation of highly regular holes of 2 nm diameter in the *h*-BN layer, with flakes of the same size found near the holes on the surface (Fig. 15.2D-F) [3]. We propose that this "can-opener" effect is due to vacancy defects, generated during the penetration of the Ar ions through the *h*-BN lattice, and their propagation along the rim of a nanomesh pore where the *h*-BN lattice is highly bent. The implantation effects are robust and quite general: they are also observed in graphene on ruthenium and for neon atoms.

[1] M.Corso *et al.*, Science 303, 217 (2004).
[2] S. Berner *et al.*, Angew. Chem. Int. Ed. 46, 5115 (2007).
[3] H. Y. Cun *et al.*, Nano Lett., DOI:10.1021/nl400449y (2013).

15.2 Disentangling surface and bulk Rashba effects in BiTeI

In collaboration with Evgueni V. Chulkov, Departamento de Fisica de Materiales, Donostia International Physics Center, 20080 San Sebastian, Spain; Vladimir N. Strocov, Swiss Light Source, Paul Scherrer Institut, 5232 Villigen, Switzerland; Imamaddin R. Amiraslanov, Physics Institute, Azerbaijan National Academy of Science, AZ1143 Baku, Azerbaijan.

In non-magnetic materials the time-reversal symmetry implies that the electronic band structure is inversion symmetric with respect to the origin in momentum-space. If the material is also inversion symmetric in real space, Kramers theorem applies, which states that all the electronic states in a crystal are spin-degenerate under these conditions, even in the presence of spin-orbit interaction (SOI). An important branch of research in *spintronics* is the hunt for materials in which this Kramers degeneracy is lifted, because they would support the production and the control of spin currents and to eventually realize spin-based logical devices.

The two ingredients for the occurrence of spin-split states in non-magnetic materials are a strong SOI and a broken inversion symmetry. At crystal boundaries, i.e. at surfaces or interfaces, the inversion symmetry is naturally absent and the so-called Rashba effect [1] can oc-

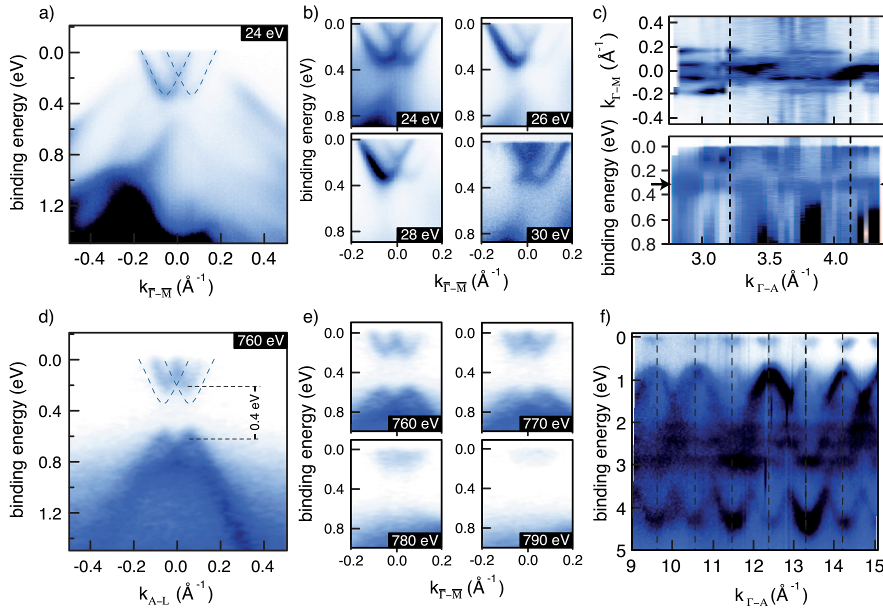

Fig. 15.3 –
Bulk and surface states of BiTeI.
(a) Ultra-violet ARPES band map revealing the presence of surface states.
(b-c) Their two-dimensional character is confirmed by photon energy dependent ARPES.
(d) Soft X-ray ARPES band map showing the large Rashba spin splitting of the bulk bands.
(e-f) Photon energy dependent band maps show strong dispersion and confirm the three-dimensional character of the bulk states.

cur, where the SOI leads to a linear-in-k energy splitting of free-electron-like dispersing states.

When magnetism is absent, the electronic *bulk* states can only be non-degenerate if the crystal unit cell itself lacks inversion symmetry. Such a bulk spin splitting is known to occur in noncentrosymmetric zinc blende and wurzite structures [2], though on a fairly small energy scale. Recently, the semiconductor BiTeI was predicted to feature a strong SOI and a large Rashba effect in the bulk bands, i.e. the occurrence of two momentum-split parabolic bands at the band edge [3]. We have performed the first angle-resolved photoemission spectroscopy (ARPES) measurements of the bulk band structure of this material [4].

BiTeI has a hexagonal crystal structure and is built up of alternating layers of bismuth, tellurium, and iodine atoms stacked along the hexagonal axis. The continuous stacking order of the layers of the three atomic species breaks the inversion symmetry.

Because of the broken inversion symmetry and the weaker bonding between the tellurium and iodine layers, an untwinned BiTeI crystal has two different terminations either purely formed of I or Te atoms, depending on the crystal face forming the surface.

Calculations in the framework of the density functional theory (DFT), performed by the group of E.V. Chulkov, predict the existence of two-dimensional surface states on the two possible surfaces. In order to disentangle the surface and the bulk contributions to the electronic structure we performed ARPES measurements in the ultra-violet (UV-ARPES) and the soft x-ray photon energy regime (SX-ARPES). In UV-ARPES, photoemission from the surface states is dominant over bulk state emission, while the latter is emphasized in the more bulk sensitive SX-ARPES.

The UV-ARPES measurements of Fig. 15.3a show the coexistence of both, the spin-split electron-like (Te-termination) and hole-like (I-termination) surface state, indicating surfaces with mixed terminations. The photon energy dependent UV-ARPES measurements in Figs. 15.3b-c exhibit no k_z dispersion (along the sample surface normal) which confirms the two-dimensional character of the observed states. For comparison Fig. 15.3d shows SX-ARPES maps of the near-gap bulk valence and conduction bands and confirms the predicted large bulk Rashba effect. The photon energy dependent SX-ARPES measurements in Fig. 15.3e-f exhibit clear k_z dispersion, commensurate with the bulk Brillouin zone, and confirm the three-dimensional bulk character of the measured states.

The soft X-ray photon energy scan of the bulk Fermi surface in Fig. 15.4a is in excellent agreement with the DFT calculations (Fig. 15.4b) and completes the picture of the complex bulk Fermi surface. Figure 15.4c illustrates the three-dimensional Fermi surface, which takes the shape of a spindle-torus distorted according to the crystal symmetry. When the chemical potential is tuned below the degeneracy point at the A point, the Fermi surface undergoes a topological transition to a regular torus. Such a toroidal, single-spin Fermi surface has unique properties and may open a pathway for the realization of exotic physical phenomena.

[1] Y. A. Bychkov and E. I. Rashba, J. Phys. C: Solid State Physics, 17, 6039 (1984).

[2] G. Dresselhaus, Phys. Rev. 100, 580 (1955).

[3] K. Ishizaka, Nature Materials 10, 521 (2011).

[4] G. Landolt, Phys. Rev. Lett. 109, 116403 (2012).

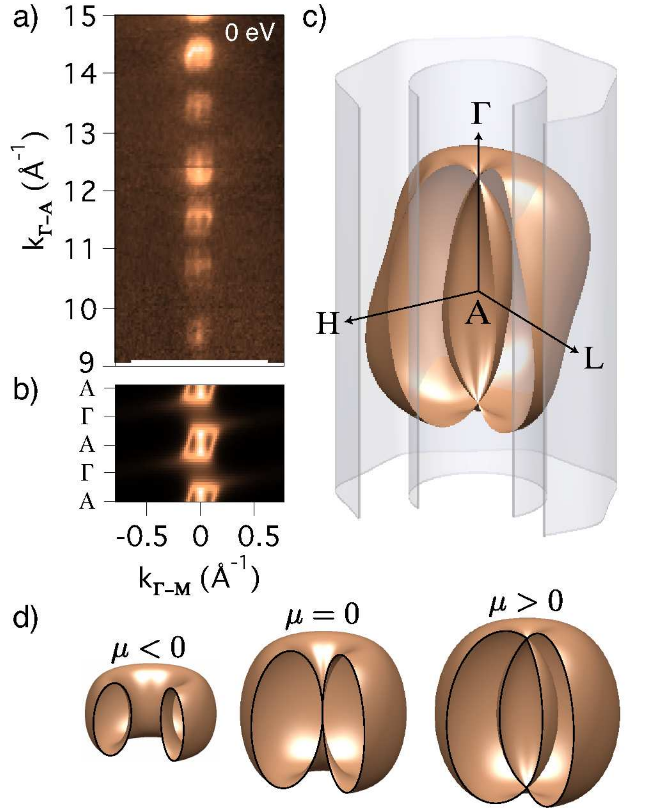

Fig. 15.4 –
(a) Soft X-ray ARPES bulk Fermi surface map.
(b) Bulk Fermi surface calculated by DFT.
(c) Schematic representation of the three-dimensional spindle-torus-like Fermi surface of the bulk states (orange) and the k_z-independent Fermi surface of the electron-like surface state (gray).
(d) Topological transition of the toroidal bulk Fermi surface as a function of the chemical potential.

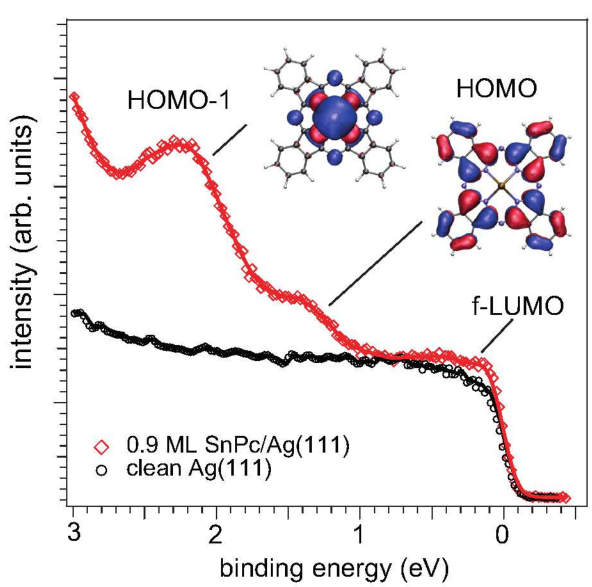

Fig. 15.5 – UPS spectra near the Fermi energy of pristine Ag(111) (black) and 0.9ML SnPc/Ag(111) (red) showing the highest occupied molecular orbital (HOMO) states beside the real-space charge distribution of the corresponding orbitals.

15.3 Photoelectron diffraction from Sn-phthalocyanine

In collaboration with Peter Krüger, Université de Bourgogne, 21078 Dijon, France; Markus Meuwly, University of Basel, 4056 Basel.

In photoemission from solid surfaces the outgoing photoelectron wave is coherently scattered at atoms in the close vicinity of the source atom. The direct and scattered waves generate an interference pattern, which contains information about the coordination of the emitter atom [1] and the spatial extent of the orbital from which the electron is emitted [2, 3]. Excited with EUV light (10-100 eV) this method is termed ultra-violet photoelectron diffraction (UPD), in the case of x-rays XPD. In both experiments, the photoemission intensity at fixed kinetic energy is recorded as function of emission direction. From the photoelectron spectrum the initial state can be chosen as shown in Fig. 15.5.

While UPD offers significant advantages in view of time-resolved measurements over the more established x-ray variant, the interpretation of the data is more difficult due to the higher complexity of the molecular initial states. Therefore, we engaged in a close collaboration with theory groups. The idea is to compute first the atomic and electronic structure for the molecule adsorbed on the surface using DFT, and then the evolution of the molecular state by means of Molecular Mechanics calculations [4]. The computed trajectories serve as input for scattering calculations, which allow the UPD patterns to be simulated and compared to experiments [3].

In order to demonstrate the capabilities of photoelectron diffraction in terms of molecular structure determination and tracking of transient structural changes, we applied XPD and UPD to a rather complex surface system: Sn-phthalocyanine (SnPc) molecules adsorbed on Ag(111) [5]. It was previously shown that SnPc grows layer-by-layer with the molecules lying flat on the Ag(111) surface [6]. At sub-monolayer coverage the adlayer has different structural phases, which are associated with a conformational change of the SnPc molecule. Conformations with the Sn atom on top of the molecular plane (*tin-up*) or with the Sn atom beneath the molecular plane (*tin-down*) were identified. The different geometrical phases can be tuned via temperature changes. The measurements show that the non-planar molecules undergo flattening upon adsorption.

In our experiments, XPD patterns were recorded from the Sn 3*d* core level and compared to single-scattering-cluster (SSC) calculations. The flattening of the molecule could be corroborated, and the azimuthal orientation obtained from XPD was in good agreement with values from scanning tunneling microscopy [9]. In photoemission [7] and DFT studies [8] it was found that the second highest occupied molecular orbital (HOMO-1) plays an important role in the chemical bonding of molecules and substrate. The HOMO-1 is of mainly p_z-character and is localized at the central Sn atom, as can be seen in the inset of Fig. 15.5. UPD measurements taken from the HOMO-1 are shown in Fig. 15.6. Again, the outcome was compared to SSC calculations and reasonable agreement was found between experiment and theory when the incommensurate ordering and the three rotational domains were taken into account (Fig. 15.6). This is surprising because at low energies multiple scattering is known to strongly influence the interference patterns. The upgrade to multiple scattering calculations for computing the electronic structure *and* the scattering patterns are part of ongoing work.

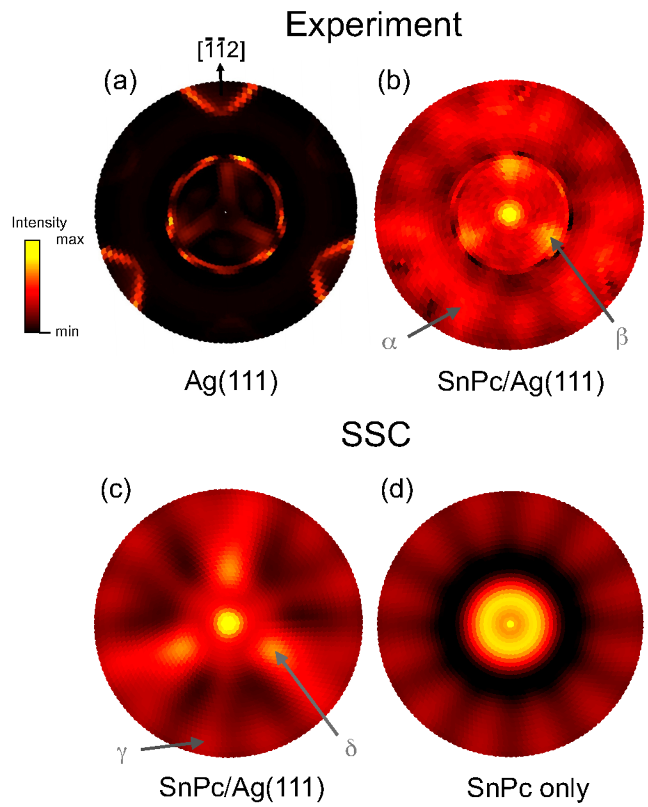

FIG. 15.6 – UPD taken with EUV light (21.2 eV) from the HOMO-1.
(a) Pattern taken from the Ag(111) substrate at the corresponding energy.
(b) Measured UPD pattern from the HOMO-1 at a coverage of 0.9 ML.
(c) SSC calculation of the pattern from a single molecule, averaging over many local registries with the Ag(111) surface due to the incommensurate adsorbate layer, and over the three rotational domains. Arrows indicate corresponding features.
(d) SSC calculation of the pattern from a single, free-standing molecule, averaged over three rotational domains.

[1] J. Osterwalder *et al.*, Chimia 60 (2006) A795.

[2] P. Puschnig *et al.*, Science 326, 702 (2009).

[3] P. Krüger, F. Da Pieve, and J. Osterwalder, Phys. Rev. B 83 (2011) 115437.

[4] I. Tubert-Brohmann, M. Schmid, and M. Meuwly, J. Chem. Theory Comput. 5 (2009) 530.

[5] M. Greif *et al.*, Phys. Rev. B 87, 085429 (2013).

[6] C. Stadler *et al.*, Nature Phys. 5, 153 (2009).

[7] M. Häming, C. Scheuermann, A. Scholl, F. Reinert, and E. Umbach, J. Elec. Spec. Rel. Phen. 174, 59 (2009).

[8] J. D. Baran and J. A. Larsson,J. Phys. Chem. C 116, 9487 (2012).

[9] M. Toader and M. Hietschold, J. Phys. Chem. C 115, 3099 (2011); *ibid.* 115, 12494 (2011).

16 Physics of Biological Systems

Conrad Escher, Hans-Werner Fink, Patrick Helfenstein (until 12.2012), Alina Horwege (until 10.2012), Tatiana Latychevskaia, Jean-Nicolas Longchamp, Mirna Saliba, Jonas Verges (since 01.2013), and Flavio Wicki

In collaboration with: Prof. Philippe Dumas, CNRS Strasbourg (France); Eugen Ermantraut, Clondiag Chip Technologies GmbH (Germany); Prof. Bruno Klaholz, University of Strassbourg (France); Prof. Jannik C. Meyer, University of Vienna (Austria); Prof. Ute Kaiser, University of Ulm (Germany); Dr. Ilona Müllerová and Dr. Luděk Frank, Institute of Scientific Instruments, Brno (Czech Republic); Dr. Soichiro Tsujino, PSI (Switzerland); Dr. Fabio Lamattina and Dr. Ivan Shorubalko, EMPA Dübendorf (Switzerland)

The structural investigation of individual biological objects by employing coherent low-energy electrons is the primary goal of our research. It involves in-line holography with low energy electrons, Fourier transform holography as well as coherent diffraction imaging and is assisted by micro-structuring techniques using a focused gallium ion beam as well as a focused helium ion beam available to us at the Swiss Federal Laboratories for materials science and technology (EMPA) in Dübendorf. Our current activities are divided in the following interconnected individual projects:

- Electron Holography and Coherent Diffraction
  Major experimental challenges are to improve the interference resolution, establish methods for creating free standing thin carrier films of graphene transparent for low-energy electrons as well as appropriate techniques to present a single protein to the coherent electron wave front. Next to these technical issues, a second, equally important requirement for achieving high resolution structural information is the reconstruction of the electron holograms; i.e., the iterative phase retrieval in coherent diffraction. This is achieved by developing numerical algorithms for the integrals governing these coherent optics problems.

- Fourier Transform Holography (FTH)
  FTH with low-energy electrons is a high resolution lens-less imaging method based on the use of an extended reference where a specimen of biological or non-biological nature is non-destructively imaged. The recording is performed by illuminating the specimen and reference object or pinhole with a parallel beam of low-energy electrons. The interference between the wave scattered by the specimen and the reference wave results in a holographic diffraction pattern. Its Fourier transform represents the autocorrelation of the transmission function of the specimen under study.

- Electron and Ion Point Sources
  Field Ion Microscopy and related techniques are employed when fabricating or operating novel electron and ion point sources. In collaboration with PSI, field emitter arrays are characterised and specified for their use as bright electron sources for the X-Ray Free Electron Laser (XFEL) project.

- DNA and Proteins in liquids
  The aim is to directly observe the dynamics of single DNA molecules in liquids by video fluorescent microscopy. In combination with molecular anchoring techniques, adopted from Clondiag Chip Technologies in Jena, we also address the energetics of the molecule. We designed DNA modifications for attaching fluorescent proteins which shall help us to obtain structural information about proteins in vacuum using electron holography and coherent diffraction. Thermal desorption spectroscopy of water from fluorescent proteins shall help us to judge under what thermal conditions proteins remain in their native state in a vacuum environment.

Selected recent achievements referring to the past year shall be discussed in some more detail below.

16.1 Coherent Diffraction Imaging (CDI)

Most of the protein structural information available today has been obtained from crystallography experiments by means of averaging over many molecules assembled into a crystal. Since biological molecules exhibit different conformations, averaging smears out structural details. That is why a strong desire to gain structural data from just a single molecule is emerging. Electrons with kinetic energies below 200 eV are the only radiation known today where elastic scattering dominates. Radiation damage-free imaging of a single biological molecule is thus possible by recording holograms and coherent low-energy electron diffraction patterns [1].

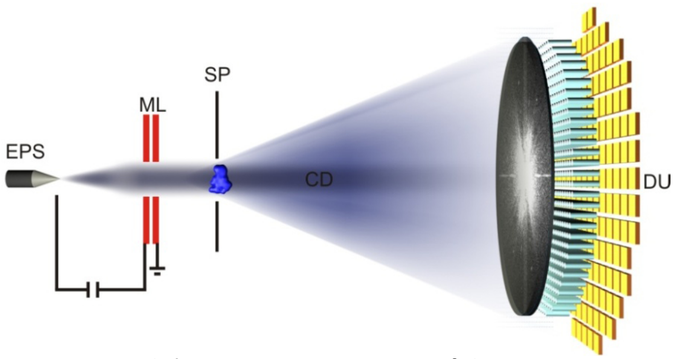

FIG. 16.1 – Schematic representation of CDI.
EPS: coherent electron point source
ML: low-aberration micro-lens to form a parallel electron wavefront
SP: sample embedded inside the coherent electron beam
CD: coherent diffraction pattern
DU: electron detector unit with high spatial resolution and fulfilling the oversampling condition.

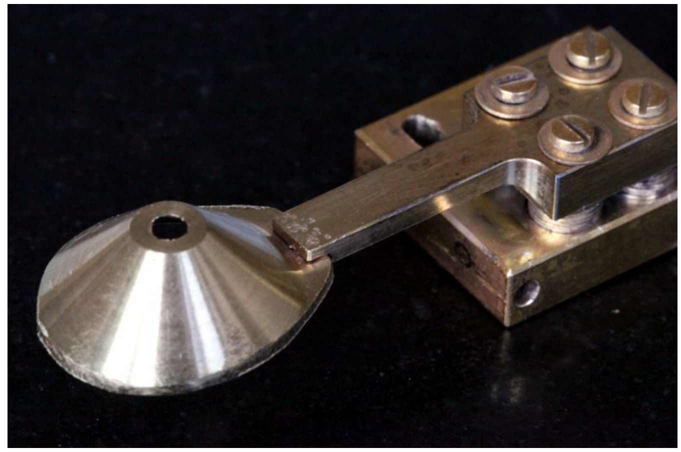

FIG. 16.2 – Dedicated sample holder to guarantee almost zero-field conditions between sample and detector. The opening angle of the cone provides a qualitative impression of the very large aperture of this microscope.

16.1.1 Recent experimental achievements

We have embarked upon using the damage-free radiation provided by coherent low-energy electrons to realise CDI and have recently been able to achieve a resolution of 2Å in imaging a freestanding graphene sample. The overall CDI setup is sketched in Fig. 16.1. A sharp tungsten tip acts as an electron point source emitting a coherent spherical wave with kinetic energies between 50 and 300 eV. A micro-lens placed a few microns away from the electron emitter forms a coherent parallel wave that impinges onto a sample some distance behind the lens. At a distant detector, the intensity of the diffraction pattern corresponding to the square amplitude of the Fourier transform of the object is recorded with high spatial resolution. In order to sample this pattern with sufficiently high frequency to match the oversampling requirement, the object must be surrounded by a no-density region.

Our ultra-high vacuum diffraction microscope has been designed and built featuring a dedicated detector system of 75 mm in diameter exhibiting a spatial resolution of about 20 μm. On the ambient pressure side, the fibre optic plate is coupled to a high-resolution CCD chip (Sinar AG, Zurich) with 8000$\times$6000 pixels and a dynamics of 16 bit. As expected, the down-scaling of the electrostatic lens with a 1 micrometer-diameter bore leads to down-scaled spherical aberrations comparable to high end commercial microscopes [2]. By means of this lens, a parallel coherent low-energy wavefront is formed that impinges onto the sample. Since there is no further lens beyond the sample, the numerical aperture of he system can be made wide open without being concerned with growing lens aberrations. In conventional high-resolution TEM, beam-limiting apertures need to be introduced such that the deviation from the optical axes is limited to a few mrad while in our setup 0.5 rad can be easily achieved. In fact, in our setup there is no beam-limiting aperture present but the opening angle is rather given by the detector diameter and the distance from the sample. However, special care needs to be exercised to guarantee an absolute field-free region between sample and detector. First experiments showed slightly asymmetric diffraction patterns and initially we suspected magnetic fields to be the cause. A series of control experiments revealed that rather electrostatic strayfields were resposible for the effect which has now been eliminated by the dedicated sample holder shown in Fig. 16.2. The piece is made from titanium, gold plated, and mounted on a four-axis manipulator enabling accurate centring of the sample in the electron beam.

16.2 Merging Holography and CDI into HCDI

Recently, we revealed the relationship between the hologram and the diffraction pattern of an object, which allows holography and coherent diffraction imaging (CDI) to be combined into a superior technique: holographic coherent diffraction imaging (HCDI). HCDI inherits fast and reliable reconstruction from holography and the highest possible resolution from CDI [3].

16.2.1 The HCDI algorithm

The Fourier transform of an in-line hologram is proportional to the complex-valued object wave in the far-field. This relationship is illustrated for experimental images in Fig. 16.3. The phase distribution of the Fourier transform of the in-line hologram provides the

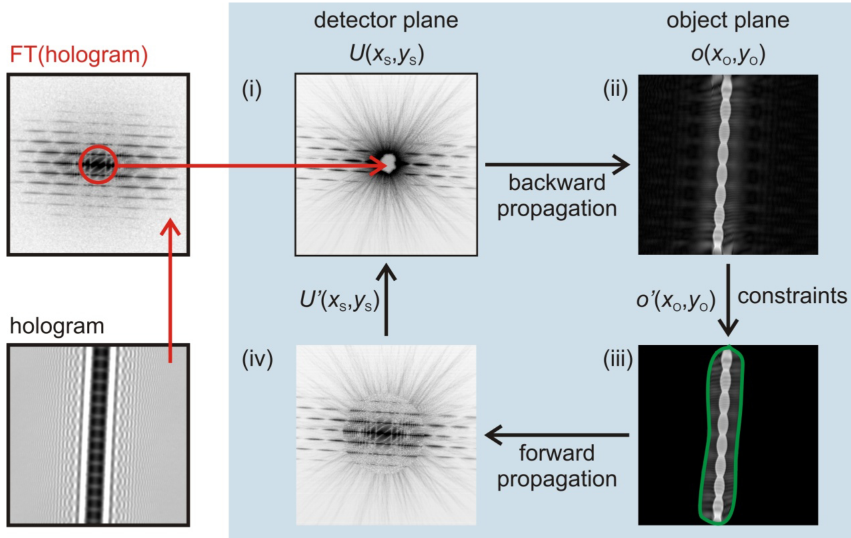

FIG. 16.3 – Illustration describing the iterative reconstruction of a diffraction pattern of an object consisting of two twisted tungsten wires. The iterative loop includes the steps (i)-(iv) as described in the main text.

phase distribution of the object wave in the far-field detector plane. The diffraction pattern is then required to refine the reconstruction of the high-resolution information by a conventional iterative procedure. In addition, the central region of the diffraction pattern, which is usually missing, can be adapted from the amplitude of the Fourier transform of the hologram; see Fig. 16.3. The iterative procedure [4] includes the following steps as also illustrated in the flow-chart diagram in Fig. 16.3:

(i) Formation of the input complex-valued field in the detector plane $U(x_s, y_s)$. After each iteration, the amplitude of the field is given by the square root of the intensity of the diffraction pattern. The amplitude of the central part is provided by the amplitude of the Fourier transform of the hologram. The phase distribution is initially set to the phase of the Fourier transform of the hologram and it is updated after each iteration.

(ii) Back propagation to the object domain by inverse Fourier transform.

(iii) Two constraints are applied to the reconstructed complex-valued object distribution $o(x_o, y_o)$ resulting in a corrected function $o'(x_o, y_o)$. Since the object exhibits a finite size $o(x_o, y_o)$ is multiplied with a loose mask which sets the values outside a certain region to zero, see Fig. 16.3. Since the wave amplitude may not increase in the scattering process [5] the pixel values where absorption would become negative are also set to zero.

(iv) The forward propagation is calculated by the forward Fourier transform of $o'(x_o, y_o)$ and thus the complex-valued wavefront $U'(x_s, y_s)$ in the detector plane is obtained. Its amplitude and phase distributions are the input values for the next iteration starting at step (i).

This novel method for fast and unambiguous phase retrieval has recently been applied to experimental data of freestanding graphene as discussed next.

16.2.2 Graphene unit cell imaging by HCDI

We have shown that coherent diffraction with low-energy electrons allows imaging a freestanding graphene sheet of 210 nm in diameter with 2Å resolution. Ultra-clean graphene was prepared following our patented platinum metal catalysis method [7, 8]. A freestanding graphene sheet is placed over a 210 nm hole ion-milled into a platinum coated SiN membrane of 50 nm thickness. The entire sheet is reconstructed from just a single diffraction pattern displaying the arrangement of more than half a million individual graphene unit cells at once. The sheet is placed over a hole in a silicon nitride membrane and the impinging coherent parallel electron wavefront is formed by a micro-machined electron lens placed in front of the electron point source (see upper left part of Fig. 16.4 which essentially equals Fig. 16.1). The initial phase for the iterative phase refinement (see above) is provided by an in-line hologram of the same sample (Fig. 16.4 bottom left).

What remains to be done is to develop methods for depositing individual clusters onto such graphene sheets and decrease the electron wavelength to about 0.5Å to resolve the atomic structure of a nanometer-sized cluster.

Fig. 16.4 also shows a graphene hologram together with a coherent diffraction pattern of the very same region. In both experimental schemes, the source of the coherent electron beam consists of a sharp W(111) tip mounted on a 3-axis piezo-manipulator for positioning with nanometer precision. For the hologram the tip is brought as close as 380 nm to the sample. For the CDI recording the distance between the electron source and the micro-lens is approximately 8 microns and the distance between lens and sample amounts to approximately 200 microns. The diffraction pattern is recorded

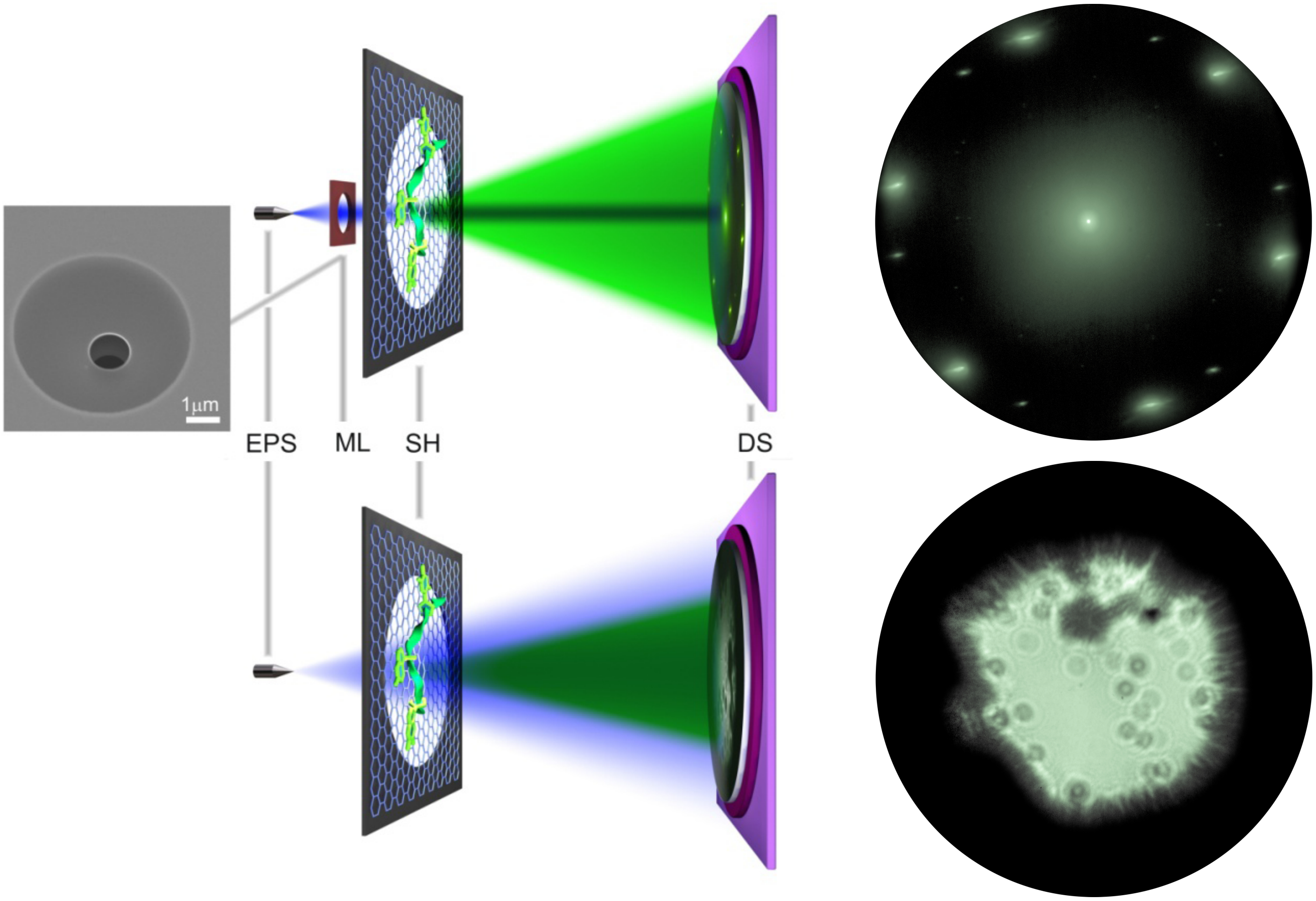

FIG. 16.4 –
Left: experimental arrangements for CDI (top) and holographic imaging (bottom) of freestanding graphene mounted on sample holder SH. See Fig.16.1 as well. The micro-lens (ML) in the CDI setup has a bore of 1 micron (see inset showing a SEM image of the lens). The detector system (DS) consists of a 75 mm diameter micro-channel-plate, followed by a phosphorous coated fibre-optic plate and a 8000×6000 pixels CCD chip.
Right: Images of freestanding graphene of 210 nm diameter resulting from the setups on the left. The diffraction pattern was taken with 236 eV electrons, the hologram with electrons of 58 eV. The outermost spots in the diffraction pattern correspond to 2.13Å as determined by the de Broglie wavelength of the electrons and the impact angle on the detector.

at 68 mm distance with a 8000×6000 pixels CCD chip with 75 mm diameter. The high dynamic range diffraction pattern is built up by combining three diffraction patterns taken with different exposure times. This pattern is then symmetrised by setting the intensity of each pair of centro-symmetric pixels to their average. Next, the diffraction pattern is transformed to spherical coordinates and multiplied with an apodization function to smoothen the edges. The number of pixels per unit cell is enhanced by zero-padding the diffraction pattern to 10,000×10,000 pixels. Accordingly, the hologram reconstruction was resampled to 10,000×10,000 pixels as well.

The overexposed region in the centre of the diffraction pattern is replaced by the corresponding 100 pixels in radius region of the square amplitude of the Fourier transform of the hologram [3]. The reconstruction uses the iterative procedure described in subsection 16.2.1. After 100 iterations, the entire 210 nm diameter freestanding graphene region is recovered with 2Å resolution, sufficient to display roughly 660’000 graphene unit cells (Fig. 16.5 left). Since there is no way to display the entire 10,000×10,000 image here, we have selected six square areas of 5 nm side length. The graphene unit cell is clearly apparent along with defects and domain boundaries present in the graphene sheet as anticipated for CVD grown graphene (Fig. 16.5 right).

To summarise, we have shown that low-energy electrons allow damage-free imaging of a 210 nm diameter graphene sheet with 2Å resolution. A single diffraction pattern, if sampled at a sufficiently high rate, provides a real-space image of more than half a million unit cells at once. Next, this graphene sheet will be used to support nanometer-sized clusters and images will be made with atomic resolution using ~1 keV electrons.

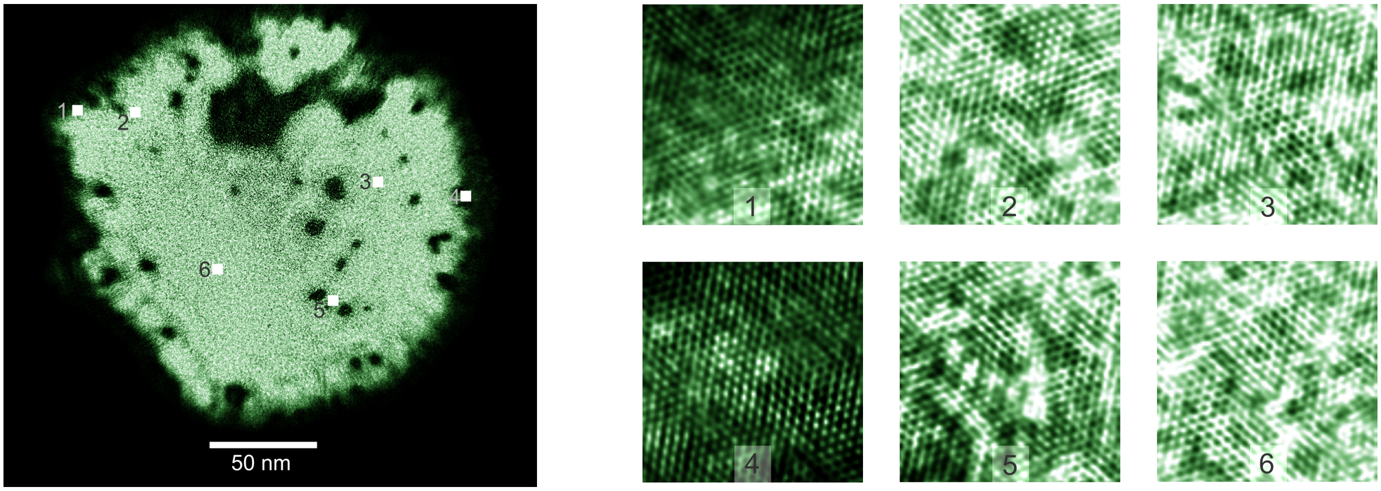

FIG. 16.5 – Left: Reconstruction of a 210 nm diameter freestanding graphene sheet. Expanded views of the six labelled 5×5 nm^2 areas are shown on the right.

16.3 Other recent achievements

- The HIM available at the EMPA enabled us to mill structures with 7 nm feature sizes, a prerequisite for FTH (see introduction) with electrons.
- The successful development of a procedure for a self aligned electron column made up of a micro-lens followed by an Einzel-lens.

16.4 Published results and theses

- A protein attached to a carbon nanotube could be imaged and cross-validated against TEM investigations in which the iron core of the protein (ferritin) could be imaged with high-energy electrons [6].
- A new method to achieve ultraclean freestanding graphene has been patented [7] and published [8].
- Clusters deposited on graphene were imaged by low-energy electron holography [9].
- A relationship between holography and coherent diffraction was found and exploited in an algorithm for fast and unambiguous phase retrieval [3].
- A method to improve the resolution in digital holography by self-extrapolation has been invented [10].
- Pulsed holography has been realised featuring a time resolution in the μs regime [11].
- The unit-cells of freestanding graphene have been imaged by coherent diffraction microscopy [12].
- Bachelor theses
  Jessica Britschgi: *4D Particle Tracking by Optical Holography revealed by manual tracking of microspheres in water from their holographic reconstructions*
  Beat Lauber: *Novel Fourier Transform Holography Setups*
- Master theses
  Simon Schwegler: *Sub-Pixel Registration Methods for Enhancement of Coherent Diffraction Images*
  Niklaus Waldvogel: *Assembly and Characterization of Tungsten Carbide Field Emitters*
  Simon Obrecht: *Thermal Desorption of Water from Green Fluorescent Protein (GFP)*
  Simon Bachmann: *Fabrication and Characterisation of ultra-clean Graphene by platinum metal catalysis* (in progress)

[1] M. Germann *et al.*, Phys. Rev. Lett. 104, 095501 (2010).
[2] E. Steinwand, J.-N. Longchamp, and H.-W. Fink, Ultramicroscopy 110, 1148 (2010).
[3] T. Latychevskaia, J.-N. Longchamp, and H.-W. Fink, Opt. Express 20, 28871 (2012).
[4] J. R. Fienup, Appl. Optics 21, 2758 (1982).
[5] T. Latychevskaia, and H.-W. Fink, Phys. Rev. Lett. 98, 233901 (2007).
[6] J.-N. Longchamp *et al.*, Appl. Phys. Lett. 101, 093701 (2012).
[7] J.-N. Longchamp, C. Escher, and H.-W. Fink, Patent, EP12189601.3 (2012).
[8] J.-N. Longchamp, C. Escher, and H.-W. Fink, J. Vac. Sci. Technol. B 31, 020605 (2013).
[9] J.-N. Longchamp *et al.*, Appl. Phys. Lett. 101, 113117 (2012).
[10] T. Latychevskaia, and H.-W. Fink, Opt. Express 21, 7726 (2013).
[11] M. Germann *et al.*, Appl. Phys. Lett. 102, 203115 (2013).
[12] J.-N. Longchamp *et al.*, Phys. Rev. Lett., Under review (2013).

17 Physical Systems Biology and non-equilibrium Soft Matter

C.M. Aegerter, D. Assmann, D. Eder (since July 2012), G. Ghielmetti, F. Lanfranconi (since February 2013), U. Nienhaus, and T. Schluck

in collaboration with: Institute of Molecular Life Sciences (K. Basler, T. Aegerter-Wilmsen, C. Lehner, S. Luschnig, D. Brunner), ETH Zürich (E. Hafen, P. Koumoutsakos), EPF Lausanne (P. Renaud), University of Lausanne (S. Bergmann), Biozentrum Basel (M. Affolter), University of Strasbourg (N. Rivier), University of Fribourg (A. Jazwinska), University of Konstanz (G. Maret, W. Bührer, T. Sperling, N. Isert), New York University (C.C. Maass), Deutsches Luft- und Raumfahrtzentrum (M. Sperl), University of Twente (A. Mosk), Universite Joseph Fourier Grenoble (S. Skipetrov, F. Graner), Technion Haifa (E. Akkermans).

Work in the group of physical systems biology and non-equilibrium soft-matter is concerned with the study of developmental biology using physical techniques, light transport in turbid media and the dynamics of systems inherently out of thermodynamic equilibrium. In turbid media, we are studying both fundamental problems, such as the transition to Anderson localization with increasing disorder in the scattering medium, as well as application oriented problems such as the development of imaging methods behind turbid structures. In developmental biology, we are partly using these imaging capabilities to study developmental processes in living organisms, and are also concerned with the influence of mechanical forces on developmental processes, e.g. growth. Finally in non-equilibrium systems, we are studying the dynamics of granular gases and foams, in particular in the presence of levitation, such that effects due to gravity can be eliminated and the generic process can be studied. In the last year, we have made considerable progress in several of these areas, two of which are discussed in detail below. These subjects concern the coarsening dynamics of levitated foams and the mechanical control of growth of the wing imaginal disc of Drosophila.

17.1 Coarsening Dynamics in Levitated Foams

Due to the immiscibility of air bubbles and water, a foam is inherently unstable and presents a generic out of equilibrium system [1]. When a foam is left alone, the final state will consist of a separated air and liquid volume. The process leading to this equilibration is called coarsening. In most foams, this process is superimposed by a flow of liquid due to gravity, which will lead to the separation much faster, but this is an inhomogeneous process, due to the stratification in density as a function of height called drainage [2]. Therefore in order to study the process of coarsening, levitated foams are needed, which we achieve by the use of diamagnetic levitation in water nitrogen mixtures in a strong magnetic field gradient [3, 4]. Using a superconducting solenoid, we can apply field up to 20 T onto a sample, leading to field gradients at the edge of the solenoid of the order of 100 T/m. This means that there is a levitation force proportional to $B\partial_z B$, which counteracts the gravitational force [5]. Given the diamagnetic susceptibility of water, the levitation force exactly cancels the gravitational force at an applied field of around 18 T [6]. Thus we can eliminate drainage in the dynamics of foams and purely study the coarsening process. This is of interest, since there are several predictions to the temporal behaviour of these dynamics, as well as a transition with increasing liquid content of the foam [7–9].

The coarsening process consists of a growth of larger bubbles on the expense of smaller ones by gas exchange between these bubbles holding different internal pressures. This (Laplace-)pressure Δp, is proportional to Δp, i.e. to the inverse of its radius, such that small bubbles preferentially blow up bigger bubbles. In dry foams the exchange of gas between bubbles takes place directly through the thin liquid films separating the bubbles[10]. This implies that the gas flow current density $j = \frac{dV}{Adt} \propto dr/dt \propto \Delta p \propto 1/r$. Here, A is the contact area of a bubble which is of order r^2 and V its volume. Solving this, one obtains that the average size of bubbles will increase with time as $\langle r \rangle \propto t^{1/2}$. This can also be derived more rigidly, as for instance done in [11], where strictly speaking the pressure difference between two different bubbles is considered.

When the bubbles are no longer in contact, i.e. at higher liquid fractions exceeding roughly 30% corresponding to the inverse structure of random closed packing, it can be surmised that the mechanism of gas exchange between bubbles will have to change and take place via gas diffusion in the liquid. Here, the diffusive current density $j \propto dr/dt$ will be determined

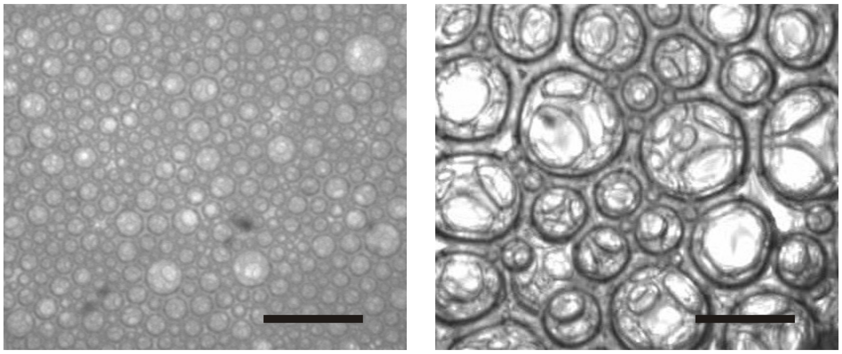

FIG. 17.1 – Images of the surface of the foam chamber showing the absolute size and polydispersity 10 min (left) and 152 min (right) after creation. The scale bars correspond to 1 mm.

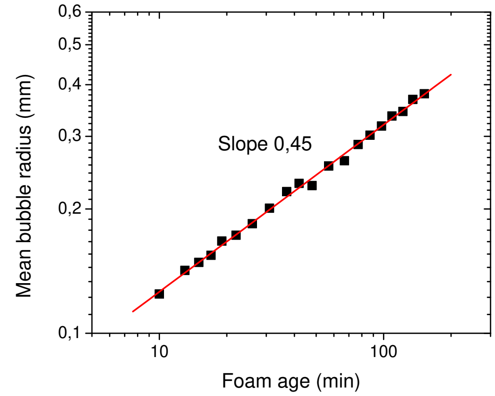

FIG. 17.2 – The mean bubble radius varies in time like $\langle r\rangle \propto t^{\beta}$ with $\beta = 0.45(5)$.

by the gradient of the concentration, i.e. the gradient in pressure difference. This means that we obtain $j \propto dr/dt \propto dp/dr$. Again using the fact that the pressure inside the bubbles is given by Laplace's law, we obtain $dr/dt \propto 1/r^2$ and hence a growth of the form $\langle r\rangle \propto t^{1/3}$. Again, this can be derived studying the detailed dynamics [7]. This qualitatively different type of coarsening is also known as Ostwald ripening and is for instance observed in the dynamics of the growth of inclusions in solids [12]. This transition has also been obtained in simulations of two-dimensional foams considering different liquid fractions[13]. Since levitated foams can be created with a varying amount of liquid and relative stability to drainage, these predictions can thus be tested experimentally with our setup. The foams used in the experiments consist of water, sodium dodecyl sulfate (SDS) as a surfactant and N_2 gas. The water-SDS mixture and the gas are put in two separate syringes, which are connected through a thin tube [14]. An initial liquid fraction of 25% corresponds roughly to an effective liquid fraction of 30%. This can be estimated from the pressure exerted by the foam in the syringes. The polydisperse foam with an average bubble radius of $r_0 \simeq 100\mu m$ (see Figures 17.1 and 17.2) thus created is then transferred to a sample-cell.

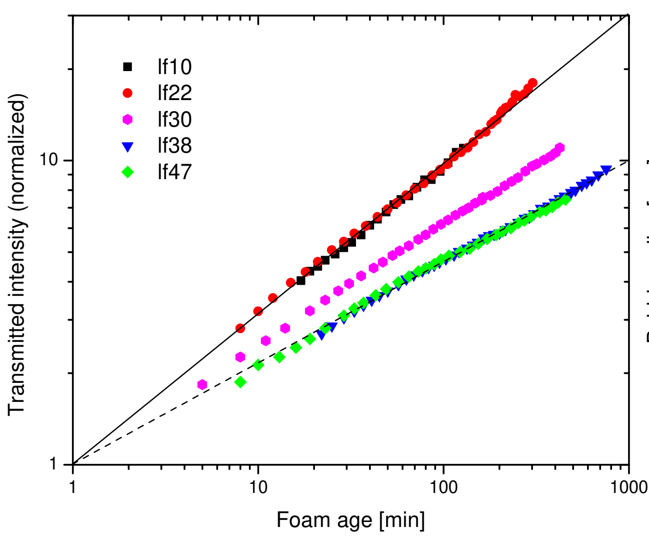

FIG. 17.3 – The bubble size determined via the optical transmittance as a function of foam age is shown for five different liquid fractions. The plot is on doubly logarithmic scales indicating power law dependence of the size with age. Straight lines with a slope of 1/2 (solid) and 1/3 (dashed) indicating the exponents of von Neumann and Ostwald dynamics are added for comparison.

In order to determine the bubble size in the bulk of a three dimensional foam, we use the multiply scattered transmitted intensity through the sample. This intensity is given by Ohm's law, i.e. $T \propto l^*/L$ [15], where L is the thickness of the sample and l^* is the transport mean free path, characterizing the turbidity of the foam. The mean free path of light in the sample has been shown before to give a determination of the bubble size with $l^* \propto r$ [16] for the bulk of the three dimensional foam, since it basically corresponds to the size of a scatterer. Thus we obtain a measure of the bubble size by a determination of the average transmitted intensity, i.e. l^* with foam age, since both the sample thickness and the incident intensity are fixed. In Fig. 17.3, this dependence of l^* with foam age is shown for a set of foams with different liquid content [6]. As can be seen in this double logarithmic plot, all foams show a scaling behavior with a power law increase of bubble size with age, $r \propto t^{\beta}$. At lower liquid fraction, the data are in good agreement with those obtained directly from the surface bubbles shown in Fig. 17.2. For dry foams, this increase shows an exponent close to $\beta = 1/2$, whereas for wet foams shows $\beta = 1/3$. These exponents are the asymptotic dynamics of the theoretical predictions for foam dynamics in the dry and wet case, respectively[7, 8].

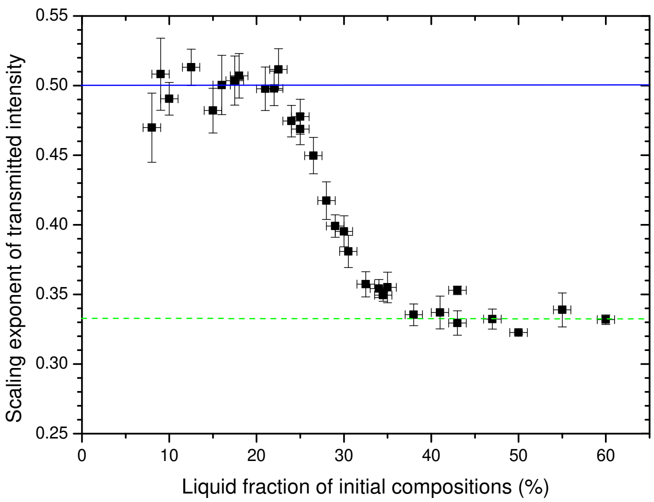

FIG. 17.4 – The bubble growth exponent, β, determined from measurements as those shown in Fig. 17.3 versus liquid fraction. The expectations from von Neumann dynamics, $\beta = 1/2$, and from Ostwald ripening, $\beta = 1/3$ are shown for comparison. The transition region between these two regimes is rather narrow at liquid fractions between 25 % and 35 %.

These results are summarized in Fig. 17.4, where the exponents fitted for all experiments within a large range of liquid fractions is plotted [6]. It can be clearly seen that below a liquid fraction of 25%, the exponents are all compatible with 1/2, whereas above an initial liquid fraction of 35%, they are all compatible with 1/3. Thus there is a clear transition in the coarsening behavior of the foams at a liquid fraction corresponding to the close packing of spheres. Both the transition as well as the values of the exponents are predicted by theory[7, 8].

[1] D. Weaire and S. Hutzler, *The Physics of Foams*, Oxford Univ. Press (1999).

[2] S.A. Koehler *et al.*, Phys. Rev. E **58**, 2097 (1998).

[3] W. Braunbeck, Z. Phys. **112**, 764 (1939).

[4] M.V. Berry and A.K. Geim, Europ. J. Phys. **18**, 307 (1997).

[5] C.C. Maass, N. Isert. G. Maret and C.M. Aegerter, Phys. Rev. Lett. **100**, 248001 (2008).

[6] N. Isert, G. Maret, C.M. Aegerter, EPJE to be published (2013).

[7] W. Ostwald, Z. Phys. Chem. **37**, 385 (1901); I.M. Lifshitz and V.V. Slyozov, J. Phys. Chem. Solids **19**, 35 (1961); C. Wagner, Z. Elektr. Inf.-Energietech. **65**, 581 (1961); A. J. Markworth, Metallography **3**, 197 (1970); W.W.Mullins, J. Appl. Phys. **59**, 1341 (1986).

[8] J. von Neumann, in *Metal Interfaces* (C. Herring ed.), 108 (1952).

[9] A. Saint-Jalmes, S. Marze, M. Safouane and D. Langevin, Microgravity sci. technol. **XVIII**, 5 (2006).

[10] J.Lambert *et al.*, Phys. Rev. Lett. **99**, 058304 (2007).

[11] R.D. MacPhearson and D.J. Srolovitz, Nature (London) **446**, 1053 (2007).

[12] A. Knaebel *et al.*, Europhys. Lett. **52**, 73 (2000).

[13] I. Fortuna *et al.* Phys. Rev. Lett. **108**, 248301 (2012)

[14] A. Saint-Jalmes, M.U. Vera and D.J. Durian, Europ. Phys. J. B **12**, 67 (1999).

[15] P. Sheng, *Introduction to Wave Scattering, Localization and Mesoscopic Phenomena*, Academic Press (1995).

[16] A.S. Gittings, R. Bandyopadhyay and D.J. Durian, Europhys. Lett. **65**, 414 (2004).

17.2 Mechanical regulation of growth in the Drosophila wing disc

The regulation of organ size is a fundamental unsolved question in developmental biology [1]. While a great body of knowledge has been accumulated over the last decades on the genetic control of biochemical pathways, several questions concerning organ growth, in particular that of its cessation, remain unanswered. Organ growth is widely studied on the example of the wing imaginal disc of Drosophila due to the availability of a host of genetic tools [2]. The wing disc is the larval precursor organ that turns into the wing of the adult fly during metamorphosis.

In the past, growth of the wing disc has mainly been studied by the induction of gene expression at early stages in a small number of cells and then studying the final outcome of the process at the end of the third instar stage shortly before metamorphosis [3]. However for a full understanding of the growth and development process, time-dependent studies that can be compared with theoretical models need to be performed. This is what we will describe in the following. Such an investigation has been difficult in the past due to the lack of imaging techniques for the wing disc inside living larvae, which we have developed over the last years [4]. In addition, we have further developed our computational models [5, 6] of the growth process in the wing disc to include not only a description of the elastic properties of the disc on a cell based level [7], but also comb-

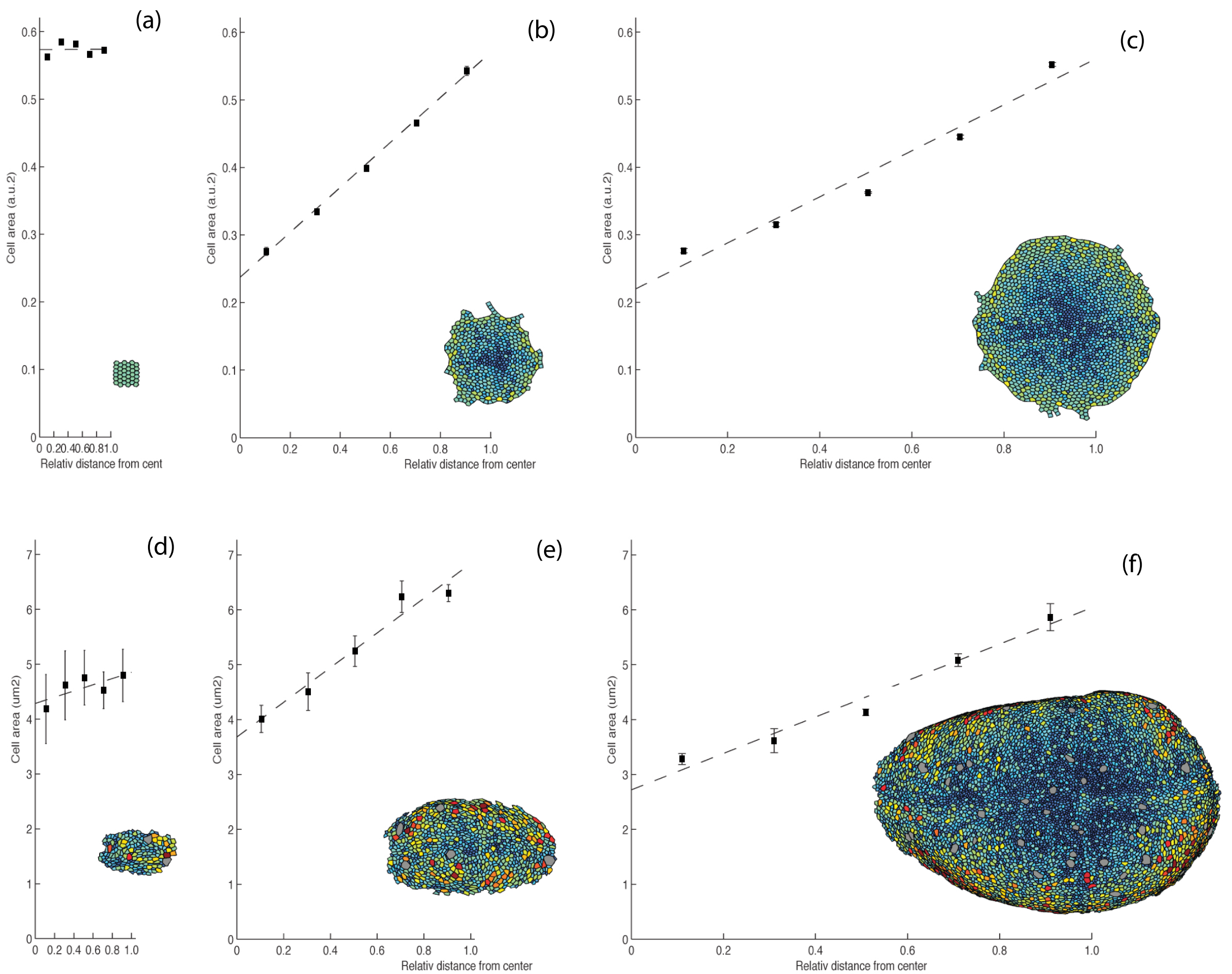

FIG. 17.5 – Comparison of predicted and measured cell area distributions. Our model predicts an initial build-up of a cell area gradient (a, b), which is flattened at later stages (c). The initial conditions (a) are compared with wing discs early in the third instar stage (d), the final simulated distributions (c) with late third instar discs (f). The pouches of the mid third instar discs (e) contain about 4 times less cells than those of the late third instar and are compared with simulated discs (b) that contain roughly the same factor less cells than the final simulated disc. The scale bar corresponds to 10 a.u. for the simulated and 25 μm for the experimental discs. Cells were colored according to their area, ranging from 0(blue) to 1.3(red) a.u.^{2} for the simulated and from 0(blue) to 16(red) μm^2 for the experimental discs. Grey cells are in mitosis and were excluded from the analysis.

ining this with the known key biochemical pathways [8, 9]. With this, we have a detailed model with which to compare to experimental results. The basic premise of the model is that mechanical feedback is used to regulate the growth of the tissue [5, 10, 11]. This means that the addition of material inside the tissue due to cell division leads to the acting of forces on the present cells. In the presence of elastic properties, these mechanical stresses can be stored in the tissue and lead to a change in growth rates of the tissue. In particular, it is assumed that compressed cells grow more slowly and stretched cells grow faster. Using this feedback, the model can explain the cessation of growth when taking into account known biochemical pathways influencing growth as well.

The occurrence of such stresses has been inferred experimentally from birefringence measurements [12], as well as from a characterization of cell-cell interactions based on the proposition that local force balances yield the geometry of the cell shapes in the tissue [13]. Starting from experimental images of cell shapes, [13] solved the inverse problem of force balance, thus determining the local forces and showing that the compressional stress strongly and negatively correlates with the apical area of a cell [13]. In addition, we have determined the local strain tensor has been determined for the tissue. It also shows radial tension in the periphery and compression in the center [8], as shown in Fig. 17.5. In addition to the measure shown in that figure, namely the apical cell area, we have also determined the direction of the deformation, which is tangential in the periphery and radial in the centre.

Using a combination of index matching, larval positioning and confocal microscopy, we are also able to image the entire developmental period of a wing disc within a single live larva [4]. This can be done with cellular resolution, as shown in Fig. 17.6, where the cell outlines are shown for a single wing disc during the time course of 120 hours covering all three larval instar stages. The individual cells can be identified and their apical area, number and topology can be determined for the different stages of development. For instance, we can determine the proliferation rate of cells at different times and correlate them with the forces acting on the cells in the tissue via the determination of the apical cell area. This is an indirect test of the assumption that growth is coupled to the mechanical stresses acting in the tissue. In fact, our detailed model [8] treats the mechanical feedback directly in this way in that the proliferation rate of a cell is given by its apical cell area. The experimental results regarding this are shown in Fig. 17.7, where during all stages of development, there is a clear dependence of the proliferation rate on mechanical force, i.e. apical cell area. This has also been observed in the growth of cell cultures [14].

Thus using in-vivo imaging and computational modelling, we have a full description of the growth process as well as of the forces acting on the tissue in these different stages, where both the distribution of cell areas in the tissue as a consequence of growth as well as the dependence of growth rate on cell area are in good agreement [8]. Finally, we can use in-vivo imaging to study external factor acting on the wing disc during development, which cannot be done using dissected tissues. Here, we have found additional evidence for the importance of mechanical forces on the development of the wing disc [4, 15]. At the time of maximal growth, during the late second instar and the beginning of the third, there are external tensional forces acting on the wing disc, as shown in Fig. 17.8. This again is in good agreement with the assumption of mechanical regulation of growth, In particular with the initial stages, where the biochemical growth factors are not yet fully developed.

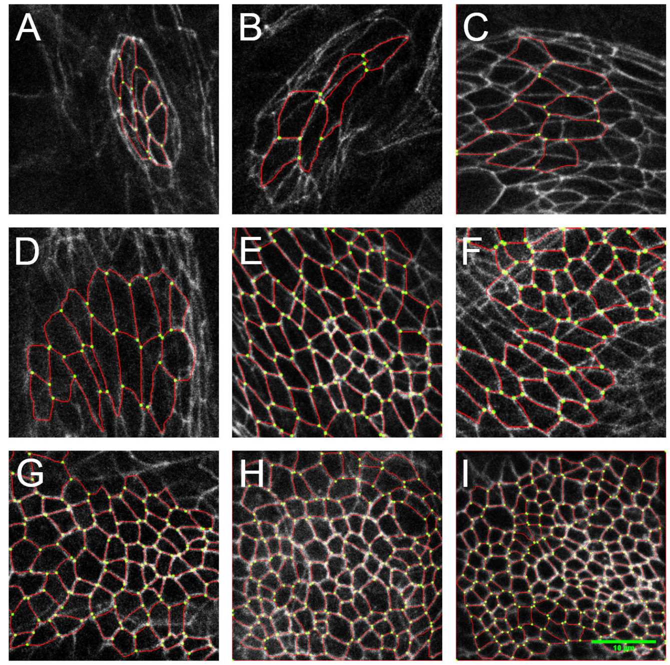

FIG. 17.6 – Cell junction outlines for the same wing disc as a function of time for nine different time points covering the whole of the developmental period spanning five days. The images correspond to time points of: A: 24 h, first instar; B: 32 h, second instar; C: 48 h; D: 56 h; E: 72 h; F: 80 h, third instar; G: 96 h; H: 104 h; and I: 120 h. The scale bar denotes 10 μm. Identified cell outlines are superimposed in red.

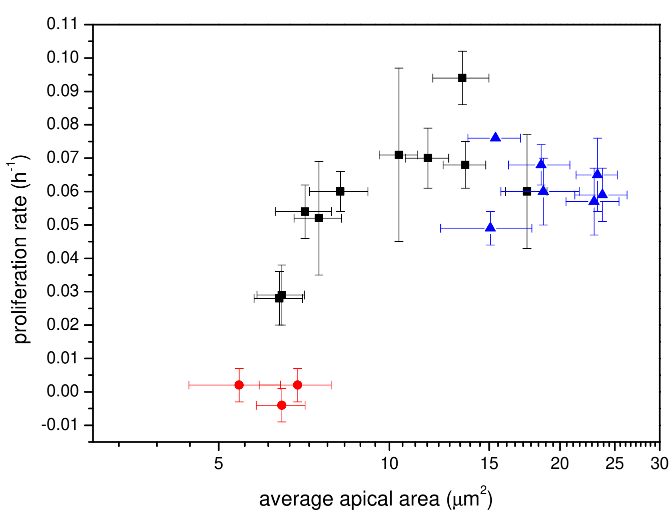

FIG. 17.7 – The correlation between the proliferation rate of cells in the wing disc and the average apical area of the cells for different times during development. Colors correspond to different instar stages: red first instar, blue second instar and black third instar.

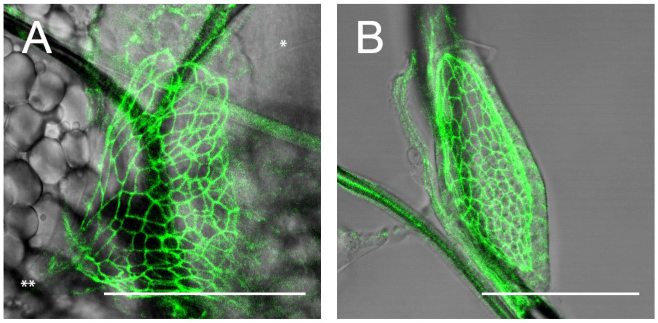

FIG. 17.8 – Images of a wing disc, where the apical cell outlines of the disc proper are marked by GFP fused to E-Cadherin. A: wing disc in vivo at the beginning of the third instar. In this image, several sources of mechanical force can be discerned. A tiny thread is attached to the wing disc on the posterior side (*). Also, the large muscle fiber between the wing, leg and haltere discs is clearly exerting a substantial force on the disc at (**). The cell outlines are correspondingly distorted. B: the same wing disc after dissection. Due to the dissection, the external force from the muscle fiber and the thread has been removed and the shape of the disc as well as that of the cell outlines has relaxed, showing a marked difference to A. The scale bar is 50μm.

[1] L. Wolpert, Development, Oxford Univ. Press (2007).

[2] A.D. Lander, Cell **144**, 955 (2011).

[3] M. Affolter, K. Basler, Nat Rev Genet. **8**, 663 (2007).

[4] U. Nienhaus, T. Aegerter-Wilmsen, and C.M. Aegerter, PLoS ONE **7**, e47594 (2012).

[5] T. Aegerter-Wilmsen, C.M. Aegerter, E. Hafen, and K. Basler, Mechanisms of Development **124**, 318 (2007).

[6] T. Aegerter-Wilmsen *et al.*, Development **137**, 499 (2010).

[7] R. Farhadifar, J.C. Röper, C. Aigouy, S. Eaton, and F. Jülicher, Curr Biol. **17**, 2095 (2007).

[8] T. Aegerter-Wilmsen *et al.*, Development **139** 3221 (2012).

[9] S. Dupont, *et al.* Nature **474**, 179 (2011).

[10] B.I. Shraiman, Proc Nat. Acad. Sci. USA **102**, 3318 (2005).

[11] L. Hufnagel, A.A. Teleman, H. Rouault, S.M. Cohen, and B.I. Shraiman, Proc Nat Acad Sci USA **104**, 3835 (2007).

[12] U. Nienhaus, T. Aegerter-Wilmsen, and C.M. Aegerter, Mechanisms of Development **126**, 942 (2009).

[13] S. Ishihara and K. Sugimura, J. Theor. Biol. **313**, 201 (2012).

[14] A. Puliafito *et al.*, Proc. Nat. Acad. Sci. USA **109**, 739 (2012).

[15] C. Dambly-Chaudiére, A. Ghysen, Y.N. Jan, and Y.L. Jan, Developmental Biology **113**, 288 (1986).

18 Mechanical Workshop

K. Bösiger, B. Lussi, R. Maier, M. Schaffner, S. Scherr, D. Dürst (apprentice) and D. Gabrielli (apprentice)

In addition to in-house projects and work for other institutes of the University we also manufactured parts for outside companies. Besides the regular maintenance and repair work we also supported various Bachelor- and Master-thesis projects.

Again over 30 institutes and local high schools were supplied with materials and technical support by the central metal and technical material store maintained by our staff. [6] That this service is appreciated by the users was demonstrated by the many visitors during the open day organized in November 2012.

Our machinery was brought up to date in various ways. For the welding shop a larger spot welding system was purchased (see Fig. 18.1). In the material shop the circular saw was replaced and for the central workshop two Schaublin 102 lathes were completely refurbished. In the student workshop two ancient Aciera milling machines have been replaced by the two completely refurbished Deckel FP1 shown in Fig. 18.2.

In September 2012 we started with the evaluation of the new milling machine for the main workshop which will replace the 21-year old Deckel FP5. Unfortunately, the new computer controlled machines have larger outer dimensions for a given work area and the available space is limited.

We conducted the basic mechanical workshop courses for the bachelor students in physics during four weeks. During this time, 9 courses were carried out which lasted 35 hours each. In October 2012 we again organized two welding courses for the physics laboratory assistant apprentices from the ETH. For people interested in a grade as a polytechnician we provided two one-week trial apprenticeships. One of the participants will start his apprenticeship in our workshop in 2013.

The workshop staff continues to get educated. Software courses in computer aided design (CAD) and computer aided manufacturing (CAM) were attended. We took welding training courses and went to the regular meetings in relation with the education of the apprentices. We visited machinery and tool manufacturers, as well as machine and tool exhibitions. In addition to the compulsory Swissmechanic courses our apprentices attended advanced training courses in turning and milling, CNC programming, pneumatics and electronics. Early 2013 we started the preparations for the intermediate and final examinations of the apprentices.

[6]For a catalogue see http://www.physik.uzh.ch/groups/werkstatt/

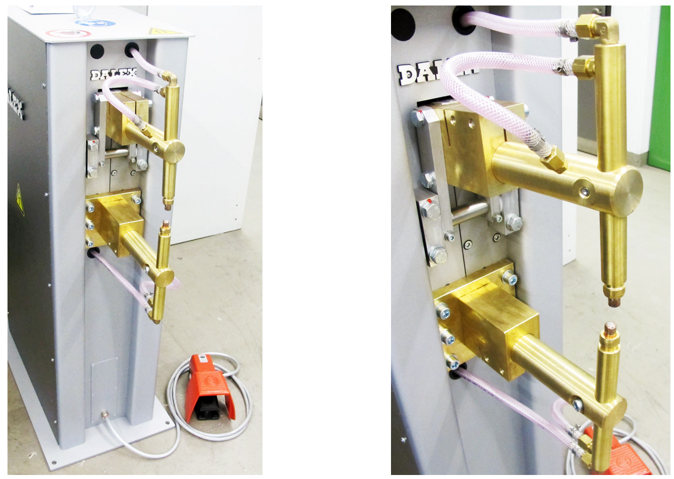

FIG. 18.1 – The new rocker arm spot welding machine.

FIG. 18.2 – New milling machines in the student workshop.

18.1 A selection of our production

- CTA Cherenkov Telescope Array (Sec. 7)
  Test setups for the FlashCam project and installation tools were manufactured. We made soldering tools, junction boxes and parts for the detectors.

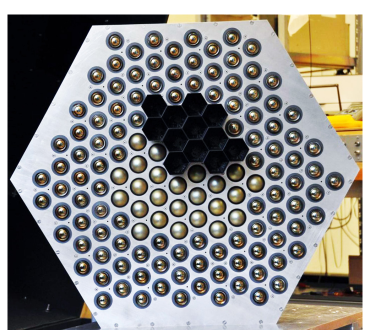

Prototype of the CTA FlashCam camera.

- Surface Physics (Sec. 15)
  We produced replacement parts made of molybdenum and stainless steel. Various laboratory equipment was completed and repaired.

Ellipsoidal mirror focussing a halogen lamp filament into a glass rod.

Molybdenum sample holder parts.

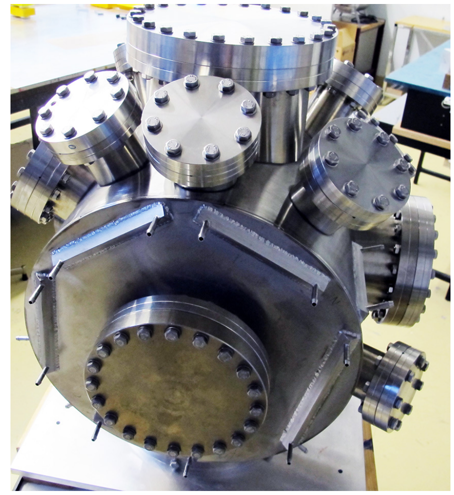

Preparation chamber of the Sinergia equipment.

- Astroparticle Physics (Secs. 3 and 4)
  An additional fourth calibration system for the GERDA experiment was built. Teflon parts for PMT test setups and a copper field shaping structure for the prototype TPC of the XENON experiment were manufactured. We also performed special welding tests for the group.

Field shaping structure for the XENON test TPC of the XENON experiment.

- Superconductivity and Magnetism (Sec. 13)
  Special high-pressure sample chambers made of high strength materials and all necessary replacement part were fabricated.

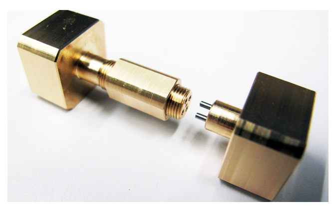

High-pressure chamber.

Various sealing rings for sample chamber.

- Physics on the nanometer scale (Sec. 16)
  We modified and maintained the custom made vapour deposition device with six coating stations. Connectors made of plastic and ceramic materials for the use in vacuum and different evaporation mask were manufactured.

Extension chamber for the thermal disorption spectrometer.

Dedicated sample holders for the low energy electron point source (LEEPS)

- CMS Barrel Pixel detector upgrade
  In September 2012 we started with the construction of the CO_2 cooling test setup for the CMS barrel pixel detector upgrade project. We performed bending tests on thin-walled stainless steel tubes with small diameters and manufactured a variety of parts and fittings made of stainless steel.

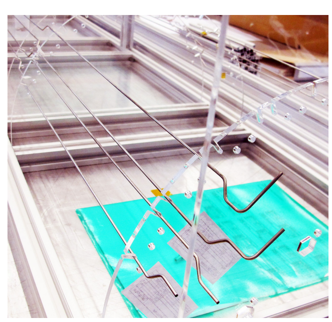

CO_2 cooling test setup - note the tubes bent with a computer controlled bending machine.

- AEgIS experiment at CERN (Sec. 2)
  We manufactured a complex thin-walled aluminum cylinder with very small fibre channels for the AEgIS tracking detector.

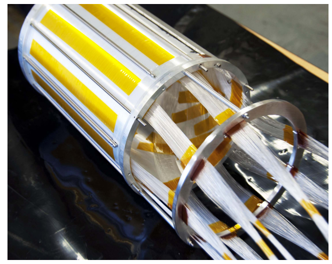

The AEgIS fibre tracking detector.

- Zoological Museum
  A set of modular table frames and a bird identification game were made for the *Galápagos* exhibition at the Museum which takes place between 11th December 2012 and 8th September 2013.

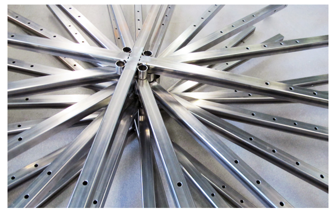

Modular table frames.

Parts for a bird identification game.

- Anthropological Institute
  We built three test boxes used to collect urine specimens from Callitrichidae (a family of New World monkeys) which is used to study the evolution of primates.

Test box for the anthropological institute.

- Institute of Neuroinformatics
  A new micro-drive generation was manufactured. These are implanted in the heads of singing birds where the activity of single neurons is recorded. The hope is to understand the mechanisms that generate complex vocal sequences and the learning process in general.

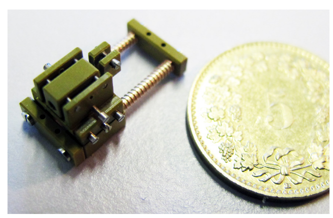

New version of a miniaturized piezodrive.

- Animal Hospital
  A series of hundred novel water bottle holders

Drinking bottle holder for the animal hospital.

- Outside company
  A series of six outdoor 16 W LED lamp stands made of stainless steel. The light direction can be adjusted over 90 degrees.

Outdoor lighting LED lamp made of stainless steel for an outside company.

19 Electronics Workshop

D. Florin, P. Soland, and A. Vollhardt

We built test setups for various research projects at the institute. We also adjusted and modified existing equipment as requested by the researchers and designed different cable adapters. We did maintenance of facilities in the various laboratories and for the LHCb experiment at CERN, fixed different faulty systems and made minor repairs.

Some more interesting projects and activities:

- Undergraduate lectures
  For the Frank-Hertz demonstration experiment we developed an improved timing control and built a completely new deflection output stage. Simple computer controlled operation is possible now and the measured curves can directly be projected with the beamer giving a clear presentation of the results.

- Phase Transitions, Materials and Applications (Sec. 14)
  Four workbenches were equipped with LED lighting. For that purpose we designed and built adjustable power supplies for brightness control.

FIG. 19.1 – Adjustable LED lighting power supply for laboratory workbenches.

- Electronics for the Cherenkov Telescope Array (CTA) experiment (Sec. 7)
  We continued the development of the active mirror control (AMC) and were able to improve the position resolution from 30 μm down to 5 μm. We started the design and construction of a 12 x 12 pixel camera for the Flashcam project. In order to test different concepts for the GAPD FlashCam electronics, especially the design of the amplifiers and bias voltage power supplies, we manufactured and assembled different printed circuit boards shown on the right. For the print soldering we used the reflow oven in the electronics labs. Meanwhile we are testing the devices. A second set of boards was produced for the University of Geneva where additional extensive tests will be made.

- Astroparticle Physics (Sec. 3)
  For the precise positioning of the calibration sources in the GERDA experiment at the Laboratori Nazionali del Gran Sasso (LNGS) in Italy a second motor control system with appropriate peripherals has been manufactured.

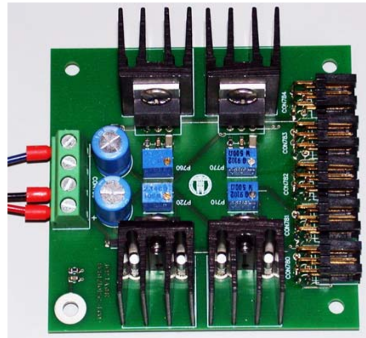

Adjustable low voltage regulator.

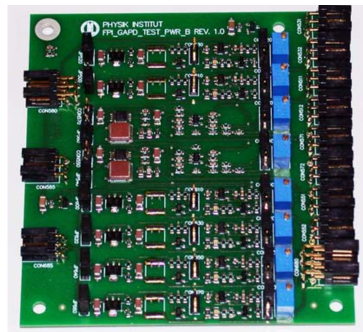

High voltage regulator board.

General purpose preamplifier module.

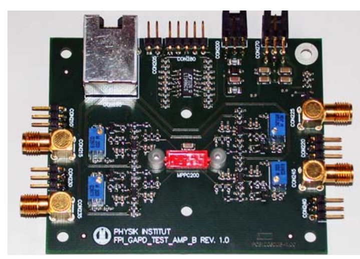

Four channel preamplifier.

High voltage generator board.

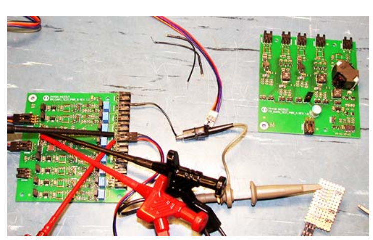

Commissioning and test setup.

FIG. 19.2 – Electronic boards for CTA.

20 Publications

20.1 Elementary particles and their interactions

20.1.1 Dark Matter

Article

- *Study of nuclear recoils in liquid argon with monoenergetic neutrons*
  C. Regenfus, Y. Allkofer, C. Amsler, W. Creus, A. Ferella, J. Rochet, and M. Walter,
  Journal of Physics: Conference Series **375** (2012) 012019.

20.1.2 AEGIS

Articles

- *The AEGIS experiment at CERN: Measuring the free fall of antihydrogen*
  AEgIS Collaboration, Hyperfine Interactions **209** (2012) 43.
- *Towards the production of an ultra cold antihydrogen beam with the AEGIS apparatus*
  James William Storey, Hyperfine Interactions **212** (2012) 109.
- *A new application of emulsions to measure the gravitational force on antihydrogen*
  C. Amsler *et al.*, J. of Instrumentation **8** (2013) P02015.
- *Exploring the WEP with a pulsed cold beam of antihydrogen*
  M. Doser, C. Amsler, *et al.* (AEgIS Collaboration), Classical Quantum Gravity **29** (2012) 184009.

Articles in press

- *Particle tracking at 4K: The Fast Annihilation Cryogenic Tracking (FACT) detector for the AEgIS antimatter gravity experiment*
  J. Storey *et al.* (AEgIS Collaboration), Nucl. Instr. and Meth.
- *Development of nuclear emulsions with 1 μm spatial resolution for the AEgIS experiment*
  M. Kimura *et al.* (AEgIS Collaboration), Nucl. Instr. and Meth.

Lectures

- Carlo Canali: *Particle tracking at 4K: The Fast Annihilation Cryogenic Tracking (FACT) detector for the AEgIS antimatter gravity experiment*
  13th Vienna Conference on Instrumentation, Vienna, Austria, 11 February 2013.

20.1.3 GERDA

Articles

- The GERDA Experiment for the Search of $0\nu\beta\beta$ decay in ^{76}Ge
  K.-H. Ackermann, M. Agostini, M. Allardt, M. Altmann, E. Andreotti, A.M. Bakalyarov, M. Balata, I. Barabanov, M. Barnabe Heider, N. Barros, L. Baudis, C. Bauer *et al.* (GERDA Collaboration), Eur. Phys. J. C 73, 2330 (2013).
- Measurement of the half-life of the two-neutrino double beta decay of Ge-76 with the Gerda experiment
  M. Agostini, M. Allardt, E. Andreotti, A.M. Bakalyarov, M. Balata, I. Barabanov, M. Barnabe Heider, N. Barros, L. Baudis, C. Bauer *et al.* (GERDA Collaboration), J. Phys. G 40, 035110 (2013).

Lectures

- G. Benato: *Improvement of the Offline Event Reconstruction for the GERDA Experiment*
  SIF Meeting 2012, Napoli, Italy, September 21, 2012.

- G. Kiran Kumar: *GERmanium Detector Array: Status and Plans*
  TEVPA-12, TIFR Mumbai, India, December 12th, 2012.

- G. Benato: *The GERDA experiment for the search of neutrinoless double beta decay*
  SPS Meeting 2012, ETH Zurich, July 21, 2012.

Theses

- *Calibration of Phase I of the GERDA Double Beta Decay Experiment*
  F. Froborg, PhD thesis, Universität Zürich, 2012.

- *Studies of Neutron Flux Suppression from a Gamma-ray Source and the GERDA Calibration System*
  M. Tarka, PhD thesis, Universität Zürich, 2012.

- *Calibration of a Germanium Detector*
  L. van der Schaaf, Bachelor thesis, Universität Zürich, 2012.

20.1.4 DIRAC

Articles

- *The DIRAC experiment at CERN*
  Angela Benelli (DIRAC Collaboration), EPJ Web of Conferences **37** (2012) 01011.

Lectures

- Angela Benelli: *The DIRAC experiment at CERN*
  Meson 2012 Conference, Krakow, Poland, 1 June 2012.

20.1.5 XENON/DARWIN

Articles

- *Dark Matter Results from 225 Live Days of XENON100 Data*
  E. Aprile *et al.* (XENON100 Collaboration), Phys. Rev. Lett. 109, 181301 (2012).

- *Direct dark matter detection: the next decade*
  L. Baudis, Phys. Dark Univ. 1, 94-108 (2012).

- *The Distributed Slow Control System of the XENON100 Experiment*
  E. Aprile *et al.*, JINST 7, T12001 (2012).

- *DARWIN: dark matter WIMP search with noble liquids*
  L. Baudis (for the DARWIN Consortium), J. Phys. Conf. Ser. 375, 012028 (2012).

Lectures

- L. Baudis: *Detectors for astroparticle physics and dark matter searches*
  Vienna Conference of Instrumentation, Vienna, February 11, 2013.

- L. Baudis: *Dark matter searches with liquid xenon*
  Physics seminar, University of Geneva, February 6, 2013.

- L. Baudis: *Dark matter WIMP searches in the Milky Way*
  Physics Colloquium, Muenster University, January 17, 2013.

- L. Baudis: *XENON100, XENON1T*
  The Physics of the Universe Summit, SpaceX, Los Angeles, January 12, 2013.

- L. Baudis: *New results from XENON100*
  TPC 2012, Paris, December 17, 2012.
- L. Baudis: *Direct dark matter WIMP searches in the Milky Way*
  Physics Colloquium, 6th AFI Symposium, Innsbruck, December 7, 2012.
- L. Baudis: *Dark matter detectors - from low-temperature crystals to cryogenic liquids*
  Cabrera Fest, Stanford University, October 7, 2012.
- L. Baudis: *Direct dark matter detection*
  IoP Colloquium, University of Amsterdam, July 5, 2012.
- L. Baudis: *Experimental review on neutrinoless double beta decay*
  What is ν? & INVISIBLES12 Meeting, GGI, Florence, Italy, June 27th, 2012.
- L. Baudis: *A review of direct WIMP search experiments*
  Neutrino 2012, Kyoto, June 9, 2012.
- L. Baudis: *Results from the XENON100 Dark Matter Search Experiment*
  Physics Seminar, Granada University, May 3, 2012.
- L. Baudis: *Direct detection of particle dark matter: where do we stand, where are we going?*
  Physics Colloquium, IFIC, Valencia University, April 26, 2012.
- M. Schumann: *New dark matter results from XENON*
  MLL Kolloquium, LMU/TU Munich, Germany, October 25th, 2012.
- M. Schumann: *XENON100 – The new Results*
  Dienstagsseminar, DESY Hamburg, Germany, October 23rd, 2012.
- M. Schumann: *XENON100 – The new Results*
  Seminar, CEA Saclay, France, October 20th, 2012.
- M. Schumann: *XENON100 – The new Results*
  Seminar, DESY Zeuthen, Germany, October 17th, 2012.
- G. Kessler: *XENON100, XENON1T and DARWIN*
  CHIPP Meeting 2012, Kartause Ittingen, Switzerland, September 14, 2012.
- M. Schumann: *XENON100 – The new Results*
  Fermilab Seminar/PATRAS12, Chicago, USA, July 20th, 2012.
- A. Manalaysay: *New Frontiers in Dark Matter Direct Detection: Probing sub-GeV DM Masses*
  PATRAS12, Chicago, USA, July 18th, 2012.
- M. Schumann: *Direct Dark Matter Searches*
  What is ν? & INVISIBLES12 Meeting, GGI, Florence, Italy, June 27th, 2012.
- A. Manalaysay: *Measurements of the low-energy response of liquid xenon*
  SPS Meeting 2012, ETH Zurich, Switzerland, June 21st, 2012.
- M. Schumann: *Dark Matter Search with XENON*
  SPS Meeting 2012, ETH Zurich, Switzerland, June 21st, 2012.
- M. Schumann: *Dark Matter Search with XENON*
  Seminar, AEC University of Bern, Switzerland, May 10th, 2012.
- M. Schumann: *Dark Matter Search with XENON*
  Nuclear Chemistry Seminar, Mainz University, Germany, May 2nd, 2012.
- M. Schumann: *Dark Matter Search with Noble Liquids*
  Rencontres de Moriond 2012, Cosmology Session, La Thuile, Italy, March 14th, 2012.

Theses

- *Material Screening and Selection for the XENON100 Dark Matter Experiment*
  A. Askin, PhD thesis, Universität Zürich, 2012.

- *Preparations for measurements of the low energy response of liquid xenon*
  P. Pakarha, master thesis, Universität Zürich, 2012.

- *Neutron Background Monitoring for XENON100*
  E. Crivelli, bachelor thesis, Universität Zürich, 2012.

- *Simulation and optimization of the electric field in a liquid xenon time projection chamber*
  H. Dujmovic, bachelor thesis, Universität Zürich, 2012.

20.1.6 CTA

Thesis

- *Contributions to High Energy and Very High Energy Gamma-Ray Astronomy*
  Ben Huber, PhD thesis, Universität Zürich, 2012.

Articles

- *A stacking method to study the gamma-ray emission of source samples based on the co-adding of $Fermi$-LAT count maps*
  B. Huber, C. Farnier, A. Manalaysay, U. Straumann, and R. Walter, Astronomy&Astrophysics **547**, A102 (2012).

20.1.7 H1

Articles

- *Measurement of Dijet Production in Diffractive Deep-Inelastic Scattering with a Leading Proton at HERA*
  H1-Collaboration, F.D. Aaron *et al.*, Eur. Phys. J. C **72** (2012), 1970.

- *Measurement of Inclusive and Dijet D^* Meson Cross Sections in Photoproduction at HERA*
  H1-Collaboration, F.D. Aaron *et al.*, Eur. Phys. J. C **72** (2012), 1995.

- *Measurement of Beauty and Charm Photoproduction using Semimuonic Decays in Dijet Events at HERA*
  H1-Collaboration, F.D. Aaron *et al.*, Eur. Phys. J. C **72** (2012), 2047.

- *Inclusive Measurement of Diffractive Deep-Inelastic Scattering at HERA*
  H1-Collaboration, F.D. Aaron *et al.*, Eur. Phys. J. C **72** (2012), 2074.

- *Determination of the Integrated Luminosity at HERA using Elastic QED Compton Events*
  H1-Collaboration, F.D. Aaron *et al.*, Eur. Phys. J. C **72** (2012), 2163.

- *Measurement of Beauty Photoproduction near Threshold using Di-electron Events with the H1 Detector at HERA*
  H1-Collaboration, F.D. Aaron *et al.*, Eur. Phys. J. C **72** (2012), 2148.

- *Inclusive Deep Inelastic Scattering at High Q^2 with Longitudinally Polarised Lepton Beams at HERA*
  H1-Collaboration, F.D. Aaron *et al.*, JHEP **09** (2012), 061.

- *Combined Inclusive Diffractive Cross Sections Measured with Forward Proton Spectrometers in Deep Inelastic ep Scattering at HERA*
  H1- and ZEUS-Collaboration, F.D. Aaron *et al.*, Eur. Phys. J. C **72** (2012), 2175.

- *Combination and QCD Analysis of Charm Production Cross Section Measurements in Deep-Inelastic ep Scattering at HERA*
  H1- and ZEUS-Collaboration, H. Abramowicz *et al.*, Eur. Phys. J. C **73** (2013), 2311.

Article in press

- *Measurement of Charged Particle Spectra in Deep-Inelastic ep Scattering at HERA*
  H1-Collaboration, C. Alexa *et al.*, Eur. Phys. J. C, arXiv:1302.1321 [hep-ex]

20.1.8 LHCb

Articles

- *Experimental constraints from flavour changing processes and physics beyond the Standard Model*
  N. Serra, Invited review for Top and Flavour physics in the LHC era, Eur. J. Phys. C **72**, Issue 8.
- *Searching for New Physics in rare B-meson decays*
  N. Serra, Nuovo Cimento C **36** (2013) 01.
- *Observations of $B_s^0 \to \psi(2S)\eta$ and $B_{(s)}^0 \to \psi(2S)\pi^+\pi^-$ decays*
  LHCb-Collaboration, R. Aaij *et al.*, Nucl. Phys. B **871** (2013) 403.
- *Prompt charm production in pp collisions at $\sqrt{s}$=7 TeV*
  LHCb-Collaboration, R. Aaij *et al.*, Nucl. Phys. B **871** (2013) 1.
- *Exclusive J/ψ and $\psi(2S)$ production in pp collisions at $\sqrt{s} = 7$ TeV*
  LHCb-Collaboration, R. Aaij *et al.*, J. Phys. G **40** (2013) 045001.
- *Analysis of the resonant components in $B^0 \to J/\psi\pi^+\pi^-$*
  LHCb-Collaboration, R. Aaij *et al.*, Phys. Rev. D87 (2013) 052001.
- *Measurement of the fragmentation fraction ratio f_s/f_d and its dependence on B meson kinematics*
  LHCb-Collaboration, R. Aaij *et al.*, JHEP **1304** (2013) 001.
- *Measurement of CP observables in $B^0 \to DK^{*0}$ with $D \to K^+K^-$*
  LHCb-Collaboration, R. Aaij *et al.*, JHEP **1303** (2013) 067.
- *Differential branching fraction and angular analysis of the $B^+ \to K^+\mu^+\mu^-$ decay*
  LHCb-Collaboration, R. Aaij *et al.*, JHEP **1302** (2013) 105.
- *Search for the rare decay $K_s \to \mu^+\mu^-$*
  LHCb-Collaboration, R. Aaij *et al.*, JHEP **1301** (2013) 090.
- *Measurement of the ratio of branching fractions BR($B^0 \to K^{*0}\gamma$)/BR($B_s^0 \to \phi\gamma$) and the direct CP asymmetry in $B^0 \to K^{*0}\gamma$*
  LHCb-Collaboration, R. Aaij *et al.*, Nucl. Phys. B **867** (2013) 1.
- *Measurement of the cross-section for $Z \to e^+e^-$ production in pp collisions at $\sqrt{s} = 7$ TeV*
  LHCb-Collaboration, R. Aaij *et al.*, JHEP **1302** (2013) 106.
- *Measurement of J/ψ production in pp collisions at $\sqrt{s} = 2.76$ TeV*
  LHCb-Collaboration, R. Aaij *et al.*, JHEP **1302** (2013) 041.
- *Measurement of the time-dependent CP asymmetry in $B^0 \to J/\psi K_s^0$ decays*
  LHCb-Collaboration, R. Aaij *et al.*, Phys. Lett. B **721** (2013) 24.
- *First evidence for the decay $B_s \to \mu^+\mu^-$*
  LHCb-Collaboration, R. Aaij *et al.*, Phys. Rev. Lett. **110** (2013) 021801.
- *Observation of $D^0 - \overline{D}^0$ oscillations*
  LHCb-Collaboration, R. Aaij *et al.*, Phys. Rev. Lett. **110**, (2013) 101802.
- *Measurement of the B^0–$\overline{B}^0$ oscillation frequency Δm_d with the decays $B^0 \to D^-\pi^+$ and $B^0 \to J\ \psi K^{*0}$*
  LHCb-Collaboration, R. Aaij *et al.*, Phys. Lett. B **719** (2013) 318.

- *A study of the Z production cross-section in pp collisions at $\sqrt{s} = 7$ TeV using tau final states*
  LHCb-Collaboration, R. Aaij *et al.*, JHEP **1301** (2013) 111.

- *Measurement of the CP asymmetry in $B^0 \to K^{*0}\mu^+\mu^-$ decays*
  LHCb-Collaboration, R. Aaij *et al.*, Phys. Rev. Lett. **110** (2013) 031801.

- *Measurement of the $D^{+/-}$ production asymmetry in 7 TeV pp collisions*
  LHCb-Collaboration, R. Aaij *et al.*, Phys. Lett. B **718** (2013) 902.

- *First evidence for the annihilation decay mode $B^+ \to D_s^+\phi$*
  LHCb-Collaboration, R. Aaij *et al.*, JHEP **1302** (2013) 043.

- *First observation of the decays $\overline{B}^0_{(s)} \to D_s^+K^-\pi^+\pi^-$ and $\overline{B}^0_s \to D_{s1}^+(2536)\pi^-$*
  LHCb-Collaboration, R. Aaij *et al.*, Phys. Rev. D **86** (2012) 112005.

- *First observation of the decay $B^+ \to \pi^+\mu^+\mu^-$*
  LHCb-Collaboration, R. Aaij *et al.*, JHEP **1212** (2012) 125.

- *A model-independent Dalitz plot analysis of $B^\pm \to DK^\pm$ with $D \to K_S^0h^+h^-$ $(h = \pi, K)$ decays and constraints on the CKM angle γ*
  LHCb-Collaboration, R. Aaij *et al.*, Phys. Lett. B **718** (2012) 43.

- *Measurements of B_c^+ production and mass with the $B_c^+ \to J/\psi\pi^+$ decay*
  LHCb-Collaboration, R. Aaij *et al.*, Phys. Rev. Lett. **109** (2012) 232001.

- *Measurement of the fraction of $\Upsilon(1S)$ originating from $\chi_b(1P)$ decays in pp collisions at $\sqrt{s} = 7$ TeV*
  LHCb-Collaboration, R. Aaij *et al.*, JHEP **1211** (2012) 031.

- *Measurement of the $B_s^0 \to J/\psi K^{*0}$ branching fraction and angular amplitudes*
  LHCb-Collaboration, R. Aaij *et al.*, Phys. Rev. D **86** (2012) 071102.

- *Study of D_{sJ} decays to $D^+K_S^0$ and D^0K^+ final states in pp collisions*
  LHCb-Collaboration, R. Aaij *et al.*, JHEP **1210** (2012) 151.

- *Measurement of the effective $B_s^0 \to K^+K^-$ lifetime*
  LHCb-Collaboration, R. Aaij *et al.*, Phys. Lett. B **716** (2012) 393.

- *Observation of the decay $B^0 \to \overline{D}^0K^+K^-$ and evidence for $B_s\overline{D}^0K^+K^-$*
  LHCb-Collaboration, R. Aaij *et al.*, Phys. Rev. Lett. **109** (2012) 131801.

- *Measurement of the B_s effective lifetime in the $J/\psi f^0(980)$ final state*
  LHCb-Collaboration, R. Aaij *et al.*, Phys. Rev. Lett. **109** (2012) 152002.

- *Measurement of prompt hadron production ratios in pp collisions at $\sqrt{s} =$ 0.9 and 7 TeV*
  LHCb-Collaboration, R. Aaij *et al.*, Eur. Phys. J. C **72** (2012) 2168.

- *Measurement of b-hadron branching fractions for two-body decays into charmless charged hadrons*
  LHCb-Collaboration, R. Aaij *et al.*, JHEP **1210** (2012) 037.

- *Observation of excited Λ_b^0 baryons*
  LHCb-Collaboration, R. Aaij *et al.*, Phys. Rev. Lett. **109** (2012) 172003.

- *Measurement of the isospin asymmetry in $B \to K^{(*)}\mu^+\mu^-$ decays*
  LHCb-Collaboration, R. Aaij *et al.*, JHEP **1207** (2012) 133.

- *Observation of double charm production involving open charm in pp collisions at $\sqrt{s}$=7 TeV*
  LHCb-Collaboration, R. Aaij *et al.*, JHEP **1206** (2012) 141.

- *Measurement of the $B_s^0 \to J/\psi K_S^0$ branching fraction*
  LHCb-Collaboration, R. Aaij *et al.*, Phys. Lett. B **713** (2012) 172.

- *Measurement of relative branching fractions of B decays to $\psi(2S)$ and J/ψ mesons*
  LHCb-Collaboration, R. Aaij *et al.*, Eur. Phys. J. C **72** (2012) 2118.

- *Measurement of the D_s^+ - D_s^- production asymmetry in 7 TeV pp collisions*
  LHCb-Collaboration, R. Aaij *et al.*, Phys. Lett. B **713** (2012) 186.

- *Measurement of the CP-violating phase ϕ_s in $B_s \to J/\psi\pi^+\pi^-$ decays*
  LHCb-Collaboration, R. Aaij *et al.*, Phys. Lett. B **713** (2012) 378.

- *Analysis of the resonant components in $B_s \to J/\psi\pi^+\pi^-$*
  LHCb-Collaboration, R. Aaij *et al.*, Phys. Rev. D **86** (2012) 052006.

- *Measurement of the polarization amplitudes and triple product asymmetries in the $B_s^0 \to \phi\phi$ decay*
  LHCb-Collaboration, R. Aaij *et al.*, Phys. Lett. B **713** (2012) 369.

- *Inclusive W and Z production in the forward region at $\sqrt{s} = 7$ TeV*
  LHCb-Collaboration, R. Aaij *et al.*, JHEP **1206** (2012) 058.

- *Measurement of the ratio of prompt χ_c to J/ψ production in pp collisions at $\sqrt{s} = 7$ TeV*
  LHCb-Collaboration, R. Aaij *et al.*, Phys. Lett. B **718** (2012) 431.

- *Measurement of $\psi(2S)$ meson production in pp collisions at $\sqrt{s} = 7$ TeV*
  LHCb-Collaboration, R. Aaij *et al.*, Eur. Phys. J. C **72** (2012) 2100.

- *Measurements of the branching fractions of the decays $B_s^0 \to D_s^\mp K^\pm$ and $B_s^0 \to D_s^- \pi^+$*
  LHCb-Collaboration, R. Aaij *et al.*, JHEP **1206** (2012) 115.

- *First observation of the decay $B_c^+ \to J/\psi\pi^+\pi^-\pi^+$*
  LHCb-Collaboration, R. Aaij *et al.*, Phys. Rev. Lett. **108** (2012) 251802.

- *Strong constraints on the rare decays $B_s \to \mu^+\mu^-$ and $B^0 \to \mu^+\mu^-$*
  LHCb-Collaboration, R. Aaij *et al.*, Phys. Rev. Lett. **108** (2012) 231801.

- *Observation of CP violation in $B^+ \to DK^+$ decays*
  LHCb-Collaboration, R. Aaij *et al.*, Phys. Lett. B **712** (2012) 203 [Erratum-ibid. B **713** (2012) 351].

- *Measurements of the branching fractions and CP asymmetries of $B^+ \to J/\psi\pi^+$ and $B^+ \to \psi(2S)\pi^+$ decays*
  LHCb-Collaboration, R. Aaij *et al.*, Phys. Rev. D **85** (2012) 091105.

- *Measurement of Υ production in pp collisions at $\sqrt{s} = 7$ TeV*
  LHCb-Collaboration, R. Aaij *et al.*, Eur. Phys. J. C **72** (2012) 2025.

- *Measurement of the ratio of branching fractions $\mathcal{B}(B^0 \to K^{*0}\gamma)/\mathcal{B}(B_s^0 \to \phi\gamma)$*
  LHCb-Collaboration, R. Aaij *et al.*, Phys. Rev. D **85** (2012) 112013.

- *First evidence of direct CP violation in charmless two-body decays of B_s mesons*
  LHCb-Collaboration, R. Aaij *et al.*, Phys. Rev. Lett. **108** (2012) 201601.

- *Search for the $X(4140)$ state in $B^+ \to J/\psi\phi K^+$ decays*
  LHCb-Collaboration, R. Aaij *et al.*, Phys. Rev. D **85** (2012) 091103.

- *Opposite-side flavour tagging of B mesons at the LHCb experiment*
  LHCb-Collaboration, R. Aaij *et al.*, Eur. Phys. J. C **72** (2012) 2022.

- *Measurement of the $B^\pm$ production cross-section in pp collisions at $\sqrt{s} = 7$ TeV*
  LHCb-Collaboration, R. Aaij *et al.*, JHEP **1204** (2012) 093.

- *Determination of the sign of the decay width difference in the B_s system*
  LHCb-Collaboration, R. Aaij *et al.*, Phys. Rev. Lett. **108** (2012) 241801.

- *Measurement of the cross-section ratio $\sigma(\chi_{c2})/\sigma(\chi_{c1})$ for prompt χ_c production at $\sqrt{s} = 7$ TeV*
  LHCb-Collaboration, R. Aaij *et al.*, Phys. Lett. B **714** (2012) 215.

- *Searches for Majorana neutrinos in B^- decays*
  LHCb-Collaboration, R. Aaij *et al.*, Phys. Rev. D **85** (2012) 112004.

- *First observation of the decays $\overline{B}^0 \to D^+K^-\pi^+\pi^-$ and $B^- \to D^0K^-\pi^+\pi^-$*
  LHCb-Collaboration, R. Aaij *et al.*, Phys. Rev. Lett. **108** (2012) 161801.

- *Observation of $X(3872)$ production in pp collisions at $\sqrt{s} = 7$ TeV*
  LHCb-Collaboration, R. Aaij *et al.*, Eur. Phys. J. C **72** (2012) 1972.

- *Measurement of charged particle multiplicities in pp collisions at $\sqrt{s} = 7$ TeV in the forward region*
  LHCb-Collaboration, R. Aaij *et al.*, Eur. Phys. J. C **72** (2012) 1947.

- *Measurement of mixing and CP violation parameters in two-body charm decays*
  LHCb-Collaboration, R. Aaij *et al.*, JHEP **1204** (2012) 129.

- *Differential branching fraction and angular analysis of the decay $B^0 \to K^{*0}\mu^+\mu^-$*
  LHCb-Collaboration, R. Aaij *et al.*, Phys. Rev. Lett. **108** (2012) 181806.

- *Absolute luminosity measurements with the LHCb detector at the LHC*
  LHCb-Collaboration, R. Aaij *et al.*, JINST **7** (2012) P01010.

- *Search for the lepton number violating decays $B^+ \to \pi^-\mu^+\mu^+$ and $B^+ \to K^-\mu^+\mu^+$*
  LHCb-Collaboration, R. Aaij *et al.*, Phys. Rev. Lett. **108** (2012) 101601.

- *Measurements of the Branching fractions for $B_{(s)} \to D_{(s)}\pi\pi\pi$ and $\Lambda_b^0 \to \Lambda_c^+\pi\pi\pi$*
  LHCb-Collaboration, R. Aaij *et al.*, Phys. Rev. D **84** (2011) 092001 [Erratum-ibid. D **85** (2012) 039904].

- *Observation of J/ψ pair production in pp collisions at $\sqrt{s} = 7$ TeV*
  LHCb-Collaboration, R. Aaij *et al.*, Phys. Lett. B **707** (2012) 52.

LHCb notes and reports

- *Search for the rare decays $B_s^0 \to \mu^+\mu^-$ and $B^0 \to \mu^+\mu^-$ with 1 fb^{-1} of 2012 data*
  F. Archilli *et al.*, LHCb-ANA-2012-081

- *Measurement of the cross section for $Z \to \mu\mu$ production in pp collisions at $\sqrt{s}$=7 TeV with the 2011 data*
  J. Anderson, W. Barter, A. Bursche, K. Müller, R. J. Wallace, LHCb-ANA-2012-025

- *Graphical comparison of the LHCb measurement of W and Z boson production with ATLAS and CMS*
  K. Müller, LHCb-ANA-2012-020

- *Measurement of the relative Z plus jet cross section*
  LHCb collaboration, LHCb-CONF-2012-016

- *Measurement of the relative Z plus jet cross section*
  A. Bursche, W. Barter, LHCb-ANA-2012-006

- *Angular analysis of $B^0 \to K^*\mu^+\mu^-$ at LHCb with 1 fb^{-1}*
  T. Blake *et al.*, LHCb-ANA-2012-051

- *Measurement of new angular observables in the decay $B^0 \to K^*\mu^+\mu^-$*
  M. De Cian, N. Serra, LHCb-ANA-2013-006

- *Measurement of the fragmentation fraction ratio f_s/f_d and its dependence on B meson kinematics*
  B. Storaci, LHCb-ANA-2011-070

Conference contributions

- Albert Bursche: *Particle production in the forward region*
  Lake Louise Winter Institute, Lake Louise, Alberta, Canada, 17 - 23 February 2013

- Nicola Chiapolini: *Electroweak physics, QCD and jets in the forward region*
  Cracow Epiphany conference on the Physics after the First Phase of the LHC, 7 - 9 January 2013, Cracow, Poland
- Olaf Steinkamp: *CP Violation at LHCb*
  International Workshop on Discovery Physics at the LHC, Kruger, South Africa, 3 - 7 December 2012
- Katharina Müller: *Measurements with electroweak bosons in the forward region at LHCb*
  DESY physics seminars, Hamburg and Berlin, Germany, 27 and 28 November 2012
- Christian Elsasser: *The LHCb Silicon Tracker - Performance & Radiation Damage*
  9th International Conference on Radiation Effects on Semiconductor Materials, Detectors and Devices, Florence, Italie, 9 - 12 October 2012
- Michel De Cian: *Physics with electroweak penguins at LHCb*
  7th International Workshop on the CKM Unitarity Triangle, Cincinnati, Ohio, USA, 28 September - 2 October 2012
- Mark Tobin: *Performance of the LHCb Tracking Detectors*
  Vertex 2012, Jeju, Republic of Korea, 16 - 21 September 2012
- Michel De Cian: *Rare B decays at LHCb*
  CHIPP annual plenary meeting, Karthause Ittingen, 13 - 14 September 2012
- Katharina Müller: *Measurements with electroweak bosons at LHCb*
  QCD@LHC, East-Lansing, Michigan, USA, 19 - 24 August 2012
- Jonathan Anderson: *Measurements with electroweak bosons at LHCb*
  International Conference on High Energy Physics 2012, Melbourne, Australia, July 2012

- Albert Bursche: *QCD and electroweak measurements at LHCb*
  HSQCD, Gatchina, Russia, July 4 - July 8, 2012
- Christian Elsasser: *Search for the Rare Decays $B^0_{(s)} \to \mu^+\mu^-$ at LHCb*
  Annual meeting of the Swiss Physical Society, Zürich, 22 June 2012
- Katharina Müller: *Electroweak results at LHCb*
  CERN seminar, Geneva Switzerland, 5 June 2012
- Nicola Serra: *$B_s \to \mu\mu$ and $B \to K^\star\mu\mu$*
  Flavour Physics and CP Violation (FPCP) 2012, Hefei, AnHui, China, 21 - 25 May 2012, proceedings published online on SLAC-eConf http://www.slac.stanford.edu/econf/editors.html
- Michel De Cian: *Rare electroweak penguin decays at LHCb*
  LHCb-Theory Workshop: Implications of LHCb measurements and future prospects, CERN, Switzerland, 16 - 18 April 2012
- Katharina Müller: *Electroweak results at LHCb*
  SM@LHC, Copenhagen, Denmark, 10 - 13 April 2012
- Jonathan Anderson: *Inclusive low mass Drell-Yan production in the forward region at $\sqrt{s} = 7$ TeV*
  XX International Workshop on Deep-Inelastic Scattering and Related Subjects (DIS 2012), Bonn, Virginia, Germany, 11 - 15 April 2012
- Albert Bursche: *Jet reconstruction with LHCb*
  XX International Workshop on Deep-Inelastic Scattering and Related Subjects (DIS 2012), Bonn, Virginia, Germany, 11 - 15 April 2012

Theses

- *Measurement of Asymmetries in the Decay $B^0 \to K^{*0}\mu^+\mu^-$ at the LHCb experiment*
  Marco Tresch, Master thesis, Universität Zürich, August 2012.

- *Study of charge sharing in the LHCb Tracker Turicensis using proton-proton collisions at the LHC*
  Philipp Gloor, Bachelor thesis, Universität Zürich, May 2012.

20.1.9 CMS

Articles

- *Search for contact interactions using the inclusive jet pT spectrum in pp collisions at sqrt(s) = 7 TeV*
  CMS-Collaboration, S. Chatrchyan *et al.*, Phys. Rev. D **87**, 052017 (2013)

- *On the mass and spin-parity of the Higgs boson candidate via its decays to Z boson pairs*
  CMS-Collaboration, S. Chatrchyan *et al.*, Phys. Rev. Lett. **110**, 081803 (2013)

- *Measurement of the $t\bar{t}$ production cross section in pp collisions at $\sqrt{s} = 7$ TeV with lepton + jets final states*
  CMS-Collaboration, S. Chatrchyan *et al.*, Phys. Lett. B **720**, 83 (2013)

- *Search for new physics in events with same-sign dileptons and b jets in pp collisions at $\sqrt{s} = 8$ TeV*
  CMS-Collaboration, S. Chatrchyan *et al.*, JHEP **1303**, 037 (2013)

- *Search for heavy narrow dilepton resonances in pp collisions at $\sqrt{s} = 7$ TeV and $\sqrt{s} = 8$ TeV*
  CMS-Collaboration, S. Chatrchyan *et al.*, Phys. Lett. B **720**, 63 (2013)

- *Search for contact interactions in opposite-sign dimuon events in pp collisions at $\sqrt{s} = 7$ TeV*
  CMS-Collaboration, S. Chatrchyan *et al.*, Phys. Rev. D **87**, 032001 (2013)

- *Search for exotic resonances decaying into WZ/ZZ in pp collisions at $\sqrt{s} = 7$ TeV*
  CMS-Collaboration, S. Chatrchyan, JHEP **1302**, 036 (2013)

- *Measurement of the ZZ production cross section and search for anomalous couplings in 2 l2l ' final states in pp collisions at $\sqrt{s} = 7$ TeV*
  CMS-Collaboration, S. Chatrchyan *et al.*, JHEP **1301**, 063 (2013)

- *Search for new physics in events with photons, jets, and missing transverse energy in pp collisions at $\sqrt{s} = 7$ TeV*
  CMS-Collaboration, S. Chatrchyan *et al.*, JHEP **1303**, 111 (2013)

- *Search for supersymmetry in final states with a single lepton, b-quark jets, and missing transverse energy in proton-proton collisions at $\sqrt{s} = 7$ TeV*
  CMS-Collaboration, S. Chatrchyan *et al.*, Phys. Rev. D **87**, 052006 (2013)

- *Search in leptonic channels for heavy resonances decaying to long-lived neutral particles*
  CMS-Collaboration, S. Chatrchyan *et al.*, JHEP **1302**, 085 (2013)

- *Search for supersymmetry in final states with missing transverse energy and 0, 1, 2, or at least 3 b-quark jets in 7 TeV pp collisions using the variable alphaT*
  CMS-Collaboration, S. Chatrchyan *et al.*, JHEP **1301**, 077 (2013)

- *Measurement of the sum of WW and WZ production with W+dijet events in pp collisions at $\sqrt{s} = 7$ TeV*
  CMS-Collaboration, S. Chatrchyan *et al.*, Eur. Phys. J. C **73**, 2283 (2013)

- *Search for heavy quarks decaying into a top quark and a W or Z boson using lepton + jets events in pp collisions at $\sqrt{s} = 7$ TeV*
  CMS-Collaboration, S. Chatrchyan *et al.*, JHEP **01**, 154 (2013)

- *Search for pair production of third-generation leptoquarks and top squarks in pp collisions at $\sqrt{s} = 7$ TeV*
  CMS-Collaboration, S. Chatrchyan *et al.*, Phys. Rev. Lett. **110**, 081801 (2013)

- *Search for third-generation leptoquarks and scalar bottom quarks in pp collisions at $\sqrt{s} = 7$ TeV*
  CMS-Collaboration, S. Chatrchyan *et al.*, JHEP **1212**, 055 (2012)

- *Observation of long-range near-side angular correlations in proton-lead collisions at the LHC*
  CMS-Collaboration, S. Chatrchyan *et al.*, Phys. Lett. B **718**, 795 (2013)

- *Observation of Z decays to four leptons with the CMS detector at the LHC*
  CMS-Collaboration, S. Chatrchyan *et al.*, JHEP **1212**, 034 (2012)

- *Search for excited leptons in pp collisions at $\sqrt{s} = 7$ TeV*
  CMS-Collaboration, S. Chatrchyan *et al.*, Phys. Lett. B **720**, 309 (2013)

- *Search for heavy neutrinos and W[R] bosons with right-handed couplings in a left-right symmetric model in pp collisions at sqrt(s) = 7 TeV*
  CMS-Collaboration, S. Chatrchyan *et al.*, Phys. Rev. Lett. **109**, 261802 (2012)

- *Search for narrow resonances and quantum black holes in inclusive and b-tagged dijet mass spectra from pp collisions at $\sqrt{s} = 7$ TeV*
  CMS-Collaboration, S. Chatrchyan *et al.*, JHEP **1301**, 013 (2013)

- *Search for heavy lepton partners of neutrinos in proton-proton collisions in the context of the type III seesaw mechanism*
  CMS-Collaboration, S. Chatrchyan *et al.*, Phys. Lett. B **718**, 348 (2012)

- *Measurement of the relative prompt production rate of chi(c2) and chi(c1) in pp collisions at $\sqrt{s} = 7$ TeV*
  CMS-Collaboration, S. Chatrchyan *et al.*, Eur. Phys. J. C **72**, 2251 (2012)

- *Search for electroweak production of charginos and neutralinos using leptonic final states in pp collisions at $\sqrt{s} = 7$ TeV*
  CMS-Collaboration, S. Chatrchyan *et al.*, JHEP **1211**, 147 (2012)

- *Measurement of the single-top-quark t-channel cross section in pp collisions at $\sqrt{s} = 7$ TeV*
  CMS-Collaboration, S. Chatrchyan *et al.*, JHEP **1212**, 035 (2012)

- *Search for resonant $t\bar{t}$ production in lepton+jets events in pp collisions at $\sqrt{s} = 7$ TeV*
  CMS-Collaboration, S. Chatrchyan *et al.*, JHEP **1212**, 015 (2012)

- *Search for the standard model Higgs boson produced in association with W and Z bosons in pp collisions at $\sqrt{s} = 7$ TeV*
  CMS-Collaboration, S. Chatrchyan *et al.*, JHEP **1211**, 088 (2012)

- *Search for a narrow spin-2 resonance decaying to a pair of Z vector bosons in the semileptonic final state*
  CMS-Collaboration, S. Chatrchyan *et al.*, Phys. Lett. B **718**, 1208 (2013)

- *Measurement of the top-quark mass in $t\bar{t}$ events with dilepton final states in pp collisions at $\sqrt{s} = 7$ TeV*
  CMS-Collaboration, S. Chatrchyan *et al.*, Eur. Phys. J. C **72**, 2202 (2012)

- *Measurement of the top-quark mass in $t\bar{t}$ events with lepton+jets final states in pp collisions at $\sqrt{s} = 7$ TeV*
  CMS-Collaboration, S. Chatrchyan *et al.*, JHEP **1212**, 105 (2012)

- *Observation of a diffractive contribution to dijet production in proton-proton collisions at $\sqrt{s} = 7$ TeV"*
  CMS-Collaboration, S. Chatrchyan *et al.*, Phys. Rev. D **87**, 012006 (2013)

- *Search for exclusive or semi-exclusive photon pair production and observation of exclusive and semi-exclusive electron pair production in pp collisions at $\sqrt{s} = 7$ TeV*
  CMS-Collaboration, S. Chatrchyan *et al.*, JHEP **1211**, 080 (2012)

- *Combined search for the quarks of a sequential fourth generation*
  CMS-Collaboration, S. Chatrchyan *et al.*, Phys. Rev. D **86**, 112003 (2012)

- *Search for pair produced fourth-generation up-type quarks in pp collisions at $\sqrt{s} = 7$ TeV with a lepton in the final state*
  CMS-Collaboration, S. Chatrchyan *et al.*, Phys. Lett. B **718**, 307 (2012)

- *Search for supersymmetry in events with b-quark jets and missing transverse energy in pp collisions at 7 TeV*
  CMS-Collaboration, S. Chatrchyan *et al.*, Phys. Rev. D **86**, 072010 (2012)

- *Study of the dijet mass spectrum in $pp \to W+$ jets events at $\sqrt{s} = 7$ TeV*
  CMS-Collaboration, S. Chatrchyan *et al.* , Phys. Rev. Lett. **109**, 251801 (2012)

- *Search for three-jet resonances in pp collisions at $\sqrt{s} = 7$ TeV*
  CMS-Collaboration, S. Chatrchyan *et al.*, Phys. Lett. B **718**, 329 (2012)

- *Observation of sequential Upsilon suppression in PbPb collisions*
  CMS-Collaboration, S. Chatrchyan *et al.*, Phys. Rev. Lett. **109**, 222301 (2012)

- *Measurement of the $t\bar{t}$ production cross section in the dilepton channel in pp collisions at $\sqrt{s} = 7$ TeV*
  CMS-Collaboration, S. Chatrchyan *et al.*, JHEP **1211**, 067 (2012)

- *Search for flavor changing neutral currents in top quark decays in pp collisions at 7 TeV*
  CMS-Collaboration, S. Chatrchyan *et al.*, Phys. Lett. B **718**, 1252 (2013)

- *Search for a W ' boson decaying to a bottom quark and a top quark in pp collisions at $\sqrt{s} = 7$ TeV*
  CMS-Collaboration, S. Chatrchyan *et al.*, Phys. Lett. B **718**, 1229 (2013)

- *Observation of a new boson at a mass of 125 GeV with the CMS experiment at the LHC*
  CMS-Collaboration, S. Chatrchyan *et al.*, Phys. Lett. B **716**, 30 (2012)

- *Search for heavy Majorana neutrinos in $\mu^+\mu^+[\mu^-\mu^-]$ and $e^+e^+[e^-e^-]$ events in pp collisions at $\sqrt{s} = 7$ TeV*
  CMS-Collaboration, S. Chatrchyan *et al.*, Phys. Lett. B **717**, 109 (2012)

- *Search for pair production of first- and second-generation scalar leptoquarks in pp collisions at $\sqrt{s} = 7$ TeV*
  CMS-Collaboration, S. Chatrchyan *et al.*, Phys. Rev. D **86**, 052013 (2012)

- *Study of the inclusive production of charged pions, kaons, and protons in pp collisions at $\sqrt{s} = 0.9$, 2.76, and 7 TeV*
  CMS-Collaboration, S. Chatrchyan *et al.*, Eur. Phys. J. C **72**, 2164 (2012)

- *Forward-backward asymmetry of Drell-Yan lepton pairs in pp collisions at $\sqrt{s} = 7$ TeV*
  CMS-Collaboration, S. Chatrchyan *et al.*, Phys. Lett. B **718**, 752 (2013)

- *A search for a doubly-charged Higgs boson in pp collisions at $\sqrt{s} = 7$ TeV*
  CMS-Collaboration, S. Chatrchyan *et al.*, Eur. Phys. J. C **72**, 2189 (2012)

- *Measurement of the underlying event activity in pp collisions at $\sqrt{s} = 0.9$ and 7 TeV with the novel jet-area/median approach*
  CMS-Collaboration, S. Chatrchyan *et al.*, JHEP **1208**, 130 (2012)

- *Search for new physics in the multijet and missing transverse momentum final state in proton-proton collisions at $\sqrt{s} = 7$ TeV*
  CMS-Collaboration, S. Chatrchyan *et al.*, Phys. Rev. Lett. **109**, 171803 (2012)

- *Search for supersymmetry in hadronic final states using MT2 in pp collisions at $\sqrt{s} = 7$ TeV*
  CMS-Collaboration, S. Chatrchyan *et al.*, JHEP **1210**, 018 (2012)

- *earch for a fermiophobic Higgs boson in pp collisions at $\sqrt{s} = 7$ TeV*
  CMS-Collaboration, S. Chatrchyan *et al.*, JHEP **1209**, 111 (2012)

- *Search for new physics with long-lived particles decaying to photons and missing energy in pp collisions at $\sqrt{s} = 7$ TeV*
  CMS-Collaboration, S. Chatrchyan *et al.*, JHEP **1211**, 172 (2012)

- *Search for stopped long-lived particles produced in pp collisions at $\sqrt{s} = 7$ TeV*
  CMS-Collaboration, S. Chatrchyan *et al.*, JHEP **1208**, 026 (2012)

- *Inclusive and differential measurements of the $t\bar{t}$ charge asymmetry in proton-proton collisions at 7 TeV*
  CMS-Collaboration, S. Chatrchyan *et al.*, Phys. Lett. B **717**, 129 (2012)

- *Search for a light pseudoscalar Higgs boson in the dimuon decay channel in pp collisions at $\sqrt{s} = 7$ TeV*
  CMS-Collaboration, S. Chatrchyan *et al.*, Phys. Rev. Lett. **109**, 121801 (2012)

- *Search for dark matter and large extra dimensions in monojet events in pp collisions at $\sqrt{s} = 7$ TeV*
  CMS-Collaboration, S. Chatrchyan *et al.*, JHEP **1209**, 094 (2012)

- *Performance of CMS muon reconstruction in pp collision events at $\sqrt{s} = 7$ TeV*
  CMS-Collaboration, S. Chatrchyan *et al.*, JINST **7**, P10002 (2012)

- *Search for new physics in events with opposite-sign leptons, jets, and missing transverse energy in pp collisions at $\sqrt{s} = 7$ TeV*
  CMS-Collaboration, S. Chatrchyan *et al.*, Phys. Lett. B **718**, 815 (2013)

- *Search for charge-asymmetric production of W ' bosons in top pair + jet events from pp collisions at $\sqrt{s} = 7$ TeV*
  CMS-Collaboration, S. Chatrchyan *et al.*, Phys. Lett. B **717**, 351 (2012)

- *Measurement of the electron charge asymmetry in inclusive W production in pp collisions at $\sqrt{s} = 7$ TeV*
  CMS-Collaboration, S. Chatrchyan *et al.*, Phys. Rev. Lett. **109**, 111806 (2012)

- *Search for narrow resonances in dilepton mass spectra in pp collisions at $\sqrt{s} = 7$ TeV*
  CMS-Collaboration, S. Chatrchyan *et al.*, Phys. Lett. B **714**, 158 (2012)

- *Search for high mass resonances decaying into τ^- lepton pairs in pp collisions at $\sqrt{s} = 7$ TeV*
  CMS-Collaboration, S. Chatrchyan *et al.*, Phys. Lett. B **716**, 82 (2012)

- *Search for a W' or Techni-ρ Decaying into WZ in pp Collisions at $\sqrt{s} = 7$ TeV*
  CMS-Collaboration, S. Chatrchyan *et al.*, Phys. Rev. Lett. **109**, 141801 (2012)

- *Search for new physics with same-sign isolated dilepton events with jets and missing transverse energy*
  CMS-Collaboration, S. Chatrchyan *et al.*, Phys. Rev. Lett. **109**, 071803 (2012)

- *Study of W boson production in PbPb and pp collisions at $\sqrt{s_{NN}} = 2.76$ TeV*
  CMS-Collaboration, S. Chatrchyan *et al.*, Phys. Lett. B **715**, 66 (2012)

- *Measurement of jet fragmentation into charged particles in pp and PbPb collisions at $\sqrt{s_{NN}} = 2.76$ TeV*
  CMS-Collaboration, S. Chatrchyan *et al.*, JHEP **1210**, 087 (2012)

- *Search for a light charged Higgs boson in top quark decays in pp collisions at $\sqrt{s} = 7$ TeV*
  CMS-Collaboration, S. Chatrchyan *et al.*, JHEP **1207**, 143 (2012)

- *Search for new physics in events with same-sign dileptons and b-tagged jets in pp collisions at $\sqrt{s} = 7$ TeV*
  CMS-Collaboration, S. Chatrchyan *et al.*, JHEP **1208**, 110 (2012)

- *Measurement of the pseudorapidity and centrality dependence of the transverse energy density in PbPb collisions at $\sqrt{s_{NN}} = 2.76$ TeV*
  CMS-Collaboration, S. Chatrchyan *et al.*, Phys. Rev. Lett. **109**, 152303 (2012)

- *Measurement of the Λ_b cross section and the $\overline{\Lambda}_b$ to Λ_b ratio with Λ_b to J/Psi Λ^0 decays in pp collisions at $\sqrt{s} = 7$ TeV*
  CMS-Collaboration, S. Chatrchyan *et al.*, Phys. Lett. B **714**, 136 (2012)

- *Search for heavy long-lived charged particles in pp collisions at $\sqrt{s} = 7$ TeV*
  CMS-Collaboration, S. Chatrchyan *et al.*, Phys. Lett. B **713**, 408 (2012)

- *Studies of jet quenching using isolated-photon+jet correlations in PbPb and pp collisions at $\sqrt{s_{NN}} = 2.76$ TeV*
  CMS-Collaboration, S. Chatrchyan *et al.*, Phys. Lett. B **718**, 773 (2013)

- *Observation of a new Xi(b) baryon*
  CMS-Collaboration, S. Chatrchyan *et al.*, Phys. Rev. Lett. **108**, 252002 (2012)

- *Search for anomalous production of multilepton events in pp collisions at $\sqrt{s} = 7$ TeV*
  CMS-Collaboration, S. Chatrchyan *et al.*, JHEP **1206**, 169 (2012)

- *Search for leptonic decays of W ' bosons in pp collisions at $\sqrt{s} = 7$ TeV*
  CMS-Collaboration, S. Chatrchyan *et al.*, JHEP **1208**, 023 (2012)

- *Search for physics beyond the standard model in events with a Z boson, jets, and missing transverse energy in pp collisions at $\sqrt{s} = 7$ TeV*
  CMS-Collaboration, S. Chatrchyan *et al.*, Phys. Lett. B **716**, 260 (2012)

- *Shape, transverse size, and charged hadron multiplicity of jets in pp collisions at 7 TeV*
  CMS-Collaboration, S. Chatrchyan *et al.*, JHEP **1206**, 160 (2012)

- *Measurement of the mass difference between top and antitop quarks*
  CMS-Collaboration, S. Chatrchyan *et al.*, JHEP **1206**, 109 (2012)

- *Search for anomalous t t-bar production in the highly-boosted all-hadronic final state*
  CMS-Collaboration, S. Chatrchyan *et al.*, JHEP **1209**, 029 (2012)

- *Azimuthal anisotropy of charged particles at high transverse momenta in PbPb collisions at* $\sqrt{s_{NN}} = 2.76$ *TeV*
  CMS-Collaboration, S. Chatrchyan *et al.*, Phys. Rev. Lett. **109**, 022301 (2012)

- *Measurement of the* $\mathrm{Z}/\gamma^* + \mathrm{b\ jet}$ *cross section in pp collisions at 7 TeV*
  CMS-Collaboration, S. Chatrchyan *et al.*, JHEP **1206**, 126 (2012)

- *Measurement of the elliptic anisotropy of charged particles produced in PbPb collisions at nucleon-nucleon center-of-mass energy = 2.76 TeV*
  CMS-Collaboration, S. Chatrchyan *et al.*, Phys. Rev. C **87**, 014902 (2013)

- *Measurement of the underlying event in the Drell-Yan process in proton-proton collisions at* $\sqrt{s} = 7$ *TeV*
  CMS-Collaboration, S. Chatrchyan *et al.*, Eur. Phys. J. C **72**, 2080 (2012)

- *Search for heavy bottom-like quarks in 4.9 inverse femtobarns of* pp *collisions at* $\sqrt{s} = 7$ *TeV*
  CMS-Collaboration, S. Chatrchyan *et al.*, JHEP **1205**, 123 (2012)

- *Search for Dark Matter and Large Extra Dimensions in pp Collisions Yielding a Photon and Missing Transverse Energy*
  CMS-Collaboration, S. Chatrchyan *et al.*, Phys. Rev. Lett. **108**, 261803 (2012)

- *Ratios of dijet production cross sections as a function of the absolute difference in rapidity between jets in proton-proton collisions at* $\sqrt{s} = 7$ *TeV*
  CMS-Collaboration, S. Chatrchyan *et al.*, Eur. Phys. J. C **72**, 2216 (2012)

Articles in press

- *Search for a standard-model-like Higgs boson with a mass of up to 1 TeV at the LHC*
  CMS-Collaboration, S. Chatrchyan*et al.*, arXiv:1304.0213

- *Measurement of the Y(1S), Y(2S), and Y(3S) cross sections in pp collisions at* $\sqrt{s}$ *= 7 TeV*
  CMS-Collaboration, S. Chatrchyan*et al.*, arXiv:1303.5900

- *Search for microscopic black holes in pp collisions at sqrt(s) = 8 TeV*
  CMS-Collaboration, S. Chatrchyan*et al.*, arXiv:1303.5338

- *Studies of jet mass in dijet and W/Z+jet events*
  CMS-Collaboration, S. Chatrchyan*et al.*, arXiv:1303.4811

- *Observation of a new boson with mass near 125 GeV in pp collisions at sqrt(s) = 7 and 8 TeV*
  CMS-Collaboration, S. Chatrchyan*et al.*, arXiv:1303.4571

- *Measurement of associated production of vector bosons and t t-bar at sqrt(s)= 7 TeV*
  CMS-Collaboration, S. Chatrchyan*et al.*, arXiv:1303.3239

- *Search for supersymmetry in hadronic final states with missing transverse energy using the variables* α_T *and b-quark multiplicity in pp collisions at* $\sqrt{s}$ *= 8 TeV*
  CMS-Collaboration, S. Chatrchyan*et al.*, arXiv:1303.2985

- *Search for the standard model Higgs boson produced in association with a top-quark pair in pp collisions at the LHC*
  CMS-Collaboration, S. Chatrchyan*et al.*, arXiv:1303.0763

- *Search for narrow resonances using the dijet mass spectrum in pp collisions at sqrt(s) = 8 TeV*
  CMS-Collaboration, S. Chatrchyan*et al.*, arXiv:1302.4794

- *Measurement of the X(3872) production cross section via decays to J/psi pi pi in pp collisions at sqrt(s) = 7 TeV*
  CMS-Collaboration, S. Chatrchyan*et al.*, arXiv:1302.3968

- *Search for a Higgs boson decaying into a b-quark pair and produced in association with b quarks in proton-proton collisions at 7 TeV*
  CMS-Collaboration, S. Chatrchyan*et al.*, arXiv:1302.2892

- *Search for new physics in final states with a lepton and missing transverse energy in pp collisions at the LHC*
  CMS-Collaboration, S. Chatrchyan*et al.*, arXiv:1302.2812

- *Study of the underlying event at forward rapidity in pp collisions at sqrt(s) = 0.9, 2.76, and 7 TeV*
  CMS-Collaboration, S. Chatrchyan*et al.*, arXiv:1302.2394

- *Searches for Higgs bosons in pp collisions at sqrt(s) = 7 and 8 TeV in the context of four-generation and fermiophobic models*
  CMS-Collaboration, S. Chatrchyan*et al.*, arXiv:1302.1764

- *Search for pair-produced dijet resonances in four-jet final states in pp collisions at sqrt(s) = 7 TeV*
  CMS-Collaboration, S. Chatrchyan*et al.*, arXiv:1302.0531

- *Measurement of the ttbar production cross section in the all-jet final state in pp collisions at sqrt(s) = 7 TeV*
  CMS-Collaboration, S. Chatrchyan*et al.*, arXiv:1302.0508

- *Measurement of the top-antitop production cross section in the tau+jets channel in pp collisions at sqrt(s) = 7 TeV*
  CMS-Collaboration, S. Chatrchyan*et al.*, arXiv:1301.5755

- *Measurement of W+W- and ZZ production cross sections in pp collisions at sqrt(s)=8 TeV*
  CMS-Collaboration, S. Chatrchyan*et al.*, arXiv:1301.4698

- *Search for physics beyond the standard model in events with tau leptons, jets, and large transverse momentum imbalance in pp collisions at sqrt(s) = 7 TeV*
  CMS-Collaboration, S. Chatrchyan*et al.*, arXiv:1301.3792

- *Interpretation of searches for supersymmetry with simplified models*
  CMS-Collaboration, S. Chatrchyan*et al.*, arXiv:1301.2175

- *Event shapes and azimuthal correlations in Z + jets events in pp collisions at $\sqrt{s} = 7$ TeV*
  CMS-Collaboration, S. Chatrchyan*et al.*, arXiv:1301.1646

- *Search for supersymmetry in events with opposite-sign dileptons and missing transverse energy using an artificial neural network*
  CMS-Collaboration, S. Chatrchyan*et al.*, arXiv:1301.0916

- *Search for supersymmetry in pp collisions at $\sqrt{s} = 7$ TeV in events with a single lepton, jets, and missing transverse momentum*
  CMS-Collaboration, S. Chatrchyan*et al.*, arXiv:1212.6428

- *Measurements of differential jet cross sections in proton-proton collisions at $\sqrt{s} = 7$ TeV with the CMS detector*
  CMS-Collaboration, S. Chatrchyan*et al.*, arXiv:1212.6660

- *Inclusive search for supersymmetry using the razor variables in pp collisions at $\sqrt{s} = 7$ TeV*
  CMS-Collaboration, S. Chatrchyan*et al.*, arXiv:1212.6961

- *Search for heavy resonances in the W/Z-tagged dijet mass spectrum in pp collisions at 7 TeV*
  CMS-Collaboration, S. Chatrchyan*et al.*, arXiv:1212.1910

- *Search for long-lived particles decaying to photons and missing energy in proton-proton collisions at $\sqrt{s} = 7$ TeV*
  CMS-Collaboration, S. Chatrchyan*et al.*, arXiv:1212.1838

- *Identification of b-quark jets with the CMS experiment*
  CMS-Collaboration, S. Chatrchyan*et al.*, arXiv:1211.4462

- *Search for Z' resonances decaying to $t\bar{t}$ in dilepton+jets final states in pp collisions at $\sqrt{s} = 7$ TeV*
  CMS-Collaboration, S. Chatrchyan*et al.*, arXiv:1211.3338

- *Measurement of differential top-quark pair production cross sections in pp colisions at $\sqrt{s} = 7$ TeV*
  CMS-Collaboration, S. Chatrchyan*et al.*, arXiv:1211.2220

- *Search for a non-standard-model Higgs boson decaying to a pair of new light bosons in four-muon final states*
  CMS-Collaboration, S. Chatrchyan*et al.*, arXiv:1210.7619

- *Measurement of the inelastic proton-proton cross section at $\sqrt{s} = 7$ TeV*
  CMS-Collaboration, S. Chatrchyan*et al.*, arXiv:1210.6718

- *Search for fractionally charged particles in pp collisions at $\sqrt{s} = 7$ TeV*
  CMS-Collaboration, S. Chatrchyan*et al.*, arXiv:1210.2311

- *Search for supersymmetry in events with photons and low missing transverse energy in pp collisions at $\sqrt{s} = 7$ TeV*
  CMS-Collaboration, S. Chatrchyan*et al.*, Phys. Lett. B.

- *Search for anomalous production of highly boosted Z bosons decaying to dimuons in pp collisions at $\sqrt{s} = 7$ TeV*
  CMS-Collaboration, S. Chatrchyan*et al.*, Phys. Lett. B.

- *Evidence for associated production of a single top quark and W boson in pp collisions at 7 TeV*
  CMS-Collaboration, S. Chatrchyan*et al.*, Phys. Rev. Lett.

- *Measurement of the Y(1S), Y(2S) and Y(3S) polarizations in pp collisions at $\sqrt{s} = 7$ TeV*
  CMS-Collaboration, S. Chatrchyan*et al.*, arXiv:1209.2922

- *Measurement of the azimuthal anisotropy of neutral pions in PbPb collisions at $\sqrt{s_{NN}} = 2.76$ TeV*
  CMS-Collaboration, S. Chatrchyan*et al.*, arXiv:1208.2470

Lectures

- Vincenzo Chiochia: *Measurements of top quark properties and decays at the Tevatron and LHC*
  Flavor Physics and CP violation conference, Hefei, China, 21 May 2012.

- Vincenzo Chiochia: *Observation of a new Ξ_b baryon with the CMS experiment*
  Colloquium on Particle Physics, PSI, Villigen, Switzerland, 18 October 2012.

- Vincenzo Chiochia: *Rare B decays at LHC and Tevatron*
  Hadron Collider Physics Symposium, Kyoto, Japan, 12 November 2012.

- Vincenzo Chiochia: *Heavy flavor physics with the CMS experiment*
  Saha Institute for Nuclear Physics (Kolkata), Indian Institute of Technology and Tata Institute of Fundamental Research (Mumbai), 5 – 8 March 2013.

- Simon de Visscher: *Heavy flavor production in association with vector bosons at CMS*
  Workshop of the LHC Electroweak working group, CERN, 2 April 2012.

- Simon de Visscher: *Heavy flavor production in association with vector bosons in CMS*
  36th International Conference on High Energy Physics, Melbourne, Australia, 4 July 2012.

- Carlotta Favaro: *Angular correlation between B-hadrons produced in association with a Z boson at the CMS experiment*
  Swiss Physical Society, ETH-Zurich, 22 June 2012.

- Carlotta Favaro: *Heavy flavor and vector bosons associated production at CMS*
  16th International Conference in Quantum Chromodynamics, Montpellier, France, 2 July 2012.

- Carlotta Favaro: *Vector boson and heavy flavor associated production at CMS*
  Lake Louise Winter Institute, Lake Louise, Canada, 17 February 2013.

- Mirena Ivova Rikova: *b-baryon studies at the CMS Experiment*
  Swiss Physical Society, ETH-Zurich, 22 June 2012.

- Barbara Millán Mejías: *Measurement of lifetime difference* $\Delta\Gamma_s$ *in the decay* $B_s \to J/\psi\phi \to \mu^+\mu^-K^+K^-$
  Swiss Physical Society, ETH-Zurich, 22 June 2012.

- H. Snoek: *Production of* b *hadrons and* b*-jet cross sections at CMS*
  Heavy Flavor Production Workshop, Berkeley, USA, 14 January 2013.

- Mauro Verzetti: *Search for 2HDM Higgs boson decaying into* τ *pairs at CMS*
  Swiss Physical Society, ETH-Zurich, 22 June 2012.

20.1.10 Miscellaneous

Articles

- *Further Evidence for Low Energy Protonium Production in Vacuum*
  E. Lodi Rizzini *et al.* (ATHENA Collaboration), Eur. Phys. J. **Plus** (2012) 127.

- *The Review of Particle Physics*
  J. Beringer *et al.* (Particle Data Group), Phys. Rev. **D86** (2012) 010001.

- *Note on scalar mesons below 2 GeV*
  C. Amsler, S. Eidelman, T. Gutsche, C. Hanhart, S. Spanier and N. A. Törnqvist, Phys. Rev. **D86** (2012) 706.

- *The* $\eta(1405)$, $\eta(1475)$, $f_1(1420)$, *and* $f_1(1510)$
  C. Amsler and A. Masoni, Phys. Rev. **D86** (2012) 759.

- *Quark Model*
  C. Amsler, T. DeGrand and B. Krusche, Phys. Rev. **D86** (2012) 199.

- *Recent studies of top quark properties and decays at hadron colliders*
  V. Chiochia, Mod. Phys. Lett. **A 27** (2012) 1230036.

- *Studies of rare* B *hadron decays to leptons at hadron colliders*
  V. Chiochia, arXiv:1302.2205

Article in press

- *Heavy flavour and vector bosons associated production*
  C. Favaro. CMS CR -2012/185.

Lectures

- A. van der Schaaf: *Lepton and Meson Decay beyond the Standard Model*
  two lectures at the FANTOM International Research School, Leuven, Belgium, June 4 - 8 2012.

- L. Baudis: *Die dunkle Seite des Universums*
  Flying Science, Verkehrsdepartement Basel, December 20, 2012.

- L. Baudis: *Geheimnisse des dunklen Universums*
  Thematische Kaffeepause, Swiss National Foundation, Bern, December 10, 2012.

- L. Baudis: *Dunkle Materie*
  Lecture for high-school teachers, Fachkonferenz Physik, Kantonsschule Enge, Zurich, November 15, 2012.

- L. Baudis: *Dunkle Materie im Universums*
  Ringvorlesung: die Welt der Quanten, Volkshochschule Zurich, May 30, 2012.

- L. Baudis: *Die dunkle Seite des Universums*
  Astronomische Gesellschaft Bern, Bern University, May 28, 2012.

20.2 Condensed matter

20.2.1 Superconductivity and Magnetism

Articles

- *Pressure-induced ferromagnetism in antiferromagnetic $Fe_{1.03}Te$*
  M. Bendele, A. Maisuradze, B. Roessli, S.N. Gvasaliya, E. Pomjakushina, S. Weyeneth, K. Conder, H. Keller, and R. Khasanov, Phys. Rev. B **87**, 060409(R) (2013).

- *Vortex lock-in transition coinciding with the 3D to 2D crossover in $YBa_2Cu_3O_{7-\delta}$*
  S. Bosma, S. Weyeneth, R. Puzniak, A. Erb, and H. Keller, Phys. Rev. B **86**, 174502 (2012).

- *Erratum: Vortex lock-in transition coinciding with the 3D to 2D crossover in $YBa_2Cu_3O_7$*
  S. Bosma, S. Weyeneth, R. Puzniak, A. Erb, and H. Keller, Phys. Rev. B **87**, 059901 (2013).

- *Hybrid paramagnon phonon modes at elevated temperatures in $EuTiO_3$*
  A. Bussmann-Holder, Z. Guguchia, J. Köhler, H. Keller, A. Shengelaya, and A.R. Bishop, New Journal of Physics **14**, 093013 (2012).

- *Isotope and multiband effects in layered superconductors*
  A. Bussmann-Holder, and H. Keller, J. Phys.: Condens. Matter **24**, 233201 (2012).

- *Polaron signatures in the phonon dispersion of high-temperature superconducting copper oxides*
  A. Bussmann-Holder, A. Simon, H. Keller, and A.R. Bishop, Europhys. Lett. **101**, 47004 (2013).

- *Direct Observation of the Quantum Critical Point in Heavy Fermion $CeRhSi_3$*
  N. Egetenmeyer, J.L. Gavilano, A. Maisuradze, S. Gerber, D.E. MacLaughlin, G. Seyfarth, D. Andreica, A. Desilets-Benoit, A.D. Bianchi, Ch. Baines, R. Khasanov, Z. Fisk, and M. Kenzelmann, Phys. Rev. Lett. **108**, 177204 (2012).

- *Conventional superconductivity and hysteretic Campbell penetration depth in single crystals $MgCNi_3$*
  R. T. Gordon, N. D. Zhigadlo, S. Weyeneth, S. Katrych, and R. Prozorov, Phys. Rev. B. **87**, 094520 (2013).

- *Magnetic field enhanced structural instability in $EuTiO_3$*
  Z. Guguchia, H. Keller, J. Köhler, and A. Bussmann-Holder, J. Phys.: Condens. Matter **24**, 492201 (2012).

- *Tuning the structural instability of $SrTiO_3$ by Eu doping: The phase diagram of $Sr_{1-x}Eu_xTiO_3$*
  Z. Guguchia, A. Shengelaya, H. Keller, J. Köhler, and A. Bussmann-Holder, Phys. Rev. B **85**, 134113 (2012).

- *Muon-Spin Rotation and Magnetization Studies of Chemical and Hydrostatic Pressure Effects in $EuFe_2(As_{1-x}P_x)_2$*
  Z. Guguchia, A. Shengelaya, A. Maisuradze, L. Howald, Z. Bukowski, M. Chikovani, H. Luetkens, S. Katrych, J. Karpinski, and H. Keller, J. Supercond. Nov. Magn. **26**, 285-295 (2013).

- *Muon-Spin Rotation Measurements of an Unusual Vortex-Glass Phase in the Layered Superconductor $Bi_{2.15}Sr_{1.85}CaCu_2O_{8+\delta}$*
  D.O.G. Heron, S.J. Ray, S.J. Lister, C.M. Aegerter, H. Keller, P.H. Kes, G.I. Menon, and S.L. Lee, Phys. Rev. Lett. **110**, 107004 (2013).

- *Strong Pressure Dependence of the Magnetic Penetration Depth in Single Crystals of the Heavy-Fermion Superconductor CeCoIn5 Studied by Muon Spin Rotation*
  L. Howald, A. Maisuradze, P. Dalmas de Réotier, A. Yaouanc, C. Baines, G. Lapertot, K. Mony, J.-P. Brison, and H. Keller, Phys. Rev. Lett. **110**, 017005 (2013).

- *Effect of external pressure on T_c of as-grown and thermally treated superconducting $Rb_xFe_{2y}Se_2$ single crystals*
  M. Kanagaraj, A. Krzton-Maziopa, G. Kalai Selvan, E. Pomjakushina, K. Conder, S. Weyeneth, R. Puzniak, and S. Arumugam, Phys. Stat. Sol. **7**, 218 (2013).

- *Effect of pressure on the Cu and Pr magnetism in $Nd_{1-x}Pr_xBa_2Cu_3O_{7-\delta}$ investigated by muon spin rotation*
  A. Maisuradze, B. Graneli, Z. Guguchia, A. Shengelaya, E. Pomjakushina, K. Conder, and H. Keller, Phys. Rev. B **87**, 054401 (2013).

- *Superconducting parameters of $BaPt_{4-x}Au_xGe_{12}$ filled skutterudite*
  A. Maisuradze, R. Gumeniuk, W. Schnelle, M. Nicklas, C. Baines, R. Khasanov, A. Amato, and A. Leithe-Jasper, Phys. Rev. B **86**, 174513 (2012).

- *Magnetoelectric Coupling in Single Crystal Cu_2OSeO_3 Studied by a Novel Electron Spin Resonance Technique*
  A. Maisuradze, A. Shengelaya, H. Berger, D.M. Djokić, and H. Keller, Phys. Rev. Lett. **108**, 247211 (2012).

- *Magnetic form factor, field map, and field distribution for a BCS type-II superconductor near its $B_{c2}(T)$ phase boundary*
  A. Maisuradze and A. Yaouanc, Phys. Rev. B **87**, 134508 (2013).

- *Relaxation of the shallow acceptor center in germanium*
  T.N. Mamedov, A.S. Baturin, V.N. Duginov, K.I. Gritsaj, R. Khasanov, A. Maisuradze, and A.V. Stoykov, JETP Letters **95**, 662 (2012).

- *Effect of external pressure on the magnetic properties of LnFeAsO (Lnă=ăLa, Ce, Pr, Sm)*
  R. De Renzi, P. Bonfà, M. Mazzani, S. Sanna, G. Prando, P. Carretta, R. Khasanov, A. Amato, H. Luetkens, M. Bendele, F. Bernardini, S. Massidda, A. Palenzona, M. Tropeano, and M. Vignolo, Supercond. Sci. Technol. **25**, 084009 (2012).

- *Superfluid density and superconducting gaps of $RbFe_2As_2$ as a function of hydrostatic pressure*
  Z. Shermadini, H. Luetkens, A. Maisuradze, R. Khasanov, Z. Bukowski, H.-H. Klauss, and A. Amato, Phys. Rev. B **86**, 174516 (2012).

- *Hidden magnetic order in CuNCN*
  A.A. Tsirlin, A. Maisuradze, J. Sichelschmidt, W. Schnelle, P. Höhn, R. Zinke, J. Richter, and H. Rosner, Phys. Rev. B **85**, 224431 (2012).

- *Spin excitations and electron paramagnetic resonance in two-layer antiferromagnetic system $Y_{1-x}Yb_xBa_2Cu_3O_{6+y}$*
  A.A. Vishina, A. Maisuradze, A. Shengelaya, B.I. Kochelaev, and H Keller, J. Phys.: Conf. Ser. **394** , 012014 (2012).

- *An endohedral single-molecule magnet with long relaxation times: $DySc_2N@C_{80}$*
  R. Westerström, J. Dreiser, C. Piamonteze, M. Muntwiler, S. Weyeneth, H. Brune, S. Rusponi, F. Nolting, A. Popov, S.-F. Yang, L. Dunsch, and T. Greber, J. Am. Chem. Soc. **134**, 9840-9843 (2012).

- *Superconductivity and magnetism in $Rb_xFe_{2-y}Se_2$: Impact of thermal treatment on mesoscopic phase separation*
  S. Weyeneth, M. Bendele, F. von Rohr, P. Dluzewski, R. Puzniak, A. Krzton-Maziopa, S. Bosma, Z. Guguchia, R. Khasanov, Z. Shermadini, A. Amato, E. Pomjakushina, K. Conder, A. Schilling, and H. Keller, Phys. Rev. B **86**, 134530 (2012).

- *Influence of short-range spin correlations on the μSR polarization functions in the slow dynamic limit: Application to the quantum spin-liquid system $Yb_2Ti_2O_7$*
  A. Yaouanc, A. Maisuradze, and P. Dalmas de Réotier, Phys. Rev. B **87**, 134405 (2013).

- *High-pressure flux growth, structural, and superconducting properties of LnFeAsO (Ln = Pr, Nd, Sm) single crystals*
  N. D. Zhigadlo, S. Weyeneth, S. Katrych, P. J. W. Moll, K. Rogacki, S. Bosma, R. Puzniak, J. Karpinski, and B. Batlogg, Phys. Rev. B. **86**, 214509 (2012).

Conference reports

- *Magnetic field tuned anisotropy in $Rb_xFe_{2-y}Se_2$*
  S. Bosma, R. Puzniak, A. Krzton-Maziopa, M. Bendele, E. Pomjakushina, K. Conder, H. Keller, and S. Weyeneth, Annual meeting of the Swiss Physical Society, Zürich, Switzerland, June 21 - 22, 2012.

- *Muon-spin rotation and magnetization studies of chemical and hydrostatic pressure effects in $EuFe_2(As_{1-x}P_x)_2$*
  Z. Guguchia, A. Shengelaya, A. Maisuradze, L. Howald, S. Weyeneth, Z. Bukowski, M. Chikovani, H. Luetkens, S. Katrych, J. Karpinski, and H.Keller, Annual meeting of the Swiss Physical Society, Zürich, Switzerland, June 21 - 22, 2012.

- *μSR investigation of magnetism and magnetoelectric coupling in Cu_2OSeO_3*
  A. Maisuradze, Z. Guguchia, B. Graneli, H. M. Rønnow, H. Berger, and H. Keller,
  Annual meeting of the Swiss Physical Society, Zürich, Switzerland, June 21 - 22, 2012.

- *Pressure dependence of the penetration depth in $CeCoIn_5$ studied by muon spin rotation*
  L. Howald, Annual meeting of the Swiss Physical Society, Zürich, Switzerland, June 21 - 22, 2012.

- *Tuning the static spin-stripe phase and superconductivity in $La_{2-x}Ba_xCuO_4$ ($x = 1/8$) by hydrostatic pressure*
  Z. Guguchia, 5th Georgian-German School and Workshop in Basic Science, Tbilisi State University, Georgia, August 6 - 10, 2012.

- *Effect of photo-induced hole doping on the Meissner screening in underdoped $YBa_2Cu_3O_{7-\delta}$*
  E. Stilp, A. Suter, E. Morenzoni, T. Prokscha, Z. Salman, H. Keller, P. Pahlke, R. Hühne, J. C. Baglo, R. Liang, and R. F. Kiefl, German Physical Society (DPG) Spring Meeting, Regensburg, Germany, March 10 - 15, 2013.

- *Vortex lock-in transition coinciding with the 3D to 2D crossover in $YBa_2Cu_3O_{7-\delta}$*
  S. Bosma, S. Weyeneth, R. Puzniak, A. Erb, and H. Keller,
  APS March Meeting, Baltimore, USA, March 18 - 22, 2013.

- *Magnetic field enhanced structural instability in $EuTiO_3$*
  Z. Guguchia, APS March Meeting, Baltimore, USA, March 18 - 22, 2013.

- *Tuning the static spin-stripe phase and superconductivity in $La_{2-x}Ba_xCuO_4$ ($x = 1/8$) by hydrostatic pressure*
  Z. Guguchia, APS March Meeting, Baltimore, USA, March 18 - 22, 2013.

- *Magnetoelectric Coupling in Single Crystal Cu_2OSeO_3 Studied by a Novel Electron Spin Resonance Technique*
  A. Maisuradze, A. Shengelaya, H. Berger, D. M. Djokić, and H. Keller,
  Annual meeting of the American Physical Society, Baltimore, USA, March 18 - 22, 2013.

- *Strong pressure dependence of the magnetic penetration depth in single crystals of the heavy fermion system $CeCoIn_5$ studied by muon spin rotation*
  L. Howald, A. Maisuradze, P. Dalmas de Réotier, A. Yaouanc, C. Baines, G. Lapertot, K. Mony, J.-P. Brison, and H. Keller, APS March Meeting, Baltimore, USA, March 18 - 22, 2013.

Invited lectures

- H. Keller: *The Race of Spins - the Raser*
  Institute for Biomedical Engineering, University and ETH Zurich, Zürich, Switzerland, April 20, 2012.

- M. Bendele: *Tuning the Superconducting and Magnetic Properties of $Fe_ySe_{1-x}Te_x$*
  Int. Conference on Superconductivity and Magnetism, ICSM 2012, Istanbul, Turkey, April 29 - May 4, 2012.

- H. Keller: *Isotope and pressure effects in layered high-temperature superconductors*
  Int. Conference on Superconductivity and Magnetism, ICSM 2012, Istanbul, Turkey, April 29 - May 4, 2012.

- S. Weyeneth: *Interplay of anisotropic superconductivity and magnetism in iron-based compounds*
  Int. Conference on Superconductivity and Magnetism, ICSM 2012, Istanbul, Turkey, April 29 - May 4, 2012.

- Z. Guguchia: *Muon Spin Rotation technique and its applications in superconductivity and magnetism*
  5th Georgian-German School and Workshop in Basic Science, Batumi State University, Georgia, August 13 - 17, 2012.

- A. Maisuradze: *Muon spin rotation (μSR) and ferromagnetic resonance (FMR) study of magneto-electric Cu_2OSeO_3*
  Institute of Condensed Matter Physics, EPF Lausanne, Switzerland, February 27, 2013.

- A. Maisuradze and H. Keller: *Pressure effects in cuprate and iron-based superconductors studied by muon spin rotation*
  Annual meeting of the American Physical Society, Baltimore, USA, March 18 - 22, 2013.

- H. Keller: *Pressure effects in unconventional superconductors studied by muon spin rotation*
  Int. Conference on Study of Matter at Extreme Conditions, SMEC 2013, Miami, USA, March 23 - 30, 2013.

20.2.2 Phase transitions and superconducting photon detectors

Articles

- *Ultra-thin TaN films for superconducting nanowire single-photon detectors*
  K. Il'in, M. Hofherr, D. Rall, M. Siegel, A. Semenov, A. Engel, K. Inderbitzin, A. Aeschbacher and A. Schilling, J. Low. Temp. Phys. **167** (2012) 809.

- *On Josephson effects in insulating spin systems*
  A. Schilling and H. Grundmann, Annals of Physics **327** (2012) 2301-2309.

- *Magnetoresistivity of thin $YBa_2Cu_3O_{7-\delta}$ films on sapphire substrate*
  P. Probst, K. Il'in, A. Engel, A. Semenov, H.-W. Hübers, J. Hänisch, B. Holzapfel and M. Siegel, Physica C **479** (2012) 173-175.

- *Synthesis of a new alkali metal-organic solvent intercalated iron selenide superconductor with $T_c \approx 45$ K*
  A. Krzton-Maziopa, E.V. Pomjakushina, V.Yu. Pomjakushin, F. von Rohr, A. Schilling and K. Conder, J. Phys.: Condens. Matter **24** (2012) 382202.

- *Emergence of superconductivity in $BaNi_2(Ge_{1-x}P_x)_2$ at a structural instability*
  D. Hirai, F. von Rohr, and R.J. Cava, Phys. Rev. B. **86** (2012) 100505(R).

- *An ultra-fast superconducting Nb nanowire single-photon detector for soft X-rays*
  K. Inderbitzin, A. Engel, A. Schilling, K.Il'in and M. Siegel, Appl. Phys. Lett. **101** (2012) 162601.

- *Dependence of count rate on magnetic field in superconducting thin-film TaN single-photon detectors*
  A. Engel, A. Schilling, K. Il'in and M. Siegel, Phys. Rev. B **86** (2012) 140506(R).

- *Superconductivity and magnetism in $Rb_xFe_{2-y}Se_2$: Impact of thermal treatment on mesoscopic phase separation*
  S. Weyeneth, M. Bendele, F. von Rohr, P. Dluzewski, R. Puzniak, A. Krzton-Maziopa, S. Bosma, Z. Guguchia, R. Khasanov, Z. Shermadini, A. Amato, E. Pomjakushina, K. Conder, A. Schilling and H. Keller, Phys. Rev. B **86** (2012) 134530.

- *The effects of disorder in dimerized quantum magnets in mean field approximations*
  A. Rakhimov, S. Mardonov, E.Ya. Sherman and A. Schilling, New J. Phys. **14** (2012) 113010.

- *Estimates for the thermodynamic signatures of vortex-lattice melting in conventional superconductors*
  O. Bossen and A. Schilling, Physica C **483** (2012) 201-206.

- *Experimental tests for macroscopic phase coherence in magnetic-quasiparticle condensates of insulating spin systems*
  A. Schilling, H. Grundmann and R. Dell'Amore, J. Phys.: Conf. Ser. **400** (2012) 032081.

- *Single-crystal growth and thermoelectric properties of $Ge(Bi,Sb)_4Te_7$*
  F. von Rohr, A. Schilling, and R.J. Cava, J. Phys.: Condens. Matter **25** (2013) 075804.

- *Soft X-ray single-photon detection with superconducting tantalum nitride and niobium nanowires*
  K. Inderbitzin, A. Engel and A. Schilling, IEEE Trans. Appl. Supercond. **23** (2013) 2200505.

- *Temperature-dependence of detection efficiency in NbN and TaN SNSPD*
  A. Engel, K. Inderbitzin, A. Schilling, R. Lusche, A. Semenov, H.-W. Hübers, D. Henrich, M. Hofherr, K. Il'in and M. Siegel, IEEE Trans. Appl. Supercond. **23** (2013) 2300505.

Article in press

- *Structure and magnetic interaction in the solid solution $Ba_{3-x}Sr_xCr_2O_8$*
  H. Grundmann, A. Schilling, C.A. Marjerrison, H.A. Dabkowska and B.D. Gaulin, Mat. Res. Bull.

Contributed Conference Presentations

- *Mixed crystals from the quantum magnets $Ba_3Cr_2O_8$ and $Sr_3Cr_2O_8$ (Poster)*
  H. Grundmann, SPG Jahrestagung, ETH Zürich, 21./22.6.2012.

- *A thermal LC-circuit for measuing heat capacities (Poster)*
  O. Bossen, SPG Jahrestagung, ETH Zürich, 21./22.6.2012.

- *Ultrafast X-ray photon detection with niobium and TaN X-SNSPDs (Poster)*
  K. Inderbitzin, SPG Jahrestagung, ETH Zürich, 21./22.6.2012.

- *Temperature-Dependence of Detection Efficiency in NbN and TaN SNSPD (Poster)*
  A. Engel, SPG Jahrestagung, ETH Zürich, 21./22.6.2012.

- *Ultrafast Soft X-Ray Superconducting Nanowire Single-Photon Detectors*
  K. Inderbitzin, Trends in NanoTechnology 2012, Madrid (Spain), 12.9.2012.

- *X-Ray Single-Photon Detection With TaN and Niobium X-SNSPDs (Poster)*
  K. Inderbitzin, Applied Superconductivity Conference 2012, Portland (OR, USA), 11.10.2012.

- *Temperature-dependence of detection efficiency in NbN and TaN SNSPD*
  A. Engel, Applied Superconductivity Conference 2012, Portland (OR, USA), 11.10.2012.

20.2.3 Surface Physics

Articles

- *Three-dimensional spin rotation at the Fermi surface of a strongly spin-orbit coupled surface system*
  P. Höpfner, J. Schäfer, A. Fleszar, J. H. Dil, B. Slomski, F. Meier, C. Loho, C. Blumenstein, L. Patthey, W. Hanke, R. Claessen, Phys. Rev. Lett. 108, 186801:1-5 (2012).

- *An endohedral single-molecule magnet with long relaxation times: DyScN@C_{80}*
  R. Westerström, J. Dreiser, C. Piamonteze, M. Muntwiler, S. Weyeneth, H. Brune, S. Rusponi, F. Nolting, A. Popov, S. F. Yang, L. Dunsch, T. Greber, J. Am. Chem. Soc. 134, 9840-9843 (2012).

- *Attosecond transversal streaking to probe electron dynamics at surfaces*
  L. Castiglioni, D. Leuenberger, M. Greif, and M. Hengsberger, in K. Yamanouchi and K. Midorikawa (eds.), *Multiphoton processes and attosecond physics*, Springer Proceedings in Physics 125, pp 365-368, Springer (Berlin, Heidelberg, 2012).

- *Adsorption of silicon on Au(110): An ordered two-dimensional surface alloy*
  H. Enriquez, A. Mayne, A. Kara, S. Vizzini, S. Roth, B. Lalmi, A. P. Seitsonen, B. Aufray, T. Greber, R. Belkhou, G. Dujardin, and H. Oughaddou, Appl. Phys. Lett. 101, 021605:1-5 (2012).

- *Hedgehog spin texture and Berry's phase tuning in a magnetic topological insulator*
  S.-Y. Xu, M. Neupane, C. Liu, D. Zhang, A. Richardella, L. A. Wray, N. Alidoust, M. Leandersson, T. Balasubramanian, J. Sanchez-Barriga, O. Rader, G. Landolt, B. Slomski, J. H. Dil, J. Osterwalder, T. R. Chang, H. T. Jeng, H. Lin, A. Bansil, N. Samarth, and M. Z. Hasan, Nature Physics 8, 616-622 (2012).

- *Disentanglement of surface and bulk Rashba spin splittings in non-centrosymmetric BiTeI*
  G. Landolt, S. V. Eremeev, Y. M. Koroteev, B. Slomski, S. Muff, T. Neupert, M. Kobayashi, V. N. Strocov, T. Schmitt, Z. S. Aliev, M. B. Babanly, I. R. Amiraslanov, E. V. Chulkov, J. Osterwalder, and J. H. Dil,
  Phys. Rev. Lett. 109, 116403:1-5 (2012).

- *Electronic structure of an organic/metal interface: pentacene/Cu(110)*
  K. Müller, A. P. Seitsonen, T. Brugger, J. Westover, T. Greber, T. Jung, A. Kara,
  J. Phys. Chem. C 116, 23465-23471 (2012).

- *Chiral distortion of confined ice oligomers (n=5,6)*
  H. F. Ma, Y. Ding, M. Iannuzzi, T. Brugger, S. Berner, J. Hutter, J. Osterwalder, T. Greber,
  Langmuir 28, 15246-15250 (2012).

- *Observation of a topological crystalline insulator phase and topological phase transition in $Pb_{1-x}Sn_xTe$*
  S.-Y. Xu, C. Liu, N. Alidoust, M. Neupane, D. Qian, I. Belopolski, J. D. Denlinger, Y. J. Wang, H. Lin, L. A. Wray, G. Landolt, B. Slomski, J. H. Dil, A. Marcinkova, E. Morosan, Q. Gibson, R. Sankar, F. C. Chou, R. J. Cava, A. Bansil, and M. Z. Hasan, Nature Communications 3, 1192:1-9 (2012).

- *Fermi nesting between atomic wires with strong spin-orbit coupling*
  C. Tegenkamp, D. Lükermann, H. Pfnür, B. Slomski, G. Landolt, and J. H. Dil,
  Phys. Rev. Lett. 109, 266401:1-5 (2012).

- *Photoelectron diffraction in the x-ray and ultraviolet regime: Sn-phthalocyanine on Ag(111)*
  M. Greif, L. Castiglioni, A. P. Seitsonen, S. Roth, J. Osterwalder, and M. Hengsberger,
  Phys. Rev. B 87, 085429:1-10 (2013).

- Excitation of coherent phonons in the one-dimensional Bi(114) surface
  D. Leuenberger, H. Yanagisawa, S. Roth, J.H. Dil, J.W. Wells, P. Hofmann, J. Osterwalder, and M. Hengsberger,
  Phys. Rev. Lett. 110, 136806:1-5 (2013).

Article in press

- *Immobilizing individual atoms beneath a corrugated single layer of boron nitride*
  H. Y. Cun, M. Iannuzzi, A. Hemmi, S. Roth, J. Osterwalder, and T. Greber, Nano Letters, in press (2012).

PhD thesis

- *A spin- and angle-resolved photoemission study of the Rashba-Bychkov effect in lead quantum well states*
  Bartosz Slomski, PhD thesis, Physik-Institut, Universität Zürich, 2013.

Master theses

- *Lateral segregation in h-BN/PtRh(111)*
  Roland Stania, Master thesis, Physik-Institut, Universität Zürich, 2012.

- *Luminescence mapping of ordered silver nanoclusters on hexagonal boron nitride nanomesh*
  Carlo Bernard, Master thesis, Physik-Institut, Universität Zürich, 2012.

- *Angle-resolved photoemission spectroscopy of the topological insulator $GeBi_{4-x}Sb_xTe_7$*
  Stefan Muff, Master thesis, Physik-Institut, Universität Zürich, 2013.

Contributed conference presentations

- *Pb/Si(111) - a potential candidate for spin-based electronics*
  B. Slomski, Swiss Light Source Symposium, PSI Villigen, 03.04.12

- *Single-layer boron nitride at the 4-inch wafer scale (Poster)*
  A. Hemmi, Graphene-Week 2012, Delft, The Netherlands, 07.06.12

- *Self-assembled monolayers of endohedral single-molecule magnets (Poster)*
  R. Westerström, Sino-Swiss Science and Technology Cooperation (SSSTC) Workshop, Meielisalp BE, 12.06.12

- *Lateral segregation on h-BN/PtRh(111) (Poster)*
  R. Stania, Sino-Swiss Science and Technology Cooperation (SSSTC) Workshop, Meielisalp BE, 12.06.12

- *Photoelectron diffraction on SnPc/Ag(111) (Poster)*
  M. Greif, Annual Meeting of the Swiss Physical Society, ETH Zürich, 21.06.12

- *Probing interfacial electron transfer dynamics in the attosecond time domain*
  L. Castiglioni, Annual Meeting of the Swiss Physical Society, ETH Zürich, 22.06.12

- *Electron dynamics in a quasi-one-dimensional topological metal: Bi(114)*
  M. Hengsberger, Annual Meeting of the Swiss Physical Society, ETH Zürich, 22.06.12

- *Atomic structure visualization of graphite and monolayer graphene by photoelectron holography*
  F. Matsui, 7th Int. Workshop on Nano-Scale Spectroscopy, ETH Zürich, 04.07.12

- *Photoelectron diffraction spectroscopy for atomic site specific property analysis of surfaces and subsurfaces*
  F. Matsui, Int. Workshop on 3D Atomic Imaging of Nano-Scale Active Sites in Materials, Institute of Solid State Physics, University of Tokyo, Kashiwa, Japan, 07.08.12

- *Influence of the large unit cell on the electronic structure of topological insulators*
  J. H. Dil, Int. Conference on Electron Spectroscopy and Structure (ICESS-12), St. Malo, France, 17.09.12

- *Spin- and angle-resolved photoemission on the topological insulator $PbBi_4Te_7$ (Poster)*
  G. Landolt, Int. Conference on Electron Spectroscopy and Structure (ICESS-12), St. Malo, France, 18.09.12

- *Disentanglement of the surface and bulk Rashba spin splitting in non-centrosymmetric BiTeI (Poster)*
  G. Landolt, Int. Conference on Electron Spectroscopy and Structure (ICESS-12), St. Malo, France, 18.09.12

- *Soft x-ray two-dimensional photoelectron structure factor analysis of graphite valence band by newly developed display-type analyzer*
  F. Matsui, Int. Conference on Electron Spectroscopy and Structure (ICESS-12), St. Malo, France, 18.09.12

- *Disentanglement of the surface and bulk Rashba spin splitting in non-centrosymmetric BiTeI*
  G. Landolt, Swiss Light Source Symposium, PSI Villigen, 02.10.12

- *4f spin shuttles*
  T. Greber, Physik-Seminar, Universität Zürich, 22.11.12

- *Photoemission from solid surfaces in strong fields and on attosecond timescales: the first surface RABBITT*
  L. Castiglioni, NCCR MUST Assembly Meeting 2013, Engelberg, 08.01.13

- *Molecular dynamics and SSC calculations: a combined study on Fe-porphyrin/Ag(111) (Poster)*
  M. Greif, NCCR MUST Assembly Meeting 2013, Engelberg, 08.-10.01.13

- *Single-molecule magnets based on mixed metal nitride cluster fullerenes*
  R. Westerström, Quo Vadis Meeting, PSI Magnetism and Materials, Lungern, 24.01.13

- *$TbSc_2N@C_{80}$/h-BN/Ni(111)*
  R. Stania, Quo Vadis Meeting, PSI Magnetism and Materials, Lungern, 24.01.13

- *Graphene on Ru(0001)*
  T. Greber, European Workshop on Epitaxial Graphene, Aussois, France, 28.01.13

- *Spin shuttles on surfaces ... and nanotents*
  T. Greber, 28th Workshop on High T_c and Novel Materials, Planneralm, Austria, 14.02.13

- *Coherent phonons in one-dimensional atomic chains: Bi(114)*
  M. Hengsberger, Workshop on Short Time Dynamics in Strongly Correlated Electron Systems - Nonequilibrium13, Ruhr-Universität Bochum, Germany, 19.02.13

- *The role of dysprosium in single-molecule magnets based on mixed metal nitride cluster fullerenes*
  R. Westerström, Frühjahrstagung der Deutschen Physikalischen Gesellschaft, Regensburg, Germany, 14.03.13

Invited lectures

- J. H. Dil: *What spin-orbit interaction teaches us: Rashba systems, topological insulators and correlated systems*
  Condensed Matter Physics Seminar, EPF Lausanne, 04.04.12

- J. Osterwalder: *Topological insulators - theory and experiment*
  Tutorial Lecture, Spring Meeting of the Materials Research Society, San Francisco, CA, USA, 09.04.12

- J. Osterwalder: *Probing the spin-momentum locking in topological insulators*
  Spring Meeting of the Materials Research Society, San Francisco, CA, USA, 10.04.12

- F. Matsui: *Photoelectron diffraction spectroscopy for subsurface atomic level characterization*
  Seminar, Max-Planck-Institut für Mikrostrukturphysik, Halle, Germany, 16.04.12
- J. H. Dil: *From quantum well states to topological insulators: spin-resolved ARPES on low-dimensional systems*
  Symposium for the 65th Birthday of Karsten Horn, Fritz-Haber-Institut, Berlin, Germany, 11.05.12
- T. Greber: *Fullerenes on surfaces: from charge switches to spin shuttles*
  XXXV Encontro Nacional de Fisica da Materia Condensada, Aguas de Lindola, Brazil, 15.05.12
- J. H. Dil: *Spin-resolved ARPES on topological insulators and low-dimensional systems*
  Statistical Physics and Low-Dimensional Systems Conference, Pont-*à*-Mousson, France, 31.05.12
- J. Osterwalder: *Spin-polarized electrons on non-magnetic surfaces: from the Rashba effect to topological insulators*
  Münchner Physik-Kolloquium, Technische Universität München, 04.06.12
- F. Matsui: *Direct observation of Si adatom from O atom at the initial stage of Si(111) surface oxidation*
  Swiss Molecule-on-Surfaces (MolCH) Meeting, Bern, 11.06.12
- R. Westerström: *Towards surface supported endohedral single-ion magnets*
  Swiss Molecule-on-Surfaces (MolCH) Meeting, Bern, 11.06.12
- M. Hengsberger: *Ultrafast dynamics in electron emission from negative-electron-affinity diamondoid monolayers*
  Symposium Frontiers of Diamondoid Science, Stanford University, Stanford, CA, 18.06.12
- T. Greber: *Investigating the interplay of geometry and magnetism in spin shuttle molecules on surfaces*
  Annual Meeting of the Swiss Physical Society, ETH Zürich, 21.06.12

- F. Matsui: *Photoelectron diffraction microscopy/spectroscopy for the local structure and property analysis of surfaces*
  Swiss Light Source Seminar, PSI Villigen, 29.06.12
- T. Greber: *Fullerenes on surfaces: from* C_{60} *to spin shuttles*
  Seminar, University of Science and Technology of China, Hefei, China, 04.07.12
- T. Greber: sp^2 *hybridized single-layer honeycomb templates*
  Int. Workshop on Nanomaterials and Nanodevices, Institute of Physics, Beijing, China, 09.07.12
- T. Greber: *Spin shuttles*
  Int. Workshop on Nanomaterials and Nanodevices, Xining, China, 12.07.12
- M. Greif: *Time resolved photoelectron diffraction (tr-PED) for measuring structural dynamics at surfaces*
  Seminar, Université de Bourgogne, Dijon, France, 12.07.12.
- T. Greber: *Functional fullerenes and endofullerenes on surfaces*
  Seminar, National Center for Nanoscience and Technology, Beijing, China, 18.07.12
- J. H. Dil: *Direct spectroscopic evidence of self-protecting topological states*
  CECAM Topological Materials Workshop, Bremen, Germany, 15.08.12
- T. Greber: *Carbon cage spin shuttles*
  24th Conference of the EPS Condensed Matter Division, Edinburgh, Scotland, 03.09.12
- J. Osterwalder: *Spin-polarized electrons on non-magnetic surfaces: from the Rashba effect to topological insulators*
  Int. Conference on Electron Spectroscopy and Structure (ICESS-12), St. Malo, France, 20.09.12
- J. Osterwalder: *Spin-resolved ARPES and resonant x-ray photoelectron diffraction at the SLS*
  25th MAX-lab Users Meeting, Lund, Sweden, 26.09.12
- J. H. Dil: *Spin-resolved ARPES research at the Swiss Light Source*
  2nd Int. School on Surface Science - Technologies and Measurements on Atomic Scale (SSS-TMAS-2), Khosta (Sochi), Russia, 01.10.12

- J. Osterwalder: *Molecular monolayers on well defined surfaces: structure, bonding and dynamics*
  Seminar, Physikalische Chemie, Universität Bern, 04.10.12

- J. H. Dil: *Disentangling the surface and bulk Rashba splittings in non-centrosymmetric BiTeI*
  PSI-IoP (Institute of Physics, Chinese Academy of Sciences) Workshop, Üetliberg, Zürich, 15.10.12

- T. Greber: *Bottom-up nanoscience with sp^2 hybridized single-layer honeycomb lattices*
  Physics Seminar, University of Leiden, The Netherlands, 07.11.12

- J. H. Dil: *Spin-polarized states and topological protection studied by spin-resolved ARPES*
  Physics Seminar, Université de Paris-Sud, Orsay, France, 13.11.12

- T. Greber: *Ice assembly in the h-BN/Rh(111) nanomesh*
  Symposium on Surfae and Nano Science (SSNS'13), Zhao, Japan, 16.01.13

- T. Greber: *From spin-shuttles to nano-tents*
  Quo Vadis Meeting, PSI Magnetism and Materials, Lungern, 25.01.13

- J. Osterwalder: *Spin-polarized electrons on non-magnetic surfaces: from the Rashba effect to topological insulators*
  Colloque en Physique, EPF Lausanne, 18.03.13

20.2.4 Physics of Biological Systems

Articles

- *Non-destructive imaging of an individual protein*
  J.-N. Longchamp, T. Latychevskaia, C. Escher, and H.-W. Fink, Appl. Phys. Lett. 101(9), 093701 (2012).

- *When holography meets coherent diffraction imaging*
  T. Latychevskaia, J.-N. Longchamp, and H.-W. Fink, Opt. Express 20(27), 28871-28892 (2012).

- *Low-energy electron transmission imaging of clusters on free-standing graphene*
  J.-N. Longchamp, T. Latychevskaia, C. Escher, and H.-W. Fink, Appl. Phys. Lett. 101(11), 113117 (2012).

- *Ultraclean freestanding graphene by platinum-metal catalysis*
  J.-N. Longchamp, C. Escher, and H.-W. Fink, J. Vac. Sci. Technol. B 31(020605 (2013).

- *Coherent diffraction and holographic imaging of individual biomolecules using low-energy electrons*
  T. Latychevskaia, J.-N. Longchamp, C. Escher, and H.-W. Fink, in *Present and Future Methods for Biomolecular Crystallography*, Springer, 2013.

- *Resolution enhancement in digital holography by self-extrapolation of holograms*
  T. Latychevskaia and H.-W. Fink, Opt. Express 21(6), 7726-7733 (2013).

- *Fabrication of metallic double-gate field emitter arrays and their electron beam collimation characteristics*
  P. Helfenstein, K. Jefimovs, E. Kirk, C. Escher, H.-W. Fink, and S. Tsujino, Journal of Applied Physics 112(9), 093307 (2012).

- *Electron beam collimation with a 40 000 tip metallic double-gate field emitter array and in-situ control of nanotip sharpness distribution*
  P. Helfenstein, V. A. Guzenko, H.-W. Fink, and S. Tsujino, Journal of Applied Physics 113(4), 043306 (2013).

Article in press

- *Pulsed electron holography*
  M. Germann, T. Latychevskaia, C. Escher, and H.-W. Fink, Appl. Phys. Lett. 102(20), 203115 (2013).

Patent

- *Method for preparing a substantially clean monolayer of graphene*
  J.-N. Longchamp, C. Escher, and H.-W. Fink, Patent EP12189601.12189603 (2012).

Oral presentations

- J.-N. Longchamp: *Probing the surface of graphene by means of low-energy electron coherent diffraction and holographic imaging*
  Symposium on Surface Science, Åre (Sweden), March 3-9, 2013.

- J.-N. Longchamp: *Coherent Low-energy (below 250eV) Electron Diffractive Imaging of Freestanding Graphene*
  Material Research Society Fall Meeting, Boston (USA), November 25-30, 2012.

- T. Latychevskaia: *Low-energy Electron Holograms and Diffraction Patterns of Individual Biomolecules*
  Material Research Society Fall Meeting, Boston (USA), November 25-30, 2012.

- T. Latychevskaia: *Coherent Low-Energy Electron Imaging - a New Tool For Structural Biology*
  45th Erice Crystallographic Course, Erice (Italy), May 31 - June 10, 2012.

- T. Latychevskaia: *When Holography Meets Coherent Diffraction Imaging*
  Digital Holography Meeting of The Optical Society of America, Miami (USA), April 28 - May 2, 2012.

- M. Saliba: *Fourier Transform Holography: A lensless non-destructive imaging technique*
  Poster presentation, Microscopy & Microanalysis 2012, Phoenix, Arizona, USA, July 29 - August 2, 2012.

- M. Saliba: *Fourier Transform Holography: A lensless non-destructive imaging technique*
  European Microscopy Congress, Manchester, UK, September 16-18, 2012.

- P. Helfenstein: *Electron Beam Properties of large Double Gate Field Emitter Arrays with an Optimized Collimation Gate Electrode Geometry*
  Poster presentation, Annual Meeting of the Swiss Physical Society, Zurich, Switzerland, 21.-22 June 2012.

- P. Helfenstein: *Electron Beam Characterization of Double Gate Field Emitter Arrays Fabricated by a Focused Ion Beam Assisted Process*
  Poster presentation, International Vacuum Nanoelectronics Conference, Jeju, Korea, 9-13 July 2012.

- P. Helfenstein: *Molybdenum Field Emitter Arrays for High-Brightness Electron Beams*
  Workshop on Cold Cathodes, Wuppertal, Germany, 3-4 September 2012.

Contributed Paper

- *Fourier Transform Holography: A lensless non-destructive imaging technique*
  M. Saliba, T. Latychevskaia, J.N. Longchamp, and H.-W. Fink, PS2.6, Proceedings of the 15thăEuropean Microscopy Congress.

20.2.5 Physical Systems Biology and non-equilibrium Soft Matter

Articles

- *Integrating force-sensing and signaling pathways in a model for the regulation of wing imaginal disc size*
  T. Aegerter-Wilmsen, M.B. Heimlicher, A.C. Smith, P. Barbier de Reuille, R.S. Smith, C.M. Aegerter, and K. Basler, Development **139**, 3221 (2012).

- *In-vivo imaging of the Drosophila wing imaginal disc over time: novel insights on growth and boundary formation*
  U. Nienhaus, T. Aegerter-Wilmsen, and C.M. Aegerter, PLoSOne **7**, e47594 (2012).

- *Direct determination of the transition to localization of light in three dimensions.*
  T. Sperling, W. Bührer, C.M. Aegerter, and G. Maret, Nature Photonics **7**, 48 (2013).

- *Muon-Spin Rotation Measurements of an Unusual Vortex-Glass Phase in the Layered Superconductor $Bi_{2.15}Sr_{1.85}CaCu_2O_{8+\delta}$.*
  D.O.G. Heron, S.J. Ray, S.J. Lister, C.M. Aegerter, H. Keller, P.H. Kes, G.I. Menon, and S.L. Lee,
  Phys. Rev. Lett **110**, 107004 (2013).

Articles in press

- *Velocity distributions of uniformly heated three dimensional granular gases*
  C.C. Maass, G. Maret, and C.M. Aegerter.

- *Mechanical Control of Organ Size in the Development of the Drosophila Wing Disc*
  T. Schluck, U. Nienhaus, T. Aegerter-Wilmsen, and C.M. Aegerter.

- *Coarsening dynamics of three dimensional levitated foams: from wet to dry*
  N. Isert, G. Maret, and C.M. Aegerter.

Theses

- *Non-linear effects in Anderson localization of light*
  W. Bührer, PhD thesis, Universität Konstanz, 2012.

- *Dynamics of levitated foams*
  N. Isert, PhD thesis, Universität Konstanz, 2013.

Conference reports

- *Mechanical growth regulation of Drosophila wing discs. (poster)*
  U. Nienhaus, T. Aegerter-Wilmsen, T. Schluck, M.B. Heimlicher, K. Basler and C.M. Aegerter,
  URPP Systemsbiology and functional Genomics conference; Brunnen, Switzerland (September 13-15, 2012).

- *Mechanical growth regulation of Drosophila wing discs. (poster)*
  U. Nienhaus, T. Aegerter-Wilmsen, T. Schluck, M.B. Heimlicher, K. Basler and C.M. Aegerter,
  EMBO tissue morphogenesis conference; Heidelberg, Germany (September 6-9, 2012).

- *Scattered light fluorescence microscopy in three dimensions*
  G. Ghielmetti and C.M. Aegerter, Annual Meeting of the Swiss Physical Society, Zürich, Switzerland (24.06.2012).

Invited lectures

- C.M. Aegerter: *Scattered light fluorescence microscopy in three dimensions*
  Biomedical Optics and Photonics, Miami, USA (29.04.2012).

- C.M. Aegerter: *Mechanical growth control in the wing imaginal disc of Drosophila*
  Single Cell Physiology, Paris, France (23.07.2012).

- C.M. Aegerter: *Transition in the coarsening dynamics of foams with different liquid content*
  Swiss Soft Matter Day, Lausanne, Switzerland (29.10.2012).

- C.M. Aegerter: *Time resolved spatial width of photons in samples showing Anderson localization*
  MesoImage Workshop "Recent developments in wave propagation and imaging in complex media", Paris, France (07.11.2012).

- C.M. Aegerter: *Luft ist nicht Nichts*
  Project day in Physics, Primarschule Elsau, Switzerland, (24.01.2013).

20.2.6 Miscellaneous

Article

- *Symmetric Jacobian for local Lyapunov exponents and Lyapunov stability revisited*
  F. Waldner and R. Klages, Chaos, Solitons & Fractals **45** (2012) 325.

Outreach

- S. Roth and D. Leuenberger: *Zukünftige Produktion der HOPPE Holding AG: Werkzeuglose Bearbeitung mit Lasern*
  Invited Consulting Seminar, HPO AG, Hotel Zürichberg, 24.07.12

- Matthias Hengsberger: *Der Laserzoo - ein Streifzug durch die Lasertechnologie*
  Supervision of a Maturarbeit (Hagar Allaham, teacher: Thomas Camenzind), Kantonsschule Zürich Nord, Zürich-Oerlikon, July until October 2012